Multi-pronged analysis of secondary lithium metal batteries with various cathode chemistries

by

Ivan Kochetkov

A thesis

presented to the University of Waterloo

in fulfillment of the

thesis requirement for the degree of

Doctor of Philosophy

in

Chemistry

Waterloo, Ontario, Canada, 2024

© Ivan Kochetkov 2024

Examining Committee Membership

The following served on the Examining Committee for this Thesis. The decision of the Examining Committee is by majority vote

Supervisor:	Linda Faye Nazar Professor, University of Waterloo
Internal Member:	Holger Kleinke Professor, University of Waterloo Aicheng Chen Professor, University of Guelph
Internal-External Member:	Yverick Rangom Assistant Professor, University of Waterloo
External Examiner:	Lingzi Sang Assistant Professor, University of Alberta

Author's Declaration

I hereby declare that I am the sole author of this thesis. This is a true copy of the thesis, including any required final revisions, as accepted by my examiners.

I understand that my thesis may be made electronically available to the public.

Abstract

Due to permanently growing demand for safe and affordable energy, the search for sustainable alternatives to fossil fuels has become one of the most critical challenges of the 21st century. Owing to their high energy density, state-of-the-art lithium-ion batteries are widely applied in different areas of human life, from military drones carrying up to 200 kg of payload to cardioverter-defibrillators. Since current Li-ion technologies have approached the edge of their applicability in electric vehicles, there is an emerging call for developing lithium batteries with better characteristics. Post-LIB technologies, including Li-O_2, Li-S, and solid-state batteries with metallic Li anode, are among the most promising alternatives to replace LIBs. However, post-LIB technologies encounter different fundamental challenges that substantially reduce the capacity retention, safety, and rate capability.

Understanding and resolving some of the challenges of post-LIBs is the focus of this dissertation, with particular attention paid to correlating readily measurable battery characteristics with interfacial processes. This thesis covers multiple topics, including Li-O_2 batteries, Li metal batteries with liquid and solid-state electrolytes, Li-S batteries with hybrid/liquid electrolytes, and all-solid-state batteries with high-energy-density cathodes. This work establishes multi-pronged approaches to study the efficacy of various electrolytes. A novel approach is demonstrated for stabilizing a Li^+-conducting garnet solid electrolyte in Li-S batteries with electron pair donor electrolytes.

Chapter 3 of the thesis presents the study of LiI as a potential charge redox mediator for nonaqueous Li-O_2 batteries. The effect of LiI on oxygen electrochemistry during battery charge and discharge is investigated by combining various characterization techniques. This chapter demonstrates that the battery performance becomes less reversible when the electrolyte contains LiI. The combination of DEMS and iodometric titrations indicates that LiI lowers the yield of the target discharge product, Li_2O_2, and triggers redox shuttling on charge. The simultaneous presence of LiI and H_2O in the electrolyte results in the irreversible 4e reduction of oxygen to LiOH.

Chapters 4 – 5 are devoted to developing lithium metal batteries with different battery configurations and cathode chemistries. In Chapter 4, a comprehensive study of the solvate ionic liquid electrolytes containing LiFSI, G_n, and TTE establishes the relationship between the length of glyme solvents and the stability of Li anodes. The combination of Raman spectroscopy, AIMD simulations,

and EIS illustrates that the kinetics of lithium metal anodes in solvate ionic liquid electrolytes containing long-chain G_n (G_3 and G_4) is impeded by the formation of the $[Li(G_n)]^+$ chelates. In contrast, the $G_1(G_2)$-based SILs' solvation structure is primarily comprised of strongly associated Li^+ and FSI^-, which reduces the interfacial resistance and activation energy barriers. However, the lithium transference number of the solvate electrolytes is limited to ~0.2, which dictates the diffusion-limited rate capability of the Li anode. The chapter demonstrates that the rate capability limit observed in the asymmetric Cu-Li and full Li||LiNCA cells agrees with the values predicted by combining the EIS results and existing Li dendrite formation models.

The stability of Li anodes in solid-state cells with sulfide-based solid electrolytes is investigated in Chapter 6. This case study demonstrates that the presence of Si^{4+} in the structure of sulfide solid-state electrolytes triggers continuous interphase growth, which may consume a 50 μm Li anode. Meanwhile, the solid electrolytes, devoid of reducible cations, facilitate Li deposition with a CE exceeding 99 % when the current density is limited to 0.1 $mA.cm^{-2}$. However, Li deposition at higher current densities is interrupted by the formation of Li dendrites. Nevertheless, the performance of Li anodes may be temporarily improved by modifying the solid electrolyte with a sacrificial dendrite scavenger or wetting the Li/solid electrolyte interface with a solvate, as developed in Chapter 4.

The novel concept of the Li-S battery with a $Li_{6.5}La_3Ta_{0.5}Zr_{1.5}O_{12}$ (LLZO) garnet solid electrolyte and an electron pair donor electrolyte, DMA, is demonstrated in Chapter 6. Numerous characterization techniques were employed to investigate the interfacial reactivity between LLZO and sulfur in DMA. Traces of LiOH and Li_2CO_3 at the surface of LLZO trigger the oxidation of sulfur and formation of $S_3^{\cdot-}$, which further reacts with LLZO, yielding an insulating layer containing thiosulfate, polythionate and La-O/La-O-S species. The interfacial instability of LLZO results in a rise in the interfacial resistance (> 5000 $\Omega.cm^2$) and rapid capacity fading of the Li-S batteries. Nonetheless, phosphorylating LLZO yields a thin (~ 10 nm) and conductive (~ 40 $\Omega.cm^2$) layer containing Li, La, and Zr phosphates, which inhibits the side reactions. Therefore, Li-S batteries with phosphorylated LLZO and DMA deliver a stable capacity of 1400 $mAh.g^{-1}$.

Chapter 7 is devoted to all-solid-state batteries with $LiNi_xCo_yMn_{1-x-y}O_2$ cathodes and Li-M-Cl ($Li_{2.5}Y_{0.5}Zr_{0.5}Cl_6$, Li_3InCl_6, $L_2Sc_{1/3}In_{1/3}Cl_4$) catholytes. The effect of M in Li-M-Cl on the battery performance is analyzed through DFT calculations, electrochemical methods, and ToF-SIMS. Cycling

solid-state batteries with $LiNi_{1/3}Co_{1/3}Mn_{1/3}O_2$ and $LiNi_{0.85}Co_{0.1}Mn_{0.05}O_2$ demonstrates that capacity fading depends on oxygen evolution in $LiNi_xMn_yCo_{1-x-y}O_2$ and the nature of M in Li-M-Cl. When $LiNi_xMn_yCo_{1-x-y}O_2$ does not undergo an OER, the cell performance is dictated by the intrinsic electrochemical stability of Li-M-Cl. However, the interfacial reactivity between $LiNi_xMn_yCo_{1-x-y}O_2$ and Li-M-Cl is more important when OER occurs. The chapter also establishes a multi-pronged approach to study the performance of new solid electrolytes in solid-state batteries with high-energy-density cathode active materials.

Acknowledgements

I want to express my sincere gratitude to my supervisor and mentor, Dr. Linda Faye Nazar. Her tremendous support and guidance, especially in the most challenging times of my professional and personal life, cannot be overestimated. I want to thank my committee members, Dr. Holger Kleinke, Dr. Pavle Radovanovic, Dr. Aicheng Chen, and Dr. Jacek Lipkowski, for their time discussing my work. I am also very thankful to Dr. Yverick Rangom and Dr. Lingzi Zhang for being my internal-external and external examiners, respectively. I am grateful to Dr. Kavish Kaup, Dr. Laidong Zhou, Dr. Baltej Singh, Dr. Robert Black, Dr. Xiao Liang and Dr. Quanquan Pang for our productive collaborative work.

I am very thankful to our collaborators. I want to thank Dr. Juergen Janek (University of Giessen) and the members of his group, Dr. Raffael Ruess and Dr. Tong-Tong Zuo, with whom I explored solid-state lithium batteries and learnt new approaches to fit EIS. Exploring the chemistry of Li-S and LLZO was only possible with the help of Dr. Jeff Sakamoto and Max Palmer. (University of Michigan). I also wish to thank Dr. Andrew Gewirth and Maria Philipp (University of Illinois Urbana-Champain), with whom I studied the solvate electrolytes. Finally, I am very thankful for the opportunity to work with Dr. Bryan McCloskey (University of Berkeley) and Dr. Dan Addison (Liox Power) at the beginning of my graduate studies.

I was also honoured to have an opportunity to work with and learn from very smart and motivated individuals. I want to thank my former and current colleagues in Dr. Nazar's group: Abhi, Seyoung, Parvin, Dipan, Lauren, Yubo, Zhou, Markus, Insang and Vipin. I also enjoyed sharing the office with Ali, Lan, and Dion.

I want to thank my family: my mother, Anastasia; my father, Roman; my younger siblings, Stepan and Sofya; and my grandfather, Ivan, for their unconditional love and support. I also cannot forget the support and love of my beloved deceased grandmothers Venera and Tatiana and my grandfather Vladilen. Additionally, I must express my gratitude to my step-uncle, Dr. Boris Bogolomolov, who remains a role model for several generations of my family even after his death. Finally, I must mention the new person in my life, Kate, who believes in me even when I am about to give up.

Table of Contents

Examining Committee Membership ii

Author's Declaration iii

Abstract iv

Acknowledgements vii

List of Figures xiv

List of Tables xvi

List of Abbreviations xvii

Chapter 1 Introduction 20

1.1 Electrochemical Energy Storage 20

1.2 Limitations of LIBs and Promising Post-LIB Technologies 21

1.3 Nonaqueous Li-O_2 and Li-S batteries 22

1.3.1 Principles of Li-O_2 and Li-S Batteries 22

1.3.2 Mechanisms and Challenges of Li-O_2 Batteries 24

1.3.3 Redox Mediators for More Efficient ORR and OER 26

1.3.4 Mechanisms and Challenges of Li-S Batteries 28

1.3.5 Approaches for Preventing LPS Redox Shuttling 30

1.3.6 Li-S Batteries with EPD Electrolytes 32

1.4 Lithium Metallic Anode 34

1.4.1 Li SEI 35

1.4.2 Models of Li Dendrite Formation 37

1.4.3 Correlations between the Challenges of LMAs 39

1.4.4 Approaches to Li Protection 40

1.4.5 Artificial Li SEIs 40

1.4.6 Advanced electrolytes for LMBs 43
1.5 Solid-state Li Batteries 46
1.6 Challenges of Li-M SSBs 48
1.7 Challenges of NCM-based Cathodes in SSBs 49
1.8 Thesis Overview 51
Chapter 2 Methods 54
2.1 X-Ray Diffraction 54
2.2 Scanning Electron Microscopy and Energy-dispersive X-Ray Spectroscopy 54
2.3 Raman Spectroscopy 55
2.4 Photoelectron Spectroscopy 57
2.5 Differential Electrochemical Mass-Spectrometry 58
2.6 Time-of-Flight Secondary Ion Mass Spectrometry 58
2.7 Ultraviolet-Visible Spectroscopy 59
2.8 Galvanostatic Cycling 59
2.9 Cyclic Voltammetry 60
2.10 Electrochemical Impedance spectroscopy 60
Chapter 3 Reversibility of Li-O_2 Batteries with LiI Redox Mediator 64
3.1 Introduction 64
3.2 Experimental methods 66
3.2.1 Materials 66
3.2.2 Preparation of Cathodes 66
3.2.3 Cell Assembly 66
3.2.4 DEMS 66
3.2.5 Quantification of Li_2O_2 67

3.2.6 Detection of $LiIO_3$ 67
3.2.7 XRD Analysis 67
3.2.8 SEM 68
3.3 Effect of LiI and H_2O on the Polarization of Li-O_2 Batteries 69
3.4 Effect of LiI on the Reversibility of Li-O_2 Batteries 70
3.5 Mechanism of LiOH Removal during Charging 72
3.6 Conclusions 73
Chapter 4 Solvate Electrolytes with LiFSI and Glyme Solvents for LMBs 74
4.1 Introduction 74
4.2 Experimental Methods 75
4.2.1 Materials 75
4.2.2 Preparation of Electrolytes 75
4.2.3 Raman Spectroscopy 75
4.2.4 SEM 76
4.2.5 AIMD Simulations 76
4.2.6 EIS of Li Symmetric Cells 77
4.2.7 Galvanostatic Polarization of Li Symmetric Cells 78
4.2.8 CE of Li Deposition 78
4.2.9 Preparation of Full Cells with NCA Cathodes 78
4.3 Solvation Structure of $114G_n$ 80
4.4 Li^+ Transport Properties of $114G_n$ 85
4.4.1 Full-range EIS of Li Symmetric Cells with $114G_1$ 85
4.4.2 Effect of G_n on Li^+-transport Rate 89
4.4.3 Diffusion-triggered Deposition of Li Dendrites 91

4.5 Effect of G_n on the Stability of Long-term Li Deposition....94
4.5.1 Stability of Li Deposition from $114G_1$....94
4.5.2 Relationship between G_n and Li Deposition Efficiency....99
4.6 Performance of LMBs with $114G_n$ Solvate Electrolytes....101
4.7 Conclusions....104
Chapter 5 Stability of Lithium Metal Anodes in SSBs with Sulfide SEs....106
5.1 Introduction....106
5.2 Experimental Methods....107
5.2.1 Synthesis of SEs....107
5.2.2 Cell Assembly....107
5.2.3 Electrochemical Measurements....108
5.2.4 XRD Analysis of Reacted SEs....109
5.3 Stability of LMA is SS Cells with Sulfide Electrolytes....109
5.3.1 LMA Stability of Sulfide SEs at OCV....109
5.3.2 CE of Li Deposition from Sulfide SEs....111
5.3.3 Limited Rate Capability of Li symmetric SS cells with β-Li_3PS_4....113
5.4 Improved Performance of LMA in SS Cells with Sulfide SEs....115
5.4.1 Dendrite-scavenging Multilayer SEs....115
5.4.2 $114G_2$-assisted Improved Performance of LMA....117
5.5 Conclusions....119
Chapter 6 Interfacial Chemistry of Ta-doped LLZO in EPD Electrolytes....120
6.1 Introduction....120
6.2 Experimental Methods....121
6.2.1 RAT of LLZO pellets....121

6.2.2 Preparation of Sulfur Cathodes 121
6.2.3 Preparation of Sulfur Symmetric cells 121
6.2.4 Preparation of Full Li||S cells 122
6.2.5 XPS Analysis 122
6.2.6 UV-Vis Measurements 122
6.3 High-energy-density Li-S Batteries with Hybrid LLZO/DMA Electrolytes 123
6.4 Reactivity Between LLZTO and S in EPD Electrolytes 124
6.5 Interfacial Reactivity between Acid-treated LLZO SEs and Sulfur in DMA 127
6.6 XPS Study of Reactivity between RAT-LLZO and S in DMA 131
6.7 Electrochemical Performance of Li-S Batteries with LLZO/DMA 132
6.8 Conclusions 135
Chapter 7 Interfacial Reactivity Between Lithium Metal Chloride Electrolytes and High-energy Density NCM 136
7.1 Introduction 136
7.2 Experimental methods 137
7.2.1 Synthesis of the SEs 137
7.2.2 Assembly of SSB Cells and Electrochemical Measurements 138
7.2.3 UPS Measurements of Chloride SEs 138
7.2.4 FIB-SEM 139
7.2.5 ToF-SIMs 139
7.2.6 DFT Calculations 139
7.3 Electrochemical Performance of NCM85 SSB with Chloride SEs 141
7.4 Voltage-dependent Interphase Growth between NCM85 and Li-M-Cl 145
7.5 Composition-dependent Electrochemical Stability of Li-M-Cl 148

7.6 Interfacial Reactivity between Ni-rich NCM and Li-M-Cl 150
7.7 Conclusions 155
Chapter 8 156
Conclusions and Future Prospects 156
8.1 Conclusions 156
8.2 Future Prospective 158
References 160
Appendix A Oxygen Evolution in the Presence of LiI 187
Appendix B Reactivity between LiI and O_2^- 187
Appendix C Determination of t_{Li} by the Bruce-Vincent Method 188

List of Figures

Figure 1.1 Timeline of battery development....20
Figure 1.2 Schematic of a LIB....21
Figure 1.3 Schematic of Li-O_2 and Li-S batteries....23
Figure 1.4 Impact of LiO_2 on Li-O_2 batteries....25
Figure 1.5 DBBQ-mediated ORRs....26
Figure 1.6 Redox reactions of sulfur in DOL/DME electrolytes....28
Figure 1.7 Li-S batteries with sparingly solvating electrolytes....31
Figure 1.8 Li-S batteries with EPD electrolytes....33
Figure 1.9 Challenges of LMA....35
Figure 1.10 Li SEI....36
Figure 1.11 Formation of Li dendrites....38
Figure 1.12 Correlation between the challenges of LMA....39
Figure 1.13 Stabilization of LMA by LHCEs....45
Figure 1.14 Solid-state lithium batteries....47
Figure 1.15 LMA challenges in SSBs....48
Figure 2.1 Processing of Raman spectra....56
Figure 2.2 Fundamentals of EIS....61
Figure 3.1 Electrochemical performance of the Li-O2 battery with LiI and H_2O....69
Figure 3.2 Effect of [LiI] on the yield of Li_2O_2....70
Figure 3.3 OER of the Li-O2 battery with 200 mM LiI and 5 K $H_2{}^{18}O$....71
Figure 3.4 Conversion of LiOH to $LiIO_3$....72
Figure 4.1. Raman spectra of LiFSI-G_n-TTE....81
Figure 4.2 AIMD simulations of $Li(G_n)_1FSI$....83
Figure 4.3 AIMD simulations of $114G_n$....84
Figure 4.4 Aging Li symmetric cells....85
Figure 4.5 EIS studies of Li symmetric cells with $114G_1$....86
Figure 4.6 G_n-dependent transport properties of $114G_n$....90
Figure 4.7 Deposition of Li dendrites from $114G_n$....92
Figure 4.8 Effect of current density and plating capacity on the CE of Li deposition from $114G_1$....96
Figure 4.9 Effect of current density of the morphology of Li deposition from $114G_1$....97

Figure 4.10 CE of Li deposition form $114G_n$ at 1 $mA.cm^{-2}$ 99
Figure 4.11 Effect of G_n and Cu substrate on the morphology of Li 100
Figure 4.12 Electrochemical performance of LMBs with NCA cathodes and $114G_n$ 102
Figure 4.13 Mechanisms of LMA degradation in Li||NCA cells with $114G_n$. 104
Figure 5.1 Reactivity of LMA with sulfidic SEs 110
Figure 5.2 CE of Li deposition from sulfidic SEs 111
Figure 5.3 Composition of the Li/sulfidic SE interphase 113
Figure 5.4 Rate capability of Li symmetric cells with β-Li_3PS_4 114
Figure 5.5 Performance of Li symmetric cells multilayer with sulfidic SE 115
Figure 5.6 Performance of the Li||TiS_2 full cell with multilayer sulfidic SE 116
Figure 5.7 Chemical stability of $Li_{5.5}PS_{4.5}Cl_{1.5}$/$114G_2$ hybrid electrolytes 117
Figure 5.8 8 Performance of Li symmetric cells with $Li_{5.5}PS_{4.5}Cl_{1.5}$/114G2 hybrid electrolytes 118
Figure 6.1 Energy density of Li-S batteries with LLZO/DMA electrolytes 123
Figure 6.2 Instability of HT-LLZO in S/DMA. 125
Figure 6.3 LLZO-triggered formation of $S_3^{\cdot -}$ 126
Figure 6.4 Effect of HCl-RAT on the surface chemistry of LLZO 128
Figure 6.5 Stability of HPO-LLZO 130
Figure 6.6 RAT-dependent interfacial stability of LLZO 132
Figure 6.7 Room temperature performance of Li-S batteries with LLZO/DMA 133
Figure 6.8 Cycling Li-S batteries with LLZO/DMA at higher C-rates. 134
Figure 7.1 Electrochemical performance of the NCM85-*chloride SE* CAMs 141
Figure 7.2 Microstructure of the NCM85-*Li-M-Cl* CAMs 143
Figure 7.3 Evolution of $R_{cathode}$ during cycling the SSB cells 144
Figure 7.4 Growth of the NCM85/chorode SE interphase 146
Figure 7.5 Oxidative stability of the chloride SEs 149
Figure 7.6 Effect of Ni content on the stability of NCM-*chloride SE* cathodes 151
Figure 7.7 ToF-SIMS Analysis of the NCM85/chloride SE interphase 154

List of Tables

Table 1.1 Approximate voltage and energy density of LIBs, Li-O_2 and Li-S batteries 23
Table 1.2 Structures of the salts, solvents, and diluents employed for the high-performance LMBs ..43
Table 2.1 Diffusion impedance at different boundary conditions 63
Table 4.1 Details of the box for the AIMD simulations 77
Table 4.2 Assignment of the individual Raman modes of FSI^- 80
Table 4.3 Deconvolution of the FSI band in 1M LiFSI/G_n, $Li(G_n)_1FSI$, and $114G_n$ electrolytes 82
Table 4.4 Fitting of the EIS of the symmetric cells with Li electrodes and $114G_1$ solvate electrolyte 88
Table 4.5 Limiting current density of $114G_n$ solvate electrolytes 91
Table 4.6 Transport properties of $114G_1$ 94
Table 4.7 Average Li consumption during the SEI formation in $114G_1$ at 1 $mA.cm^{-2}$ 95
Table 6.1 Details of the 345 $Wh.kg^{-1}$ Li-S battery with LLZO/DMA electrolyte 124
Table 6.2 Chemical composition of the LLZO surface. 129
Table 7.1 Interfacial growth of NCM85-*SE* cathodes 147
Table 7.2 Reactivity between $Li_{1-x}NiO_2$ and Li-M-Cl SEs 152

List of Abbreviations

AGG	Ionic aggregates
AIMD	Ab initio molecular dynamics
ALD	Atomic layer deposition
CAM	Cathode active material
CE	Coulombic efficiency
CEI	Cathode electrolyte interphase
CIP	Contact ion pairs
CVA	Cyclic voltammetry
DBBQ	2,5-di-tert-butyl-1,4-benzoquinone
DEC	Diethyl carbonate
DEMS	Differential electrochemical mass-spectrometry
DFT	Density function theory
DMA	Dimethylacetamide
DMDMB	2,3-dimethoxy-2,3-dimethylbutane
DMF	Dimethylformamide
DMI	1,3-dymethyl-2-imidazolidinone
DOL	1,3-dioxolane
E/S	Electrolyte-to-sulfur ratio
EC	Ethylene carbonate
ED	Energy density
EDX	Energy dispersive X-ray spectroscopy
EIS	Electrochemical impedance spectroscopy
EPD	Electron pair donor
FE	Fluorinated ether
FEC	Fluoroethylene carbonate
FWHM	Full width at half maximum
G_1, DME	1,2-dimethoxyethane
G_2	Diethylene glycol dimethyl ether
G_3	Triethylene glycol dimethyl ether
G_4, TEGDME	Tetraethylene glycol dimethyl ether

GF	Glass fibre
HCE	High-concentration electrolytes
HCl-LLZO	HCl-treated LLZOLLZO
HPO-LLZO	H_3PO_4-treated LLZOLLZO
HRTEM	High-resolution transmissive electron microscopy
ICSD	Inorganic Crystal Structure Database
KB	Ketjen black
LE	Liquid electrolyte
LHCE	Localized high-concentration electrolytes
LIB	Lithium-ion batteries
LIC	Li_3InCl_6
LiFSI	Lithium bis(fluorosulfonyl)imide
LiM-SSB	Solid-state battery with metallic Li anode
LiTFSI	Lithium bis(trifluorofluorosulfonyl)imide
LLZO (Ta-doped)	$Li_{6.5}La_3Ta_{0.5}Zr_{1.5}O_{12}$
LMA	Lithium metal anode
LMB	Lithium metal battery
LPS	Lithium polysulfide
LSIC	$Li_2Sc_{0.5}In_{0.5}Cl_4$
LUMO	Lowest unoccupied orbital
LYZC	$Li_3Zr_{0.5}Y_{0.5}Cl_6$
MCI	Mixed conducting interphase
MLD	Molecular layer deposotion
NCA	$LiNi_{0.8}Co_{0.15}Al_{0.05}O_2$
NHE	Normal hydrogen electrode
NCM	$LiNi_xMn_yCo_{1-x-y}O_2$
NCM111	$LiNi_{1/3}Co_{1/3}Mn_{1/3}O_2$
NCM85	$LiNi_{0.85}Co_{0.1}Mn_{0.05}O2$
OCP, OCV	Open circuit potential, open circuit voltage
OER	Oxygen evolution reaction
ORR	Oxygen reduction reaction

$Pyr_{14}TFSI$	1-Butyl-1-methylpyrrolidinium bis(trifluorofluorosulfonyl) imide
RAT	Rapid acid treatment
RM	Redox mediator
SEI	Solid electrolyte interphase
SEM	Scanning electrolyte interphase
SE	Solid electrolyte
SIL	Solvate ionic liquid
SL	Sulfolane
SLEI	Solid-liquid electrolyte interphase
SOA	State-of-art
SSB	Solid-state battery
SSIP	Solvent-separated ion pair
TEP	Triethyl phosphate
THF	Tetrahydrofuran
ToF-SIMS	Time-of-flight secondary ion mass-spectroscopy
UPS	Ultra-violet spectroscopy
UV-Vis	UV-visible
XPS	X-ray photoelectron spectroscopy
XRD	X-ray diffraction

Chapter 1
Introduction

1.1 Electrochemical Energy Storage

Ever-increasing energy consumption is one of the most alarming problems of today's society. This issue has been resolved for nearly two centuries through harvesting energy stored by chemical bonds in hydrocarbons or, simply speaking, by burning non-renewable fossil fuels. However, a growing demand for affordable, safe, and eco-friendly energy storage makes the fossil fuel economy unsustainable and motivates the search for renewable alternatives.

Generating electricity with rechargeable batteries is one of the most promising avenues to our sustainable future. Since Alessandro Volta's and Johann Ritter's pioneer work in the early 1800s, tremendous success has been achieved in pursuing batteries with higher energy density and longer cycling life. The timeline of the most important discoveries related to the battery research field was nicely summarized by Winter *et al*[1] (**Figure 1.1**).

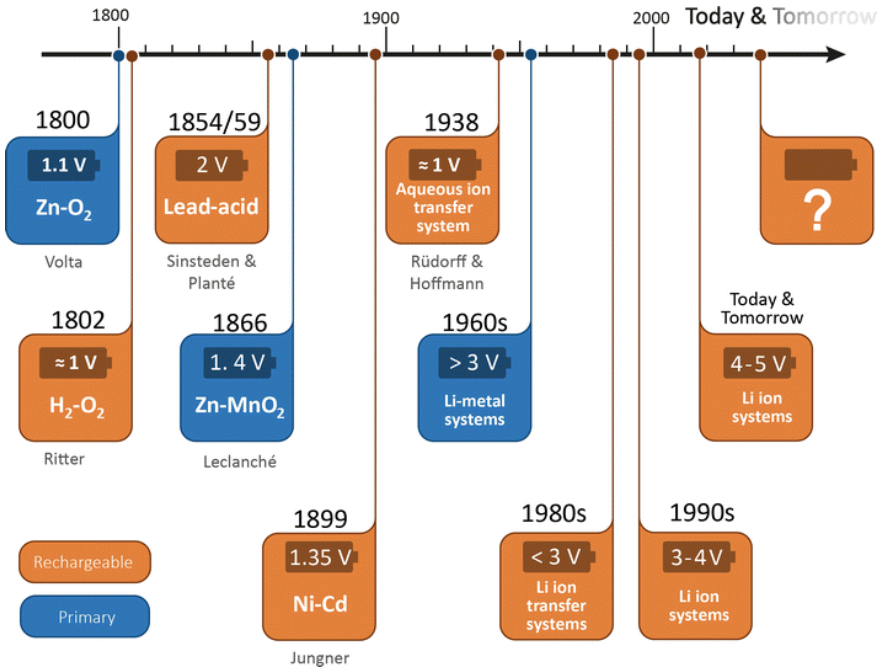


Figure 1.1 Timeline of battery development. Reprinted with permission from Ref. 1.

In a simple electrochemical battery, electricity is generated by the reaction between an oxidizing and reducing agent, which resembles a bulk redox reaction. However, the half-reactions

occurring in the battery are spatially separated and occur at different electrodes. Electrons withdrawn from the reducing agent are transferred to the oxidizing agent through an external load, which generates an electrical current. The battery contains a positive and negative electrode. The positive electrode (cathode) has a higher potential than the negative electrode (anode) and is reduced upon spontaneous discharge. Of note, inert electrodes at which reduction occurs (i.e., reduction of O_2 to Li_2O_2 at carbon surface) are also labelled cathodes in the battery research field.

A schematic representation of a rechargeable lithium-ion battery (LIB) containing a $LiCoO_2$ cathode, a graphite anode, and a conventional organic electrolyte is shown in **Figure 1.2**.[2] Initially, the $C_6||LiCoO_2$ battery is in the discharged state, and it has to be charged first. On charge, x Li^+ and x electrons are deintercalated from $LiCoO_2$ and intercalated to C_6, forming $Li_{1-x}CoO_2$ and Li_xC_6 (**Equations 1.1-1.3**). The electrons are transferred through an external circuit, while Li^+ ions move through the electrolyte via a series of solvation/desolvation and mass-transport steps. The reversed reaction occurs on discharge, and the battery can be cycled until its capacity reaches a minimum cutoff.

Cathode: $LiCoO_2 \leftrightarrow Li_{1-x}CoO_2 + xLi^+_{solv.} + xe^-$ **Equation 1.1.1**

Anode: $C_6 + xLi^+_{solv.} + xe^- \leftrightarrow Li_xC_6$ **Equation 1.1.2**

Net: $LiCoO_2 + C_6 \leftrightarrow Li_{1-x}CoO_2 + Li_xC_6$ **Equation 1.1.3**

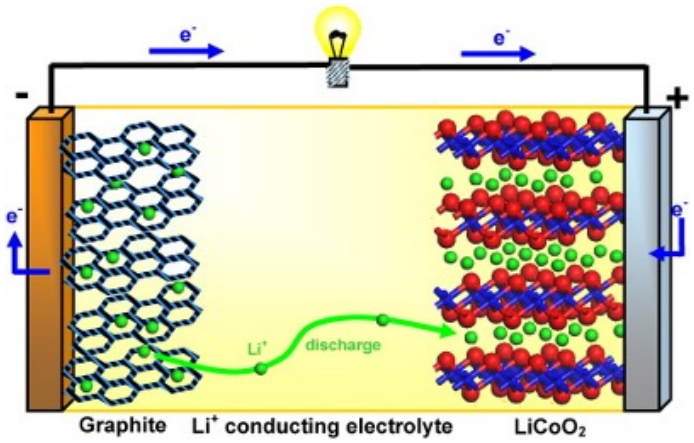


Figure 1.2 Schematic of a LIB. Reprinted with permission from Ref. 2.

1.2 Limitations of LIBs and Promising Post-LIB Technologies

Since the first LIBs were commercialized by Sony Corporation in 1991, the energy density of LIBs has constantly been increasing. Thus, state-of-the-art (SOA) LIBs with intercalation electrodes and liquid

electrolytes are exponentially reaching their maximum energy density of ~ 260 $Wh.kg^{-1}$.[1] However, automotive applications require better batteries, which deliver 350 $Wh.kg^{-1}$ and meet other strict technical requirements such as long-term cyclability (1000 cycles), temperature range between -30 and 50 °C, and cost of $\$100.kWh^{-1}$.[3] Therefore, the development of post-LIB technologies has become one of the most promising and demanded directions to pursue a sustainable future.

The search for more efficient alternatives to the LIB technology includes different research directions, such as lithium batteries, which employ cheap and high-capacity cathodes (i.e., oxygen,[4] sulfur,[5,6] CO_2[6]), metallic Li anodes, and solid-state electrolytes. Furthermore, the development of non-lithium batteries is another promising opportunity to reduce the cost and avoid lithium shortages. For instance, despite their lower energy density, sodium-based batteries could significantly reduce prices compared to LIBs.[7] The field of rechargeable multivalent batteries with Mg and Zn anodes is also interesting due to the high volumetric energy density of Mg and Zn.[8] Nevertheless, only aqueous Zn^{2+}-ion batteries may compete with LIBs regarding total energy density and cyclability.[9]

Since my research is focused on advanced Li batteries, multivalent batteries are not discussed in the Introduction. The Introduction is devoted to the principles and challenges of post-LIBs, including high-capacity conversion cathodes (O_2 and S), lithium batteries employing Li anodes, and solid-state lithium batteries.

1.3 Nonaqueous Li-O_2 and Li-S batteries

1.3.1 Principles of Li-O_2 and Li-S Batteries

Li-O_2 and Li-S batteries generate electricity via conversion reactions at the cathode and exhibit numerous advantages compared to conventional LIBs. Oxygen and sulfur are abundant and offer high theoretical capacities of 1165 and 1675 $mAh.g^{-1}$, respectively, when discharged to Li_2O_2 and Li_2S, respectively Moreover, Li-S and Li-O_2 batteries can be charged at a voltage below 4 V, which reduces the risk of electrolyte oxidation. Although the working voltage of oxygen and sulfur-based cathodes is lower than that of intercalation-type cathodes, nonaqueous Li-O_2 and Li-S batteries exhibit much higher theoretical energy density (**Table 1.1**).[10]

Table 1.1 Approximate voltage and energy density of LIBs, Li-O_2 and Li-S batteries. Reprinted from Ref. 10.

Battery	Cell Voltage (V)	Theoretical specific energy ($Wh.kg^{-1}$)	Theoretical energy density ($Wh.L^{-1}$)
C_6||$LiCoO_2$	3.8	387	1015
Li-O_2	3.0	3505	3436
Li-S	2.2	2567	2199

The schematics of Li-O_2 and Li-S batteries containing nonaqueous ether-based electrolytes and carbon-based positive electrodes are shown in **Figure 1.3**. The Li-O_2 battery cathode employs lightweight, high-surface electrodes to maximize the utilization of O_2, whereas the positive sulfur electrode is a mix of elemental sulfur and conductive additives. Additionally, both types of cathodes contain 5 to 10 weight percent of a polymer binder, which helps to maintain the mechanical integrity and withstand the volume changes during cycling.

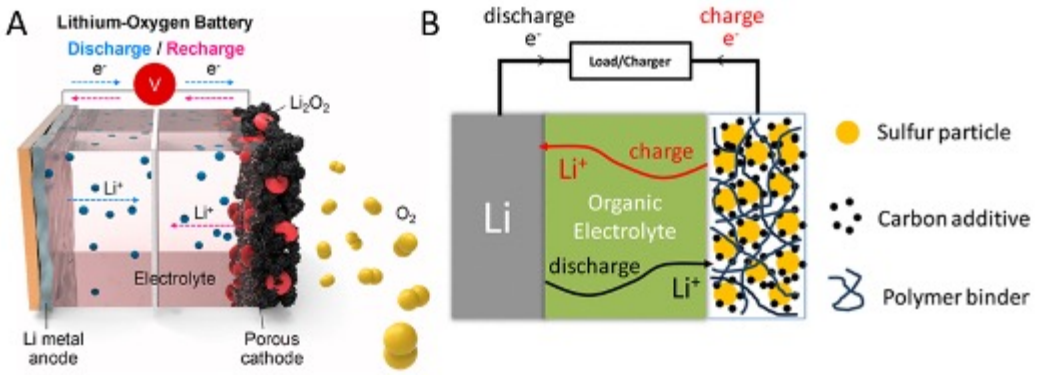


Figure 1.3 Schematic of Li-O_2 and Li-S batteries. (A) Li-O_2 and (B) Li-S battery batteries. Reprinted with permission from Ref. 4 and 5, respectively.

Since there is a significant difference between the electrochemistry of oxygen and sulfur in nonaqueous electrolytes, the reaction mechanisms and challenges of aprotic Li-O_2 and Li-S batteries are discussed separately. However, the Li-O_2 and Li-S batteries exhibit some similarities in their general operation principle and challenges. For example, the limited rate capability and capacity retention of Li-O_2 and Li-S batteries are caused by the low electronic conductivity of discharge products, formation of reactive intermediates, and instability of lithium metal anodes.

1.3.2 Mechanisms and Challenges of Li-O_2 Batteries

At room temperature, the oxygen reduction reaction (ORR) in the nonaqueous Li-O_2 battery yields lithium peroxide (Li_2O_2).[11] The mechanism of ORR is complex because there are two pathways to form Li_2O_2 as the ultimate discharge product. The first step involves a $1e^-$ reduction of dissolved O_2 to lithium superoxide (LiO_2). Depending on the solvent donor number (DN), [12] applied current density,[13] and presence of solubilizing electrolyte additives,[14] the LiO_2 intermediate either dissolves into the electrolyte or precipitates at the positive electrode surface. After that, LiO_2 may be electrochemically reduced to Li_2O_2. However, since LiO_2 is unstable and reactive, it undergoes two competing processes: chemical decomposition to Li_2O_2 and side reactions with the electrolyte components.[15] Interestingly enough, some studies report on the presence of LiO_2 in the discharge product under very specific experimental conditions.[16,17] The mechanism of ORR involving soluble LiO_2 is summarized in **Equations 1.4-1.9**:

$$Li^+_{solv.} + O_{2(solv.)} + e^- \rightarrow LiO_{2(solv.)} \qquad \textbf{Equation 1.4}$$

$$2LiO_{2(solv.)} \rightarrow Li_2O_{2(s)} + O_{2(solv.)} \qquad \textbf{Equation 1.5}$$

$$LiO_{2(solv.)} + O_{2(solv.)} + e^- \rightarrow Li_2O_{2(s[1])} \qquad \textbf{Equation 1.6}$$

$$Li^+_{solv.} + O_{2(solv.)} + e^- \rightarrow LiO_2^* \qquad \textbf{Equation 1.7}$$

$$LiO_2^* + Li^+_{(solv.)} + e^- \rightarrow Li_2O_{2(s)} \qquad \textbf{Equation 1.8}$$

$$2LiO_2^* \rightarrow Li_2O_{2(s)} + O_{2(solv.)} \qquad \textbf{Equation 1.9}$$

The morphology of Li_2O_2 deepens on the mechanism of ORR. If the ORR involves the dissolution of LiO_2, Li_2O_2 exhibits a distinctive toroidal shape. Otherwise, Li_2O_2 films are formed.[13] Unfortunately, the ORR in aprotic electrolytes unavoidably forms LiO_2 intermediate, which rapidly reacts with organic solvents,[18–22] salts,[23,24] polymer binders,[25] and conductive carbon network.[26–28] This lowers the yield of Li_2O_2 to below 90 % after the first discharge[29] and forms an insulating layer around the Li_2O_2 particles, as schematically illustrated in **Figure 1.4 A, B.**

[1] s = solid

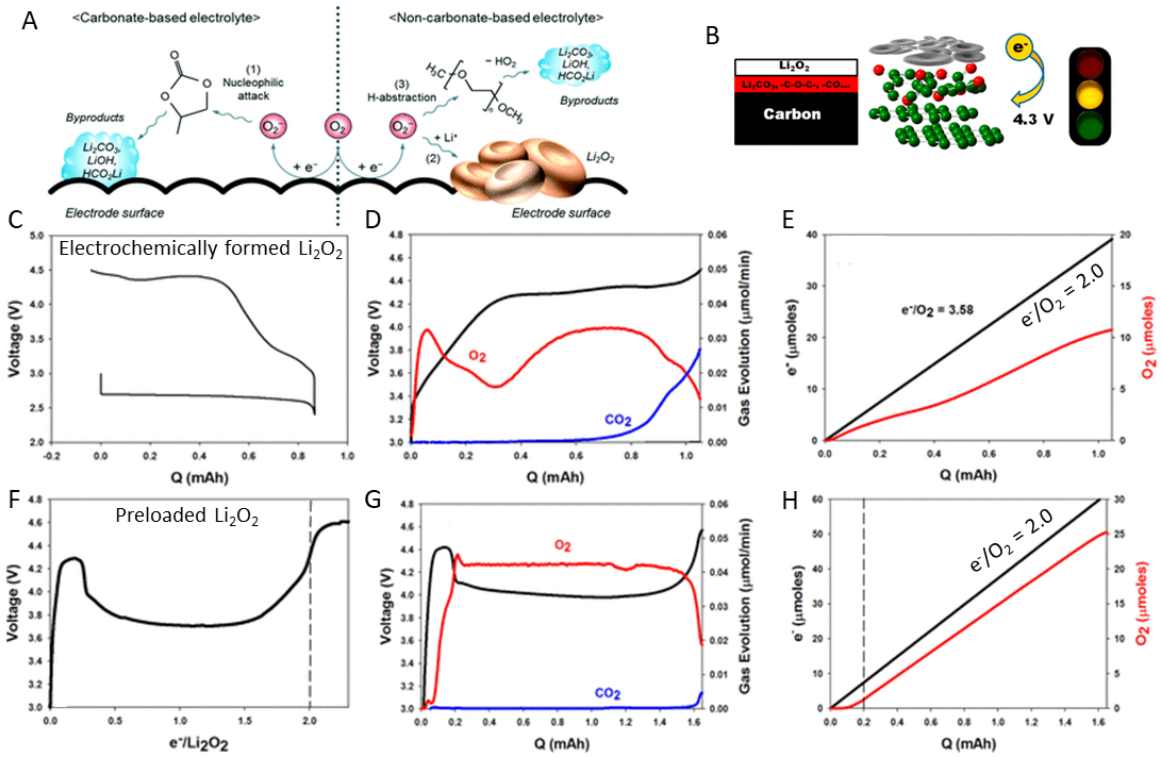


Figure 1.4 Impact of LiO_2 on Li-O_2 batteries (A) Schematic illustration of side reactions triggered by LiO_2 during the ORR in organic electrolytes. Reprinted with permission from Ref. 15. (B) Passivation of the carbon/Li_2O_2 interface by Li_2O_2 and LiO_2. (C-E) Polarization and gas evolution exhibited by the Li-O_2 cell previously discharged to form Li_2O_2. (F-H) Changing polarization and gas evolution of the Li-O_2 battery preloaded with commercial Li_2O_2. Panels B - H are reprinted with permission from Ref. 28.

Inefficient oxygen evolution reaction (OER) during charge is another challenge preventing the commercialization of nonaqueous Li-O_2 batteries. Unlike the ORR, the oxidation of Li_2O_2 to O_2 occurs through the formation of Li^+-deficient $Li_{2-x}O_2$.[30,31] This step is kinetically limited by the low electrical conductivity of Li_2O_2.[32] The formation of an insulating carbon/Li_2O_2 interphase during the ORR is another factor affecting the charging step. **Figure 1.4 C** shows that the oxidation of electrochemically formed Li_2O_2 requires a voltage exceeding 4 V.[28] This lowers the rate of oxygen evolution and triggers the release of CO_2 (**Figure 1.4 D**). Indeed, while the theoretical rate of O_2 release is $2e^-/O_2$, the electrochemically formed Li_2O_2 exhibits a lower rate of 3.58 e^-/O_2 (**Figure 1.4 E**). On the contrary, the electrodes preloaded with commercial Li_2O_2 can be charged at a lower voltage and release O_2 more efficiently despite the large size of commercial Li_2O_2 particles (**Figure 1.4 F-H**).

1.3.3 Redox Mediators for More Efficient ORR and OER

As discussed in the previous section, the major challenges of Li-O_2 batteries are the electrolyte decomposition and inefficient oxidation of Li_2O_2. The first challenge can be addressed by developing electrolytes with a higher stability against LiO_2. For example, our group demonstrated 2,3-dimethoxy-2,3-dimethylbutane (DMDMB) solvent generates much fewer decomposition products than 1,2-dimethoxyethane (DME).[22] However, DMDMD can barely dissolve conventional Li salts (i.e., LiTFSI), which limits its applicability. The search for solvents compatible with LiO_2 is a contentious topic. Although some groups report on the improved stability of Li-O_2 batteries with acetonitrile,[33] hexamethylphosphoramide,[34] or Pyr_{14}TFSI ionic liquid[35] electrolytes, the origins of their better performance still need to be understood. Furthermore, suppressing the reactivity of LiO_2 does not address the limitations caused by the low conductivity of Li_2O_2.

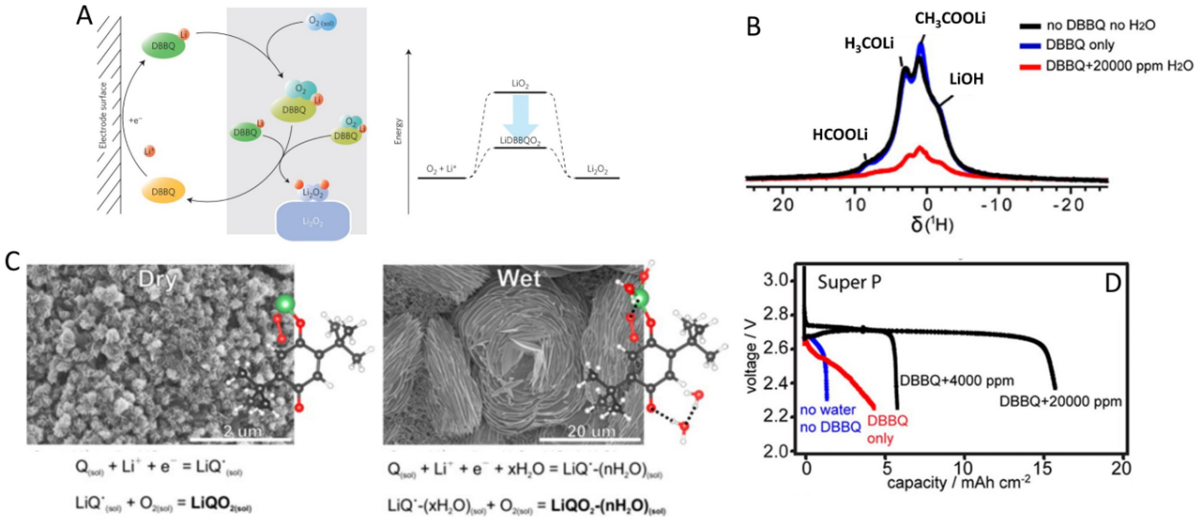


Figure 1.5 DBBQ-mediated ORRs. (A) Proposed mechanism of the ORR in the presence of DBBQ. Reprinted with permission from Ref. 37. (B) ^{1}H NMR of the carbon cathodes after the discharge in different electrolytes. The peaks of lithium formate, acetate and hydroxide are generated by the side-reactions. (C) Morphology of Li_2O_2 deposited in dry and wet electrolytes containing DBBQ. (D) Discharge of Li-O_2 batteries with four different electrolytes. Panels B – D are reprinted with permission from Ref. 38.

Modifying the electrolyte composition by incorporating special additives, which accelerate the formation and oxidation of Li_2O_2, is a promising approach to overcome some challenges of Li-O_2

batteries. These additives are called redox mediators (RMs) since they enable fast electrochemical kinetics. The RMs are classified into two groups: discharge and charge RMs. The first group contains reducible compounds, with a reduction potential below 2.96 V vs. Li^+/Li. Typically, their redox potential falls between 2.4 and 2.7 V. Recently, the improved performance of Li-O_2 batteries with various quinone,[36–38] viologen,[39] and transition metal phthalocyanine[40,41] RMs have been reported.

The case study of 2,5-di-*tert*-butyl-1,4-benzoquinone (DBBQ) demonstrates the complexity of ORR in the presence of RMs. DDBQ is expected to promote the formation of Li_2O_2 away from the electrode surface **(Figure 1.5 A)**. In brief, a DBBQ molecule is electrochemically reduced faster than O_2. As a result, the reduced DBBQ reacts with O_2 and a solvated Li^+ ion, yielding the transition state $LiDBBQO_2$. The transition state, in turn, decomposes to Li_2O_2 and regenerates DBBQ, which is again reduced at the electrode surface. Although the pioneer study by Bruce et *al.* [37] suggested that the formation of LiO_2 in the presence of DBBQ is avoided, the follow-up work by Grey et *al.* comprehensively proved that this occurs only in the presence of water.[38] As evidenced by ^1H NMR, DBBQ does not suppress the reactivity of LiO_2 in dry electrolytes (**Figure 1.5 B**). However, if the electrolyte contains DBBQ and 20000 ppm H_2O, the side-product amount significantly drops. The authors attributed this improvement to the formation of more soluble intermediates, which also results in the precipitation of larger Li_2O_2 particles (**Figure 1.5 C**) and an increase in the discharge capacity (**Figure 1.5 D**).

The second group of RMs for Li-O_2 batteries aims to lower the charging voltage and improve the oxygen evolution. These RMs have an electrode potential between 3 and 4 V and must be initially reduced. During charge, the RM is oxidized at the cathode surface yielding RM^+. Subsequently, the RM^+ chemically reacts with Li_2O_2, releasing O_2 and regenerating the RM. The efficiency of this approach has been demonstrated for a variety of inorganic and organic RMs, such as LiI,[42,43] LiBr[44], 2,2,6,6-tetramethylpiperridinyloxyl (TEMPO),[45] tetrathiafylvalene (TTF),[46] and tris[4-(diethylamino)phenyl]amine (TDPA).[47] The case of TDPA is specifically interesting since TDPA exhibits two fast reversible redox reactions at 3.1 and 3.5 V vs. Li^+/Li, which facilitates the oxidation of Li_2O_2 at low voltages.

Although the oxidation of Li_2O_2 in the presence of RMs is simple at first glance, some details of the reaction mechanism remain unclear. The formation of LiO_2 and singlet oxygen ($^1O_2$) is one of these important details. Although the release of $^1O_2$ is under heavy debate, there is convincing evidence

that the RMs degrade during battery charging.[48–52] The relationship between the efficiency of oxygen evolution and the reduced charging voltage in the presence of RMs is another heavily discussed topic. As demonstrated in Chapter 3, the seemingly improved electrochemical performance of the Li-O_2 battery with LiI is observed. However, the presence of LiI results in the decreased reversibility of ORR and OER.

1.3.4 Mechanisms and Challenges of Li-S Batteries

The general working principle of Li-S batteries is based on the conversion of elemental sulfur (S_8) to Li_2S (**Equation 1.10**).

$$16Li^{+}_{solv.} + S_{8(s)} + 16e^{-} \leftrightarrow 8Li_2S_{(s)} \qquad \textbf{Equation 1.10}$$

The conversion mechanism depends on the ratio between the electrolyte volume (in mL) and the total mass of sulfur (in grams), called the E/S ratio. For simplicity, the mechanisms of discharge and charge reactions are exemplified by a Li-S battery containing 1,2-dimethoxyethane/1,3-dioxolane (DOL/DME) electrolyte with an E/S ratio exceeding 20, following the review paper by Pang et *al.*[53]

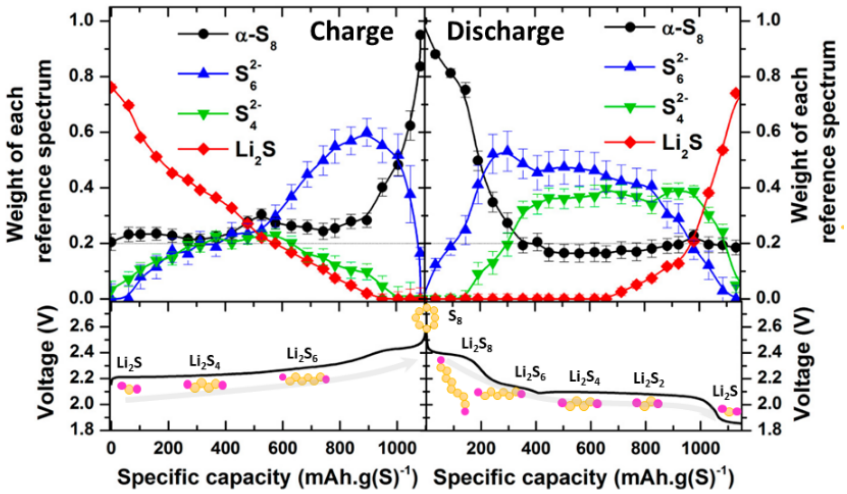


Figure 1.6 Redox reactions of sulfur in DOL/DME electrolytes. The top panel shows the evolution of sulfur-containing species, and the bottom panel shows the 1st charge/discharge cycle. Reprinted with permission from Ref. 54.

The typical voltage profile of the Li-S battery and the transformations between the sulfur species are shown in **Figure 1.6**.[54] At the beginning of discharge, S_8 undergoes a $2e^-$ reduction, which

results in the ring opening and yields soluble Li_2S_8 (**Equation 1.11**). The reduction of S_8 to Li_2S_8 gives rise to the first voltage plateau between 2.2 and 2.3 V.

$$S_{8(s)} + 2e^- \rightarrow S^{2-}_{8(solv)} \qquad \textbf{Equation 1.11}$$

Subsequently, Li_2S_8 is reduced to soluble Li_2S_6 and then to Li_2S_4, as shown in **Equations 1.12-1.13**. The latter process causes a voltage drop and the appearance of an oversaturation knee at 300-400 $mAh.g^{-1}$. Li_2S_6 can also be formed through the chemical disproportionation of Li_2S_8 (**Equation 1.14**).

$$S^{2-}_{8(solv)} + 2e^- \rightarrow S^{2-}_{6(solv)} \qquad \textbf{Equation 1.12}$$

$$S^{2-}_{6(solv)} + 2e^- \rightarrow S^{2-}_{4(solv)} \qquad \textbf{Equation 1.13}$$

$$4S^{2-}_{8(solv)} \rightarrow \mathbf{S_8} + 4S^{2-}_{6(solv)} \qquad \textbf{Equation 1.14}$$

The further reduction of Li_2S_4 triggers the formation of insoluble Li_2S_2 and Li_2S (**Equations 1.15-1.17**). The precipitation of these products within the electrode matrix increases the cell resistance, which quickly drops the voltage to a cutoff value of approximately 1.7 V before the theoretical capacity of sulfur (1675 $mAh.g^{-1}$) is achieved. An average room temperature discharge capacity of Li-S batteries with DOL/DME is limited to 1200-1300 $mAh.g_S^{-1}$.

$$S^{2-}_{4(solv)} + 2e^- + 4Li^+_{(solv)} \rightarrow 2\mathbf{Li_2S_{2(s)}} \qquad \textbf{Equation 1.15}$$

$$S^{2-}_{4(solv)} + 6e^- + 8Li^+_{(solv)} \rightarrow 4\mathbf{Li_2S_{(s)}} \qquad \textbf{Equation 1.16}$$

$$Li_2S_{2(s)} + 2e^- + 2Li^+_{(solv)} \rightarrow 2\mathbf{Li_2S_{(s)}} \qquad \textbf{Equation 1.17}$$

While charging the Li-S battery, leftover lithium polysulfides (LPS) aid the solubilization of Li_2S through the formation of Li_2S_4 (**Equation 1.18**). After that, Li_2S_4 is oxidized to Li_2S_6 (**Equation 1.19**). Finally, solid S_8 is generated by the oxidation of Li_2S_6 (**Equations 1.19-1.20**).

$$2Li_2S_{(s)} + 3S^{2-}_{6(solv.)} \rightarrow 4Li^+_{(solv.)} + 5S^{2-}_{4(solv.)} \qquad \textbf{Equation 1.18}$$

$$S^{2-}_{4(solv)} \rightarrow S^{2-}_{6(solv)} + 2e^- \qquad \textbf{Equation 1.19}$$

$$4S^{2-}_{6(solv)} \rightarrow 3S_{8(s)} + 8e^- \qquad \textbf{Equation 1.20}$$

Large-scale production of practical Li-S batteries is seriously limited by several challenges. The volume change upon the conversion between S_8 and Li_2S is one of them.[55] Since the deposition of

Li_2S expands the cathode volume by ~ 80 %, the electrode architecture experiences significant mechanical stresses, which may result in the loss of electrical contact, increased polarization, and capacity drop. This challenge may be addressed by incorporating advanced polymeric binders into the cathode structure. For example, cross-liked polymers based on carboxymethyl cellulose[56] and polyethylene glycol polyacrylates[57] significantly suppress the mechanical degradation of sulfur electrodes at high active material loadings.

Another group of challenges is related to the formation of LPS. Although LPS aid the electrochemical conversion between two insulating solids, their susceptibility to the reduction by Li metal results in a reduced discharge capacity and increased charging time.[55] The impact of LPS redox shuttling is exacerbated in the case of practical Li-S batteries due to the rapid consumption of Li metal.[58] Furthermore, the efficiency of LPS-mediated reactions at low E/S ratios is reduced due to LPS precipitation.[59] For example, the minimum E/S ratio facilitated by DOL/DME is approximately 4, while a 350 $Wh.kg^{-1}$ practical Li-S battery has to be operated under an E/S ratio below 3.[60]

1.3.5 Approaches for Preventing LPS Redox Shuttling

The approaches for preventing LPS shuttling usually focus on designing advanced cathodes and electrolytes. For example, the electrode structure may be modified by incorporating host materials with high affinity to LPS. This confines LPS within the electrode, which prevents redox shuttling. The absorption of LPS by the hosts is facilitated by the strong interactions at the LPS/host interface. N, S-doped carbon materials and C_3N_4/rGO[56] composites efficiently bind LPS owing to the strong interactions of Li^+ and S^{2-} with the dopants. Lewis acid-base interactions result in excellent capacity retention of the Li-S batteries with MXene-based host materials.[61] If a host material is redox-active with a redox potential between 2.4 – 3.05 V, it binds LPS and catalyzes the conversion of sulfur by forming thiosulfate as an intermediate.[62]

Modifying the electrolyte structure is a simpler alternative for suppressing the LPS shuttling. At the dawn of the Li-S research, this was achieved by employing $LiNO_3$ as an electrolyte additive.[63] The reduction of $LiNO_3$ at the surface of metallic Li creates an efficient passivating film, suppressing the reactivity between Li and LPS. However, this approach only postpones the failure of metallic Li anodes since $LiNO_3$ is constantly consumed to rebuild the passivation layer.

Suppressing the solubility of LPS is a more promising pathway towards a stable Li-S battery. This approach aims to reduce the solubility of LPS to a low but particular value (typically, below 100

mM in S atom) by designing so-called sparingly solvating electrolytes.[53] Often, sparingly solvating electrolytes are prepared by increasing the salt concentration, which reduces the solubility of LPS.

A typical sparingly solvating high-concentration electrolyte contains a Li^+ salt (usually lithium bis(trifluoromethanesulfonyl)imide (LiTFSI)), a solvent, and a diluent. The diluent is a fluorinated ether (FE) with a low polarity, which reduce the electrolyte viscosity but does not coordinate Li^+. The lowest solvent-to-salt molar ratio depends on a solvent's solvating power. In moderately solvating systems (acetonitrile, [64] sulfolane [65]) the maximum [Li^+]/[solvent] ratio is around 0.5. On the other hand, glymes can dissolve an equimolar amount of LiTFSI. [66, 67646566]

The mechanism of LPS shuttling suppression is schematically shown in **Figure 1.7 A**. Since the solubility is limited to 0.1 M (in S atom), the LPS are spatially confined within the cathode and cannot diffuse towards the Li anode. Therefore, Li-S batteries with a simple carbon/S_8 cathode and $Li(G_2)_{0.8}$TFSI/FE electrolyte exhibits an improved capacity retention and prolonged cycling life (**Figure 1.7 B**). Furthermore, reducing the solvent-to-salt ratio stabilizes lithium anodes by suppressing their reactivity. (**Figure 1.7 C**).

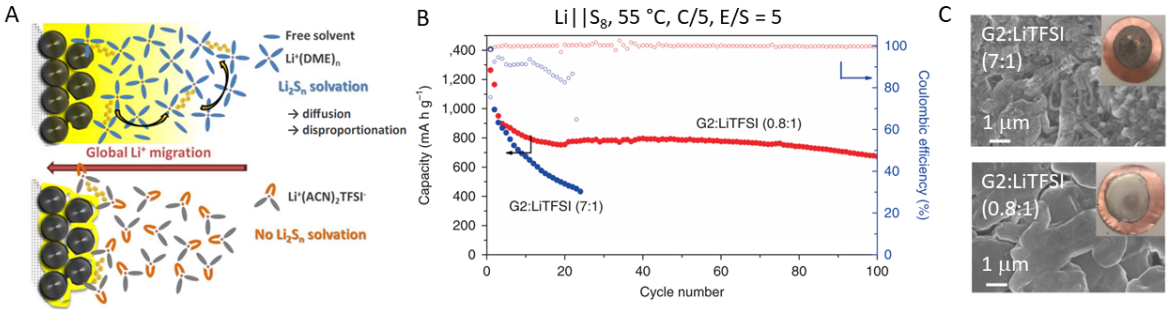


Figure 1.7 Li-S batteries with sparingly solvating electrolytes. (A) Schematic illustration of the mass transport within the cathodes. Reprinted from Ref. 64. (B) Capacity retention of the Li-S cell with $Li(G_2)_{0.8}$TFSI/FE; (C) Improved stability of LMAs in $Li(G_2)_{0.8}$TFSI/FE. Panels B and C are reprinted from Ref. 66.

Unfortunately, the reduced kinetics of sulfur redox is the price of suppressing LPS shuttling in sparingly solvating electrolytes. Although the $S_8 \leftrightarrow Li_2S$ conversion still proceeds through the formation of soluble intermediates, the battery can only be efficiently cycled at 50 - 70 °C. Thus, although employing sparingly solvating electrolytes is an exciting approach from the fundamental point of view, its practical applicability in pursuing high-energy-density Li-S batteries is questionable.

1.3.6 Li-S Batteries with EPD Electrolytes

Since high-energy-density Li-S batteries have to be operated under E/S ratios below 3, there is an emerging call for novel electrolytes with a high solubility of LPS. This requirement for low E/S can be met if Li-S batteries employ an electron pair donor (EPD) solvent such as dimethylacetamide (DMA), dimethylformamide (DMF), and 1,3-dimethyl-2-imidazolidinone (DMI). These solvents exhibit a remarkably higher solubility of LPS compared to DOL/DME. For example, the solubility of LPS in DMA is 32 M (in S atom), as opposed to 6.6 M (in S atom) exhibited by DOL/DME. Given the density of DMA (0.86 $g.mL^{-1}$), the solubility of LPS is equivalent to the E/S ratio of one, which meets the standards of practical Li-S batteries.[60]

In addition to the increased solubility of LPS, EPD electrolytes offer more intriguing sulfur electrochemistry. Earlier, our group demonstrated that the pathways of S_8 reduction in DMA significantly differ from those in ether-based solvents due to the stabilization of the trisulfur radical ($S_3^{\cdot-}$).[68] The stability of $S_3^{\cdot-}$ in DMA can be explained by the Pearson's hard soft acid base theory: the strong interactions between Li^+ and DMA lower the acidity of Li^+, thus driving the formation of ion pairs between Li^+ and soft base $S_3^{\cdot-}$.[69]

The mechanism of sulfur reduction in DMA was studied by *operando* XANES measurements (**Figure 1.8 A**).[68] Initially, S_8 is electrochemically reduced to S_8^{2-}, which then forms S_6^{2-} and regenerates S_8, following **Equations 1.11** and **1.14**. This step results in the plateau at 2.7 V. Subsequently, S_6^{2-} disproportionates to two $S_3^{\cdot-}$ radicals (**Equation 1.21**).

$$S^{2-}_{6(solv)} \rightarrow 2S^{\cdot-}_{3(solv)} \qquad \textbf{Equation 1.21}$$

$S_3^{\cdot-}$ is further reduced to S_3^{2-} (**Equation 1.22**) and S_4^{2-} (**Equation 1.23**). Additionally, S_4^{2-} can also be formed through the reduction of S_8^{2-} (**Equation 1.24**). S_4^2 reacts with elemental S_8 to regenerate $S_3^{\cdot-}$ (**Equation 1.25**).

$$S^{\cdot-}_{3(solv)} + e^- \rightarrow S^{2-}_{3(solv)} \qquad \textbf{Equation 1.22}$$

$$2S^{2-}_{3(solv)} + 2S^{\cdot-}_{3(solv)} \rightarrow 3S^{2-}_{4(solv)} \qquad \textbf{Equation 1.23}$$

$$S^{2-}_{8(solv)} + 2e^- \rightarrow 2S^{2-}_{4(solv)} \qquad \textbf{Equation 1.24}$$

$$4\ S^{2-}_{4(solv)} + S_{8(s)} \rightarrow 2\ S^{\cdot-}_{3(solv)} \qquad \textbf{Equation 1.25}$$

Finally, S_4^{2-} is reduced to Li_2S (**Equation 1.26**), which may react with S_8, regenerating $S_3^{\cdot-}$ (**Equation 1.27**).

$$4S^{2-}_{4(solv)} + 8Li^{+}_{(solv)} + 6e^{-} \rightarrow 4Li_2S_{(s)} \qquad \textbf{Equation 1.26}$$

$$8Li_2S_{(s)} + 5S_{8(s)} \rightarrow 16Li^{+}_{(solv)} + 16S^{\cdot-}_{3(solv)} \qquad \textbf{Equation 1.27}$$

While charging Li-S batteries with EPD electrolytes, $S_3^{\cdot-}$ mediates the oxidation of Li_2S to S_8 through the formation of Li_2S_4.

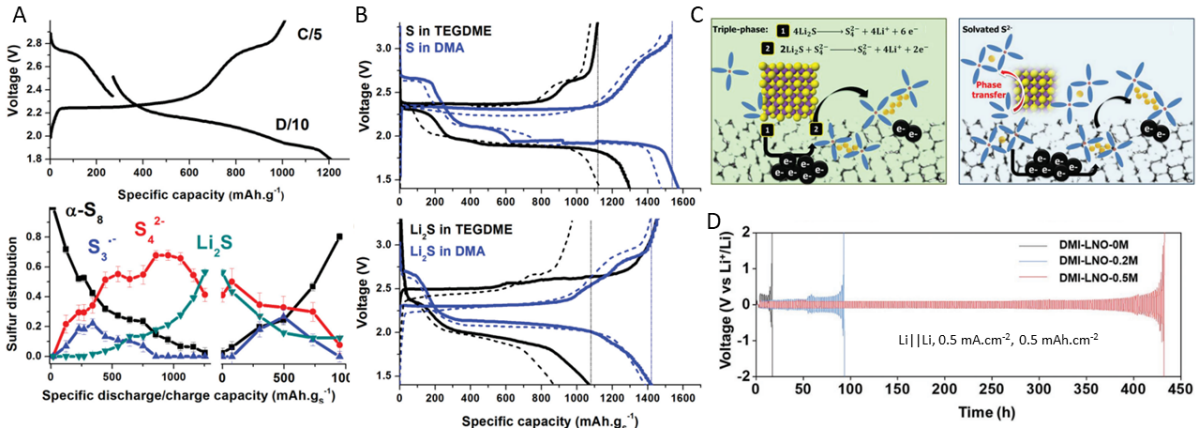


Figure 1.8 Li-S batteries with EPD electrolytes. (A) *Operando* XANES of Li-S batteries with 1 M LiTFSI/DMA electrolyte. The top panel shows the voltage profile, the bottom panel shows the evolution of sulfur species during the 1st cycle. (B) Comparison of the performance of Li||S_8 (top panel) and Li||Li_2S (bottom panel) batteries with 1 M LiITFSI/DMA and 1 M LiTFSI/tetraglyme electrolytes. The 1st cycle is in solid lines and the 2nd is in dashed lines. (C) The mechanism of Li_2S oxidation in Li-S cells with conventional glyme (left panel) and EPD (right panel) electrolytes. Panels A-C are reprinted with permission from Ref. 68. (D) Polarization of Li-symmetric cells with $LiNO_3$/DMI electrolytes demonstrating the instability of Li. Reprinted with permission from Ref. 70.

As demonstrated in **Figure 1.8 B** (top panel), the formation of $S_3^{\cdot-}$ increases the discharge capacity from 1300 mAh.g_S^{-1} in TEGDME to almost 1600 mAh.g_S^{-1} in DMA. Furthermore, DMA reduces the battery polarization, improving its energy efficiency. Notably, charging Li-S batteries with DMA occurs at 2.3 V, while those containing TEGDME require a charging voltage of 2.5 V (**Figure 1.8 B**, bottom panel). This phenomenon is ascribed to the $S_3^{\cdot-}$-aided dissolution of Li_2S into DMA. In the absence of $S_3^{\cdot-}$, Li_2S has to be oxidized through the sluggish triple-phase process, which is illustrated

in **Figure 1.8 C**. Interestingly, the improved oxidation of Li_2S in the cells with DMA could also be explained by its non-zero solubility. Although the exact solubility of Li_2S in DMA is unknown, it is approximately 0.1 M in DMI, another example of an EPD solvent. [70]

Unfortunately, EPD electrolytes severely react with metallic Li even in the presence of $LiNO_3$ (**Figure 1.8 D**). For example, the symmetric cells with Li electrodes and DMI-based electrolytes containing 0.5 M $LiNO_3$ can withstand only 430 hours when cycled at 0.5 $mA.cm^{-2}$ (0.5 $mAh.cm^{-2}$). This indicates that Li-S batteries employing EPD electrolytes must have a protected Li anode, which is separated from the catholyte by a Li^+-conducting dense membrane. In the previous studies of Li-S batteries with DMA electrolytes, an Ohara LIC-GC^{TM} membrane was used to separate the Li anode from the DMA.[68] However, the Li-S batteries containing Ohara membranes also requires more electrolytes to wet the Li surface, which decreases the overall energy density. Therefore, the design of Li-S batteries with EPD electrolytes and protected Li anodes is a promising pathway toward efficient energy storage systems. The development of thes battery is presented in Chapter 6.

1.4 Lithium Metallic Anode

The development of rechargeable batteries with lithium metallic anodes (LMBs) has always been a promising research direction due to the high gravimetric theoretical capacity (3860 $mAh.g^{-1}$) and low electrode potential (-3.04 V vs. NHE) of lithium metal anodes (LMAs). However, replacing state-of-the-art (SOA) LIBs with LMBs remains impossible due to the low cyclability and safety hazards arising from LMAs. [71,72] Since the behavior of LMAs in liquid electrolytes is more detailed than that in solid-state electrolytes, the subsequent sections are primarily devoted to the mechanochemical challenges of LMBs with liquid electrolytes.

The most common limitations of LMAs in liquid electrolytes are summarized in **Figure 1.9**. It is important to note that many of these challenges are correlated, which causes their negative effects during cycling to be occur more rapidly.

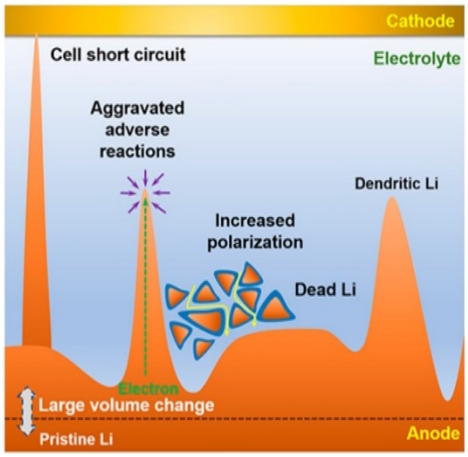


Figure 1.9 Challenges of LMA. Reprinted with permission from Ref. 71.

1.4.1 Li SEI

LMAs simultaneously react with the electrolyte components producing surface impurities called a solid electrolyte interphase (SEI). The driving force for SEI formation is the electrochemical potential of LMA being above the electrolyte's lowest unoccupied molecular orbital (LUMO).[73] The electron transfer from Li to the electrolyte components results in the formation of Li SEI, which inhibits further reactions. The passivating effect of the SEI is determined by the solubility of its components in the electrolyte.

The SEI composition depends on the reactivity of electrolyte components.[74,75] In electrolytes with organic carbonate solvents, a ~ 20 nm thick SEI contains lithium alkyl carbonates, Li_2CO_3, Li_2O, and organic products of solvent polymerization.[76–78] The reduction of organic carbonates at the Li/electrolyte interface yields a mosaic SEI containing many grain boundaries. The inner layer of SEI is dense and comprised of inorganic Li compounds (Li_2O, Li_2CO_3), while the outer layer is more porous since it contains lithium alkyl carbonates and products of electrolyte polymerization (**Figure 1.10 A**). Additionally, the SEI often contains the products of electrolyte salt decomposition, such as LiF.[79]

Ether solvents are another group of organic solvents employed in LMBs. Due to their low redox potential (< 0 V vs. Li^+/Li), [80] ether solvents cannot be electrochemically reduced by lithium

metal. However, some ethers may chemically react with Li. For example, reacting Li with DOL results in ring-opening polymerization, which forms $CH_3CH_2OCH_2CH_2OLi$, HCO_2Li, and polyDOL.[81] Nevertheless, the SEI formed in ether solvents primarily contain the products of salt decomposition (LiF, Li_3N, Li_2O).[74]

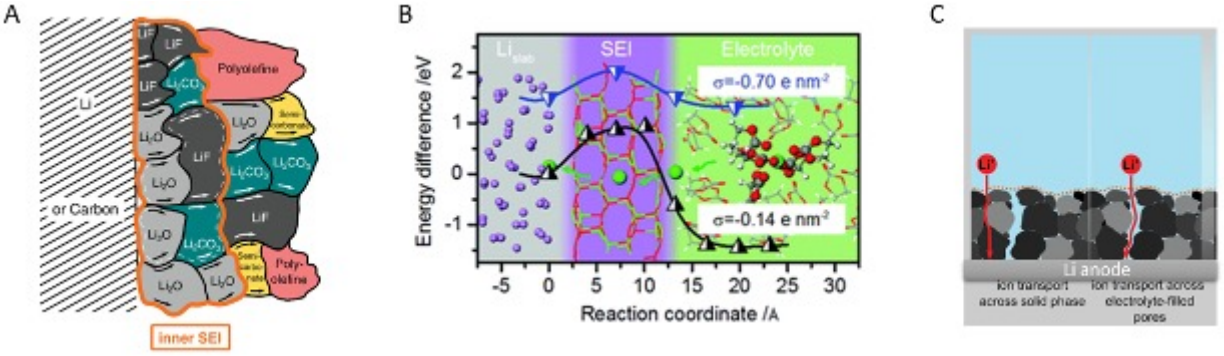


Figure 1.10 Li SEI. (A) Mosaic structure of Li SEI. Reprinted with permission from Ref. 77. (B) Energy landscape of the charge transfer reactions at the $Li/Li_2CO_3/Li^+$-EC electrolyte interface calculated at two surface charge densities. Reprinted with permission from Ref. 82. (C) Two possible mechanisms of Li^+ transport across the SEI. Reprinted with permission from Ref. 77.

Due to the multi-layer and mosaic SEI structure, understanding its role in the electrochemistry of LMA is challenging. The possible mechanism of Li^+ reduction in liquid electrolytes is demonstrated in the computational study by Qi *et al.* [82] The energy landscape (**Figure 1.10 B**) of Li^+ transport across the interfaces formed between Li, Li_2CO_3, and ethylene carbonate illustrates that the reduction of Li^+ is a multi-step process. It involves the desolvation and transport of Li^+ ions across the SEI to the anode surface where the reduction finally occurs. It is worth mentioning that the desolvation of Li^+ liberates coordinating solvent molecules, which subsequently react with Li, thickening the SEI.

[82]Since the majority of SEI components are poor ionic conductors, the mechanism of Li^+ transport across the SEI layer is ambiguous. Peled *et al.* suggested that Li^+ ions are transported along the SEI grain boundaries.[77] Additionally, a non-zero SEI porosity facilitates the charge transport by the infusion of electrolyte.[83] On the other hand, Li^+ diffusion through amorphous and nanocrystalline SEI components is also possible. For example, nanocrystalline Li_2O and LiF might exhibit ionic conductivities up to 10^{-8} $\Omega^{-1}.cm^{-1}$ [184,85] although a recent computational study by Xu *et al.* questions the possibility of Li^+ transport in LiF and highlights the importance of Li_2CO_3.[86] Interestingly enough, the

decomposition of some advanced electrolytes produces LiH ($\sigma_{ionic} \approx 10^{-5}\ \Omega^{-1}.cm^{-1}$), which improves the Li^+-conductance.[87]

1.4.2 Models of Li Dendrite Formation

Since the deposition of metallic Li from liquid electrolytes is a complex process, the unified model explaining all nuances of Li plating has not been fully developed. The first model of Li dendritic growth was proposed by Chazalviel *et al.*[88] According to the Chazalviel model (also called the space charge model), if an applied current reaches a limiting current density (j_{lim}), it can only be sustained for a certain period of time, called Sand's time (τ_{Sand}) (**Equation 1.28**). The limiting current calculated by the Cottrell equation depends only on the electrolyte's transport properties (**Equation 1.29**). Once τ_{Sand} has passed, anions become depleted at the surface. The anion depletion creates a very large space charge and electric field near the anode surface, leading to a ramified growth of Li deposits.

$$\tau_{Sand} = \pi D_{salt} \frac{(z_{Li} c_b F)^2}{4(j(1-t_{Li}))^2} \qquad \textbf{Equation 1.28}$$

$$j_{lim} = \frac{c_b D_{salt} F}{2\sqrt{\pi}(1-t_{Li})L} \qquad \textbf{Equation 1.29}$$

where c_b is the bulk salt concentration, D is the ambipolar salt diffusion coefficient, F is the Faraday constant, z_{Li} is the charge number of Li^+ ($z_{Li} = 1$), and L is the interelectrode distance.

Given the values of D_{salt}, c_b, and t_{Li} exhibited by 1 M $LiPF_6$/EC-DMC[89] and interelectrode distance of 25 μm, the limiting current density in this electrolyte is ~ 200 $mA.cm^{-2}$. In practice, Li dendrites are observed at much lower current densities, which contradicts with the Chazalviel model.[90] However, this model can still be employed to predict the stability of Li deposition. For example, Bazant *et al.* [91] demonstrated that τ_{Sand} points at the onset of Li dendrite formation, as shown in **Figure 1.11 A, B**.

The limited applicability of the Chazalviel model is caused by its simplicity. In particular, it is based on the assumption that Li is devoid of any SEI. A comprehensive study to understand the relationship between the SEI and mechanism of Li deposition was presented by Bazant et al. (**Figure 1.11 C**).[92] At low current densities (below $0.3j_{lim}$), Li^+ can freely diffuse across the SEI and uniformly deposit beneath it for some time. The deposition of Li causes an increase in internal pressure, and, at a certain point, deposited Li squeezes out through a pinhole in the SEI layer. This pathway leads to the formation of whisker-type dendrites. If an applied current density exceeds j_{lim}, tip-growing dendrite

morphology is dominant, and the growth obeys the Chazalviel model. When the current density is between $0.3j_{lim}$ and j_{lim}, the Li growth rate is comparable to the rate of SEI formation, which results in the incomplete coverage of the deposited Li by the SEI. This triggers the formation of mossy Li instead of Li whiskers. This detailed model clearly illustrates the importance of SEI conductivity and mechanical stability in suppressing nonuniform Li deposition.

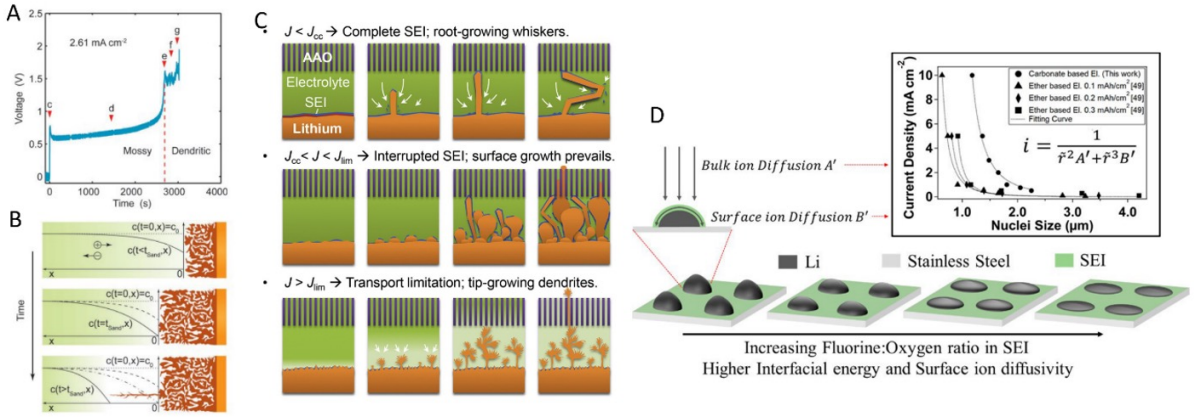


Figure 1.11 Formation of Li dendrites. (A) Voltage response of the Li symmetric cells with 1 M $LiPF_6$/EC-DMC electrolyte at 2.61 $mA.cm^{-2}$. Point *e* shows the onset of Li dendrite formation. (B) Theoretical interpretation of Li deposition growth mechanisms. Panels A, B are reprinted with permission from Ref. 91. (C) Illustration of Li dendrite formation under different current density conditions. Reprinted with permission from Ref. 92. (D) Dependence of Li nucleation on the electrolyte's properties. Reprinted with permission from Ref. 93.

Understanding the process of Li nucleation further sheds light on the roots of Li dendrite deposition. Archer *et al.*[93] studied the nucleation and growth of Li by employing the model earlier developed by Barton.[94] This model treats Li nuclei as noninteracting hemispheres with radius *r*. The total overpotential of Li deposition (η) depends on several factors: charge transfer overpotential, diffusion overpotential, interfacial surface energy overpotential, and overpotential due to Li^+ transport across the SEI.

$$\eta=\frac{RT}{\alpha F}\ln\frac{j}{j_0}+\frac{jrRT}{D_{salt}c_b f^2}+\frac{2\gamma V}{Fr}+\frac{jr^2RT}{D_{SEI}c_{SEI}F^2} \qquad \textbf{Equation 1.30}$$

where j and j_0 are the current density and the exchange current density; D_{SEI} and c_{SEI} are the SEI Li diffusivity and concentration, γ is the interfacial energy; α, V, R, T are the charge transfer coefficient, molar volume of Li, universal gas constant and temperature, respectively.

Archer's work demonstrates that the size of Li nuclei depends on the rate of Li^+ transport across the SEI and in the bulk electrolyte, as shown in **Figure 1.11 C**. This dependence is obeyed even if an applied current density is below j_{lim}. It is important that the diffusivity of Li^+ in the bulk electrolyte and at the interface are not the only factors that determine the stability of Li deposition. According to **Equation 1.30**, the overpotential depends on the interfacial energy, which is controlled by the electrolyte composition. For instance, fluoroethylene carbonate (FEC) lowers the electrolyte/electrode contact angle and also increases the fraction of LiF in the SEI. These changes induced by FEC facilitate a faster transport of Li^+ at the surface and increase the average nuclei radius.

1.4.3 Correlations between the Challenges of LMAs

Suppose an LMA undergoes multiple plating and stripping steps upon continuous cycling of the LMB. In this case, the formation of SEI and Li dendrites is enhanced by the generation of Li pits during stripping. [95] The pitting of the LMA is caused by the low diffusivity of Li atoms in the bulk anode. When the flux of Li^+ ions in the electrolyte cannot be matched by the flux of atoms in the anode, pits are formed which reduces the local current density and decreases the Li^+ flux. The failure of LMAs is schematically shown in **Figure 1.12 A**.

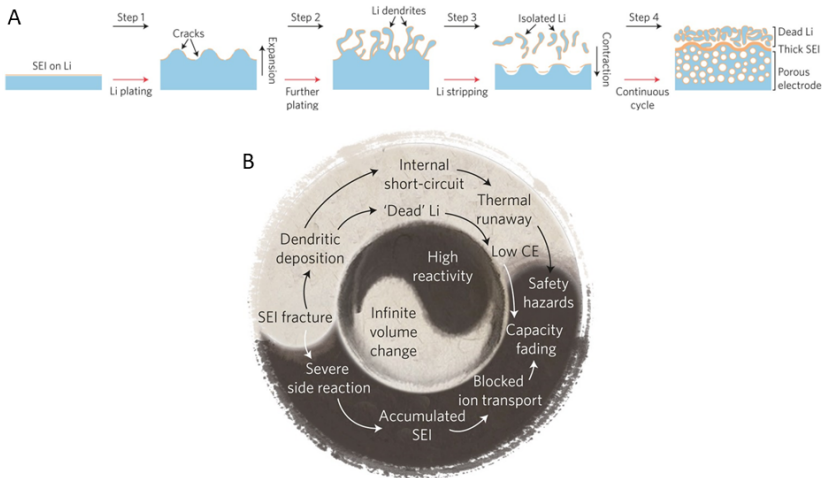


Figure 1.12 Correlation between the challenges of LMA (A) Schematical illustration of LMA upon continuous cycling. Uneven deposition, stripping and SEI formation lead to the formation of dead Li. (B) The relationship between the challenges of LMAs. Panels A and B are reprinted with permission from Ref. 72.

The initial Li deposition increases the surface area, which may contain cracked SEI. When Li is stripped, volume contraction fractures the SEI, which drives additional side reactions at the Li surface, thereby increasing the battery's resistance and electrolyte consumption. The creation of pits leads to the disintegration of LMAs and formation of inactive Li (so-called dead Li). Upon continuous cycling, the challenges amplify each other and result in anode failure, as illustrated by Cui *et al.*[96] (**Figure 1.12 B**).

1.4.4 Approaches to Li Protection

As discussed in the previous sections, the formation of Li SEI and nonuniform deposition of Li are the most important challenges of LMAs. Therefore, the development of stable LMAs is one of the most competitive directions in battery research. The approaches to stabilize LMAs in LMBs with liquid electrolytes can be separated into several major groups: modification of Li with artificial SEIs, design of advanced electrolytes, development of 3D host materials to accommodate Li, and cycling LMBs under elevated pressure and temperature.

1.4.5 Artificial Li SEIs

This approach aims to create an SEI with predetermined properties to prevent Li reactivity with liquid electrolytes and improve the morphology of deposited Li. Ideal artificial SEIs must exhibit sufficient Li^+ conductivity, chemical stability in organic electrolytes, and mechanical stability to resist stresses induced by Li plating and stripping. The LMA surface can be modified before cell assembly (ex-situ) or by employing electrolyte additives which generate an SEI during cycling (in-situ)

Ex-situ SEI can be generated by numerous techniques, including physical deposition techniques (atomic layer deposition (ALD) and molecular layer deposition (MLD)), direct application of a premade SEI layer, and solution-based chemical reactions with SEI precursors. ALD is often applied to deposit a thin (< 20 nm) and uniform layer of Al_2O_3.[97,98] In a typical ALD process, trimethylaluminum (TMA) reacts with O_2 plasma, causing the products to condense at the Li surface. Deposited Al_2O_3 is then reduced by Li, yielding a thin layer of Li^+-conducting Li_xAlO_2. Modifying Li via MLD is a promising alternative to ALD since it forms a uniform hybrid organic/inorganic coating with a thickness of 5 nm. For example, alucone may be deposited following a two-step protocol. First, TMA reacts with OH^- groups at the Li surface, forming Al-O linkages and a methyl-terminated surface. In the second step, the surface Al-CH_3 groups react with ethylene glycol, resulting in Al-O-R linkages.

The neighboring Al-CH_3 groups are cross-linked by ethylene glycol, providing flexibility and mechanical strength. Furthermore, the coating quality can be improved if ALD and MLD are combined.[99]

Due to the high cost of ALD and MLD, tuning the Li surface composition with a predesigned SEI is more promising for practical applications. This approach may be utilized to apply hybrid polymer/inorganic coatings. The polymer component is necessary for mechanical stability during volume changes upon Li plating and stripping, and the inorganic component provides a Li^+-conducting conduit. Applying a hybrid PDMS/β-Li_3PS_4 coating layer to LMA's surface exemplifies this approach. A layer of β-Li_3PS_4 is deposited on LMA by doctor blading an β-Li_3PS_4/THF slurry, followed by the infiltration of the β-Li_3PS_4 membrane with PDMS.[100] Since β-Li_3PS_4 exhibits an ionic conductivity of 0.2-0.3 mS.cm^{-1} at 25 °C, the hybrid membrane does not increase the internal cell resistance. PDMS/β-Li_3PS_4-protected LMAs improve the lifetime of the Li||$Li_4Ti_5O_{12}$ cells with 1 M LiTFSI/DOL-DME electrolyte to 2000 cycles at 5 C (2.1 mA.cm^{-2}) rate. An exciting approach to modify Li with an all-organic layer made of (poly(oligo(ethylene glycol) methyl ether methacrylate)-grafted, hypercrosslinked poly(4-chloromethylstyrene) nanospheres with a single-ion-conducting lithiated Nafion was developed by Wu et *al*.[101] Due to high mechanical stability of the all-oraginic polymer coating, stable Li deposition for 100 cycles at 0.2 C/1 C charging/discharging rate was achieved in high capacity (4 mAh.cm^{-2}) Li||$LiNi_{0.6}Co_{0.2}Mn_{0.2}$ cells with a 1.0 M $LiPF_6$/EC-DEC electrolyte.

The stability of LMAs was significantly improved by interfacing Li with carbonaceous materials. Wo and Archer employed the films of phosphate-functionalized reduced graphene oxide (PrGO) to create protective Li coatings.[102] The PrGO coating was fabricated by the Langmuir-Blodgett process and coated on Li by roll-pressing. Since PrGO contains functional groups with high affinity to Li metal, the overpotential for Li nucleation is decreased. The cells comprised of a PrGO-Li anode and a high capacity (4.1 mAh.cm^{-2}) $LiNi_{0.8}Mn_{0.1}Co_{0.1}O_2$ along with the advanced electrolyte (0.6 M LiTFSI + 0.4 M LiBOB + 0.4 M LiF + 0.1 M $LiNO_3$ + 0.05 M $LiPF_6$ + 0.03 M $LiBF_4$ in EC-DMC with 1 wt% FEC, 2wt%VC, and 3 wt% di-2,2,2-trifluoroethyl carbonate) retained over 80 % of their initial capacity after 200 cycles.

Ex-situ Li protection via treating Li foil with a precursor-containing solution is another promising approach. Our group demonstrated its efficacy by reacting lithium with reducible metal chlorides. The chemical reaction between an MCl_n/THF (M = In, Zn, Bi, As) solution and Li foil yields

a ~ 10 μm thick hybrid Li_xM_y alloy/LiCl layer.[103] The Li-rich Li_xM_y alloys exhibit electronic and ionic conductivity. However, incorporating LiCl into the membrane lowers its electronic conductivity and establishes an electric field gradient, which forces Li deposition underneath the membrane. Liang *et al.* further infused the Li_xM_y alloy/LiCl membranes with a LiTFSI/poly(ethylene glycol)diacrylate-based polymer electrolyte to improve their flexibility.[104]

Since MX_n (M = Al, In, Sn, X = Cl, Br, I, TFSI, NO_3^-) are Lewis acids, MCl_n/DOL solutions undergo acid-catalyzed ring-opening polymerization of DOL. For example, reacting Li with an AlI_3/DOL solution yields Li_xAl_y infused with poly(DOL).[105] This protective coating prevents the redox shuttling of LPS in the Li-S batteries with DOL/DME electrolyte.

Although *ex-situ* coated LMAs demonstrate a significantly improved performance, the mechanical stability of the coating layers under high mechanical stress is sometimes questionable. Therefore, tuning the composition of conventional carbonate and DOL/DME electrolytes is a pathway to reconstruct the SEI *in situ*. For instance, a hybrid SEI consisting of $Li_{13}In_3$/LiF is formed on the surface of Li if InF_3 is added to 1 M $LiPF_6$/EC-DMC or 1 M LiTFSI/DOL-DME. Notably, a similar effect was also documented for various MX_n additives: $SiCl_4$,[106] $In(NO_3)_3$,[107] and $Mg(TFSI)_2$[108]

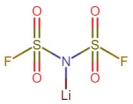
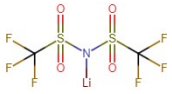
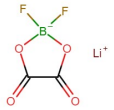
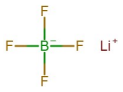
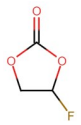
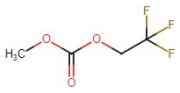
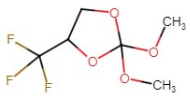
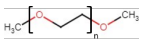
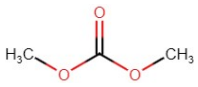
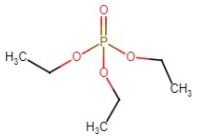
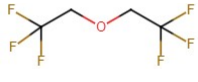
Lithium polysulfides, such as Li_2S_6, sometimes exhibit a very intriguing behavior when interfaced against Li metal. For instance, Li_2S_6 aids the dissolution of P_2S_5 into DOL/DME through the formation of a L_2S_6-P_2S_5 transition complex.[109] The reaction between the complex and Li yields a layer of Li_3PS_4. The generation of surface Li_3PS_4 simultaneously addresses two major challenges of LMAs. On the one hand, Li_3PS_4 separates Li from the electrolyte, suppressing the side reactions. On the other hand, a sufficient ionic conductivity of Li_3PS_4 homogenizes Li^+ flux across the SEI, which prevents the nucleation of Li dendrites. The efficiency of L_2S_6-P_2S_5 electrolyte additives is illustrated by the stable cycling of Li symmetric cells at 8 $mA.cm^{-2}$.

Simultaneous decomposition of LPS and $LiNO_3$ electrolyte additives at the LMA surface is another example of generating the SEI *in-situ*.[63,110–112] The cumulative effect of $LiNO_3$ and LPS arises from the oxidation of LPS by $LiNO_3$ yielding Li_2SO_3, Li_2SO_4, and $LiNO_2$. These reaction products are further reduced by Li, which yields a dense inorganic SEI. The SEI composition depends on the electrolyte formulation but can be described as a mixture of Li_2O, Li_2S, $Li_xN_yO_z$, and $Li_xS_yO_z$. Unfortunately, the low solubility of $LiNO_3$ in carbonate electrolytes[113] limits the applicability of $LiNO_3$ to ether-based (DOL/DME and G_2) electrolytes.

1.4.6 Advanced electrolytes for LMBs

The previous section describes the modification of Li anodes for LMBs employing conventional electrolytes. In contrast, this section focuses on advanced electrolytes for high-energy-density LMBs. The selected chemicals employed in the design of the advanced electrolytes are shown in **Table 1.2**. Generally speaking, the advanced electrolytes can be divided into two groups according to the solvent-to-salt molar ratio.

Table 1.2 Structures of the salts, solvents, and diluents employed for the high-performance LMBs

Salts for advanced electrolytes			
LiFSI		LiTFSI	
Lithium difluoro(oxalate)borate (LiDFBOB)		Lithium tetrafluoroborate ($LiBF_4$)	
Solvents for advanced electrolytes with a moderate salt concentration			
Fluoroethylne carbonate (FEC)		Methyl (2,2,2-trifluoroethyl) carbonate (FEMC)	
1,1,1-trifluoro-2,3-dimethoxypropane (TFDMP)		2,2-Dimethoxy-4-(trifluoromethyl)-1,3-dioxolane (DTL)	
1,4-dimethoxylbutane (FDMB)			
Solvents for HCE and LHCE			
G_n (G_1 (DME) – G_4)		Sulfolane (SL)	
Dimethyl carbonate (DMC)		Triethyl phosphate (TEP)	
Non-coordinating diluents			
2,2,2-Trifluoroethyl 1,1,2,2-tetrafluoroethyl ether (TTE)		Bis(2,2,2-trifluoroethyl) ether (BTFE)	

The first group includes electrolytes with a relatively low salt-to-solvent molar ratio below 2.5. The second electrolyte group is high-concentration electrolytes with a high salt-to-solvent ratio above 2.5. Since my PhD research was partially focused on studying the electrolytes from the second group, this section is mainly devoted to high-concentration advanced electrolytes.

The composition of advanced electrolytes can be generalized as a combination of a fluorinated Li^+ salt and a fluorinated solvent. Fluorinated electrolytes improve the performance of LMB due to the formation of LiF-rich interphases at the negative and positive electrodes. Furthermore, fluorinated electrolytes exhibit better oxidative stability, lower flammability, and depressed melting point. In comparison their nonfluorinated counterparts, fluorinated solvents usually exhibit a weaker binding to Li^+ ions, which improves the battery kinetics at subzero temperatures.[114–118]

High-concentration advanced electrolytes are usually prepared by dissolving lithium bis(fluorosulfonyl)imide (LiFSI) or LiTFSI into conventional organic solvents at concentrations slightly below the solubility limit at room temperature. The solubility of Li^+ salts in the selected solvents (**Table 1.2**) decreases in the following order: TEP<SL<DMC<G_n. This trend correlates with solvent's chelating ability. Since G_n solvents possess the highest chelating power, LiFSI (LiTFSI) dissolves into G_n at a salt-to-solvent ratio exceeding one.[66]

The electrolytes containing LiFSI and G_1 are good examples to explain the working principle of high-concentration advanced electrolytes. These electrolytes sometimes are classified according to the solvent-to-salt ratio. The equimolar mixtures are called solvate ionic liquids (SILs) since their behavior is similar to normal ionic liquids. If the salt-to-solvent ratio is below 1:1, electrolytes are denoted as high-concentration electrolytes (HCE). An HCE containing a non-coordinating diluent is also called a localized high-concentration electrolyte (LHCE).[119] Diluents are fluorinated ethers miscible with HCEs. Since diluents do not coordinate Li^+, their preliminary role is a reduction of electrolyte viscosity.[120]

The simplified solvation structures of SOA electrolytes, HCEs, and LHCEs are shown in **Figure 1.13 A**. There are several critical differences between the structures. SOA electrolytes exhibit a significantly higher fraction of free solvent molecules than (L)HCEs, which results in the formation of a thick SEI with low Li^+-conductivity. Furthermore, Li^+ ions are primarily coordinated by solvent molecules in the case of SOA electrolytes. This reduces the charge transfer rate at the anode interface and lowers the efficiency of Li deposition.

On the other hand, the solvation structure of (L)HCEs is devoid of free solvent molecules, which reduces the electrolyte flammability and suppresses side reactions at the Li surface.[120] Increasing the salt-to-solvent ratio also reduces the fraction of free anions by strengthening the ionic interactions between Li^+ and the anion, as shown in **Figure 1.13 A**. However, the formation of complex network of ions in HCEs increases their viscosity and limits the stability of LMBs with HCEs.[121] Therefore, non-coordinating diluents are required to improve the performance of LMBs.[121]

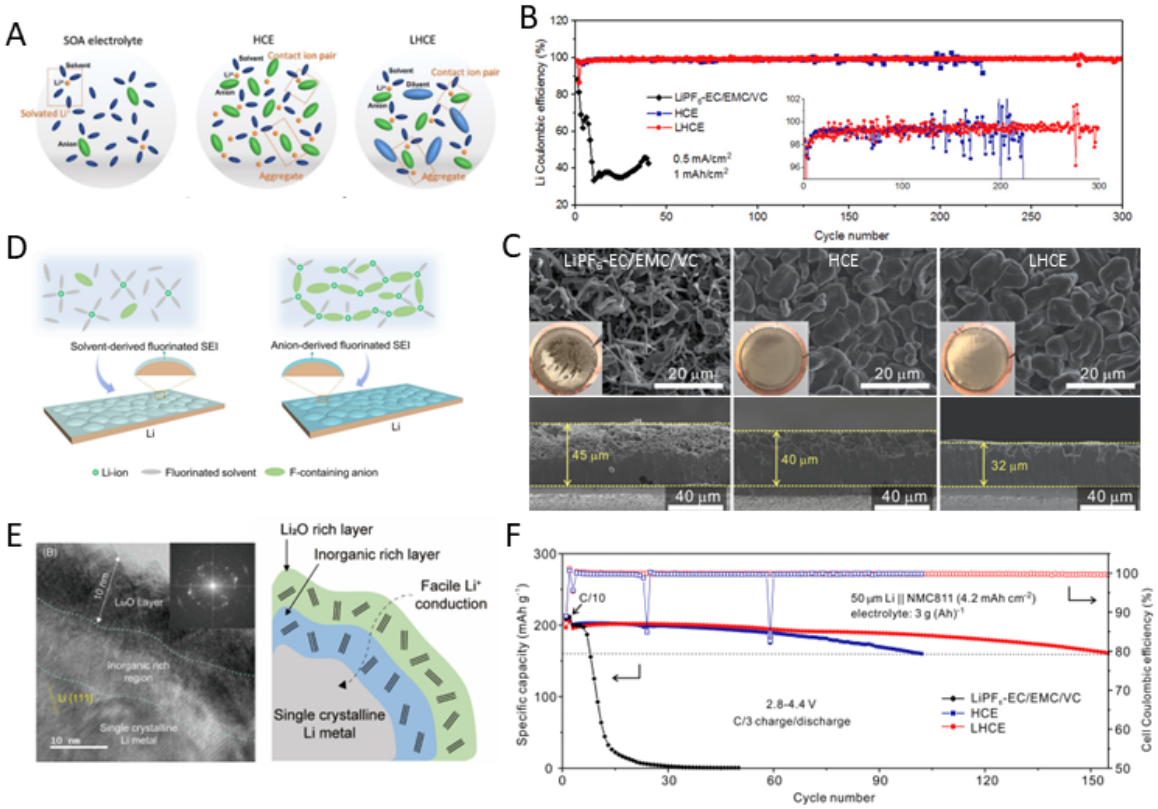


Figure 1.13 Stabilization of LMA by LHCEs. (A) Schematic solvation structure of the liquid electrolytes employed in LMBs. Reprinted from Ref. 120. (B) Li Coulombic efficiency of Cu-Li cells with SOA electrolytes, HCEs, and LHCEs. (C) Surface and cross-sectional SEM of Li deposited from the electrolytes shown in Panel B. Panel B and C are reprinted from Ref. 121. (D) Different mechanisms of the SEI formation in SOA electrolytes and LHCEs. Reprinted with permission from Ref. 122. (E) Cryo-HRTEM image of the dual-layered inorganic-rich SEI layer after plating in G_1-based HCE and the schematics of Li^+ transport across the SEI. Reprinted with permission from Ref. 123. (F) Cycling performance of the high-voltage LMBs with different electrolytes. Reprinted with permission from Ref. 121.

The improved stability of the LMA in (L)HCEs is demonstrated by a higher Coulombic efficiency (CE) of Li deposition. Indeed, the CE of Li deposition in SOA electrolytes is limited to 50-60 % due to parasitic reactions (**Figure 1.13 B**). Meanwhile, when a steady state is achieved, (L)HCEs exhibit only a 1 % loss in Li capacity. SEM analysis of plated Li also confirms an improved stability of Li in the cells with (L)HCEs (**Figure 1.13 C**). While Li deposition from SOA electrolytes yields Li with needle-like morphology, dense columnar Li is observed when (L)HCEs are employed.[121] The better performance of LMAs in advanced electrolytes correlates to a stronger association between Li^+ and anion in (L)HCEs than in SOA electrolytes because incorporating FSI^- or $TFSI^-$ into the first coordination sphere of Li^+ ion yields SEIs with a high fraction of LiF (**Figure 1.13 D**).[122] A recent computational and cryo-HRTEM study demonstrates that the decomposition of (L)HCE yields the double-layer inorganic SEI.[123] The inner layer contains LiF, Li_2S, and Li_3N; the outer layer primarily contains Li_2O (**Figure 1.13 E**). The inorganic SEI exhibits a uniformly distributed Li^+ conductance, which reduces the chance of nucleating Li dendrites. Furthermore, the decomposition of (L)HCE at the positive electrode surface also creates a LiF layer, thus enabling efficient high-voltage LMBs (**Figure 1.13 F**).

1.5 Solid-state Li Batteries

Due to the safety hazards of high-energy-density Li batteries with liquid electrolytes, developing solid-state batteries (SSB) is the primary direction of current battery research.[124,125] Solid electrolytes (SEs) are much less flammable than their liquid counterparts. Furthermore, SEs remain conductive even at -40 °C.[126] Therefore, SSBs exhibit much greater applicability for EV applications. For instance, BMW plans to present a vehicle powered by an SSB in 2025.[127]

In addition to their higher safety, lithium metal solid-state batteries (LiM-SSBs) offer a 40 % increase in gravimetric and a 70 % increase in volumetric energy density compared to SOA LIBs. This is achieved by substituting bulky porous graphite anodes with dense and thin LMAs. Additionally, the energy density and manufacturing costs of LiM-SSBs can be further improved if LMAs are removed from the cell architecture.[125]

A typical LiM-SSB contains a Li anode, SE, and positive electrode (**Figure 1.14**). Positive electrodes contain redox-active lithium intercalation or conversion materials (often denoted as cathode active materials (CAMs)) mixed with SEs. In turn, SEs can be divided into two large groups: polymer and inorganic SE. Although the polymer SEs exhibit easier processability and lower cost than inorganic

SEs, their ionic conductivity achieves the threshold of 10^{-4} mS.cm^{-1} only at a temperature above 60 °C, limiting the rate capability of SSBs.[128] On the contrary, inorganic SEs exhibit much higher ionic

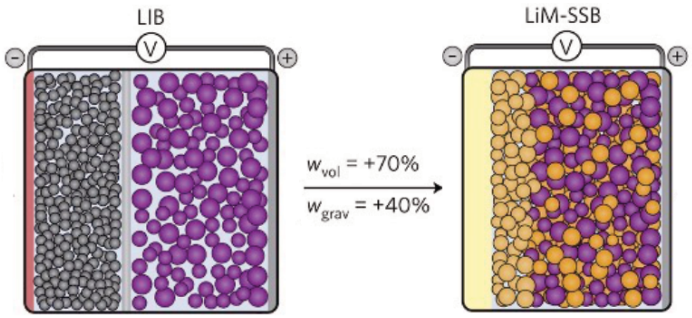


Figure 1.14 Solid-state lithium batteries. Schematical architectures of SOA LIBs, LI-SSBs, and LiM-SSBs. Reprinted with permission from Ref. 124.

conductivity at the expense of their costs. Inorganic SEs are usually divided into three major groups according to their anionic sublattice: oxide-based (including phosphates, borates, and sulfates), [129–131] sulfides,[132–136] and halides.[137–145] Since sulfide SEs exhibit the highest room temperature ionic conductivity (up to 20 mS.cm^{-1}) and relative compatibility with negative electrodes, they have been the most common SEs employed in the development of LiM-SSBs.

SSBs deliver high energy density only if they employ thick positive electrodes made of high-capacity materials (i.e., S_8, Li_2S, or Ni-rich $LiNi_xMn_yCo_{1-x-y}O_2$). Since my PhD research was primarily focused on SSBs with $LiNi_xMn_yCo_{1-x-y}O_2$ cathodes, the subsequent part of the Introduction is focused on the challenges of LiM-SSBs with sulfide SEs and $LiNi_xCo_yMno_{1-x-y}O_2$ (NCM).

1.6 Challenges of Li-M SSBs

The chemomechanical limitations of LMAs preventing the commercialization of LiM-SSBs[125] include the interfacial reactivity between SEs and LMAs, volume changes induced by Li plating and stripping, and formation of Li dendrites. It is noteworthy that the morphological instability of Li during cycling has a similar origin to the LMBs with liquid electrolytes, except for the different mechanisms of dendrite propagation through inorganic SEs. While liquid electrolytes fill all available space inside batteries, the microstructure of organic electrolytes contains grain boundaries and various mechanical defects, including voids and cracks. This accelerates the penetration of Li dendrites as shown in **Figure 1.15 A**.[146] Moreover, a non-zero electronic conductivity of SEs might trigger Li deposition within SE's voids.[147] Additionally, pitting on the Li surface while discharging LiM-SSBs reduces the contact area and decreases the battery capacity (**Figure 1.15 B**).[148]

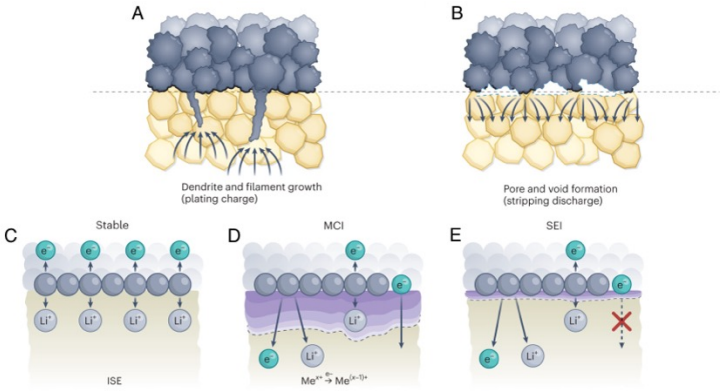


Figure 1.15 LMA challenges in SSBs. (A) Formation of Li dendrites and (B) pores and voids upon cycling the LiM-SSBs. Different interfacial compatibility between Li and the SEs showing the examples of a (C) stable interface, (D) kinetically unstable mixed-conducting interphase (MCI), and (E) kinetically stable SEI. Reprinted with permission from Ref. 125.

The LMA compatibility of SEs depends on their chemical composition (**Figure 1.15 C – E)**. Unfortunately, the case of no chemical reactions at the Li/SE interface is rare due to the high reducing power of Li. Among existing inorganic SEs, only $Li_7La_3Zr_2O_{12}$ (LLZO) does not react with Li. However, the observed compatibility between LLZO and Li results from the slow kinetics of Zr^{4+} reduction because the partial reduction of Zr^{4+} to Zr^{3+} is thermodynamically favourable.[149] The formation of mixed-conducting interphases (MCIs) or SEIs between Li and SEs is a more common

scenario. As demonstrated in **Figure 1.15 D**, a typical MCI exhibits non-zero electronic conductivity, which results in continuous interphase growth and consumption of metallic Li. On the contrary, since the electronic conductivity of SEIs is low, its thickness is limited to approximately 100 nm.[150]

The composition of SEs dictates whether MCIs or SEIs will be formed at the Li/SE interface. If an SE contains a metal or a semimetal, the growth of MCI is more likely, as proven by the case studies on the interphase formation between Li and $Li_{1.5}Al_{0.5}Ti_{1.5}(PO_4)_3$,[150] $Li_{10}GePS_{12}$,[151] and Li_3InCl_6.[152] For example, the reaction between Li and $Li_{10}GePS_{12}$ yields electronically conducting Li_xGe, which promotes the propagation of this interphase into the bulk Li (**Equation 1.31**).[151]

$$Li + Li_{10}GeP_2S_{12} \rightarrow Li_3P + Li_2S + Li_xGe \qquad \textbf{Equation 1.31}$$

In the case of SEs, which do not contain a metal/semimetal, the interphase exhibits self-limiting growth (**Figure 1.15 E**) due to the formation of electronically insulating products such as Li_2S, LiCl, and Li_3P. This interfacial behavior is demonstrated by Li_6PS_5Cl[153] and $Li_7P_3S_{11}$[154] (**Equation 1.32-1.33**).

$$8Li + Li_6PS_5Cl \rightarrow Li_3P + 5Li_2S + LiCl \qquad \textbf{Equation 1.32}$$

$$32Li + Li_7P_3S_{11} \rightarrow 11Li_3P + 3Li_2S \qquad \textbf{Equation 1.33}$$

It is worth mentioning that typical approaches to overcome the limitations of LMAs in LiM-SSBs are focused on the surface modification of LMAs or SSEs. This is generally achieved by applying metal (Ag,[155] Au,[156] In,[157] etc.) or carbon-based coatings, [158–161,] which react with Li metal to yield Li^+-conducting protective interlayers.

1.7 Challenges of NCM-based Cathodes in SSBs

Pursuing high-energy-density SSBs for EV applications requires mass production of SEs with ionic conductivity exceeding 5 $mS.cm^{-1}$.[162] Sulfidic SEs are the only SEs that exhibit high conductivity and relatively simple and scalable manufacturing. However, the performance of SSBs containing sulfide electrolytes is limited by the chemical and electrochemical reactivity of SEs.

The oxidation of S^{2-} causes electrochemical instability of sulfide SEs. Unlike the oxidation of Li_2S in organic electrolytes, the mechanism of SEs' oxidation is still under debate. Wagenmaker proposed that SEs are oxidized through a multi-step process initiated by the simultaneous oxidation and delithiation of SEs.[163] The simplified reaction illustrating the oxidation of Li_6PS_5Cl (**Equation 1.34**)

indicates that S and LiCl are formed.[164] Since the reaction products are insulators, the electrochemical decomposition of sulfide SEs increases battery resistance and lowers energy density.

$$Li_6PS_5Cl \rightarrow LiCl + Li_3PS_4 + S + 2Li^+ + 2e^- \quad \textbf{Equation 1.34}$$

The chemical instability between NCM CAMs and sulfidic SEs is a more compelling challenge of SSBs.[165,166] Delithiation of NCM and oxidation of Ni^{3+} to Ni^{4+} drive the surface oxidation of SEs, which produces a variety of insulating products (i.e., phosphates, sulfites, sulfates, LiCl, etc.).[167] Therefore, SSBs employing sulfide SEs and NCM-based CAMs suffer from rapid capacity fading, increasing polarization and low cyclability. Furthermore, oxygen redox processes in Ni-rich NCM (i.e., $LiNi_{0.6}Co_{0.2}Mn_{0.2}O_2$) trigger the release of SO_2 on charge.[168]

There are two primary strategies to improve the NCM/sulfide SE interface. The first approach is focused on coating NCM particles with Li^+-conducting buffer layers to avoid a direct contact between NCM and SEs. Since these coatings are usually made of oxides (i.e., $LiNbO_3$,[169] Li_3BO_3,[170] and ZrO_2[171]) with low ionic conductivity, their thickness has to be below 20 nm, which is hard to achieve without utilizing expensive techniques such as ALD. Furthermore, coating NCM particles reduces the electronic conductivity of the cathode composite,[145] which affects the rate capability of SSBs.

The alternative approach aims to replace sulfide SEs with chloride SEs. Since chloride SEs do not undergo electrochemical oxidation at voltages below 4.2 V,[172] SSBs with halide SE do not require any additional coating for NCM. However, chloride SEs always contain a central metal cation M (In, Zr, Sc), which makes them prone to the reduction at a potential below 1 V vs. Li^+/Li[152] Therefore, they must be separated from an anode by a layer of a sulfide SE. Recently, various chloride SEs with nominal composition of Li-M-Cl and ionic conductivity of 1-2 $mS.cm^{-1}$ have been successfully synthesized.[137–145] However, the relationship between the composition of the chloride SEs, specifically the nature of central metal cation M, and their performance in SSB remains unclear. Resolving the impact of central metal cation M on cycling performance of SSBs containing high-energy-density Ni-rich CAMs is detailed in Chapter 7.

1.8 Thesis Overview

This thesis describes a methodological approach to understanding the relationship between interfacial processes occurring in Li-O_2, Li-S, and solid-state Li batteries and their cycling performance. The thesis is separated into eight chapters.

Chapter 1 introduces the basics of rechargeable Li batteries to a reader. The chapter is divided into several blocks, devoted to the principle and challenges of Li batteries employing conversion (O_2 and S-based) cathodes, metallic Li anodes, and solid-state electrolytes. The theory behind lithium metal anode instability is provided. Chapter 2 briefly describes the experimental methods employed in this thesis. Chapter 2 also provides the fundamentals of electrochemical impedance spectroscopy (EIS) since this method is widely utilized in the thesis.

Chapter 3 focuses on the mechanisms of discharge and charge reactions in nonaqueous Li-O_2 batteries containing a LiI redox mediator. The combination of numerous characterization techniques demonstrates that LiI lowers the reversibility of Li-O_2 batteries despite a seemingly lowered charging voltage. This work was performed in collaboration with Dr. R. Black, Dr. C. Burke, Dr. B. McCloskey (University of California, Berkeley), Dr. V. Giordani, and Dr. D. Addison (Liox Power). Dr. Black and I conducted galvanostatic cycling of Li-O_2 batteries, electrochemical mass-spectrometry measurements, and chemical titrations of the electrodes. I also contributed to the manuscript preparation. The results presented in Chapter 3 are included in the publication: Implications of $4e^-$ Oxygen Reduction via Iodide Redox Mediation in Li-O_2 Batteries. C. M. Burke, R. Black, I. Kochetkov, V. Giordani, D. Addison, L.F. Nazar, B.D. McCloskey, *ACS Energy Letters* **2016**, *1* (4), 747-756. Copyright 2016: American Chemical Society.

Chapter 4 presents the investigation of solvate ionic liquid electrolytes for high-energy-density Li metal batteries. The electrolytes containing LiFSI, G_n (n = 1 - 4), and TTE (1:1:4 molar ratio) were systematically studied by combining numerous spectroscopic, electrochemical, and calculation

methods. This work demonstrates the relationship between the electrolyte solvation structure and stability of Li deposition. In this chapter, I completed all the analysis and characterization except for DFT calculations. Dr. B. Singh performed DFT calculations of the electrolytes. The results of this chapter are unpublished.

Chapter 5 presents a case study of the performance of LMAs in SSBs with sulfide solid electrolytes. It demonstrates that LMAs are relatively stable in contact with β-Li_3PS_4 and $Li_{5.5}PS_{4.5}Cl_{1.5}$ but severely react with $Li_{10.35}Sn_{0.27}Si_{1.08}P_{1.65}S_{12}$ and $Li_{3.25}Si_{0.25}P_{0.75}S_4$ SE. The chapter demonstrates the improved performance of LMAs in SSB cells employing $Li_{5.5}PS_{4.5}Cl_{1.5}$/ $Li_{10.35}Sn_{0.27}Si_{1.08}P_{1.65}S_{12}$ multilayer SEs and solvate ionic liquid interlayers. The results demonstrated in this Chapter are unpublished. In this work, I completed all the synthesis and characterization experiments. The results of this chapter are unpublished.

Chapter 6 demonstrates the complex interfacial chemistry of Ta-doped LLZO garnet solid electrolytes in Li-S batteries with EPD electrolytes. Due to LiOH surface impurities, pristine LLZO undergoes a series of chemical reactions with sulfur-containing species, forming a highly resistive (5000 $\Omega.cm^2$) passivating layer at the surface of LLZO. However, tuning LLZO surface composition by reacting with phosphoric acid produces a thin Li^+-conducting protective coating, which lowers the interfacial resistance to 40 $\Omega.cm^2$. Therefore, Li-S hybrid cells with phosphorylated LLZO and DMA deliver a high and stable discharge capacity of 1400 $mAh.g^{-1}$. This work was completed in collaboration with A. Shyamsunder, M. Palmer (University of Michigan) and Dr. J. S. Sakamoto (University of Michigan). In this work, I modified the surface of LLZO pellets and studied their stability against sulfur in DMA using EIS and XPS. M. Palmer and I conducted electrochemical characterization of Li-S batteries with LLZO via EIS and galvanostatic cycling. A. Shyamsunder performed UV-vis, NMR and some XPS measurements. I also contributed to the manuscript preparation in collaboration with A. Shyamsunder

and M. Palmer. The results of this work are published: Surface Chemistry of LLZO Garnet electrolytes with Sulfur in Electron Pair Donor Solvents. Abhinandand Shyamsunder, Max Palmer, Ivan R. Kochetkov, Jeff Sakamoto, Linda F. Nazar, *ACS Applied Materials and Interfaces* **2023**, *15* (45), 52571-52580. Copyright 2023 American Chemical Society.

Chapter 7 establishes the relationship between the composition of Li-M-Cl solid electrolytes and their stability in SSB cells with Ni-rich cathode materials. The critical role of central metal cations $M^{3+/4+}$ is demonstrated through the combination of numerous methods, including EIS, ToF-SIMs, and DFT calculations. This work also presents the systematic approach to investigate the stability of SSB cells with novel SEs. This work was done in collaboration with Dr. K. Kaup, Dr. L. Zhou, Dr. R. Reuss (University of Giessen, Germany), Dr. T.T. Zuo (University of Giessen, Germany), and Dr. J. Janek (University of Giessen, Germany). In collaboration with Dr K. Kaup, I investigated the stability of SSB cells via galvanostatic cycling. I also conducted and analyzed EIS and cyclic voltammetry measurements. Dr. Reuss conducted FIB-SEM of the cathodes. Dr. Zuo performed the ToF-SIMS analysis. Dr. B. Singh performed DFT calculations of the interfacial stability. These results are published in the following publication: Different interfacial reactivity of lithium metal chloride electrolytes with high voltage cathodes determines solid-state battery performance. Ivan R. Kochetkov, Tong-Tong Zuo, Raffael Ruess, Baltej Singh, Laidong Zhou, Kavish Kaup, Jürgen Janek, Linda F. Nazar. *Energy and Environmental Science* 2022, **15**, 3933-3944. Copyrights: The Royal Society of Chemistry 2022.

Chapter 8 concludes the thesis. This chapter provides some final thoughts on the development of stable Li batteries.

Chapter 2
Methods

2.1 X-Ray Diffraction

X-ray diffraction (XRD) is the most common technique to determine the structure of crystalline materials. X-rays, electromagnetic radiation with wavelengths of (1 – 10) 10^{-10} m, are elastically scattered due to the interactions with atoms' electrons. If a material has a periodic crystal structure, the scattered X-rays undergo constructive interference in specific directions, according to Bragg's law (**Equation 2.1**):

$$n\lambda = 2d_{hkl}\sin\theta \qquad \textbf{Equation 2.1}$$

where λ is the wavelength, d_{hkl} is the spacing between the diffracting planes, θ is the incident angle, and n is an integer.

The constructing interference enhances the intensity of scattered radiation and results in the appearance of peaks at certain angles. The dependence of scattering intensity on twice the incidence angle (2θ) is called an XRD pattern, which is unique for each crystalline material.

Powder XRD patterns are generated by rotating the detector and the X-ray source from 0 to θ relative to the stationary sample holder loaded with fine-grind powdery samples or electrodes extracted from electrochemical cells.

All XRD patterns shown in this work were collected on a PANalytical Empyrean X-ray diffractometer operating at 40 kV and 40 mA and using Cu-Kα radiation (λ = 015405 nm). Samples were loaded onto zero-background silicon holders. Air-sensitive samples were covered with an air-tight Kapton film. The crystalline phases were identified by comparing the experimental XRD patterns to the Inorganic Crystal Structure Database (ICSD) using the HighScorePlus software.

2.2 Scanning Electron Microscopy and Energy-dispersive X-Ray Spectroscopy

Scanning electron microscopy (SEM) is a powerful tool to study the surface morphology of various materials. Scanning electron microscopes operate in a reflection mode, and its general operating principle is described below.

The primary electron beam is generated by thermal evaporation from the cathode surface. The beam is accelerated through an electric field of 5-30 kV and focused into a collimated beam using magnetic condenser lenses. Bombarding a sample with primary electrons initiates multiple ionization and energy release mechanisms, which provides the necessary information about microstructure and chemical composition of the sample. A typical SEM experiment studies the microstructure by analyzing secondary and backscattered electrons. Inelastic scattering of the primary beam close to the sample surface generates secondary electrons and aids in visualizing the sample morphology. On the contrary, elastic scattering generates the backscattered electrons. Since heavier elements scatter electrons more efficiently, the contrast in backscattered images illustrates the distribution of light and heavy elements at the surface.

The generation of X-rays by the elements at the surface, is another mechanism of interactions between the sample and primary electrons. In energy-dispersive X-ray spectroscopy (EDX), the hole X-ray emission spectrum is detected simultaneously. Since the emission spectrum is unique for each element, EDX is able to analyze the sample's elemental composition.

Scanning electron microscopy was carried out using a Zeiss Ultra field-emission SEM instrument with an EDX detector. Air-sensitive samples were assembled in an Ar-filled glovebox and loaded into the SEM chamber with minimum air exposure.

2.3 Raman Spectroscopy

Raman spectroscopy is named after Sir C. V. Raman, who first observed the inelastic scattering of light. A sample is irradiated by an intense visible or UV light with a frequency ν_0, and the scattered light is detected in a direction perpendicular to the incident beam. The scattered light consists of elastic (Realeight) and inelastic parts (Raman). Raman scattering is weak and has frequencies of $\nu_0 \pm \nu_m$, where ν_m is the vibrational frequency of a sample. The $\nu_0 - \nu_m$ and $\nu_0 + \nu_m$ are called the Stockes and anti-Stockes lines, respectively. The frequency ν_m is called the Raman shift and is usually recalculated to the energy scale (cm^{-1}).

The fundamentals of Raman spectroscopy may be illustrated by an example of a diatomic molecule.[173] The electric field of the incident radiation (*E*) induces a dipole moment (*P)*:

$$P = \alpha E = \alpha E_0 \cos(2\pi\nu_0 t) \qquad \textbf{Equation 2.2}$$

α is a proportionality constant called polarizability. If a molecule is vibrating with a frequency ν_m, the nuclear displacement (q) is

$$q = q_0 \cos(2\pi \nu_m t) \qquad \textbf{Equation 2.3}$$

where q_0 is a vibrational amplitude. For small q_0, α is a linear function of q. Hence,

$$\alpha = \alpha_0 + \left(\frac{\partial \alpha}{\partial q}\right)_0 q_0 \qquad \textbf{Equation 2.4}$$

$$P = \alpha_0 E_0 \cos(2\pi \nu_0 t) + \frac{1}{2}\left(\frac{\partial \alpha}{\partial q}\right)_0 q_0 E_0 [\cos\{2\pi(\nu_0+\nu_m)t\}+\cos\{2\pi(\nu_0-\nu_m)t\}] \qquad \textbf{Equation 2.5}$$

The first term represents Rayleigh scattering, and the second term denotes Raman scattering. Raman scattering occurs exclusively when $\left(\frac{\partial \alpha}{\partial q}\right)_0$ is not equal to zero. Since Stokes scattering is much stronger than anti-Stokes scattering, only Stokes lines are analyzed in Raman spectroscopy.

All Raman spectra were recorded from liquid samples using a DeltaNu Advantage (785 nm) spectrometer. Air-sensitive samples were sealed in glass cuvettes in an Ar-filled glovebox. Since some of the studied samples are highly fluorescent, multiple (300-600) fast Raman scans were acquired and summed. The background was subtracted by the asymmetric least square smoothing, as shown in **Figure 2.1**. The peaks were fitted with the Voight function, with the HWHM limited to 15 cm^{-1}.

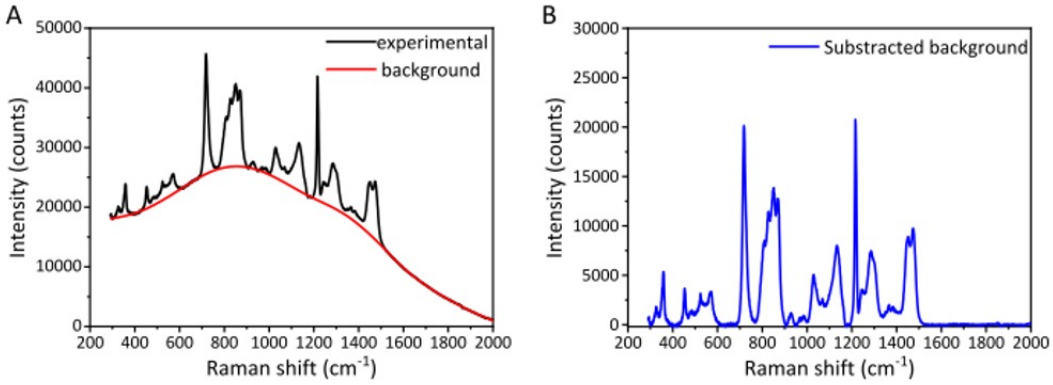


Figure 2.1 Processing of Raman spectra. Raman spectrum (A) before and (B) after background subtraction

2.4 Photoelectron Spectroscopy

Photoelectron spectroscopy is one of the widely used techniques applied for surface analysis. The photoemission spectra are generated by irradiating the surface with ultraviolet or X-ray photons. The first technique is ultraviolet photoelectron spectroscopy (UPS), and the second is X-ray photoelectron spectroscopy (XPS).

UPS and XPS have the same working principle. Bombarding the surface with photons of energy E_0 ejects photoelectrons. Since UPS employs UV radiation, the valance electrons are removed, and their kinetic energy (KE) is measured. The ionization energy (IE) is calculated via the Einstein equation, representing the transitions of the valence electrons. Overall, UPS provides high-resolution valence band spectra.

$$IE = E_0 - KE \qquad \textbf{Equation 2.6}$$

In this thesis, UPS was carried out at the University of Giessen (Germany) by Dr. R. Reuss using a PHI5000 Versa Probe II system (Physical Electronics Inc) equipped with a He-Iα source (21.22 eV).

XPS employs soft X-rays (Al Kα or Mg). The primary beam interacts with the sample and ejects photoelectrons from the core levels. The binding energy of an electron is also calculated by the Einstein equation (**Equation 2.7**).

$$E_B = E_0 - KE - \Phi \qquad \textbf{Equation 2.7}$$

where Φ is the work function of the sample but also includes the additional energy losses induced by the instrument.

XPS is a powerful tool to study the oxidation state and local chemical environment of the elements at the surface since the depth penetration of XPS is ~ 1 nm. If an XPS instrument is equipped with an Ar^+ sputtering gun, the chemical composition of multilayer interfaces can be studied. For example, the combination of XPS and Ar^+ sputtering provides a comprehensive insight into the surface chemistry of LLZO, as shown in Chapter 6.

In this thesis, XPS analysis was performed on a ThermoESCALAB 250 instrument. XPS analysis was performed on a Thermo ESCALAB 250 instrument. The samples were transported to the spectrometer chamber without air exposure. All spectra were fitted with Gaussian-Lorentzian functions

and a Shirley-type background using the CasaXPS software. The binding energy values were all calibrated using the C 1s peak at 284.8 eV.

2.5 Differential Electrochemical Mass-Spectrometry

Differential electrochemical mass-spectrometry (DEMS) is an analytical technique that quantifies gas evolution or consumption during electrochemical reactions. In a typical DEMS measurement, the electrochemical cell is constantly purged by Ar flow. The released gases enter a quadrupole mass spectrometer where they are ionized. Ion currents from the ionized species are then measured separately according to their m/z ratio.

The ion current produced by a gas linearly depends on the gas concentration.

$$I(t) = B(t) + S \cdot G(t) \qquad \textbf{Equation 2.8}$$

Here, S ($A.ppm^{-1}$) is the calibration factor measured before the DEMS experiments.

The gas evolution rate is calculated according to **Equation 2.9**

$$\frac{dG(t)}{dt} = \frac{[G(t)]\ (ppm)}{10^{-6}} \cdot Q\ (ml_{Ar}.min^{-1}) \qquad \textbf{Equation 2.9}$$

Here, Q is the flow rate of the carrier gas.

The DEMS measurements were performed using the homemade setup to quantify O_2 and CO_2 evolution exhibited by the cathodes containing electrochemically formed Li_2O_2.[174] More details of the setup can be found in Ref. 172.

2.6 Time-of-Flight Secondary Ion Mass Spectrometry

Time-of-flight secondary Ion Mass Spectroscopy (ToF-SIMS) is a surface-sensitive analytical technique that probes the chemical composition of the surface by bombarding it with a beam of Bi^+ ions. The interaction between the incident ion beam and the material triggers the release of the secondary ions from the surface.

The samples for ToF-SIMS were prepared at the University of Waterloo and shipped in air-tight containers to the University of Giessen (Germany). Dr. T.T. Zuo performed the measurements using a ToF-SIMS 5-100 system (IONTOF GmbH). The additional details of the ToF-SIMS measurements are provided in Chapter 6.

2.7 Ultraviolet-Visible Spectroscopy

Ultraviolet-visible (UV-Vis) spectroscopy is an absorption spectroscopy in which UV-visible light is absorbed by a compound. The amount of absorbed radiation depends on the concentration of the analyte according to the Beer-Lambert law (**Equation 2.10**)

$$A = \log_{10}\left(I_0/I\right) = \varepsilon c L \qquad \textbf{Equation 2.10}$$

Here, A is the absorbance, I_0 is the intensity of the incident light at a given wavelength, I is the intensity of the absorbed light, ε is the molar absorptivity, c is the analyte concentration and L is the path length through the sample.

In this thesis, the samples for UV-vis spectroscopy were prepared in an Ar-filled glovebox. The measurements were carried out using a Thermo Scientific Evolution 201 UV-vis spectrometer at a wavelength between 400 and 800 nm.

2.8 Galvanostatic Cycling

Galvanostatic cycling is the most common technique used to study lithium batteries. The electrochemical performance of lithium batteries can be examined by using a two-electrode or a three-electrode setup. In the two-electrode setup, the voltage difference is measured between the positive and negative electrodes, and thus, the measured voltage is affected by the polarization of both electrodes. In the case of the three-electrode setup, the potential of the working electrode is measured relative to the third electrode, which remains unpolarized. This electrode is called the reference electrode.

Since the electrochemical performance of lithium batteries has to be studied under a limited electrolyte amount, the design of three-electrode Li batteries is complicated. Hence, the two-electrode setup is usually used to analyze the behavior of Li batteries. In a typical galvanostatic experiment, a constant current is applied until a cutoff voltage, or a cutoff capacity is reached. Then, the current direction is changed, and the reversed electrochemical reaction occurs. The process can be repeated if a target capacity is achieved.

Galvanostatic cycling is often used to calculate the reversibility of Li^+ intercalation or conversion reactions. Coulombic efficiency (CE) is a measure of reversibility. It is defined as the ratio between the discharge and charge capacity of the cell (**Equation 2.11**).

$$CE = \frac{Q_{discharge}}{Q_{charge}} \cdot 100\ \% \qquad \textbf{Equation 2.11}$$

In this thesis, galvanostatic cycling was used to study the efficiency of Li deposition from liquid and solid-state electrolytes and the performance of Li batteries with various conversion and intercalation cathodes. The cells were cycled at room temperature (23 - 26 °C range) using a Biologic VMP3 potentiostat.

2.9 Cyclic Voltammetry

Cyclic voltammetry (CV) is commonly used to study redox reactions. In a classic CV experiment, the potential of the working electrode (measured relative to the reference electrode) is linearly swept from the open circuit voltage (OCV) to a minimum or maximum cutoff value. In the first case, the electrode reaction is reduction; in the second case, the electrode reaction is oxidation. Once the cutoff potential is reached, the scan direction is reversed, and the cell is cycled until the experiment goal is achieved. CV is a powerful tool for studying the thermodynamic and kinetic processes occurring at the working electrode. Furthermore, CV is widely used to measure diffusion coefficients of electroactive species and the relationship between chemical and electrochemical processes.[175]

In this thesis, CV was used to estimate the oxidative stability of halide SEs in SSB cells. The details of the measurements are provided in Chapter 5.

2.10 Electrochemical Impedance spectroscopy

Electrochemical impedance spectroscopy (EIS) is a non-destructive technique based on perturbing the electrochemical system at the steady state with an alternating signal of small amplitude and measuring the response. There are two modes of generating the signal: applying alternating voltage (PEIS) and applying alternating current (GEIS). Since PEIS is more often used in battery research, the details of PEIS measurements are discussed.[176] The impedance (*Z(w)*) is the ratio of the applied voltage to the measured current.

$$Z(t) = \frac{V(t)}{I(t)} = \frac{V_m \sin(\omega t)}{I_m \sin(\omega t + \varphi)} = \lfloor Z \rfloor e^{j\varphi} = \lfloor Z \rfloor (\cos\varphi + j\sin\varphi) = Z' + jZ'' \qquad \textbf{Equation 2.12}$$

Here, V_m and I_m are the amplitudes of the applied voltage and measured current, respectively; ω is the angular frequency; ϕ is the phase shift, and j is the imaginary unit (j^2 = -1). Z' is real impedance representing resistance on the x-axis, and -Z'' is imaginary impedance representing the reactance on the y-axis, $|Z|$ is the magnitude of the impedance.

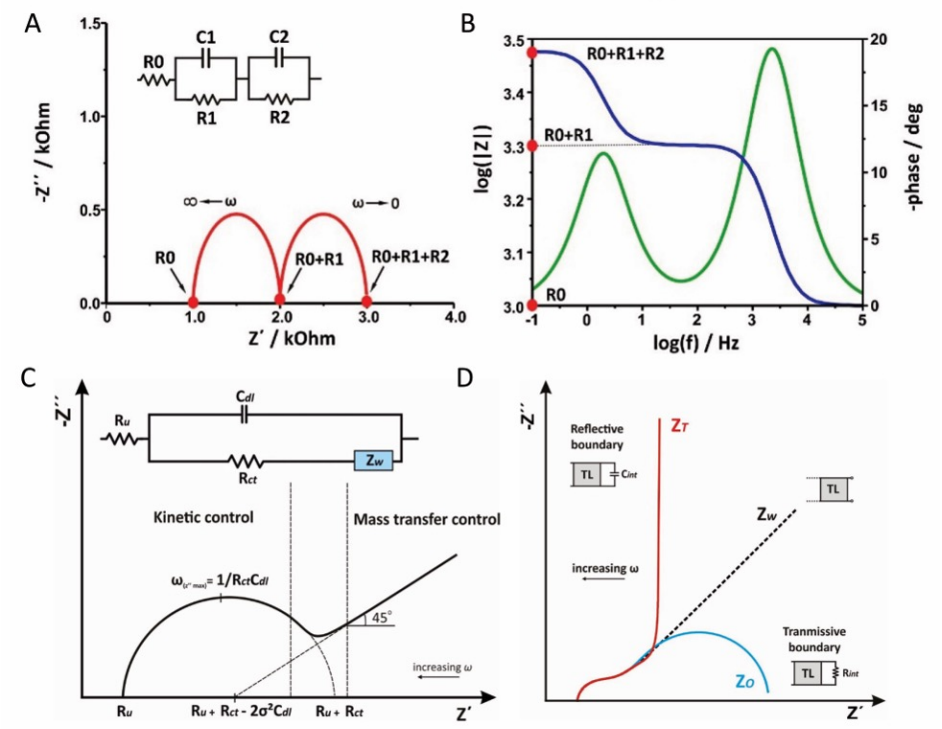


Figure 2.2 Fundamentals of EIS. Examples of the (A) Nyquist and (B) Bode plots of the R_0+R_1/C_1+R_2/C_2 electrical circuit. (C) Simple Randles circuit showing the regimes of kinetic and mass transfer control. (D) Three different shapes of the diffusion impedance showing the effect of boundary conditions. Reprinted with permission from Ref. 176.

Since the impedance contains both real and imaginary parts, its magnitude measured at different frequencies is plotted in the complex plane as demonstrated in **Figure 2.2 A**, called the Nyquist plot. Since the ongoing electrochemical and chemical processes dictate its shape, accurate analysis of the Li batteries by the EIS is a powerful tool. The most common approach to fit the experimental data is building an equivalent electrical circuit, which models the processes occurring in the cell. The equivalent circuit contains several basic elements: resistors (R), capacitors (C), inductors (L), and diffusion elements (W). For example, the circuit shown in **Figure 2.2 A** contains the series

connection of two parallel R/C components, which generate two frequency-separated semicircles. The EIS data can also be presented in the Bode plot (**Figure 2.2 B**), which shows the impedance and phase angle's dependence on the perturbation frequency.

It is noteworthy that there are several mnemonical rules for assigning the electrical elements to the ongoing physical processes. For example, R often denotes the resistance to the motion of charge carriers (i.e., Li^+ ions or electrons). Meanwhile, *C* represents the reconstruction of the electric double layer at the electrode/electrolyte interface. Due to the electrode surface roughness, the capacitor is often replaced by a constant phase element (CPE, Q), the impedance of which (Z_{CPE}) is described by **Equation 2.13**

$$Z_{CPE} = \frac{1}{Y_0(j\omega)^n} \qquad \textbf{Equation 2.13}$$

Here, Y_0 in $F.s^{n-1}$ is the parameter containing the capacitance information, and *n* is a constant ranging from 0 to 1. If n equals to 1, the CPE behaves like an ideal capacitor; if n is 0, the CPE is a resistor. For n = 0.5, the CPE represents diffusion impedance.[177]

The simplest way to illustrate the method of equivalent circuits is to consider a fast and reversible electrochemical reaction at the surface of an inert flat electrode (**Equation 2.14**).

$$O_{(solv.)} + ne^- \leftrightarrow R_{(solv.)} \qquad \textbf{Equation 2.14}$$

The redox reaction above results in the Nyquist plot (**Figure 2.2 C**) fitted by the Randles circuit. The plot exhibits three frequency-separated processes. The kinetics of the redox reaction dictates the cell impedance within the high-frequency range. The parallel connection of R_{ct} and C_{dl} represents the redox reaction. Here, R_{ct} describes the resistance to the electron transfer across the interface, and C_{dl} represents the capacitance of the double layer formed at the electrode surface. As shown in **Figure 2.2 C,** the semicircle is shifted from the origin due to the solution resistance (R_s).

As the frequency of the applied voltage decreases, the electrochemical cell enters a region of mass-transfer control where the diffusion of redox active species dictates the total impedance. The linear part of the Nyquist plot shown in **Figure 2.2 C** is called Warburg impedance (Z_W). Z_W represents the time-dependent semi-infinite diffusion of the redox active species towards the electrode. However, the semi-infinite diffusion does not describe the real electrochemical systems. Indeed, the electrodes are always separated by a finite distance. Therefore, the diffusion resembles the semi-infinite one until the time τ_d (**Equation 2.15**)

$$\tau_{\mathrm{d}} = \frac{2\pi \mathrm{L}}{\mathrm{D}} \qquad \textbf{Equation 2.15}$$

Here, *D* is the diffusion coefficient of the redox species, and L is the diffusion length.

After τ_d, the impedance depends on the permeability of the diffusion region to the diffusing species. A steady-state concentration gradient is established if the boundary is transmissive, and the diffusion impedance exhibits a resistive behavior. In the case of the reflective boundary, the diffusion region is not permeable, which results in capacitor-like behavior. The typical shapes of the different types of diffusion impedance are shown in **Figure 2.2 B**, and their mathematical expressions for are provided in **Table 2.1**.

Table 2.1 Diffusion impedance at different boundary conditions

Boundary conditions	Diffusion impedance
Time-dependent semi-infinite	$Z_W(\omega) = A_w\left(\sqrt{j\omega}\right)^{-1}$
Transmissive	$Z_T(\omega) = A_w\left(\sqrt{j\omega}\right)^{-1}\tanh\left(B\sqrt{j\omega}\right)$
Reflective	$Z_R(\omega) = A_w\left(\sqrt{j\omega}\right)^{-1}\coth\left(B\sqrt{j\omega}\right)$

In the case of lithium batteries, intercalation-type electrodes exhibit diffusion impedance with a reflective boundary, while LMAs exhibit diffusion impedance with a transmissive boundary. EIS analysis of lithium batteries is always a complicated process because an employed equivalent circuit depends on the battery configuration. The details of the equivalent circuits selected for fitting are provided in Chapters 4, 5, and 6. In this thesis, all EIS data was acquired using a Bioloigic VMP3 potentiostat and fitted using the Relaxis software.

Chapter 3
Reversibility of Li-O_2 Batteries with LiI Redox Mediator

This chapter is adapted with permission from Implications of 4e-Oxygen Reduction via Iodide Redox Mediation in Li-O_2 Batteries. Colin M. Burke, Robert R. Black, Ivan R. Kochetkov, Vincent Giordany, Dan Addison, Linda F. Nazar and Bryan B. McCloskey, *ACS Energy Letters* **2016**, *1* (4), 747-756. Copyright 2016: American Chemical Society.

3.1 Introduction

As discussed in the Introduction (Sections 1.3.1-1.3.3), charging Li-O_2 batteries at voltages below 4 V requires redox mediators. An RM is reversibly oxidized at the electrode surface at a potential between 2.96 and 4 V vs. Li^+/Li. Its oxidized form then reacts with Li_2O_2, releasing O_2 and regenerating the RM. LiI is a particularly interesting example of a RM due to its relatively high solubility in ether solvents and appropriate electrode potentials of 3.1 and 3.6 V vs. Li^+/Li (**Equations 3.1-3.2**).[178]

$$3I^- \rightarrow I_3^- + 2\boldsymbol{e}^- \ (E^0 = 3.1 \text{ V vs. } \mathbf{Li}^+/\text{Li}) \qquad \textbf{Equation 3.1}$$

$$2I_3^- \rightarrow 3I_2 + 2\boldsymbol{e}^- \ (E^0 = 3.6 \text{ V vs. } \mathbf{Li}^+/\text{Li}) \qquad \textbf{Equation 3.2}$$

The efficacy of LiI in reducing the polarization and improving the capacity retention of Li-O_2 cells were demonstrated by Kwak[178] and Liu.[43] Furthermore, Liu *et al.* demonstrated that LiI triggers the $4e^-$ ORR in the presence of trace water. However, the detailed role of LiI in the oxidation of Li_2O_2 and especially LiOH remains unclear.

This work provides quantitative insight into the effect of LiI and H_2O on the electrochemistry of nonaqueous Li-O_2 batteries with simple carbon cathodes and ether-based electrolytes. The combination of chemical titrations and DEMS illustrates that LiI deteriorates the reversibility of ORR and OER. The synergy of LiI and H_2O triggers the $4e^-$ oxygen reduction to LiOH. Unlike Li_2O_2, LiOH does not undergo reversible oxidation while charging the battery, which implies that Li-O_2 cells with LiI and H_2O behave like non-rechargeable primary batteries. Additionally, this work proves that observing the reduction in charging polarization and disappearance of LiOH may lead to a false positive conclusion regarding the efficacy of LiI as a promising RM. In fact, redox shutting of I-containing

species lowers the charging voltage from ~ 4 to 3.5 V and converts LiOH to $LiIO_3$ without oxygen release.

3.2 Experimental methods

3.2.1 Materials

LiI (Sigma Aldrich) and LiTFSI (Sigma Aldrich) were dried under a dynamic vacuum at 150 °C for 24 hours before use. 1,2-dimethoxyethane (DME) was purchased from Sigma Aldrich and dried over activated 3 Å molecular sieves. PTFE (1 μm particle-size powder) was purchased from Sigma Aldrich and used as received. Ketjenblack® (KB) was received from Toyota. Research-grade oxygen and argon were purchased from Praxair. 99% 90% $H_2{}^{18}O$ was purchased from Cambridge Isotopes. Li foil (0.38 mm thick, Sigma Aldrich) was polished with a toothbrush before cell assembly. Whatman glass fiber (GF) separators were dried under a dynamic vacuum at 300 °C for 24 hours before use.

3.2.2 Preparation of Cathodes

The KB carbon electrodes were prepared by a slurry method. In a typical electrode preparation, 20 mg of PTFE and 500 μL of isopropanol were sonicated for 1 hour. After that, the PTFE/isopropanol suspension was diluted with ethanol and ground with KB carbon until a thick paste was formed. The KB to PTFE ratio was 85:15 w/w. The mixture was applied to 11 mm stainless steel discs and dried at room temperature for several hours. Finally, the electrodes (1-2 $mg_{KB}.cm^{-2}$) were dried at a dynamic vacuum at 150 °C for 24 hours before cell assembly.

3.2.3 Cell Assembly

Li-O_2 cells were assembled in an argon glovebox with $p(O_2)/p < 0.1$ ppm and $p(H_2O)/p < 0.1$ ppm using the hermetically sealed modified Swagelok design. A typical Li-O2 cell contains a KB cathode, an 11 mm Li anode, and two 12 mm GF separators wetted with 160 μL of an electrolyte. The electrolytes containing 0.25 M of Li^+ ions were prepared by dissolving LiTFSI and LiI into DME. To prepare "wet" electrolytes, the predetermined amount of H_2O was quickly transferred to the electrolyte inside the glovebox. Finally, the cells were filed with O_2 gas (1.5 atm). The cells were cycled at a current density of 0.1 $mA.cm^{-2}$.

3.2.4 DEMS

DEMS measurements were performed using the home-made setup employing a gas flow controller (Bronkhurst F-200CV) and a quadrupole mass spectrometer (Stanford Research Systems, RGA 200). Prior to the measurements, the mass spectrometer was calibrated to establish the relationship between

the measured ion current and the concentration of O_2 and CO_2. The details can be found in Ref. 172. In a typical measurement, the electrode and separators were transferred from the Swagelok cell to a commercial electrochemical flow cell (EL-Cell, ECC-DEMS) containing a fresh Li anode. The DEMS cell was then charged under the continuous Ar flow, and the release of O_2 and CO_2 was quantified.

3.2.5 Quantification of Li_2O_2

The amount of Li_2O_2 in discharged cathodes was determined through iodometric titrations as described in Ref. 48. In brief, Li-O_2 batteries with various concentrations of LiI were discharged to 2 $mAh.cm^{-2}$ and disassembled inside a glovebox. The cathode and the separator facing the cathode were transferred to a vial, and then 5 mL of Millipore H_2O was added. The content of the vial was transferred to a conical flask, and the vial was rinsed with extra water. Subsequently, the Li_2O_2-containing flask was diluted with 25 mL of the buffer-catalyst solution comprised of KI, $(NH_4)_6Mo_7O_{24}{\cdot}4H_2O$, NaH_2PO_4, and $Na_2HPO_4^{2-}$. The buffer was prepared by dissolving 67 g of KI, 65 mg $(NH_4)_6Mo_7O_{24}{\cdot}4H_2O$, 0.11 mol of $H_2PO_4^-$, and 0.03 mol of HPO_4^{2-} into 1 L of Millipore water. After the addition of starch to the titration flask, the solution colour quickly turned to dark violet, thus indicating the oxidation of KI by the O_2^{2-} anion. Finally, the solution was titrated with a standard $Na_2S_2O_3$ solution. The titrations were repeated three times for each experimental point.

3.2.6 Detection of $LiIO_3$

The electrode and separators were extracted from the cells, washed with THF, dried under vacuum at the ambient temperature for one hour, and removed from the glovebox in a 20 mL vial. 5 mL of H_2O and MnO_2 powder were added to the vial. The vial content was left for 2 hours under magnetic stirring to allow the complete oxidation of O_2^{2-} by MnO_2. After that, the vial content was filtrated using a 0.2 μm syringe filter, which fully removed MnO_2. The clear solution containing LiIO3 and LiOH was mixed with 50 mg KI and 0.5 mL of 5 M H_2SO_4, and starch. Finally, the dark blue solution was titrated with a standard $Na_2S_2O_3$ solution.

3.2.7 XRD Analysis

XRD analysis of KB cathodes was performed with a PANalytical Empyrean X-ray diffractometer operating at 40 kV and 40 mA and using Cu-Kα radiation (λ = 015405 nm). Samples were mounted on a silicon low-background holder using a moisture-protective barrier.

3.2.8 SEM

KB cathodes were extracted from Li-O_2 cells in an Ar-filled box. The cathodes were washed with 2-3 mL of THF and vacuum-dried at room temperature for 1 hour. After that, the samples were loaded on SEM sample holders and transferred to the chamber of a Zeiss Ultra field-emission SEM instrument with minimal air exposure.

3.3 Effect of LiI and H_2O on the Polarization of Li-O_2 Batteries

The relationship between the concentrations of H_2O and LiI and polarization of Li-O_2 batteries is demonstrated in **Figure 3.1 A**. Although the discharge profile is seemingly independent of the electrolyte composition, XRD analysis of the discharged cathodes indicates the formation of LiOH instead of Li_2O_2 in electrolytes containing 0.2 M LiI and 5K H_2O (**Figure 3.1 B**). The precipitation of LiOH and its removal during discharging and charging were also confirmed through the combination of chemical titrations and DEMS by Dr. Burke. These details can be found in our joint publication (*ACS Energy Lett.* 2016, 1, 4, 747). It is worth noticing that the final product of the ORR is changed by the synergetic effect of LiI and H_2O. This is confirmed by the lack of LiOH detected in the Li-O_2 batteries after discharging in LiI-free electrolytes with H_2O.[179]

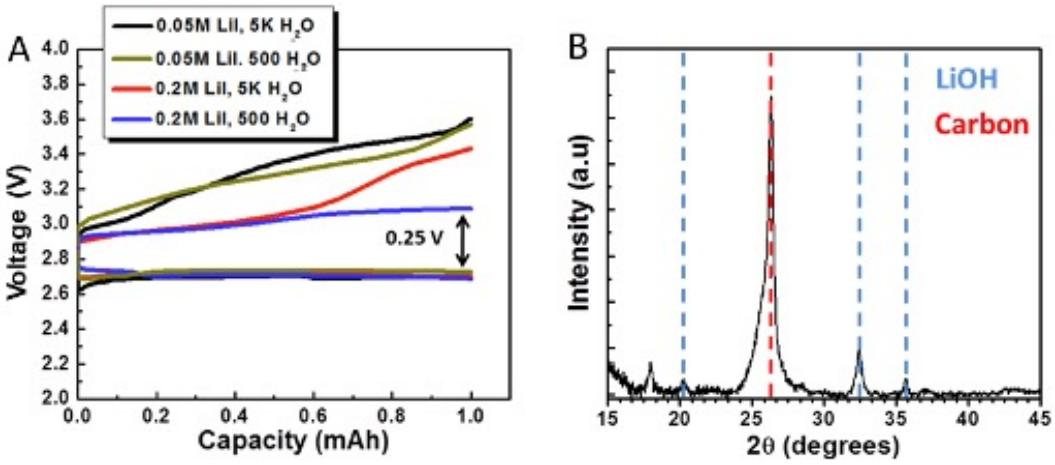


Figure 3.1 Electrochemical performance of the Li-O2 battery with LiI and H_2O. (A) Voltage profiles of Li-O_2 cells with Ketjenblack electrodes in LiTFSI/DME with various concentrations of LiI and H_2O at a current density of 0.1 mA.cm^{-2}. The total Li^+ concentration (LiI+LiTFSI) was fixed to 0.3 M; (B) XRD pattern of the carbon electrode from the cell with 0.2 M LiI + 5K H_2O

In agreement with Liu,[43] the presence of LiI lowers the battery polarization during charge. The Li-O_2 battery with 0.2 M LiI and 5K H_2O exhibits a low overpotential of 0.25 V. This is significantly lower than the polarization usually observed in LiI-free cells. However, the improved voltage profile does not necessarily imply that the OER is improved by LiI. To understand the effect of LiI and H_2O on battery charge, DEMS and chemical titrations were employed.

3.4 Effect of LiI on the Reversibility of Li-O_2 Batteries

We initially explored the effect of LiI on the formation of Li_2O_2 and oxygen evolution in nominally dry (< 50 ppm) electrolytes. **Figure 3.2 A** demonstrates the relationship between the polarization of Li-O_2 batteries with various LiI concentrations. Unlike the cells shown in **Figure 3.1 A**, those in **Figure 3.2 A** were connected to the mass spectrometer and charged until oxygen evolution was no longer observed. The corresponding DEMS data can be found in **Appendix A1**. Under the modified charge termination conditions, it becomes clear that LiI impacts the reversibility of the ORR and OER. Although increasing the concentration of LiI noticeably lowers charging voltage, it also leads to a significant overcharge. While the LiI-free control cell (black curve in **Figure 3.2 A**) requires a charge capacity of 1 mAh to oxidize Li_2O_2, the OER in the presence of 200 mM LiI needs almost 1.4 mAh. This behavior indicates that the reactivity between oxidized iodine-containing species (I_3^- and I_2) increases the charge consumption during oxidation, thus lowering the energy efficiency.

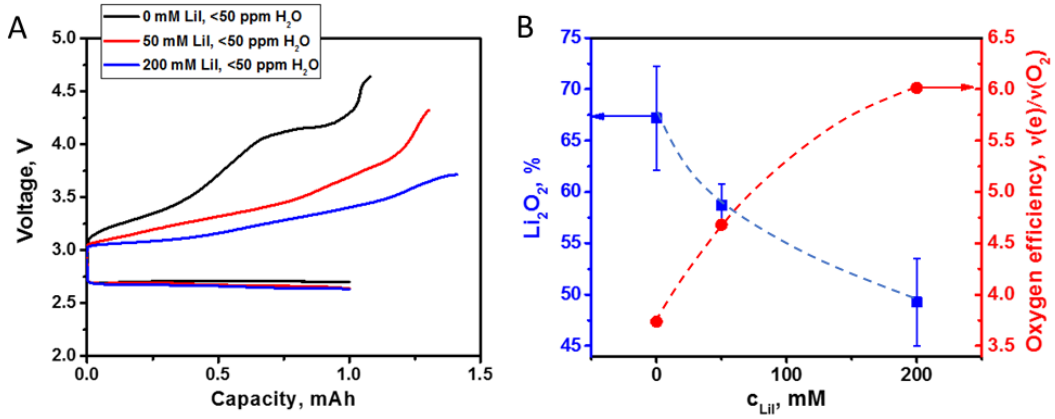


Figure 3.2 Effect of [LiI] on the yield of Li_2O_2. (A) Voltage profiles of the Li-O_2 battery containing 0, 50, and 200 mM LiI. The batteries were cycled at 0.1 mA.cm^{-2}. (B) Dependance of Li_2O_2 yield (blue squares) and efficiency of OER (red circles) on the concentration of LiI. The efficiency of OER was calculated by dividing the charge capacity (in moles) by the amount of evolved O_2. The corresponding DEMS curves are provided in **Figure A1.1**

The observed redox shuttling can be quantified by dividing the number of electrons consumed on charge by the amount of released oxygen. In the case of LiI-free electrolytes, the ratio of 3.5 significantly exceeds the theoretical value of 2.0, which indicates that the oxidation of Li_2O_2 and electrolyte occurs simultaneously. Modifying the electrolyte with LiI further decreases the efficiency

of Li_2O_2 oxidation. For example, oxidizing one mole of Li_2O_2 in electrolytes with of 200 mM LiI requires 6 moles of electrons (**Figure 3.2 B, right Y-axis**).

In addition to overcharging Li-O_2 batteries, LiI lowers the yield of Li_2O_2. The iodometric titrations of the cathodes discharged in electrolytes containing 0, 50, and 200 mM LiI demonstrate that the yield drops from 66 % in the LiI-free electrolytes to 50 % in electrolytes containing 200 mM LiI. The control reaction between LiI and [K(18-crown-6)]O_2 confirms the reactivity between LiI and Li_2O_2 (**Appendix B1**). Although the reaction mechanism details remain unclear, the reactivity between LiI and Li_2O_2 might be caused by H_2O_2 formed as a result of the O_2^- nucleophilic attack of DME.[178]

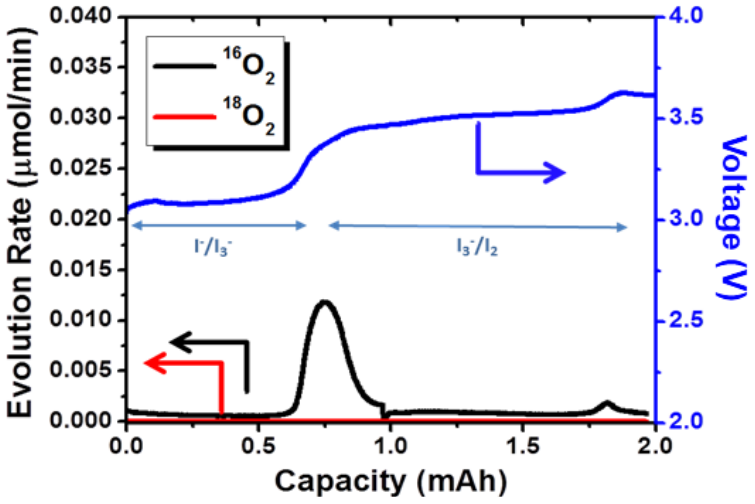


Figure 3.3 OER of the Li-O2 battery with 200 mM LiI and 5 K $H_2{}^{18}O$. The discharged KB electrode (1 mAh) was charged in the DEMS cell at 0.1 $mA.cm^{-2}$

The simultaneous presence of LiI and H_2O has a more severe effect on the OER efficiency. **Figure 3.3** shows the oxygen evolution from the cathode extracted from the cell discharged with 200 mM LiI and 5 K $H_2{}^{18}O$. If the OER involved the oxidation of LiOH, we would observe the evolution of $^{16,18}O_2$ and $^{18}O_2$. However, only $^{16}O_2$ appears in DEMS during charging, which indicates that LiOH does not participate in the OER. Nevertheless, the electrodes charged in the cells with LiI and H_2O do not contain LiOH (**Figure 3.4 A**), which suggests that LiOH is consumed by the chemical reactions during charge.

3.5 Mechanism of LiOH Removal during Charging

LiI undergoes two oxidation reactions, generating LiI_3 and I_2 (**Equations 3.1-3.2**). The oxidized iodine-containing products then react with Li_2O_2 releasing O_2 (**Equations 3.3-3.4**)

$$Li_2O_2 + LiI_3 \rightarrow 3LiI + O_2 \qquad \textbf{Equation 3.3}$$

$$Li_2O_2 + I_2 \rightarrow 2\,LiI + O_2 \qquad \textbf{Equation 3.4}$$

However, if LiI and H_2O convert Li_2O_2 to LiOH, LiI_3 and I_2 might undergo disproportionation by reacting with LiOH (**Equation 3.5-3.6**).

$$6LiOH + 3LiI_3 \rightarrow 8LiI + LiIO_3 + 3H_2O \qquad \textbf{Equation 3.5}$$

$$6LiOH + 3I_2 \rightarrow 5LiI + LiIO_3 + 3H_2O \qquad \textbf{Equation 3.6}$$

XRD and EDX analysis of the cathodes extracted from the cells with 0.2 M LiI and 5 K H_2O confirms the conversion of LiOH to $LiIO_3$. Indeed, the XRD pattern of the cycled KB cathode contains $LiIO_3$ (**Figure 3.4 A**), and the O/I ratio is 3, which is indicative of $LiIO_3$ (**Figure 3.4 B**).

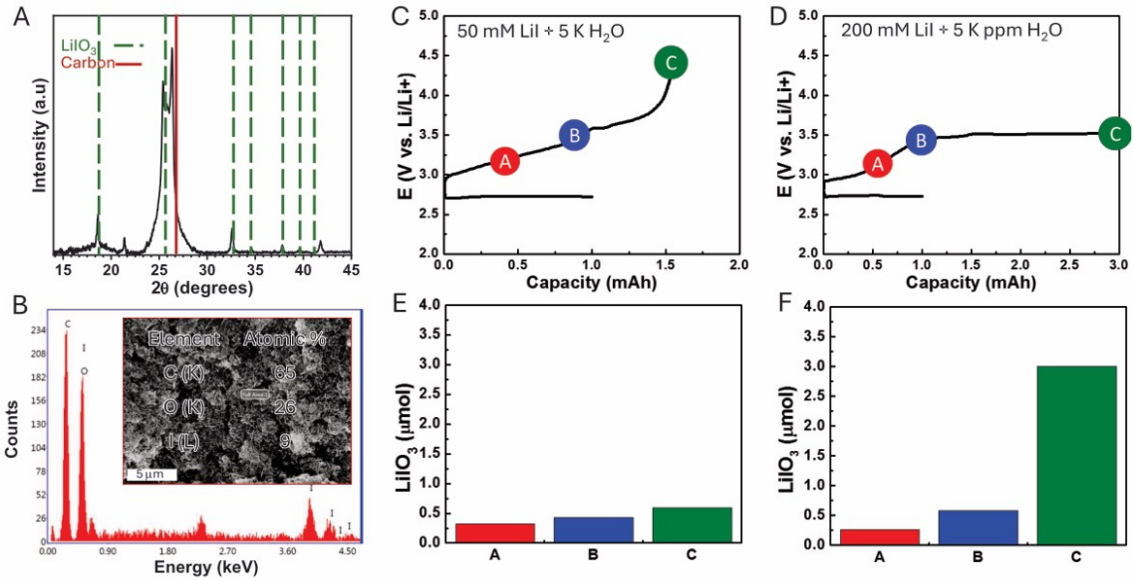


Figure 3.4 Conversion of LiOH to $LiIO_3$. (A) XRD and (B) EDX of the KB cathodes after charging the Li-O_2 battery with 200 mM LiI and 5 K H_2O. Polarization profiles of the cells with (C) 50 mM and (D) 200 mM LiI. Evolution of the amount of accumulated $LiIO_3$ in the presence of (D) 50 mM and (F) 200 mM LiI.

Titrating the electrodes extracted from the cells with 50 mM and 200 mM LiI and 5 K H_2O at numerous states of charge illustrates that the formation of $LiIO_3$ primarily occurs during the oxidation of I_3^- to I_2. Given a 100 % efficiency of LiOH formation and a discharge capacity of 1 mAh, the theoretical yield of $LiIO_3$ is 6.2 μmol. However, charging the battery with 50 mM LiI produces 0.5 μmol of $LiIO_3$ (equivalent to a yield of 6.5 %) due to reaching the cutoff voltage 4.5 V (**Figure 3.4 C, E**). This indicates that the reaction between LiOH and I_3^-/I_2 is kinetically limited, which is not surprising due to the low solubility of LiOH in DME. In contrast, the Li-O_2 battery with 200 mM LiI suffers from prolonged charging which is evidenced by the plateau at 3.5 V **(Figure 3.4 D)**. This yields 3.0 μmol of $LiIO_3$ due to the extended reaction between LiOH and continuously regenerated I_2 (**Figure 3.4 F**).

3.6 Conclusions

This work demonstrates the negative effect of LiI on the performance of Li-O_2 batteries. During the ORR in dry electrolytes, the reactivity of LiI lowers the yield of Li_2O_2, as confirmed by iodometric titrations of the discharged cathodes. In the case of "wet" electrolytes, LiI triggers the formation of LiOH. While charging the battery, LiOH does participate in the OER. Instead, it reacts with electrochemically generated I-containing species (I_3^- and I_2), yielding $LiIO_3$. Therefore, Li-O_2 batteries with a simple carbon cathode and LiI behave like non-rechargeable primary batteries.

This work demonstrates the importance of comprehensive multi-pronged analysis to study the behavior of Li-O_2 batteries with redox mediators. In particular, the effect of redox mediators on OER and ORR products should be quantified to explain the improved cyclability of batteries with redox mediators. In addition, the observed redox shuttle of I_3^- and I_2 suggests that incorporating protected lithium metal anodes in Li-O2 batteries with redox mediators is essential for future research.

Chapter 4
Solvate Electrolytes with LiFSI and Glyme Solvents for LMBs

4.1 Introduction

Developing advanced liquid electrolytes with a high salt-to-solvent ratio is one of the most promising solutions to address the challenges of LMAs, such SEI formation and Li dendrite deposition.[71] Among the variety of different solvent/salt combinations, high-concentration solutions of lithium bis(fluoro)sulfonyl imide (LiFSI) in monoglyme (G_1) are of particular interest due to the formation of inorganic and compact SEIs upon the decomposition of LiFSI[123] and intrinsically low reduction potential of G_1.[80] For example, LHCEs containing LiFSI/G_1 and 2,2,2-Trifluoroethyl 1,1,2,2-tetrafluoroethyl ether (TTE) diluent facilitate stable cycling of the LMBs under practical conditions.[121] However, the thermal stability of G_1-containing LHCEs is arguable due to the high flammability of G_1.[180] Therefore, replacing G_1 with its longer-chained and less flammable counterparts (G_2-G_4) could be a strategy to improve the thermal stability of the LMBs.[181] Unfortunately, increasing the glyme length slows down the transport of Li^+ across the cell due to the chelation of Li^+ ions by G_n. Nevertheless, establishing the effect of G_n on the stability of Li deposition from LiFSI-containing liquid electrolytes remains an important task.

In this work, we report on the comprehensive study of liquid electrolytes containing LiFSI, G_n, and TTE in a molar ratio of 1:1:4. Since LiFSI and G_n are in stochiometric amounts, the electrolytes are denoted as solvate ionic liquid electrolytes (SILs), following the studies of high-concentration solutions of LiTFSI in G_n solvents.[119] The relationship between the solvation structure of SILs and the kinetics of LMAs was investigated through the combination of Raman spectroscopy, AIMD simulations and EIS. The formation of isolated $[Li(G_n)]^+$ chelates in $114G_3$ and $114G_4$ weakens the association between Li^+ and FSI^- and impedes the desolvation of the Li^+ ions and their transport across the SEI. In contrast, the solvation structure of $114G_1$ and $114G_2$ contains the 3D structure of Li^+-FSI^- ionic aggregates, which reduces the interfacial resistance and lowers the activation energy barrier. However, the lithium transference of 0.22 limits the rate capability of LMAs. Although Li deposition occurs with a CE of ~ 99.5 % after the formation of a stable SEI, the bulk's slow diffusivity of Li^+ triggers short-circuiting of Cu-Li and Li||NCA full cells when a current density above 1 $mA.cm^{-2}$ is applied.

4.2 Experimental Methods

4.2.1 Materials

LiFSI was purchased from Gotion and dried under a dynamic vacuum at 120 °C for 48 hours. Monoglyme (G_1), diglyme (G_2), triglyme (G_3), and tetraglyme (G_4) solvents were purchased from Sigma, distilled, and dried over activated molecular sieves. G_1 was distilled at ambient pressure, and G_2 - G_4 were distilled under vacuum. 2,2,2-Trifluoroethyl 1,1,2,2-tetrafluoroethyl ether (TTE) (SynQuest Labs) was stored over activated molecular sieves to remove traces of moisture. $LiNi_{0.8}Co_{0.15}Al_{0.5}O_2$ (NCA) cathode tape laminated on an aluminum foil with a nominal active material loading of 18.9 $mg.cm^{-2}$ was purchased from NEI and used as received. Thin (50 μm) Li foil laminated on 8 μm Cu was purchased from China Energy Lithium Co. and used as received without polishing. 3501 Celgard separators (surfactant-coated, 25 μm thick, 55 % porosity) were kindly provided by NSERC.

4.2.2 Preparation of Electrolytes

The electrolytes were prepared in an Ar-filled glovebox ($p(O_2)/p < 0.5$ ppm, $p(H_2O)/p < 0.5$ ppm) by dissolving LiFSI in 2 mL of G_n under magnetic stirring. In the case of $114G_n$, an equimolar LiFSI/G_n solution was prepared at ~ 60 °C, and a required volume of TTE was slowly added. Finally, the solutions were filtered through a Millex PVDF syringe filter (Sigma, pore size 0.22 μm) to remove the traces of exfoliated molecular sieves. Finally, the solvate electrolytes with a nominal molar ratio between LiFSI, G_n, and TTE of 1:1:4 were cooled to 25 °C. The molar ratio between Gn and TTE was experimentally selected to achieve a viscosity comparable to the conventional electrolytes. The room temperature viscosities of $114G_1$, $114G_2$, $114G_3$, and $114G_4$ are 3.6, 4.7, 6.1, and 5.2 cPs, respectively.

4.2.3 Raman Spectroscopy

Raman spectra between 200 and 2000 cm^{-1} were obtained using a DeltaNu Advantage (785 nm) spectrometer. The electrolytes were loaded in an Ar-filled glovebox and sealed to avoid exposure to air. The measurement settings were adjusted to reduce the fluorescence and improve the signal-to-noise ratio. Typically, 300-600 spectra were recorded and summed before fitting. The background was subtracted by asymmetric least square smoothing. The FSI band (710-760 cm^{-1}) was deconvoluted into multiple Voight peaks. The Gaussian and Lorentzian widths were limited to 15 cm^{-1}.

4.2.4 SEM

Scanning electron microscopy imaging was carried out using a Zeiss Ultra field-emission SEM instrument. 2032 coin cells were disassembled inside the glovebox, and Li deposited on a Cu working electrode was washed with 1 mL of G_1 three times and then dried for 3 hours under dynamic vacuum at 25 °C. The Cu/Li samples were loaded inside the box and quickly transferred to the SEM chamber to avoid air exposure.

4.2.5 AIMD Simulations

The solvation structure of $114G_n$ was investigated using molecular dynamic simulations. The molecular structures of LiFSI salt, glymes, and TTE were optimized using the Gaussian 16 (G16) package with a hybrid functional B3LYP and the 6-31G(d,p) basis set. The initial structure of each LiFSI-DME-TTE system was generated by randomly placing LiFSI, DME, and TTE molecules in a cubic simulation box, following experimental densities and molar ratios (**Table 4.1**). Due to the higher computational cost of ab-initio MD (AIMD), the initial structural configurations were first optimized with classical MD using the all-atom optimized potentials for liquid simulations (OPLS-AA) force field. These simulations were conducted using the LAMMPS package in a canonical (NVT) ensemble at 300K with a timestep of 1 fs. Long-range electrostatic interactions were calculated using the particle-particle particle-mesh (pppm) solver method. To ensure thorough mixing of molecular species, the system was initially heated to elevated temperatures, reaching 800 K in 100 ps, equilibrated for 500 ps, and then cooled down to 300 K in 100 ps. Finally, the system was evolved at 300K for 1 ns to achieve full equilibration, and the resulting configurations were used as initial structures for AIMD simulations.

AIMD simulations were performed using planewave pseudopotentials with projector augmented wave (PAW) potentials for core electrons and the Perdew–Burke–Ernzerhof (PBE) exchange-correlation functional within the generalized gradient approximation (GGA), as implemented in the Vienna ab-initio simulation package (VASP). A plane wave energy cutoff of 500 eV was chosen, and the convergence criteria for electronic self-consistent iterations were set to 1×10^{-5} eV. AIMD simulations were carried out for 10-20 ps with a timestep of 1 fs, and various local structural parameters were derived from these simulations. The number of atoms and size of the simulated electrolytes are shown in **Table 4.1.**

Table 4.1 Details of the box for the AIMD simulations

Electrolyte	$N_{Li\text{-}FSI}$	N_{Glymes}	N_{TTE}	Total number of atoms in the box	Box length (Å)
$Li(G_1)_1FSI$	10	10	0	260	15.74
$Li(G_4)_1FSI$	6	6	0	282	15.11
$114G_1$	3	3	12	294	16.13
$114G_4$	3	3	12	357	16.82

4.2.6 EIS of Li Symmetric Cells

Symmetric 2032 stainless steel cells (MTI) were assembled with 380 μm Li (Sigma Aldrich, 11 mm diameter) electrodes and a 90 μm Whatman glass fibre filter infiltrated with 200 μL $114G_n$. The 2032 cells contain two 0.25 mm thick stainless steel spacers and one spring. Li foil was softly polished by a toothbrush to obtain a shiny silver surface. The Li symmetric cells were aged at 25 °C for 20 - 24 hours until a stable Nyquist plot was reached. The EIS was recorded in the frequency range between 1 MHz and 0.2 Hz every hour during storage. The voltage amplitude was 5 mV for all the measurements discussed in this Chapter. Impedance spectra of the stored Li symmetric were measured from 1 MHz to 1 mHz. The voltage amplitude was 5 mV for all the experiments.

The EIS measurements were performed at 25, 30, 35, 40, 45, and 50 °C to determine the activation energy of the steps of Li^+ from $114G_n$. Before the measurements at a new temperature, the cells were equilibrated for 3-4 hours. The EIS measurements were performed for all four $114G_n$ with 2 - 4 reproducible repeats for each solvate composition. The activation energy of resistance and diffusion were calculated using **Equations 4.1**-**4.2**:

$$\ln(\mathrm{T}\cdot R^{-1}) = \mathrm{A} + \frac{E_a}{k}\cdot T^{-1} \qquad \textbf{Equation 4.1}$$

$$\ln(\mathrm{D}) = \ln(D_0) - \frac{E_a}{k}\cdot T^{-1} \qquad \textbf{Equation 4.2}$$

A and D_0 are constants, k is the Boltzmann constant, and T is the absolute temperature.

4.2.7 Galvanostatic Polarization of Li Symmetric Cells

The short circuit time of Li deposition from $114G_n$ was measured by applying a constant current (0.25, 0.5, 0.75, 1, 1.5, 2, 3, and 4 $mA.cm^{-2}$) to a 2032 Li symmetric cell with one GF separator. The cells were polarized once until short-circuiting. The measurements were repeated 3-4 times to calculate the average duration of Li deposition at each current density. All polarization experiments were performed at 25 °C.

4.2.8 CE of Li Deposition

Cu-Li 2032-coin cells were assembled in an Ar-filled box with a 14 mm Cu positive electrode, a single 18 mm 3501 Celgard separator, and a 12 mm hand-polished Li negative electrode. Cu foil (8 μm, MTI) was rinsed with acetone without prior washing with HCl, dried under vacuum at 60 °C overnight, and transferred to the glove box. The electrolyte volume was fixed to 40 μL.

During a continuous measurement of CE, a fixed amount of Li was plated on Cu and then stripped with a voltage cutoff of 1 V. These Cu-Li cells were cycled until short-circuiting. CE of each cycle was calculated as the ratio of stripping capacity to plating capacity (**Equation 4.3**), and cumulative CE was calculated as a ratio between the cumulative stripped and plated Li (**Equation 4.4**):

$$\text{CE}=\frac{Q_{\text{stripped}}}{Q_{\text{plated}}}\cdot 100\ \% \qquad \textbf{Equation 4.3}$$

$$\text{Cumulative CE}=\frac{Q_{\text{stripped,total}}}{Q_{\text{plated, total}}}\cdot 100\ \% \qquad \textbf{Equation 4.4}$$

CE was also tested using the Aurbach method at 1 $mA.cm^{-2}$. Initially, Q_{Li} 5 $mAh.cm^{-2}$ of Li was deposited, and then 1 $mAh.cm^{-2}$ was repeatedly stripped and plated for 20 cycles. Finally, Li was completely stripped from Cu (Q_{Li}), and the CE was calculated:

$$\text{CE} = \frac{20\ \text{mAh.cm}^{-2}+Q_{\text{Li}}}{25\ \text{mAh.cm}^{-2}}\cdot 100\ \% \qquad \textbf{Equation 4.5}$$

4.2.9 Preparation of Full Cells with NCA Cathodes

Al-clad 2032 coin cells were assembled to test the performance of $114G_n$ electrolytes under semi-practical conditions. Li||NCA cells contain an NCA (12 mm diameter) cathode, a 50 μm Li (14 mm diameter) anode, and a single 3501 Celgard separator (18 mm diameter). The electrolyte loading was

40 μL $114G_n$ per cell. The Li||NCA cells were cycled twice at 0.1 C (1 C = 200 $mA.g_{NCA}^{-1}$) in the voltage range of 2.7-4.3 V, and then the rate was increased to 0.333 C.

Anodeless Cu||NCA cells with $114G_1$ were assembled similarly, except that 8 μm Cu was used instead of Li electrode. The Cu||NCA cells were cycled twice at 0.1 C in the voltage range of 2.7-4.3 V. After the second cycle, only the discharge current was increased to 0.333 C.

All the cells were cycled at 25 °C with 3-4 repeats per each experimental point. The cells were cycled under a pressure of ~ 0.1 MPa generated by the deformed stainless-steel spring.

4.3 Solvation Structure of $114G_n$

The structure of selected compositions from the LiFSI-G_n-TTE system was investigated via Raman spectroscopy and DFT calculations. Two prominent features are observed in the spectra within the range from 690 to 910 cm^{-1} (**Figure 4.1**). The band observed between 710 and 780 cm^{-1} arises from the S-N-S stretching, and its shape and position correlate to the binding between Li^+ and FSI^-.[182] The FSI^- band can be deconvoluted into three components based on the strength of binding between the ions: uncoordinated FSI^- or solvent-separated ion pairs (FSI-SSIP), contact ion pairs (FSI-CIP), and FSI-AGG-I and FSI-AGG-II (two types of ion aggregates_. The FSI-SSIP, FSI-CIP, FSI-AGG-I, and FSI-AGG-II were assigned to the following regions, according to previously published research on LiFSI-based electrolytes: below 720 cm^{-1}, 725-735 cm^{-1}, 735-750 cm^{-1}, and above 750 cm^{-1}, respectively.[182–184] It is important to mention that the fluorescence of LiFSI limits a precise quantitative analysis of the $Li(G_n)_1FSI$ and $114G_n$ electrolytes. Consequently, the deconvolution of the FSI^- band is semi-quantitative. The Raman activity observed between 780 and 900 cm^{-1} is attributed to the CH_2 rocking and C-O stretching of free G_n.[185,186] The breathing of $[Li(G_n)]^+$ contributes to the additional peak at 870-880 cm^{-1}.[187] The increase in Li^+ concentration results in the corresponding decrease in the ratio between the peaks of free and solvating G_n. The details of the peak assignment for the FSI^- region are provided in **Table 4.2.**

Table 4.2 Assignment of the individual Raman modes of FSI^-

	Raman band	Details
FSI^-	FSI-SSIP (715-720 cm^{-1})	FSI^- is separated from Li^+ by a G_n
	FSI-CIP (725-735 cm^{-1})	FSI^- is coordinated by one Li^+ ion
	FSI-AGG-I (740-745 cm^{-1})	FSI^- is coordinated by 2 Li^+ ions
	FSI-AGG-II >750 cm^{-1}	FSI^- is coordinated by 3 Li^+ ions

The association between Li^+ and the FSI^- ion depends on LiFSI concentration and G_n length. In the case of 1 M LiFSI/G_n electrolytes with *n* ranging from 2 to 4 (**Figure 4.1 A**), the predominant coordination of FSI^- is FSI-SSIP, with a fraction exceeding 80 %. On the contrary, the presence of FSI-CIP in 1 M LiFSI/G_1 at a 50 % level suggests that the association between Li^+ and FSI^- in G_1 is strengthened. The increase in the $[Li^+]/[G_n]$ ratio results in the upshift of the FSI^- band and the disappearance of non-coordinating G_n (**Figure 4.1 B**). The observed change in the position and shape of the FSI^- peak indicates that the interactions between Li^+ and FSI^- in $Li(G_n)_1FSI$ are significantly stronger than in 1 M solutions. This is evidenced by the decreasing fraction of FSI-SSIP in all four $Li(G_n)_1FSI$. In particular, the fraction of SSIP-FSI in $Li(G_3)_1FSI$ and $Li(G_4)_1FSI$ drops to 5 and 25 %,

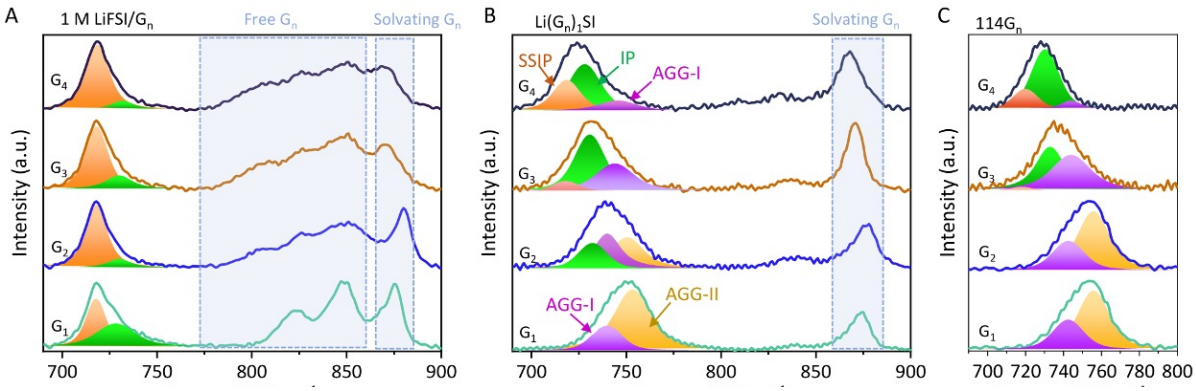


Figure 4.1. Raman spectra of LiFSI-G_n-TTE. (A) 1 M LiFS/G_n, (B) $Li(G_n)_1FSI$, and (C) $114G_n$ electrolytes from the range of 690-900 cm^{-1}. The solid lines show the experimental data, and the filled areas show the contribution of SSIP (peach), IP (green), and AGG (purple) coordination of FSI^-. The region between 800 and 900 cm^{-1} in Panel C is not shown because of the interference between G_n and TTE.

respectively. In contrast, the association between Li^+ and FSI^- eliminates FSI-SSIP from the structures of $Li(G_1)_1FSI$ and $Li(G_2)_1FSI$, as summarized in **Table 4.3**.

The upshift of the FSI^- band (**Figure 4.1 B**) also indicates the increase in the fraction of FSI-AGGs as *n* decreases from four to one. Indeed, most of FSI^- in $Li(G_3)_1FSI$ and $Li(G_4)_1FSI$ exist in the form of FSI-CIP, contributing to 55-60 %. However, the fraction of FSI-CIP in $Li(G_2)_1FSI$ and $Li(G_1)_1FSI$ is significantly lower: 20% and 0 %, respectively. The higher fraction of FSI-CIP in $114G_n$ containing G_3 and G_4 is caused by the chelation of a Li^+ ion by a single solvent molecule, which is impossible in the case of G_1 and G_2.[188,189] Instead, the faction of FSI-AGGs grows as G_n becomes

shorter. This is illustrated by the concentrations of FSI-AGG-I and FSI-AGG-II in $Li(G_1)_1FSI$ (20 and 80 %) and $Li(G_2)_1FSI$ (40 and 40 %).

The dilution of $Li(G_n)_1FSI$ (n=3,4) with non-coordinating TTE results in a rightward shift of the FSI^- band (Figure 4.1 C), indicating a stronger association between Li^+ and FSI^- in $Li(G_3)_1FSI$ and $Li(G_4)_1FSI$. This change is evidenced by the reduction in FSI-SSIP from 25% to 20% and 5% to 2%, respectively, for $114G_3$ and $114G_4$. Additionally, the concentration of AGG-FSI-I drops from 15% to 5%, suggesting that most of FSI^- exists as FSI-CIP in $114G_4$. Unlike $114G_4$, FSI^- in $114G_3$ exhibits roughly an equal distribution between FSI-CIP and FSI-AGG-I, as shown in **Table 4.3**. Meanwhile, the Raman spectra of $114G_1$ and $114G_2$ are not strongly affected by the addition of TTE, except for the transformation of FSI-CIP into FSI-AGGs in the structure of $Li(G_2)_1FSI$. It is noteworthy that the growing fraction of FSI-AGGs with the decrease in *n* agrees with the trend exhibited by the total ionic conductivity: $114G_4$ (4.1 $mS.cm^{-1}$) > $114G_3$ (2.3 $mS.cm^{-1}$) > $114G_2$ (1.2 $mS.cm^{-1}$) > $114G_1$ (0.98 $mS.cm^{-1}$).

Table 4.3 Deconvolution of the FSI band in 1M LiFSI/G_n, $Li(G_n)_1FSI$, and $114G_n$ electrolytes. The fraction of each component has an estimated error of 5 %

	1 M LiFSI/G_n				$Li(G_n)_1FSI$				$114G_n$			
n	1	2	3	4	1	2	3	4	1	2	3	4
SSIP (%)	50	85	80	85	0	0	5.0	25	0	0	2.0	20
CIP (%)	50	15	20	15	0	20	55	60	0	0	48	75
AGG-I (%)	0	0	0	0	20	40	35	15	30	50	50	5.0
AGG-II (%)	0	0	0	0	80	40	0	0	70	50	0	0

Further investigation of Li^+ coordination and the solvation structures of $Li(G_n)_1FSI$ and $114G_n$ electrolytes was performed using *ab initio* molecular dynamics (AIMD) simulations. Due to the high cost of AIMD calculations of systems containing more than 300 atoms, the solvation structures of the electrolytes with G_1 and G_4 were calculated to illustrate the effect of Li^+ chelation on the coordination of FSI^-. In order to estimate the atomic coordination number Z (r) around Li^+, the radial distribution functions (g (r)) were integrated with respect to the interatomic distances (**Figure 4.2 A, D**). The first coordination shell around a Li^+ ion in $Li(G_4)_1FSI$ contains, on average, 1.7 FSI^- oxygen atoms (O_{FSI})

and 3.3 G_4 oxygen atoms (O_{G4}) (**Figure 4.2 A**). These numbers indicate the existence of multiple configurations of FSI^-. This is directly illustrated by the snapshot of $Li(G_4)_1FSI$ (**Figure 4.2 B**). In agreement with the results of Raman spectroscopy, $Li(G_4)_1FSI$ contains FSI-SSIP, FSI-CIP, and FSI-AGG-I, as shown in **Figure 4.2 C**. Notably, the snapshot of $Li(G_4)_1FSI$ also demonstrates that FSI-CIP and FSI-AGG-I contain the Li^+ ions, which G_4 chelates.

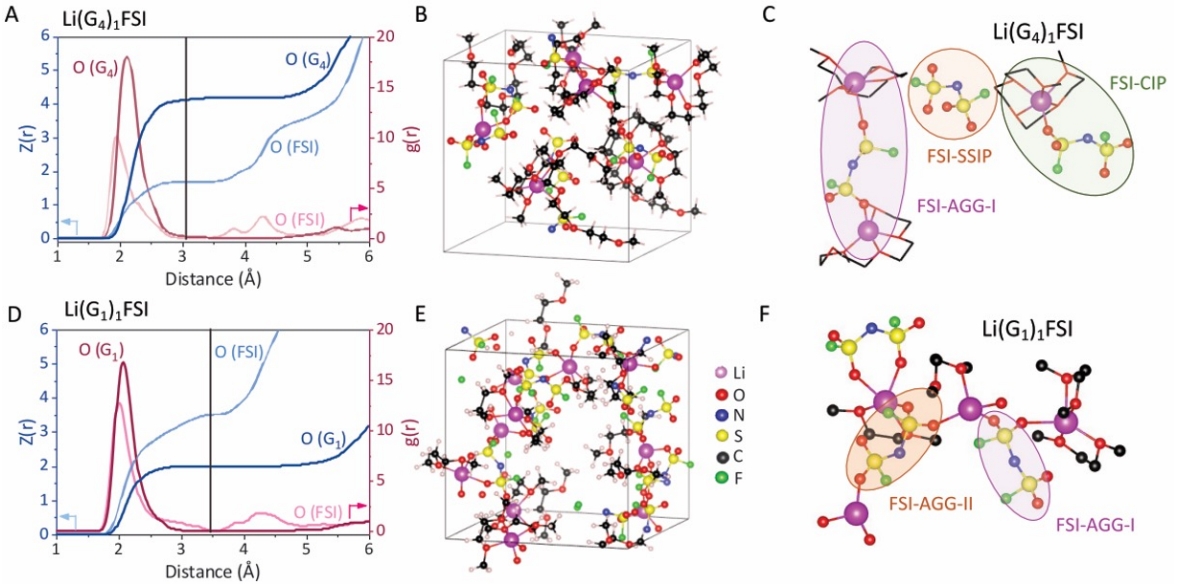


Figure 4.2 AIMD simulations of $Li(G_n)_1FSI$. RDF and CN of a Li^+ cation in (A) $Li(G_4)_1FSI$ and (D) $Li(G_1)_1FSI$. The black vertical lines represent the cutoff of the 1st coordination sphere around Li^+. AIMD snapshots of the simulation boxes representing the structures of (B) $Li(G_4)_1FSI$ and (E) $Li(G_1)_1FSI$. The detailed solvation structure around Li^+ in (C) $Li(G_4)_1FSI$ and (F) $Li(G_1)_1FSI$. H atoms are not shown for clarity.

Since a single G_1 molecule cannot chelate a Li^+ ion, the solvation structure of $Li(G_1)_1FSI$ contains only FSI-AGGs, which is illustrated by the increase in O_{FSI} in the first coordination shell around Li^+ from 1.7 in $Li(G_4)_1FSI$ to 3.5 in $Li(G_1)_1FSI$ (**Figure 4.2 D**). The snapshot of $Li(G_1)_1FSI$ demonstrates that the connectivity between the FSI species in $Li(G_1)_1FSI$ is significantly different from that in $Li(G_4)_1FSI$ (**Figure 4.2 E**). Indeed, the FSI-AGG-I and FSI-AGG-II in $Li(G_1)_1FSI$ are incorporated into the chains (**Figure 4.2 F**), which creates the 3D electrolyte network.

AIMD simulations of $114G_n$ confirm the role of TTE in controlling the association between Li^+ and FSI^-, previously demonstrated by Raman spectroscopy. In particular, the presence of TTE decreases the fraction of FSI^- in the first coordination sphere around Li^+, as evidenced by the change in O_{FSI} and O_{G4} from 1.7 and 3.5 in $Li(G_4)_1FSI$ to 1.2 and 5.0 in $114G_4$, respectively. This change in the coordination numbers confirms that TTE shifts the equilibrium between FSI-CIP and FSI-AGG-I to the formation of FSI-CIP. The snapshot of $114G_4$ demonstrates that its solvation structure contains only FSI-CIP separated by the TTE molecules and is devoid of FSI-SSIP and FSI-AGG-I (**Figure 4.3 B, C**). It is noteworthy that the absence of FSI-SSIP and FSI-AGG-I in the DFT-predicted structure of $114G_4$ is possibly caused by the relatively small simulation size, which includes three LiFSI molecules, and the low fractions of FSI-SSIP and FSI-AGG-I.

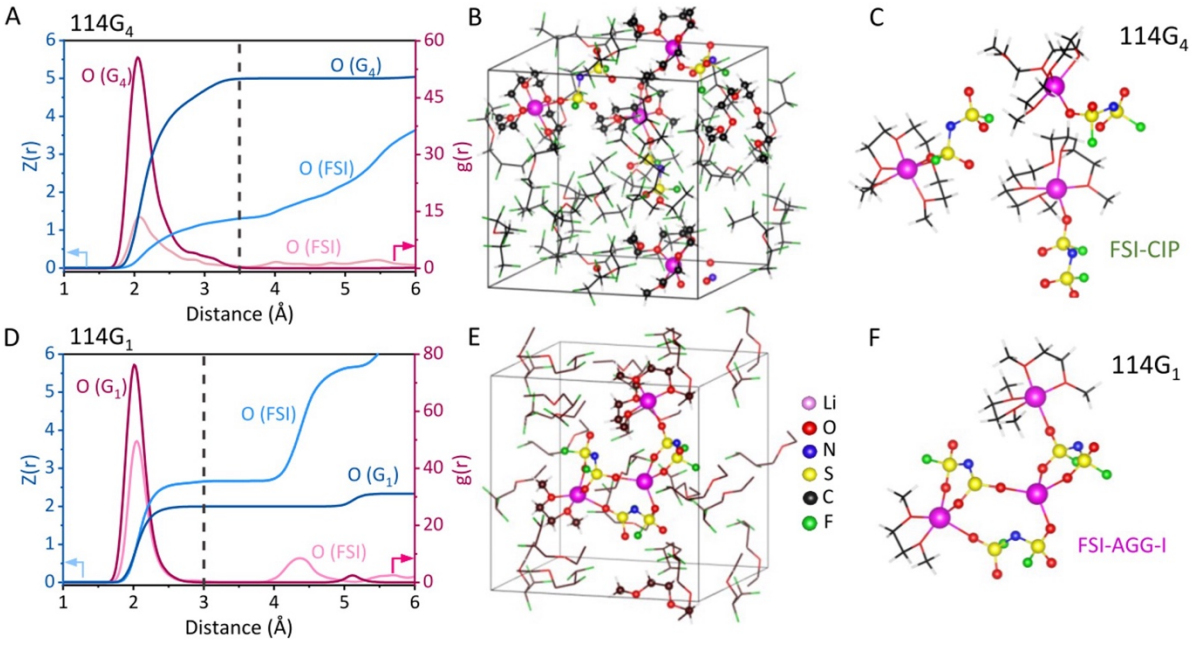


Figure 4.3 AIMD simulations of $114G_n$. RDF and CN of a Li^+ cation in (A) $114G_4$ and (D)$114G_1$. The dashed vertical lines represent the cutoff of the 1st coordination sphere around Li^+. AIMD snapshots of the simulation boxes representing the structures of (B) $114G_4$ and (E) $114G_1$. The detailed solvation structure around Li^+ in (C) $114G_4$ and (F) $114G_1$. H atoms are not shown for clarity.

AIMD simulations of $114G_1$ demonstrate that the average number of O_{FSI} is reduced to 2.6 from 3.5 in $Li(G_1)_1FSI$, while the average number of O_{G1} is unchanged and equals 2. The reduction in

O_{FSI} is also accompanied by the disappearance of FSI-AGG-II from the solvation structure of $114G_1$, as demonstrated by the snapshots in **Figure 4.3E**. Nevertheless, the FSI-AGG-I are still connected and form a structure similar to that of $Li(G_1)_1FSI$. Interestingly, TTE decreases the fractions of FSI-AGG-II in $114G_1$ and FSI-CIP in $114G_4$. This phenomenon could be ascribed to the dipole-dipole interactions between G_n and TTE, as demonstrated earlier for the LiFSI-DMC-TTE electrolytes.[190]

4.4 Li^+ Transport Properties of $114G_n$

4.4.1 Full-range EIS of Li Symmetric Cells with $114G_1$

The transport properties of solvate electrolytes were determined by EIS. An accurate EIS analysis of symmetric cells with Li electrodes deconvolutes frequency-separated processes, such as Li^+ transport at the surface and within the bulk electrolyte. Since the timescale of bulk transport of Li^+ is approximately several hours, the symmetric cell must necessarily reach the steady state before EIS measurements to reduce the impact of side reactions at the Li surface.

The representative temporal evolution of the Nyquist plot of a cell with Li electrodes and $114G_1$ within the frequency range between 10^6 and 10^{-1} Hz is shown in **Figure 4.4 A**. The equivalent circuit employed to fit the EIS data contains two semicircles, which are attributed to the resistance of the Li/solvate interface (R_{int}) and the resistance of a porous SEI (R_{pores}). The time dependence of R_{int} and R_{pores} indicates the formation of a stable interphase after 20 hours of aging (**Figure 4.4 B**).

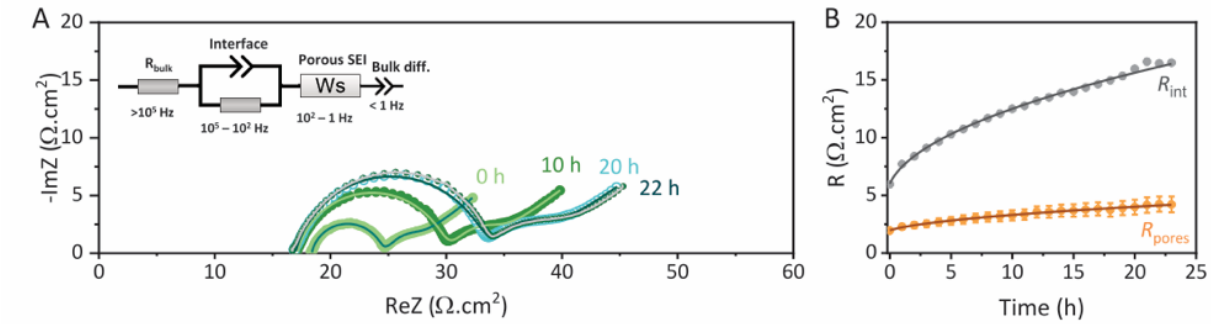


Figure 4.4 Aging Li symmetric cells. (A) Nyquist plot of the symmetric cell with Li electrodes and $114G_1$ electrolyte within the frequency range between 10^6 and 10^{-1} Hz at 25 °C (circles) at different 0, 10, and 22 hours of storage. The inset shows the equivalent circuit. (B) Evolution of R_{int} and R_{pores} on storage.

It is noteworthy that the interpretation and fitting of the EIS of Li symmetric cells is often ambiguous since it is complicated by the high reactivity of Li and the presence of a native SEI on its surface. In this work, I employed the simplified fitting scheme previously proposed by M. Gaberšček *et al*[191] and extended the EIS measurements to the frequency of 1 mHz to determine the Li^+-transport properties in the bulk electrolyte, as was demonstrated by B. Roling *et al*.[192] The equivalent circuit used to fit the spectra of Li symmetric cells is shown in **Figure 4.5 A.**

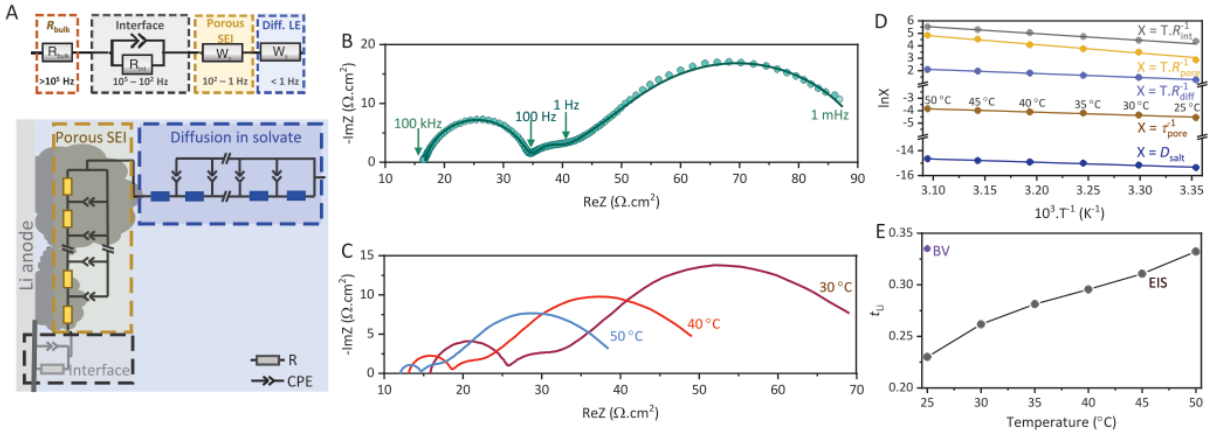


Figure 4.5 EIS studies of Li symmetric cells with 114G$_1$(A) Full-range equivalent circuit of the Li symmetric cells (B) Representative Nyquist plot of the Li-symmetric cell with 114G$_1$ solvate electrolyte at 25 °C. The experimental data are in circles, and the solid line is fitting. (C) Nyquist plots of the Li-symmetric cell with 114G$_1$ electrolyte at 25 - 50 °C. (D) Arrhenius plot for R_{int}, R_{pore}, $(\tau_{pore})^{-1}$, and D_{salt}; (E) Temperature dependence of t_{Li} measured for 114G1 via EIS (black circles). The purple circle shows t_{Li} measured by the Bruce-Vincent method at room temperature.

The model correctly describes three frequency-separated features exhibited by a typical Li symmetric cell with solvate electrolytes (**Figure 4.5 B**). The depressed semicircle ($\alpha > 0.8$) within the frequency range 10^5-10^2 Hz represents the charge transfer step at the surface of metallic Li. This step includes the desolvation of Li^+ ions and their transfer across the dense part of the SEI. Since these processes cannot be deconvoluted using EIS,[75] the sum of their resistances equals the diameter of the semicircle (R_{int}). At a medium frequency of 10^2 - 1 Hz, the EIS response is generated by the motion of the solvated Li^+ ions within the porous part of the SEI. Since this process is diffusion-driven, it can be modelled as a finite-length diffusion impedance with transmissive boundary conditions (**Equation 4.6**):

$$Z_{pore} = R_{pore}\frac{\tanh[(i\omega\tau_{pore})^{\alpha}]}{(i\omega\tau_{pore})^{\alpha}} \qquad \textbf{Equation 4.6}$$

where the prefactor R_{pore} is the resistance of the porous SEI. The time constant (τ_{pore}) depends on the SEI thickness and ambipolar diffusion coefficient of LiFSI within the SEI (**Equation 4.7**)

$$\tau_{pore} = \frac{d_{pore}^2}{4D_{salt}} \quad \textbf{Equation 4.7}$$

The low-frequency behavior is also under diffusion control, and the impedance below 1 Hz is described by **Equation 4.8**:

$$Z_{diff} = R_{diff} \frac{\tanh[(i\omega\tau_{diff})^{\alpha}]}{(i\omega\tau_{diff})^{\alpha}} \quad \textbf{Equation 4.8}$$

The value of time constant τ_{diff} is further used to calculate the ambipolar salt diffusion coefficient (**Equation 4.9**):[192]

$$D_{salt} = \frac{L^2}{4\tau_{diff}} \quad \textbf{Equation 4.9}$$

where L is the interelectrode distance of 90±10 μm.

The results of fitting the EIS spectrum shown in **Figure 4.5 B** are summarized in **Table 4.3**. α_{int}, α_{pore}, and α_{diff} values are 0.87, 0.48, and 0.40, respectively. This demonstrates that the redox reaction at the Li surface is the redox reaction. In contrast, diffusion governs the movement of solvated Li^+ ions within the porous SEI and the bulk electrolyte.[177] Quantification of the diffusion components of the Nyquist plot provides the values of τ_{pore} and τ_{diff}, which can be employed to estimate the thickness of the porous SEI. Indeed, the combination of **Equations 4.7 and 4.9** results in **Equation 4.10**:

$$d_{porous\ SEI} = L \cdot \sqrt{\frac{\tau_{pore}}{\tau_{diff}}} \quad \textbf{Equation 4.10}$$

The approximate thickness of the SEI formed between Li and $114G_1$ solvate electrolyte is 75 nm. Notably, the estimation of the SEI thickness via EIS is in good agreement with the values obtained by the direct measurements via atomic force microscopy (AFM). The thickness of the SEI formed during Li plating on a Cu substrate from LiFSI/G_1 electrolytes varies between 25 and 75 nm.[193]

$114G_1$ exhibits a room temperature ambipolar diffusion coefficient of ~ $2.1 \cdot 10^{-7}$ $cm^2.s^{-1}$. This value is similar to that of $Pyr_{13}FSI$/LiFSI ionic liquid electrolytes.[192] However, it is an order of magnitude lower than the diffusion coefficient exhibited by the conventional $LiPF_6$/organic carbonate

electrolytes.[89] Furthermore, the fact that the diffusion impedance (R_{diff}) is significantly greater than R_{int} and R_{SEI} hints that the bulk Li^+-transport is an alarming limitation of $114G_1$.

The temperature dependence of the Li^+ transport in $114G_1$ solvate electrolyte and its quantification are summarized in **Figures 4.5 C, D,** and **Table 4.4**. The activation energy calculated for R_{int} is 580 meV, which indicates that this step is primarily controlled by the desolvation of Li^+ ions at the Li surface. In truth, the desolvation energy of 580 meV falls in between the values reported for weakly solvating organic carbonate/acetate electrolytes (300-400 meV)[194] and diluted G_1-based electrolytes exhibiting moderate solvation of Li^+ ions (700-800 meV).[195] The activation energies of the processes occurring during the motion of the solvated Li^+ ions in the porous SEI are comparable to those in the bulk electrolyte. In particular, the activation energy for τ_{SEI} and D_{salt} are 240 and 205 meV, respectively. This confirms that transporting the solvated Li^+ ions across the SEI is a diffusion-controlled process in the case of $114G_1$.

Table 4.4 Fitting of the EIS of the symmetric cells with Li electrodes and $114G_1$ solvate electrolyte at 25 °C

	Parameter	Value	E_a (meV)		Parameter	Value	E_a (meV)
Interface	Q_{int} ($s^{\alpha int}\Omega^{-1}.cm^{-2}$)	$(1.9\pm0.2)\cdot10^{-5}$		Electrolyte	R_{bulk} ($\Omega.cm^2$)	16±1	
	α_{int}	0.80±0.01			R_{diff} ($\Omega.cm^2$)	55±1	310±15
	R_{int} ($\Omega.cm^2$)	17.1±0.1	580±20		α_{diff}	0.40±0.01	
Porous SEI	R_{pore} ($\Omega.cm^2$)	4.0±0.5	460±15		τ_{diff} (s)	95±1	205±5
	α_{pore}	0.48±0.01			D_{salt} ($cm^2.s^{-1}$)	$(2.1\pm0.5)\cdot10^{-7}$	
	τ_{pore} (s)	0.080±0.005	240±15				

The sluggish bulk transport of the solvated Li^+ ions in $114G_1$ is further evidenced by the low lithium transference number (t_{Li}) of 0.22 at 25 °C (**Figure 4.5 E**), which indicates that Li^+ ions carry only 22 % of the total current. It is worth mentioning that the estimation of t_{Li} by EIS is more precise than the polarization measurements.[196] In particular, t_{Li} obtained through EIS agrees with the value predicted by the DFT simulations of similar LiTFSI/G_1 system.[197] In contrast, the traditional Bruce-Vincent[198] method yields an overestimated value of 0.34 (**Appendix C1**). While t_{Li} does increase with

temperature, it remains as low as 0.4 at 50 °C, which suggests that the diffusion limitations of $114G_1$ electrolyte are not avoided at higher temperatures.

4.4.2 Effect of G_n on Li^+-transport Rate

The relationship between G_n length and the transport properties of the $114G_n$ solvate electrolytes was comprehensively studied by EIS (**Figure 4.6**). Panels A and B summarize the impact of G_n on the Li^+ transport properties at the Li metal interface. A discernible correlation is observed between glyme length, magnitude, and activation energy of R_{int}, R_{pore}, and τ_{int}^{-1}. In particular, R_{int} and E_a (R_{int}) exhibit almost a linear increase with n, rising from 16 Ω.cm^2 and 580 meV for $114G_1$ to 195 Ω.cm^2 and 910 meV for $114G_4$. Since the charge transfer at the interface primarily depends on the desolvation of Li^+ ions, the higher magnitude of R_{int} and its activation energy for $114G_4$ indicates that the chelation of Li^+ ions by G_n impedes the desolvation process. In other words, the kinetics of Li^+ reduction in $114G_n$ is improved when FSI-AGGs are formed instead of FSI-CIP. It is worth mentioning that a similar effect of weakened Li^+-solvent binding is observed if electrolytes employ weakly solvating solvents, i.e., dioxalanes[195] and 1,2-diethoxyethane.[199]

The correlation between R_{pore} and G_n provides additional evidence for the slower interfacial Li^+ transport in $114G_3$ and $114G_4$ systems (**Figure 4.6 B-i and B-ii)**. This is clearly illustrated by the 27.5-fold increase in the magnitude of R_{pore} and its activation energy from 4.0 Ω.cm^2 and 480 meV in $114G_1$ to 110 Ω.cm^2 and 800 meV in $114G_4$, respectively. The magnitude of τ_{pore}^{-1} also drops from 12.5 s^{-1} ($114G_1$) to 2.5 s^{-1} ($114G_4$), suggesting that the diffusion of the solvated Li^+ ions within the porous SEI is sluggish. Moreover, the activation energy of τ_{pore}^{-1} almost quadruples with n from 200 meV ($114G_1$) to 780 meV ($114G_4$). This suggests that the chemical composition of the SEI might also depend on G_n. While the investigation of this relationship between the chemical composition of the SEI and G_n is beyond the scope of this work, the improved Li^+ transport within the porous SEI formed between Li and $114G_1$ may be attributed to the fact that it is formed primarily through the decomposition of FSI.[123,193,200]

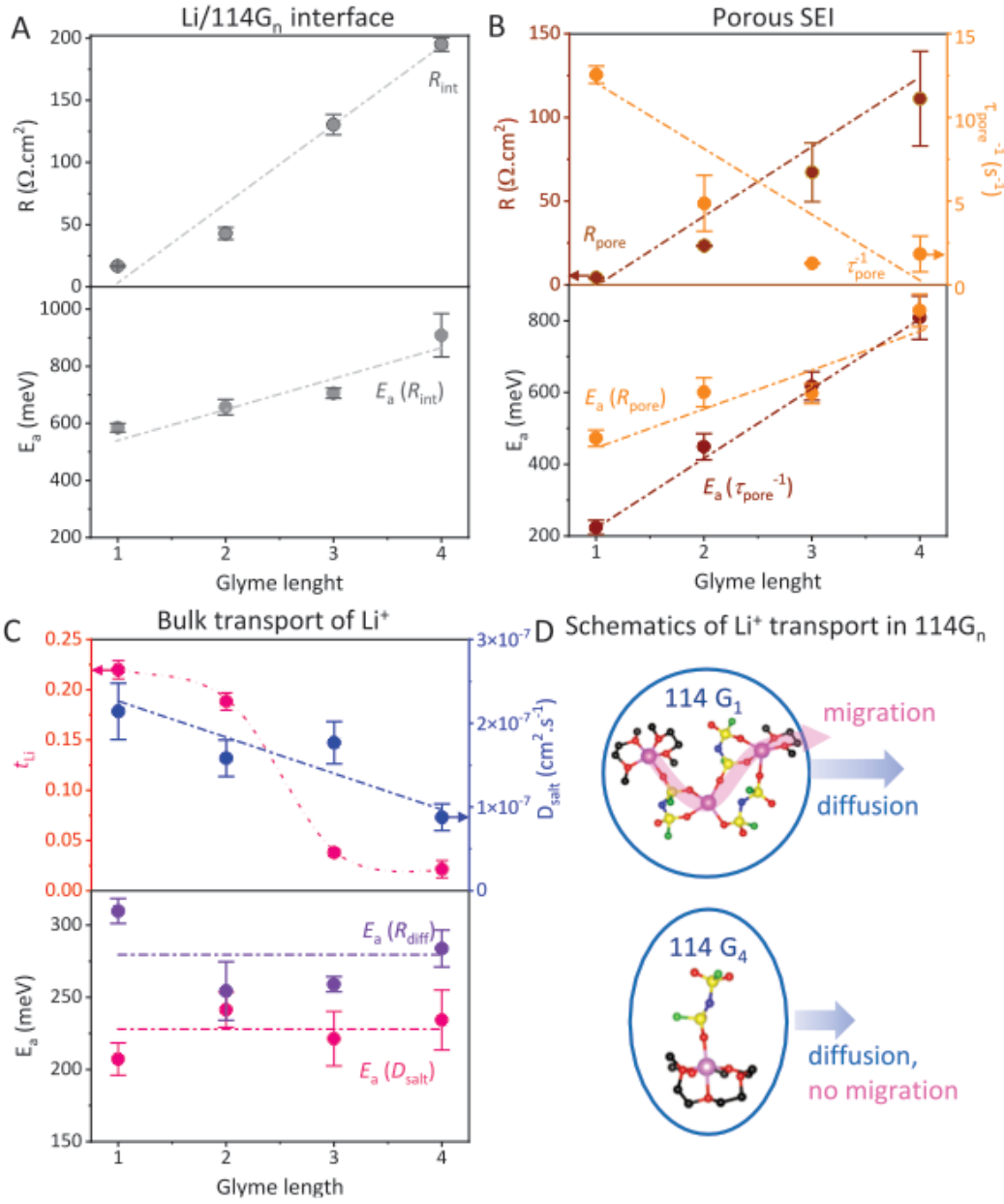


Figure 4.6 G_n-dependent transport properties of 114G_n. G_n-dependence of (A-i) R_{int}, (B-i) R_{pore} (left brown Y-axis), τ_{pore}^{-1} (right orange Y-axis), (C-i) t_{Li} (left red Y-axis), and D_{salt} (blue right Y-axis). Panels (A-ii), (B-ii), and (C-ii) show the G_n dependence of the activation energy of the corresponding parameters. The dashed lines illustrate the trendlines. (D) Schematic illustration of the mechanisms of Li^+ transport in 114G_1 and 114G_4.

Figure 4.6 C-i illustrates that the chelation of Li^+ ions also impairs the bulk transport of Li^+ in $114G_1$. It is illustrated explicitly by the sharp drop in t_{Li} from 0.2 to 0.04. This decrease is caused by the transformation of FSI-AGGs to FSI-CIP, which tunes the mechanism of Li^+ transport in $114G_n$. As demonstrated earlier, the motion of Li^+ in the SILs containing G_3 and G_4 is facilitated by the slow vehicular diffusion of the bulk $[Li(G_n)]^+$ ions, which results in t_{Li} below 0.05.[65,192,197] In contrast, the higher magnitude of t_{Li} has been computationally predicted for the SILs employing G_1 and G_2 due to the increased migration contribution to the total Li^+ transport.[197] In the case of $114G_1$ and $114G_2$, this is confirmed by the presence of the FSI-AGGs framework, which facilitates the migration of Li^+ driven by the electric field between the battery electrodes.

The ambipolar salt diffusion coefficient decreases with n by approximately 2.3 times from $2.1 \cdot 10^{-7}$ $cm^2.s^{-1}$ ($114G_1$) to $9.0 \cdot 10^{-8}$ $cm^2.s^{-1}$ ($114G_4$), which is significantly smaller than the ratio between τ_{SEI}^{-1} of $114G_1$ and $114G_4$. Combined with the fact that the activation energy of D_{salt} is invariant with respect to n (**Figure 4.6 C-ii**), this suggests that FSI-AGGs and FSI-CIP diffuse with a comparable rate within the temperature range between 25 and 50 °C. The values of t_{Li} and D_{salt} suggest that the bulk transport of Li^+ in $114G_n$ is dictated by diffusion, although migration contributes at the level of approximately 20 % in the case of $114G_1$ and $114G_2$. This also predicts the potential diffusion limitations for the deposition of Li^+ from $114G_n$, which is illustrated by the low values of the limiting current density (j_{lim}) calculated using **Equation 1.29** (**Table 4.5**).

Table 4.5 Limiting current density of $114G_n$ solvate electrolytes

Electrolyte	j_{lim} ($mA.cm^{-2}$)
$114G_1$	3.3
$114G_2$	2.3
$114G_3$	2.2
$114G_4$	1.1

4.4.3 Diffusion-triggered Deposition of Li Dendrites

In order to investigate the relationship between the stability of Li deposition and Li^+ transport properties of the solvate electrolytes, a one-step galvanostatic deposition of Li was performed utilizing a simple coin cell design with symmetric Li electrodes and a Whatman GF separator (**Figure 4.7 A)**. Due to the

high porosity, GF separators absorb a sufficient volume of a solvate electrolyte and do not mechanically suppress Li dendrites. Hence, the duration of Li deposition before short-circuiting is primarily controlled by the properties of the solvate electrolyte and the SEI, which is formed on the Li surface.

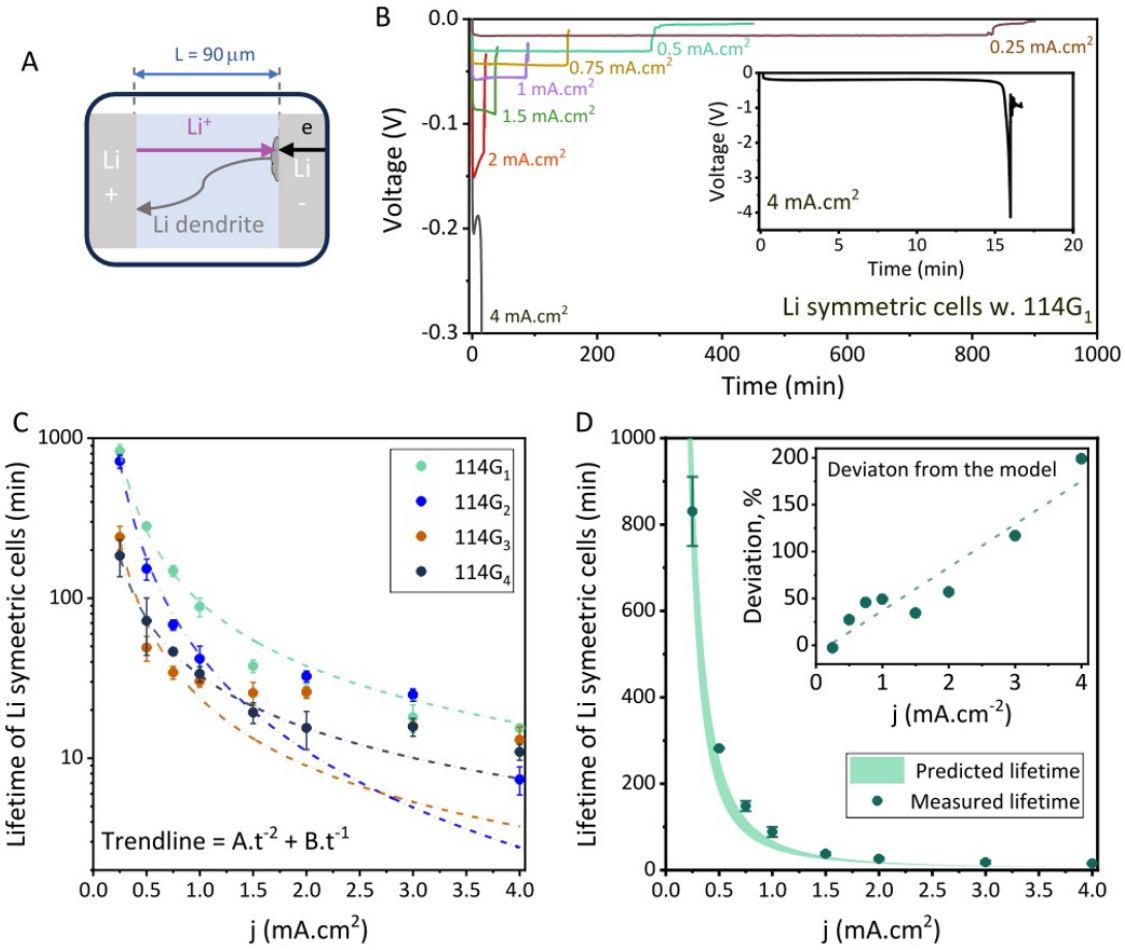


Figure 4.7 Deposition of Li dendrites from 114G$_n$. (A) Schematic setup of a Li symmetric used to determine the duration of Li deposition before short-circuiting. (B) Polarization of the Li symmetric cells with 114G$_1$ at a current density of 0.5-4 mA.cm^{-2}. The inset shows the polarization at 4 mA.cm^{-2}. (C) Relationship between the lifetime of Li symmetric cells and applied current density. The trendlines (dashed lines) are calculated using the equation shown in the panel. (D) Applicability of the Chazalviel model to predict the lifetime of the cells with 114 G$_1$. The insert shows the relative deviation from the model.

The polarization curves of the Li symmetric cells with $114G_1$ exhibit two different shapes, contingent upon the magnitude of the applied current density, as illustrated in **Figure 4.7 B**. When the current density is 2 mA.cm^2 or less, the cell polarization profile exhibits a stable plateau suddenly interrupted by a sharp voltage drop to 0 V. If the applied current density is above 2 mA.cm^{-2}, the voltage drop occurs after its magnitude has exponentially approached 4 V. The change in the voltage profile at 2 mA.cm^{-2} (31 % of j_{lim}) indicates the transition of the Li deposition regime from the root-growing whiskers to the surface-growing dendrites, as proposed by Bazant et *al*.[92]

Although the formation of Li dendrites is partially controlled by the SEI formation when the current density is below 1 mA.cm^{-2}, the lifetime of the Li symmetric cells still can be approximated by the Chazalviel diffusion model of Li dendrite growth[88]. According to the model, the growth of Li dendrites begins at the time instant, so-called Sand's time (τ_{Sand}), when Li^+ ions are consumed at the electrode surface. The total lifetime of Li symmetric cells is the sum of τ_{Sand} and $\tau_{growth,}$ the time required for the penetration of Li dendrites through a GF separator (**Equation 4.5**)

$$\text{Lifetime} = \pi D_{salt}\left(\frac{ec_{Li}}{2j(1-t_{Li})}\right)^2 + \frac{2\sigma_{ion}LkT}{jeD_{salt}}t_{Li} \qquad \textbf{Equation 4.11}$$

where j is an applied current density, L is the interelectrode spacing, c_{Li} is the concentration of Li^+ ions, and σ_{ion} is the total ionic conductivity of $114G_1$. The parameters and constants employed to calculate the lifetime of the cells with $114G_1$ are summarized in **Table 4.6**.

In general, the lifetime of Li symmetric cells containing $114G_n$ adheres to the trendline predicted by the Chazalviel model, except for the positive residuals observed at higher current densities (**Figure 4.7 C**). As n increases, the formation of Li dendrites occurs faster, which agrees with the Li^+ transport rate dependance on G_n. A detailed illustration of the Chazalviel model's adequate predictive capability is further illustrated in the case of $114G_1$.

The results of the direct implementation of the Chazalviel model to predict the short-circuiting time are summarized in **Figure 4.7 D**. When the applied current density is less than 2 mA.cm^{-2}, the deviation of the experimentally measured cell lifetime from the model does not exceed 50 %. This suggests that this simple model reasonably approximates the duration of Li deposition prior to short-circuiting. Meanwhile, the observed rise in deviation from the model as the applied current density increases indicates that high surface area Li deposits undergo partial passivation due to the electrolyte decomposition. Hence, the penetration of Li dendrite through the GF separator is postponed, and the

cell lifetime exceeds the predicted value. It is noteworthy that the observed deviation from the model becomes less pronounced when it is rescaled with respect to the plating capacity. For instance, the predicted lifetime at 4 mA.cm^2 deviates from the real one by approximately 10 minutes, equivalent to 0.67 mAh.cm^2 or below 20% of the amount of Li deposited during a single charge in a practical LMB.

Table 4.6 Transport properties of 114G$_1$. These parameters were used to predict the lifetime of the Li symmetric cells with 114G$_1$ electrolyte via the Chazalviel model. D_{salt} and t_{Li} were calculated via EIS. σ_{ion} was measured directly, and c_{Li} was calculated from the electrolyte density.

Parameter	Value	Constant	Value
D_{salt} (cm^2.s^{-1})	2.12±0.48	T (K)	298
t_{Li}	0.22±0.02	k (J.K^{-1})	$1.38 \cdot 10^{-23}$
c_{Li} (M)	1.1	e (C)	$1.61 \cdot 10^{-19}$
L (μm)	90±10	F (C.mol^{-1})	96500
σ_{ion} (mS.cm^{-1})	0.98±0.01		

4.5 Effect of G$_n$ on the Stability of Long-term Li Deposition

4.5.1 Stability of Li Deposition from 114G$_1$

As demonstrated in the section above, stable deposition of Li from solvate electrolytes cannot be achieved if a highly porous GF is employed. Hence, the effect of plating capacity and applied current density was examined by cycling Cu-Li asymmetric cells with Celgard 3501 separators. Since 114G$_1$ exhibits the fastest rates of the interfacial and bulk transport of Li^+, it was selected to investigate the effect of applied current density and deposition capacity on the stability of long-term Li cycling. In order to separate these effects, the Cu-Li cells were cycled utilizing three different protocols.

Regardless of the Li quantity cycled, the voltage profiles of Cu-Li cells exhibit a similar evolution during cycling at a current density of 1 mA.cm^{-2} for all tested plating capacities ranging from 1 to 5 mhA.cm^{-2} (**Figure 4.8 A**). The first cycle of Li deposition starts with a voltage dip caused by the reduction of FSI^- and the formation of Li nuclei. The nucleation overpotential falls in a range between -200 and -100 mV. The variability in nucleation potential that has been observed can be attributed to

the existence of an uneven native oxide layer on the Cu surface. Following the nucleation step, Li is deposited in the steady-state regime with an overpotential of approximately 80 mV until the desired plating capacity is reached. The subsequent stripping of deposited Li reveals that 4.5 to 12 % of deposited Li is lost due to the formation of the SEI and precipitation of electrochemically inactive "dead Li."[201] The repeated sequence of plating and stripping results in a more curved voltage profile, as evidenced by the polarization observed after 400 hours. As Dasgupta *et al.*[95] demonstrated, the occurrence of voltage minima during the plating and stripping steps signifies the formation of Li dendrites and pulverization of the lithium surface due to pitting.

Table 4.7 The average Li consumption during the SEI formation in $114G_l$ at 1 mA.cm^{-2}. The Li loss is the capacity lost when the CE surpasses 99 %. The errors are calculated via replicated measurements (3 – 4 cells per deposition capacity).

Plating capacity (mAh.cm^{-2})	Li loss during the SEI formation (mAh.cm^{-2})
1	2.7±0.3
2	2.5±0.1
3	2.1±0.4
4	2.0±0.1
5	1.6±0.1

The evolution of Cu-Li cells Coulombic efficiency (CE) is illustrated in **Figure 4.8 B**. With increased Li plating capacity from 1 to 5 mAh.cm^{-2}, the 1st cycle CE grows from 88 % to 96.5 %. In addition, the higher Li plating capacity leads to a faster stabilization of the CE at a level between 99.4 and 99.6 %. This also reduces Li consumption upon SEI buildup during the initial cycling stage (**Table 4.6**). These findings are consistent with the previous study of high-concentration $LiNO_3/G_2$

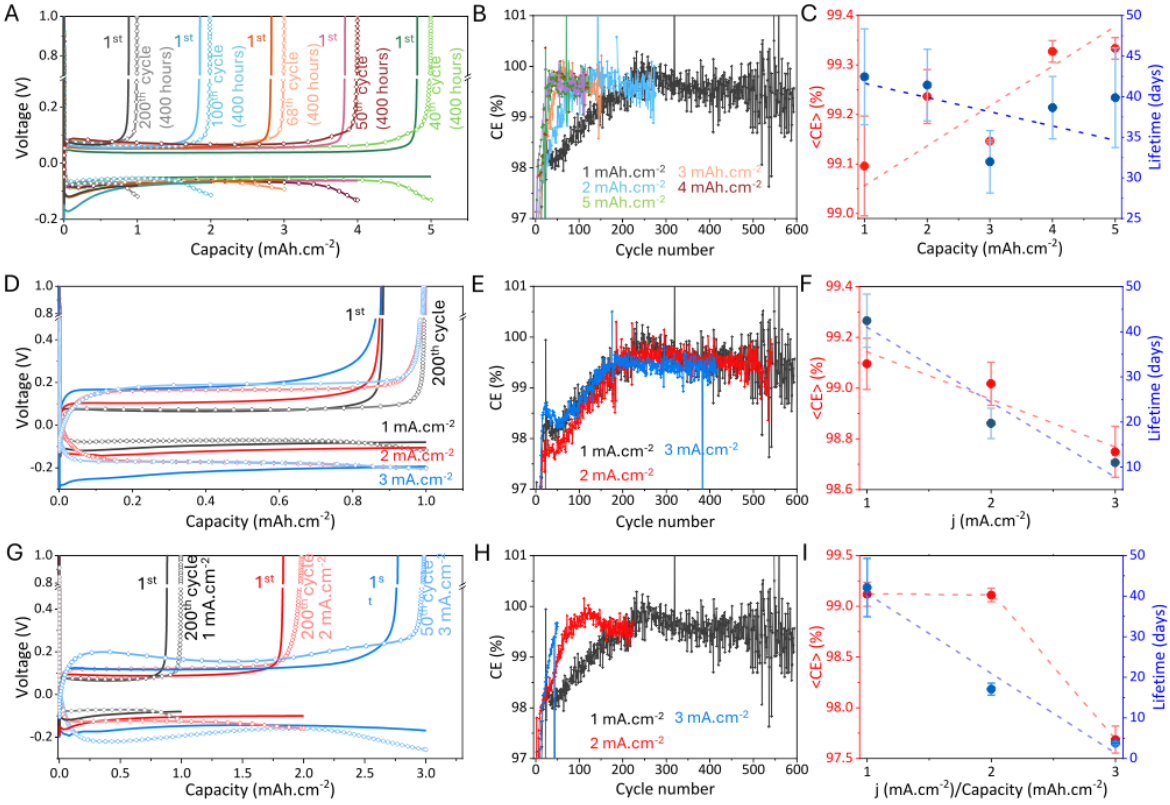


Figure 4.8 Effect of current density and plating capacity on the CE of Li deposition from 114G$_1$. (A)Voltage profiles and (B) CE of the Cu-Li cells with 114G$_1$ at 1 mA.cm^{-2} and plating capacities of 1-5 mAh.cm^{-2}. (C) Dependence of the cumulative CE and lifetime of the cells shown in (A) on the amount of plated Li. (D) Rate capability and (E) CE of Li deposition (1 mAh.cm^{-2}) at 1-3 mA.cm^{-2}. (F) Dependence of the cumulative CE and lifetime of the cells shown in (D) on applied current density. (G) Rate/capacity capability and (H) CE of the Cu-Li cells with a fixed deposition time of 1 hour at 1-3 mA.cm^{-2}. (I) Dependence of the cumulative CE and lifetime of the cells shown in Panel G on applied current density. The solid and solid-circle lines in (A), (D), and (G) show the change in voltage profiles. The dashed lines in (C), (F), and (I) represent the corresponding trendlines.

electrolytes.[111] According to the average values of Li loss summarized in **Table 4.7**, an additional 1.5 – 3 mAh.cm^2 of lithium is necessary to compensate for the losses during the SEI buildup stage. Due to the virtually limitless supply of Li provided by a 380 μm thick Li anode, the Cu-Li cells can be cycled for 30 - 45 days before short-circuiting. However, this inevitable Li loss might be crucial for the performance of practical LMBs due to their thinner lithium anodes. Notably, the lifetime of Cu-Li cells cycled at 1 mA.cm^{-2} decreases with plating capacity, as demonstrated by the linear trendline in **Figure 4.8 C**.

The influence of applied current density on lithium deposition stability is more pronounced than that of the plating capacity. This is demonstrated by the performance of Cu-Li cells cycled at 1, 2, and 3 mA.cm^{-2} while maintaining a capacity limit of 1 mAh.cm^{-2} (**Figure 4.8 D-F**). Following Ohm's law, the polarization of the cells during the first cycle of Li deposition and stripping increases with current density (**Figure 4.8 D**). However, the overlapping plating profiles of the cells subjected to 200 cycles at 2 and 3 mA.cm^{-2} suggest that the increase in Li surface area is considerably more noticeable at 3 mA.cm^{-2}. Further demonstrating the limited rate capability of 114G$_1$, the steady state CE decreases from 99.6 to 99.4 % as the current density increases from 1 to 3 mA.cm^{-2} (**Figure 4.9 E**). In addition, the faster accumulation of Li dendrites at higher current densities reduces the cumulative CE and the average lifetime. In particular, a reduction from 99.1 % over 44 days at 1 mA.cm^{-2} to 98.8 % over 11 days at 3 mA.cm^{-2} is displayed in **Figure 4.9 F**.

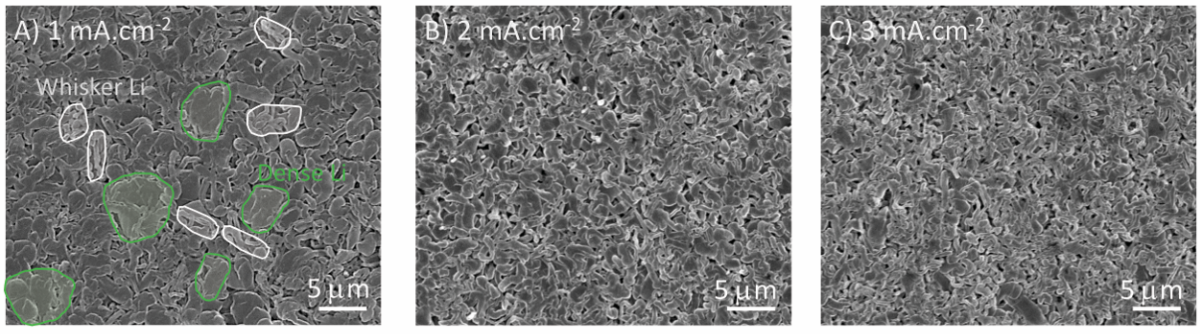


Figure 4.9 Effect of current density of the morphology of Li deposition from 114G$_1$. The morphology of Li deposits formed at (A) 1, (B) 2, and (C) 3 mA.cm^{-2}. Two different morphologies of deposited Li are highlighted in (A).

The simultaneous increase in the applied current density and Li plating capacity has a detrimental impact on the stability of Li deposition (**Figure 4.9 G-I**). With *j* increasing from 1 to 3

mA.cm^{-2} while the plating time remains constant at 1 hour, the 1st cycle deposition plateau disappears, which indicates that deposition of 3 mAh.cm^{-2} in 1 hour from 114G$_1$ is hardly achieved (**Figure 4.9 G**). Indeed, this is suggested by the conscious "V-shape" profile of the 1st deposition and stripping at 3 mA.cm^{-2}. Except for the V-shape" becoming more pronounced, the evolution of the voltage profile exhibited by the Cu-Li cells cycled according to this protocol is identical to that shown in **Figure 4.9 D**.

Although the cyclability of Cu-Li cells decreases when the current density exceeds 1 mA.cm^{-2} and a higher Li capacity is plated, the CE of the Cu-Li cells rises throughout continuous cycling and ultimately exceeds 99.5 % at 2 and even 3 mA.cm^{-2} (**Figure 4.9 H)**. This suggests that the decomposition of 114G$_1$ can yield a quasi-stable SEI even at 3 mA.cm^{-2} when 3 mAh.cm^{-2} of Li is deposited. Nevertheless, the process of SEI formation is not efficient enough to sustain long-term cycling since the cells undergo short-circuiting after approximately 200 and 50 cycles at 2 and 3 mA.cm^{-2}, respectively. When cycling at 3 mA.cm^{-2} with 3 mAh.cm^{-2} plated Li, the cell shutdown occurs before reaching the steady-state CE. This results in the cumulative CE and the average lifetime of 97.6 % and 5 days, significantly lower than the 99.1 % and 18 days observed when cycling 2 mAh.cm^{-2} of Li at 2 mA.cm^{-2} (**Figure 4.9 I**).

The morphology of Li formed by depositing 1 mAh.cm^{-2} on a Cu foil further illustrates the limited rate capability of the 114G$_1$ solvate electrolyte. The morphology evolution of deposited Li is consistent with the deposition mechanism proposed by Bazant *et al.*[92] At a current density of 1 mA.cm^{-2} (~30 % of j_{lim}), the primary shape of Li is granular, which is simar to the morphology of Li deposited from 4 M LiFSI/G$_1$[74] and 1 LiFSI - 1.2 G$_1$-3 TTE.[121] Nonetheless, there is a small but visible fraction of Li with the whicker morphology. When the current density increases to 2 and then 3 mA.cm^{-2}, most of the deposited Li has whicker morphology. This transition observed above 1 mA.cm^{-2} (~30 % of j_{lim}) agrees with Bazant's estimate that the change in Li deposition morphology occurs when Li is plated at 0.3·j_{lim}. Thus, the Li deposition morphology analysis confirms that the 114G$_1$ solvate electrolyte has a rate capability limit of approximately 1 mA.cm^{-2} at 25 °C and ~ 0.1 MPa.

4.5.2 Relationship between G_n and Li Deposition Efficiency

As discussed above, a relatively dense Li layer is deposited from $114G_1$ if the applied current density does not exceed 1mA.cm^{-2}. Hence, the effect of G_n on Li deposition from $114G_n$ solvate electrolytes was investigated at 1 mA.cm^{-2}. The relationship between CE and lifetime of the Cu-Li cells is displayed in **Figure 4.10**.

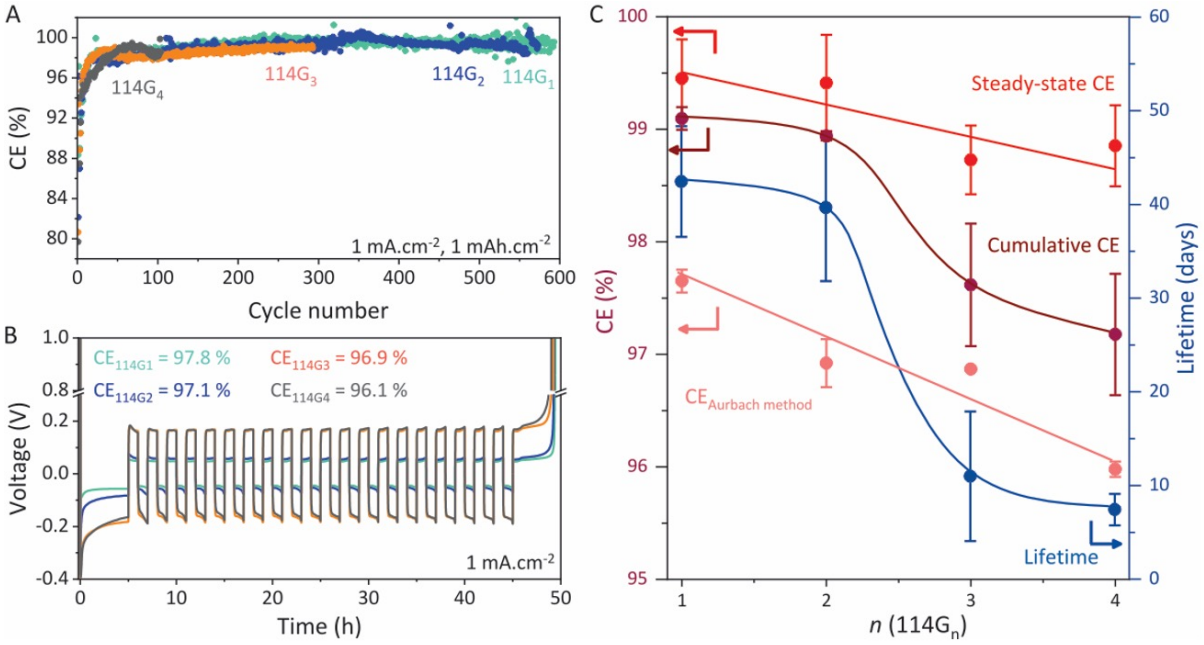


Figure 4.10 CE of Li deposition form $114G_n$ at 1 mA.cm^{-2}. The CE-values were determined by (A) the long-term cycling Cu-Li cells and (B) the Aurbach method. (C) The G_n-dependence of the CE-values and lifetime of the Cu-Li cells cycled 1 mA.cm^{-2}. The error bars are calculated based on 3-5 repeats for each measurement. The solid lines are the corresponding trendlines.

The Cu-Li cells exhibit a similar pattern in CE evolution throughout the continuous cycling process (**Figure 4.10 A**). The initial growth of the CE from 80-85 % takes approximately 100 cycles due to the SEI stabilization. After that, the cells deliver stable CEs above 98.5 % until Li dendrite short-circuiting occurs. The steady-state CE and the lifetime of the cells depend on the length of G_n but exhibit different trends, as shown in **Figure 4.10 C**. In particular, the steady-state CE exhibits a quasi-linear decrease with *n* from 99.4 % ($114G_1$) to 99.0% ($114G_4$). Meanwhile, the average lifetime of the cells with $114G_1$ and $114G_2$ is approximately 40 days, but it drops significantly to 9 - 10 days when $114G_3$ and $114G_4$ are employed.

This striking difference could be explained in terms of the solvate properties. On the one hand, the decomposition of FSI^- yields the stable SEI, resulting in a high CE. Therefore, the dependence of steady-state CE on G_n is primarily dictated by the amount of FSI^- in the 1st coordination sphere around Li^+. On the other hand, the formation of Li dendrites is triggered by the low values of D_{salt} and t_{Li} exhibited by all four $114G_n$ solvate electrolytes. Consequently, the cells with $114G_3$ and $114G_4$ suffer from faster short-circuiting and lower cumulative CE compared to those with $114G_1$ and $114G_2$. Interestingly, the critical role of t_{Li} is particularly indicated by the similar dependence of cell lifetime and t_{Li} on G_n.

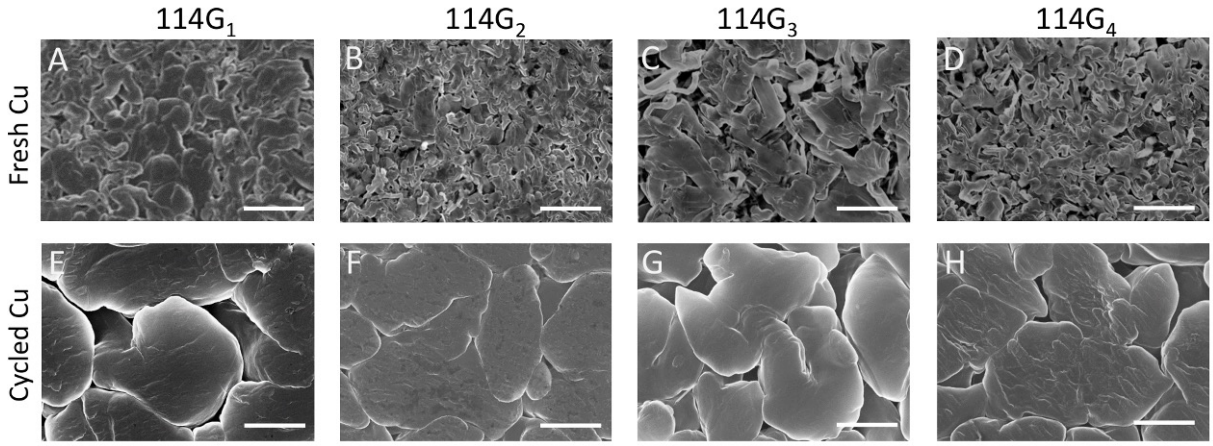


Figure 4.11 Effect of G_n and Cu substrate on the morphology of Li. Morphology of Li deposited from $114G_n$ solvate electrolytes at 1 $mA.cm^{-2}$ onto an uncycled (A - D) and the Cu foil (E - H) previously employed to determine the CE of Li deposition by the Aurbach method. The scale bar is 5 μm.

Given that a thick Li anode employed in the Cu-Li cells provides an almost infinite supply of Li to compensate for the loss in Li caused by the initial SEI formation, the CE measured by continuous cycling of the Cu-Li cells may be overestimated relative to the practical LMBs with a limited quantity of Li. To account for this potential error, the CE of Li deposition from the solvate electrolytes was also measured by the Aurbach method.[202] This method is based on measuring the CE of Li deposition by cycling limited amounts of Li. As shown in **Figure 4.10 B**, the CEs measured by the Aurbach method for $114G_1$, $114G_2$, $114G_3$, and $114G_4$ are 97.8, 97.1, 96.9, and 96.1 %, which is approximately between 1.5 and 2.5 % lower than the CE at the steady state. These values of the CE are equivalent to the Li losses of 0.55, 0.725, 0.775, and 0.975 $mAh.cm^{-2}$, respectively, which indicates that a practical LMB employing any of $114G_n$ solvate electrolyte would need at least 1-2 $mAh.cm^{-2}$ of additional Li to

account for the SEI formation. Notably, the CE measured by the Aurbach method exhibits a similar dependence on G_n as the previously discussed cumulative CE (**Figure 4.10 C**), which further illustrates that FSI-AGGs formation benefits Li deposition from the solvate electrolytes.

The importance of SEI formation to achieve stable Li deposition from the solvate electrolytes is confirmed by SEM analysis of electroplated Li. When Li is deposited onto a fresh Cu foil, the nucleation and growth of Li occur concurrently with the formation of SEI. As a result, Li deposition on the fresh Cu foil is primarily controlled by the rates of interfacial and bulk transport of Li^+ ions in $114G_n$. This is demonstrated by the transition from granular (**Figure 4.11 A**) to whisker-type morphology (**Figure 4.11 D**). **Figure 4.11 E-H** shows the morphology of Li deposited on the Cu current collector after measuring the CE by the Aurbach method. Since the SEI had been formed before Li plating, the deposition process is primarily influenced by the rate of bulk transport of Li^+ ions rather than the interfacial properties of $114G_n$. As a result, Li plated onto the recycled SEI is relatively dense and devoid of whiskers, which, in turn, illustrates how Cu-Li cells with $114G_n$ achieve a high CE at the steady state.

4.6 Performance of LMBs with $114G_n$ Solvate Electrolytes

The behavior of $114G_n$ solvate electrolytes was evaluated by cycling full Li||NCA and anode-free Cu||NCA cells under semi-practical conditions, which are a high cathode loading of ~ 3.5 $mAh.cm^{-2}$, a thin (50 μm) Li anode and a moderate electrolyte loading of 10 $\mu L.(mAh)^{-1}$ to avoid the cell dry-out. The ratio between the capacity of the anode and the cathode (the N/P ratio) is 2.75, which is acceptable for the practical LMBs.[203] The performance of the representative full cells with $114G_n$ electrolytes is summarized in **Figure 4.12**.

The length of G_n determines capacity retention and lifetime of the full cells (**Figure 4.12 A**). The decisive role of G_n is demonstrated by the initial activation cycle at 0.1 C (0.35 $mAh.cm^{-2}$). Indeed, the Li||NCA cell with $114G_1$ (**Figure 4.12 B**) exhibits the initial voltage plateau at ~ 3.85 V, which significantly differs from the electrochemical profile of the cell with $114G_4$ (**Figure 4.13 C**). Indeed, the activation of the Li||NCA cells with $114G_4$ begins with the initial voltage spike to almost 4.3 V, caused by the slow interfacial transport of chelated Li^+ ions. Overall, the low total Li^+-conductivity of $114G_4$ limits the capacity of NCA to 160 $mAh.g_{NCA}^{-1}$, as opposed to the values of 175-185 $mAh.g_{NCA}^{-1}$ typical for the cells $114G_1$. Since the decomposition of fluorinated electrolytes during the 1st cycle yields the formation of stable SEIs and CEIs,[121,122] the 2nd cycle at 0.1 C is devoid of the initial

overpotential. The discharge capacity increases to approximately 196 - 199 mAh.g_{NCA}^{-1} in the case of Li||NCA cells with $114G_1$, $114G_2$ and the anode-free NCA cells with $114G_1$ (**Figure 4.12 D**). On the other hand, the 2nd cycle capacity of the cells employing the chelating G_3 and G_4 decreases to ~187 and 166 mAh.g^{-1}_{NCA}, respectively.

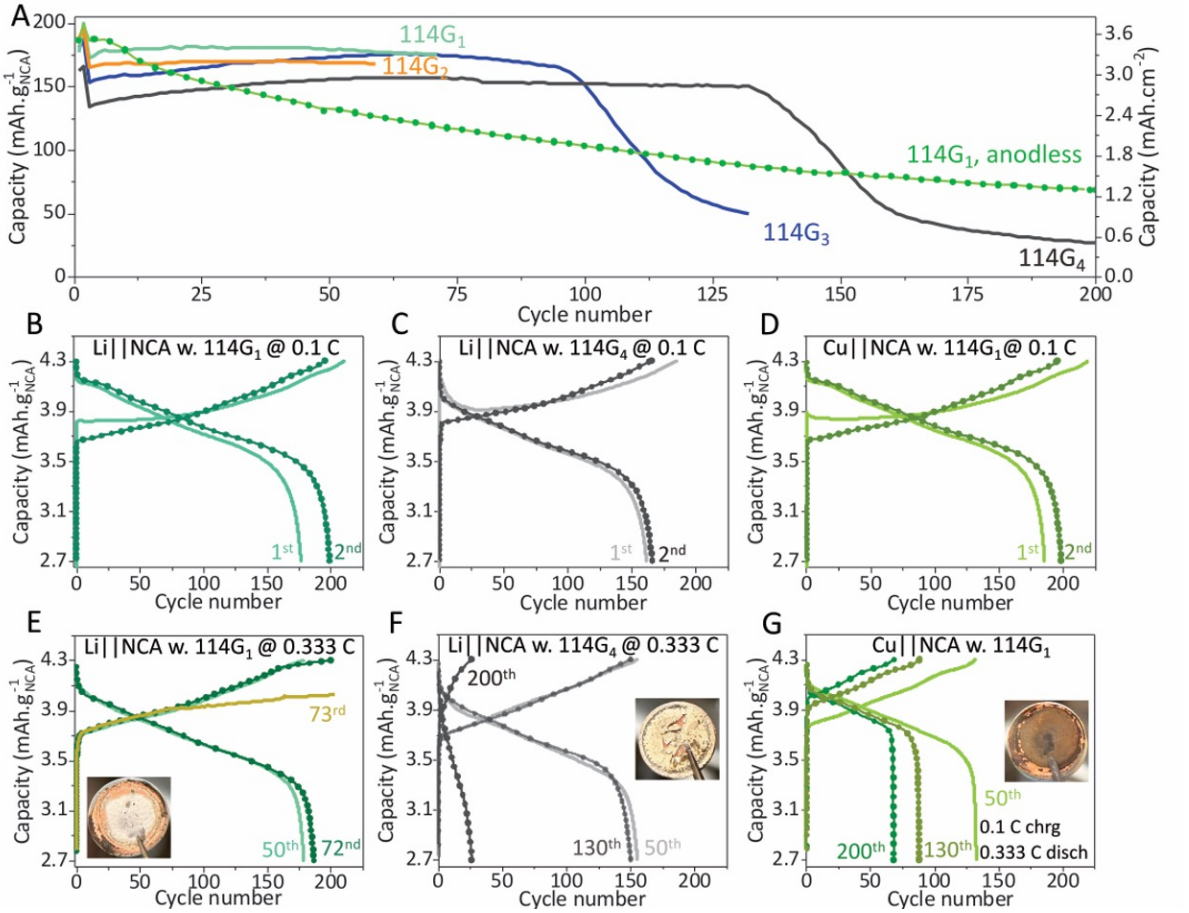


Figure 4.12 Electrochemical performance of LMBs with NCA cathodes and $114G_n$. (A) Capacity retention of Li||NCA and Cu||NCA cells with $114G_n$ cycled between 2.7 and 4.3 V. Li||NCA cells were activated for two cycles at 0.1 C and then cycled at 0.333 C. Cu||NCA cells were activated at 0.1 C for two cycles, and then cycled at 0.1 C (charge) and 0.333 C. (discharge). Activation cycles of Li||NCA cells with (B) $114G_1$ and (C) $114G_4$ and (D) Cu||NCA cells with $114G_1$. The selected cycles of Li||NCA cells with (E) $114G_1$ and (F) $11FG_4$ at 0.333 C and the (G) Cu||NCA cells at 0.1 C charge and 0.333 C discharge. The inset photos in (E–G) show the anodes after cell failure.

The strong relationship between the performance of NCA full cells with $114G_n$ and G_n becomes more pronounced when the C-rate is increased to 0.333 C (1.167 $mA.cm^{-2}$). Consistent with the Li^+-conductivities dependence on G_n, the discharge capacity of Li||NCA cells with $114G_1$, $114G_2$, $114G_3$, and $114G_4$ decreases to 180, 175, 160, and 135 $mAh.g_{NCA}^{-1}$, respectively. It then continuously increases to the steady-state values, which descend in the following order: $114G_1$ (180 $mAh.g^{-1}_{NCA}$) > $114G_2 \approx 114G_3$ (171 – 173 $mAh.g^{-1}_{NCA}$) > $114G_4$ (155 $mAh.g^{-1}_{NCA}$). The phenomenon of the initial capacity increase is common for polycrystalline Ni-rich NCA and NCM materials. The capacity increase can be attributed to the formation of microcracks at high degrees of delithiation, which augment the electrochemically active surface area.[204] It is noteworthy that the discharge capacity delivered by the Li||NCA cells with $114G_1$ and $114G_2$ increases to the steady-state values over approximately 10 – 20 cycles. In comparison, the cells with $114G_3$ and $114G_4$ require almost 60 cycles. Subsequently, the steady-state capacity is maintained prior to the cell failure for approximately 50 cycles in the case of $114G_1$, $114G_2$, and $114G_3$ but 100 cycles in the case of $114G_4$.

Li||NCA full cells exhibit two distinctive failure modes, dependent on the length of G_n. In the case of the cells containing $114G_1$ and $114G_2$, the shutdown is caused by short-circuiting after approximately 70 cycles. An example of this is illustrated in **Figure 4.12 E** by the ~0.4 V voltage drop at the 71st cycle. Meanwhile, the Li||NCA cells with $114G_3$ and $114G_4$ do not undergo short-circuiting. On the contrary, these cells exhibit an increase in polarization (**Figure 4.12 F**), which results in the severe capacity fading to < 50 $mAh.g_{NCA}^{-1}$. It is noteworthy that the Cu||NCA cells with $114G_1$ also exhibit capacity decay when cycled under 0.1 C charge/0.3 C discharge current (**Figure 4.12 G**). However, the capacity decrease of the Cu||NCA cells is flatter, and its shape is typical for the LMBs with limited Li reservoirs cycled at a low pressure.[180,205]

The observed difference in the failure scenario of Li||NCA full cells can be elucidated through a visual post-mortem examination of the cycled cells. In contrast to the shorted Li||NCA cells utilizing $114G_1$, which retain residual Li metal (**Figure 4.12 E inset**), those employing 114G4 electrolyte undergo dry-out, as evidenced by the formation of a thick precipitate on the Cu current collector (**Figure 4.12 F inset**). Therefore, it is rational to hypothesize that the extended lifetime of Li||NCA cells containing $114G_3$ and $114G_4$ is attributable to more extensive passivation of Li dendrites by the electrolyte decomposition products, as opposed to their counterparts containing $114G_1$ and $114G_2$. Indeed, the charging current density of 1.167 mA.cm^{-2} is equivalent to 35 % of j_{lim} in the case of $114G_1$, but it surpasses 100 % in the case of $114G_4$. Hence, charging the Li||NCA cells with $114G_3$ or $114G_4$ occurs with the formation of high surface area dendrites, which exhibit higher reactivity towards the solvate electrolytes when compared to the dendrites deposited from 114G1 and $114G_2$. In other words, $114G_3$ and $114G_4$ might act as the dendrite scavengers until the complete electrolyte consumption. This possible mechanism is schematically illustrated in **Figure 4.13**.

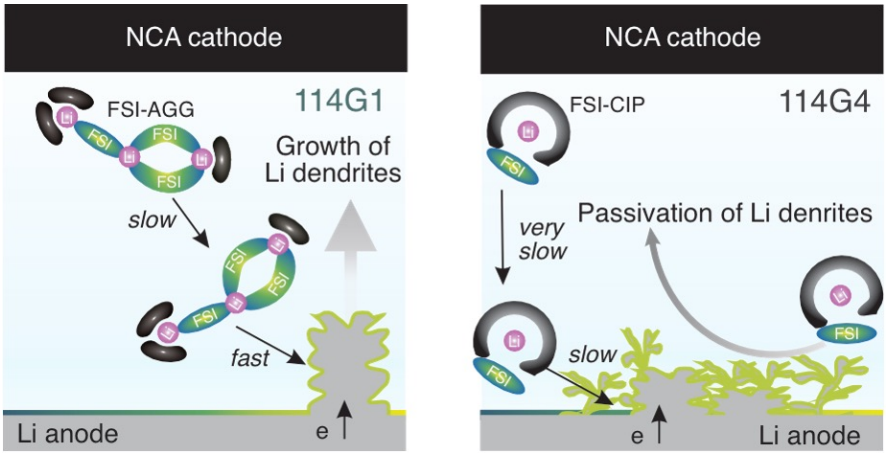


Figure 4.13 Schematic illustration of the degradation mechanisms observed the Li||NCA cells with $114G_1$ (left) and $114G_4$ (right). The propagation of a single Li dendrite (left) illustrates the short-circuiting mechanism typical for of the full cells with 114G1. The right panel demonstrates the passivation of Li in $114G_4$.

4.7 Conclusions

This Chapter presents the comprehensive study of the $114G_n$ solvate electrolyte using various techniques. Combining Raman spectroscopy, theoretical calculations, and full-range EIS analysis

establish the relationship between the composition, structure, and Li^+-transport properties. In agreement with AIMD simulations of $114G_1$ and $114G_4$, the results of Raman spectroscopy suggest that ionic association between Li^+ and FSI^- is noticeably enhanced if a single G_n molecule cannot chelate a Li^+ cation. Therefore, the solvation structure of $114G_1$ (and $114G_2$) contains clusters of multiple FSI-AGGs separated by the TTE molecules. In contrast, TTE-separated isolated FSI-CIP is the predominant configuration of FSI^- in $114G_4$. Enhancing the coordination of Li^+ by FSI^- improves the interfacial kinetics of LMAs, which is illustrated by the lowest values of the interfacial resistance and activation energy barriers observed for $114G_1$.In addition to impeding Li^+ transport across the SEI and desolvation of Li^+ ions, the chelation of Li^+ by G_n reduces the lithium transference number from 0.2-0.22 in $114G_1$ and $114G_2$ to less than 0.05 in $114G_3$ and $114G_4$.

The results of low-frequency EIS suggest that $114G_n$ solvate electrolytes suffer from slow Li^+-diffusivity in the bulk. $114G_1$ exhibits the highest values of D_{salt} ($2.1 \cdot 10^{-7}$ $cm^2.s^{-1}$) and t_{Li} (0.22). However, these values are noticeably lower than those in SOA carbonate electrolytes. Polarizing Li symmetric cells further confirms the diffusion-limited stability of LMAs. The Chazalviel model provides a relatively correct estimate of the short-circuiting time if the cells do not contain Celgrad separators. Cycling Cu-Li asymmetric cells demonstrates that the solvate electrolyte facilitates steady-state Li deposition with a CE exceeding 99 %. However, the diffusion limitations trigger the Li consumption of 1.5-3 $mAh.cm^{-2}$ during the initial SEI buildup. The performance of the Li||NCA full cells indicates the different failure modes of LMAs in $114G_1$ ($114G_2$) and $114G_3$ ($114G_4$). In the case of the full cells with $114G_1$ ($114G_2$), the LMA suffers from shorting after ~70 cycles at 1.167 $mA.cm^{-2}$, while those employing $114G_3$ ($114G_4$) shut down due to the SEI buildup after 120-150 cycles. Interestingly, the observed difference may be explained by applying Bazant's Li dendrite formation model[92] and the transport properties of the solvate electrolytes measured by EIS.

Since the electrochemical results presented in this Chapter were obtained at ambient temperature and pressure (25 °C, 0.1 MPa), there is enough room to optimize the cycling conditions and tune the composition of the solvate electrolytes to improve the overall cell performance.

Chapter 5
Stability of Lithium Metal Anodes in SSBs with Sulfide SEs

5.1 Introduction

As discussed in the Introduction, the design of high-energy density Li batteries is focused on replacing flammable liquid electrolytes with safer and more conductive solid SEs and incorporating LMAs instead of graphite anodes. However, the instability of LMA/SE interface and the formation of Li dendrites greatly impede the development of high-energy-density rechargeable SSBs with LMA.[125] In particular, one of the most conductive sulfide SEs, $Li_{10}GeP_2S_{12}$, reacts with Li, yielding a constantly growing MCI.[151] In contrast to $Li_{10}GeP_2S_{12}$, Ge^{4+}-free sulfide SEs (Li_6PS_5Cl[153] and $Li_7P_3S_{11}$[154]) are more compatible with LMA. At the time this work was performed, our group had developed several Ge^{4+}-free sulfide SEs with a Li^+-conductivity above 1 $mS.cm^{-1}$ and unknown compatibility with LMA, which motivated this research project.

Herein, I report on a case study of the interfacial compatibility between LMAs and several SEs developed in our group: an entropically-stabilized $Li_{3.25}Si_{0.25}P_{0.75}S_4$[206] and highly conductive $Li_{10.35}Sn_{0.27}Si_{1.08}P_{1.65}S_{12}$ and $Li_{5.5}PS_{4.5}Cl_{1.5}$[134] SEs. It is demonstrated through the combination of electrochemical characterization techniques that Si^{4+}/Sn^{4+}-containing SEs react with Li, increasing the cell resistance and consuming Li metal. In contrast, Si^{4+}/Sn^{4+}-free SEs ($Li_{5.5}PS_{4.5}Cl_{1.5}$ and β-Li_3PS_4) exhibit better stability with LMA. For example, the CE of Li deposition from β-Li_3PS_4 exceeds 99 % at the current density of 0.1 $mA.cm^{-2}$. However, cycling Li SS cells with β-Li_3PS_4 is challenging when a current density exceeds 0.2-0.3 $mA.cm^{-2}$, as demonstrated by the combination of galvanostatic cycling and EIS of Li symmetric cells.

The final part of the Chapter describes two relatively successful strategies to improve the performance of Li symmetric SS cells. The first approach is based on incorporating a layer of $Li_{10.35}Sn_{0.27}Si_{1.08}P_{1.65}S_{12}$ as a Li dendrite scavenger. The effect of this approach on the stability of LMAs was evaluated in Li symmetric and full Li||TiS_2 SS cells. The second approach describes the incorporation of solvate electrolyte interlayers to stabilize the Li/SE interface. In particular, the stability of Li symmetric cells with $Li_{5.5}PS_{4.5}Cl_{1.5}$/$114G_2$ hybrid electrolytes was investigated by galvanostatic cycling and EIS.

5.2 Experimental Methods

5.2.1 Synthesis of SEs

The SEs were synthesized inside an Ar-filled glovebox with $p(O_2)/p < 0.1$ ppm and $p(H_2O)/p < 0.1$ ppm. β-Li_3PS_4 was synthesized by drying $Li_3PS_4 \cdot 3THF$ (BASF, Germany) under a dynamic vacuum at 150 °C for 24 hours. Dr. Zhou generously provided $Li_{3.25}Si_{0.25}P_{0.75}S_4$. The solid-state synthesis of $Li_{3.25}Si_{0.25}P_{0.75}S_4$ is described in Ref. 205. $Li_{10.35}Sn_{0.27}Si_{1.08}P_{1.65}S_{12}$ was synthesized by the solid-state reaction between Li_2S (Sigma Aldrich), P_2S_5 (Sigma Aldrich), SiS_2 (Sigma Aldrich) and SnS_2 (Sigma Aldrich) according to the procedure developed by Dr. Kaup. In brief, the reagents were hand-ground for 40 minutes, pelletized and placed in a glassy-carbon crucible in a sealed quartz tube under vacuum. The sample was held at 650 °C for 48 hours. The ramping and cooling rates were 5 °C.min^{-1}. $Li_{5.5}PS_{4.5}Cl_{1.5}$ was synthesized by Dr. Adeli following the procedure described in Ref. 134. The precursor pellets comprised of hand-ground Li_2S (Sigma Aldrich), P_2S_5 (Sigma Aldrich), and LiCl (Sigma Aldrich) were placed in a glassy carbon crucible and sealed under vacuum. The sample was heated to 550 °C at 0.5 °C.min^{-1}, held for 6 hours and cooled to ambient temperature at 0.5 °C.min^{-1}.

5.2.2 Cell Assembly

SS cells were assembled inside an Ar-filled glovebox. In a typical cell preparation, 100 mg of SE was pressed in a 10 mm diameter PEEK cylinder at 3 tons for 5 minutes. After that, the electrodes were placed against the SE. Asymmetric Cu-Li cells contained a 10 mm Cu foil and an 8 mm Li disc (50 µm Cu|Li, China Lithium Energy). Symmetric SS cells with Li electrodes contained two 10 mm Li electrodes. Finally, the cell was placed in an airtight pressure cage and tightened with a torque wrench set at 4 N·m, equivalent to approximately 25 MPa.

In the case of symmetric Li SS cells containing a trilayer sandwich $Li_{5.5}PS_{4.5}Cl_{1.5}/Li_{10.35}Sn_{0.27}Si_{1.08}P_{1.65}S_{12}/Li_{5.5}PS_{4.5}Cl_{1.5}$ SE, a 60 mg of $Li_{5.5}PS_{4.5}Cl_{1.5}$ were uniformly spread over each side of a 100 mg pellet of $Li_{10.35}Sn_{0.27}Si_{1.08}P_{1.65}S_{12}$ and then pressed at 3 tons. The remaining steps of the cell preparation were similar to the SS Li symmetric cells containing a single SE.

The Li||TiS_2 full cells were prepared following a similar protocol. The CAM was prepared through the hand-grinding of 50 wt. % TiS_2 (Sigma Aldrich) and 50 wt. % $Li_{5.5}PS_{4.5}Cl_{1.5}$ for 30 minutes. Then, a bilayer pellet containing 80 mg $Li_{5.5}PS_{4.5}Cl_{1.5}$ and 80 mg $Li_{10.35}Sn_{0.27}Si_{1.08}P_{1.65}S_{12}$ was pressed

at 1.5 T. After that, 13 mg of CAM was pressed against the $Li_{10.35}Sn_{0.27}Si_{1.08}P_{1.65}S_{12}$ side at 3 T for 5 minutes. Finally, a 10 mm Cu|Li anode was placed against the $Li_{5.5}PS_{4.5}Cl_{1.5}$ side, and the cell was tightened to a torque of 4 N·m.

Hybrid cells containing a $Li_{5.5}PS_{4.5}Cl_{1.5}$ pellet and $114G_2$ solvate electrolyte were assembled into 2032 coin cells (MTI Corp.). In a typical preparation procedure, $Li_{5.5}PS_{4.5}Cl_{1.5}$ was pressed into a 14 mm pellet with an approximate density of 90 %. The pellet was placed between two 16 layers of 3501 Celgrad filled with 40 μL $114G_2$ (20 μL per separator). Finally, the hybrid electrolyte was placed between two stainless steel current collectors to prepare the symmetric hybrid cells. In the case of asymmetric Cu-Li hybrid cells, 12 mm Cu working and 10 mm Cu|Li counter electrodes were employed. The pressure generated inside a 2032 coin cell was approximately 0.1 MPa.

5.2.3 Electrochemical Measurements

Time-resolved cyclic voltammetry of the symmetric Li cells was performed every hour immediately after cell assembly. The voltage was swept at 0.5 $mV.s^{-1}$ from OCV to 3 mV and then reversed to -3 mV. The overlapping voltammograms were typically observed after three cycles.

Li symmetric SS cells with $Li_{5.5}PS_{4.5}Cl_{1.5}$ and trilayer SE pellets were cycled at a current density of 0.5 $mA.cm^{-2}$ with a plating capacity of 1 $mAh.cm^{-2}$ until short-circuiting. Li symmetric SS cells with β-Li_3PS_4 were cycled at 0.025 - 0.75 $mA.cm^{-2}$ (five cycles at each current density). Each plating/stripping cycle was 2 hours. EIS was measured before each increase in current density. EIS was recorded from the frequency range between 1 MHz and 200 mHz with an amplitude of 5 mV.

Asymmetric Cu-Li cells were cycled at a current density of 0.1 mA.cm-2 with a plating capacity of 0.1 mAh.cm-2. During the stripping step, the cutoff voltage was 1 V. The Cu-Li cells were cycled until short-circuiting or the drop in plating capacity to below 0.05 $mAh.cm^{-2}$. Li||TiS_2 SSB cells containing multilayer SEs were cycled at 0.2 C between 1.5 and 2.9 V until hard short-circuiting.

The interfacial compatibility between $Li_{5.5}PS_{4.5}Cl_{1.5}$ and $114G_2$ was investigated through time-resolved EIS of the 2032 coin cells with a hybrid $Li_{5.5}PS_{4.5}Cl_{1.5}$/$114G_2$ electrolyte and stainless steel electrodes. EIS was recorded within the frequency range between 1 MHz and 200 mHz with an amplitude of 100 mV.

The stability of Li deposition from the hybrid $Li_{5.5}PS_{4.5}Cl_{1.5}$/$114G_2$ electrolytes was investigated by continuous cycling asymmetric the Cu-Li cells at 0.5 $mA.cm^{-2}$ (1 $mAh.cm^{-2}$). Before

the long-term cycling, 5 mAh.cm^{-2} of Li (equivalent to 50 % of available Li) was deposited on the Cu foil at 0.2 mA.cm^{-2}. EIS of the Cu-Li cells was recorded within the frequency range between 1 MHz and 200 mHz with an amplitude of 5 mV.

All electrochemical measurements were performed at a room temperature of 25 °C using a VMP3-1 Biologic potentiostat.

5.2.4 XRD Analysis of Reacted SEs

Li symmetric SS cells containing $Li_{10.35}Sn_{0.27}Si_{1.08}P_{1.65}S_{12}$ and $Li_{3.25}Si_{0.25}P_{0.75}S_4$ SEs were disassembled inside a glovebox. The reacted Li foil was removed from the SE pellet without significant effort, thus exposing the interphase for the XRD study. The pellets were mounted on a zero-background holder and sealed with a thin polyimide Kapton film to prevent air exposure.

The reactivity between $Li_{5.5}PS_{4.5}Cl_{1.5}$ and $114G_2$ was probed by stirring the SE powder in the solvate for 48 hours at 80 °C inside the Ar glovebox. The reacted powder was precipitated through centrifugation and dried under a dynamic vacuum at 120 °C for 24 hours. Finally, the powder was loaded on a zero-background holder and sealed with an air-tight Kapton film for XRD measurements.

XRD was measured with a PANalytical Empyrean X-ray diffractometer operating at 40 kV and 40 mA and using Cu-Kα radiation (λ = 015405 nm).

5.3 Stability of LMA is SS Cells with Sulfide Electrolytes

5.3.1 LMA Stability of Sulfide SEs at OCV

The stability of LMAs in SS cells was initially investigated under open circuit voltage (OCV) using time-resolved CVA of Li symmetric SS cells with β-Li_3PS_4, $Li_{10.35}Sn_{0.27}Si_{1.08}P_{1.65}S_{12}$, and $Li_{3.25}Si_{0.25}P_{0.75}S_4$ SEs. Since cell polarization was limited to ± 3 mV from the OCV, cyclic voltammograms (CVs) of Li symmetric SS cells are linear (**Figure 5.1 A**). Therefore, the interfacial resistance between Li and an SE (R_{int}) can be approximated according to **Equation 5.1**.

$$R_{int} = \left(\frac{dI}{d\eta}\right)^{-1} - R_{bulk} \qquad \textbf{Equation 5.1}$$

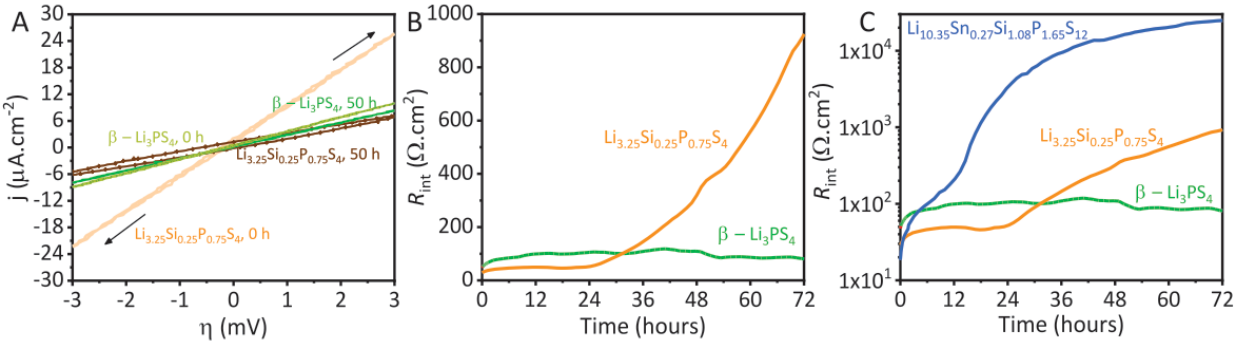


Figure 5.1 Reactivity of LMA with sulfidic SEs. (A) CVs of symmetric Li SS cells containing β-Li_3PS_4 (olive – new cell, and green – after 50 hours of storage) and $Li_{3.25}Si_{0.25}P_{0.75}S_4$ (orange – new cell and brown– after 50 hours of storage) SEs at a rate of 1 $mV.s^{-1}$ (B) Evolution of R_{int} of the Li symmetric cells with β-Li_3PS_4 (green) and $Li_{3.25}Si_{0.25}P_{0.75}S_4$ (orange). (C) Evolution of R_{int} of the Li symmetric cells with β-Li_3PS_4 (green) and $Li_{3.25}Si_{0.25}P_{0.75}S_4$ (orange), and $Li_{10.35}Sn_{0.27}Si_{1.08}P_{1.65}S_{12}$ (blue). Due to the much higher resistance of the cells with $Li_{10.35}Sn_{0.27}Si_{1.08}P_{1.65}S_{12}$, the Y-axis is plotted in logarithmic scale.

The different evolution of cyclic voltammograms exhibited by the SS cells with β-Li_3PS_4 and $Li_{3.25}Si_{0.25}P_{0.75}S_4$ SEs visualizes the effect of Si^{4+} on the interfacial stability. While R_{int} of the cells with β-Li_3PS_4 remains at the same level of approximately 80 $\Omega.cm^2$, that of the cells containing $Li_{3.25}Si_{0.25}P_{0.75}S_4$ reaches 900 $\Omega.cm^2$ after three days of aging (**Figure 5.1 B**). Furthermore, CVs of the cell with β-Li_3PS_4 remain linear after 50 hours of storage, whereas the aged cells containing $Li_{3.25}Si_{0.25}P_{0.75}S_4$ SE exhibit a noticeable hysteresis between plating and stripping scans. It is noteworthy that the observed difference in interfacial stability exhibited by β-Li_3PS_4 and $Li_{3.25}Si_{0.25}P_{0.75}S_4$ is induced when only a quarter of P^{5+} is substituted with Si^{4+}. As the ratio between the fractions of a semimetal and P^{5+} increases, the growth of R_{int} during aging is enhanced. This is illustrated by the fact that the cells containing $Li_{10.35}Sn_{0.27}Si_{1.08}P_{1.65}S_{12}$ displayed a more pronounced increase in R_{int}. **Figure 5.1 C** demonstrates that R_{int} of the cells containing $Li_{10.35}Sn_{0.27}Si_{1.08}P_{1.65}S_{12}$ is approximately 25 $k\Omega.cm^2$ after 72 hours of aging, which exceeds that of the cells with $Li_{3.25}Si_{0.25}P_{0.75}S_4$ by more than 20 times.

Overall, the observed relationship between the change in R_{int} during cell aging and the composition of SEs is consistent with the studies of $Li_{10}GeP_2S_{12}$,[151] Li_6PS_5Cl,[153] and $Li_7P_3S_{11}$.[154] However, we note that the temporal evolution of R_{int} exhibited by the cells with $Li_{3.25}Si_{0.25}P_{0.75}S_4$ and $Li_{10.35}Sn_{0.27}Si_{1.08}P_{1.65}S_{12}$ is exponential. In contrast, the interfacial resistance between Li and $Li_{10}GeP_2S_{12}$ exhibits a self-limited growth, with R_{int} proportional to $t^{0.5}$.[151] This different behavior could indicate

that the interphase formed between Li and $Li_{3.25}Si_{0.25}P_{0.75}S_4$ ($Li_{10.35}Sn_{0.27}Si_{1.08}P_{1.65}S_{12}$) retains sufficient conductivity to maintain continuous growth. Interestingly enough, a similar exponential increase in R_{int} behavior was observed in the case study of the Li/Li_3InCl_6 interface.[152]

5.3.2 CE of Li Deposition from Sulfide SEs

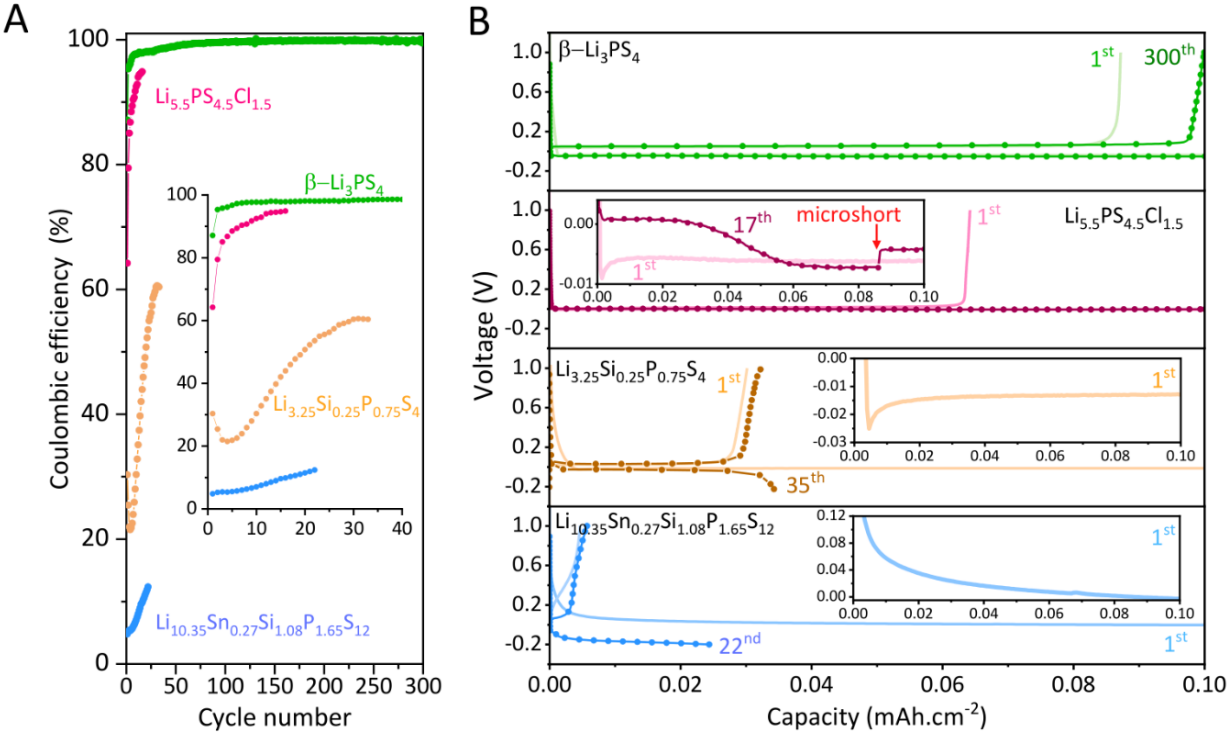


Figure 5.2 CE of Li deposition from sulfidic SEs. (A) CE of the Cu-Li SS cells containing β-Li_3PS_4 (green), $Li_{3.25}Si_{0.25}P_{0.75}S_4$ (orange), $Li_{10.35}Sn_{0.27}Si_{1.08}P_{1.65}S_{12}$ (blue), and $Li_{5.5}PS_{4.5}Cl_{1.5}$ (pink) SEs The insert shows the CE evolution during the initial 40 cycles. (B) The 1st and the last polarization of the Cu-Li cells at 0.1 mA.cm^{-2}. The arrow indicates short-circuiting of the cell containing $Li_{5.5}PS_{4.5}Cl_{1.5}$.

The efficiency and stability of Li deposition from SEs were evaluated by continuous cycling of asymmetric SS cells with copper working and Li counter electrodes. The CE of Li deposition was measured only at a low current density of 0.1 mA.cm^{-2} with a 0.1 mAh.cm^{-2} capacity cutoff to reduce the danger of cell shorting due to Li dendrites. The CE of Cu-Li cells containing β-Li_3PS_4, $Li_{3.25}Si_{0.25}P_{0.75}S_4$, $Li_{10.35}Sn_{0.27}Si_{1.08}P_{1.65}S_{12}$, and $Li_{5.5}PS_{4.5}Cl_{1.5}$ SE is displayed in **Figure 5.2 A**.

The relationship between the CE of Li deposition and SE's composition is consistent with the trend observed in the CV measurements. In particular, the CE of Li deposition form β-Li_3PS_4 exceeds

99% after the initial 50 cycles and stabilizes at a level of (99.7±0.2) %. The stability of Li deposition form β-Li_3PS_4 is also confirmed by the identical polarization profile observed after 300 cycles, as shown in **Figure 5.2 B**. On the contrary, $Li_{5.5}PS_{4.5}Cl_{1.5}$ exhibits a considerably less stable Li deposition than β-Li_3PS_4 although the conductivity of $Li_{5.5}PS_{4.5}Cl_{1.5}$ is almost 10 $mS.cm^{-1}$. Indeed, the initial CE of Cu-Li cells with $Li_{5.5}PS_{4.5}Cl_{1.5}$ is only 65 %, as opposed to 87 % exhibited by those with β-Li_3PS_4. Although the CE observed for $Li_{5.5}PS_{4.5}Cl_{1.5}$ approaches 95 % after 15 cycles, the cumulative CE remains low due to early short-circuiting. Typically, the lifetime of cells with $Li_{5.5}PS_{4.5}Cl_{1.5}$ is limited to 20 cycles at a current density of 0.1 $mA.cm^{-2}$, as illustrated by the representative galvanostatic polarization profile shown in **Figure 5.2 B**. It is noteworthy that the superior performance exhibited by the cells containing β-Li_3PS_4 could be partially explained by a higher density of β-Li_3PS_4 SE pellets. Indeed, a typical density of β-Li_3PS_4 SE pellets is approximately 95%, while that of $Li_{5.5}PS_{4.5}Cl_{1.5}$ pellets does not exceed 90 %.

Significantly lower CEs are observed for the cells containing $Li_{3.25}Si_{0.25}P_{0.75}S_4$ and $Li_{10.35}Sn_{0.27}Si_{1.08}P_{1.65}S_{12}$ (**Figure 5.2 A**). Specifically, the initial CE of the cells with $Li_{3.25}Si_{0.25}P_{0.75}S_4$ is 30 %, whereas that of $Li_{10.35}Sn_{0.27}Si_{1.08}P_{1.65}S_{12}$ is only 5 %. The higher M/P ratio triggers a greater LMA instability of $Li_{10.35}Sn_{0.27}Si_{1.08}P_{1.65}S_{12}$ in comparison with $Li_{3.25}Si_{0.25}P_{0.75}S_4$. This is also confirmed by the more pronounced electrochemical activity observed for $Li_{10.35}Sn_{0.27}Si_{1.08}P_{1.65}S_{12}$ (**Figure 5.2 B**). Indeed, the Cu-Li cell containing $Li_{3.25}Si_{0.25}P_{0.75}S_4$ exhibits a typical Li plating at negative voltages. In contrast, the voltage of the cell with $Li_{10.35}Sn_{0.27}Si_{1.08}P_{1.65}S_{12}$ remains positive, thus indicating the prevalence of SE electrochemical reduction. The subsequent cycling of SS cells with $Li_{3.25}Si_{0.25}P_{0.75}S_4$ and $Li_{10.35}Sn_{0.27}Si_{1.08}P_{1.65}S_{12}$ occurs with a minor increase of CE to 60 % and 18%, respectively.

Due to the rapid consumption of Li and continuous decomposition of SEs, Cu-Li cells employing $Li_{3.25}Si_{0.25}P_{0.75}S_4$ and $Li_{10.35}Sn_{0.27}Si_{1.08}P_{1.65}S_{12}$ do not undergo short-circuiting. Instead, these cells exhibit a rapid increase in polarization accompanied by the decrease plating capacity (**Figure 5.2 B**). As a result, the lifetime of Cu-Li containing $Li_{3.25}Si_{0.25}P_{0.75}S_4$ and $Li_{10.35}Sn_{0.27}Si_{1.08}P_{1.65}S_{12}$ is limited to 30 cycles. The post-mortem inspection of the disassembled cells via XRD confirms the disappearance of metallic Li, the initial amount of which was 10 $mAh.cm^{-2}$. It is noteworthy that Li_2S is the only crystalline component of the interphase (**Figure 5.3**), which indicates that the Si and Sn-containing SEI components are amorphous.

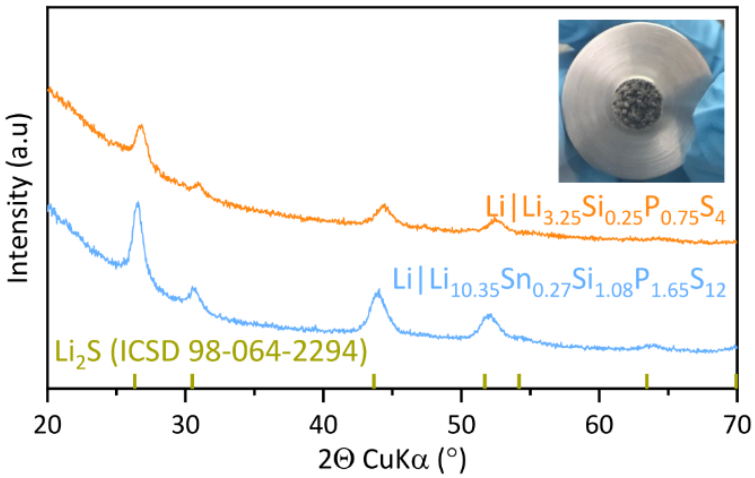


Figure 5.3 Composition of the Li/sulfidic SE interphase. Diffraction patterns of Li counter electrodes extracted from the Cu-Li cells containing $Li_{3.25}Si_{0.25}P_{0.75}S_4$ (orange) and $Li_{10.35}Sn_{0.27}Si_{1.08}P_{1.65}S_{12}$ (blue) SEs. The inset shows the cycled Li electrode.

5.3.3 Limited Rate Capability of Li symmetric SS cells with β-Li_3PS_4

As demonstrated earlier, the deposition of Li with CE exceeding 99 % can be achieved only when β-Li_3PS_4 is employed. However, since the Cu-Li cells were cycled under a low current density of 0.1 mA.cm^{-2} with a low-capacity cutoff of 0.1 mAh.cm^{-2}, the applicability of β-Li_3PS_4 under more practically realistic conditions remains unclear. To address this uncertainty, the rate capability of LMAs was investigated by cycling Li symmetric cells with β-Li_3PS_4 under various current densities and Li plating capacities. Applied current dendsity and capacity were gradually increased from 0.025/0.025 to 0.75 mA.cm^{-2}/0.75 mAh.cm^{-2}.

The polarization of Li symmetric SS cell with β-Li_3PS_4 SE and the evolution of its Nyquist plot are shown in **Figure 5.4 A, B**. When a current density is below 0.2 mA.cm^{-2}, the polarization curves exhibited a nearly square shape, which confirms the stability of LMAs. Raising the current density to 0.2 mA.cm^{-2} increases the curviness of the polarization, profile thus suggesting that Li cycling becomes less stable (**Figure 5.4 A)**. The further increase in current density results in unstable fluctuating voltages at 0.35 mA.cm^{-2} and 0.5 mA.cm^{-2}. Furthermore, the average cell voltage at 0.35 and 0.5 mA.cm^{-2} is below the linear trend obeyed at the lower current densities (**Figure 5.4 C, left Y-**

axis), which suggests the formation of soft short circuits.[207] Finally, hard short-circuiting occurs once a current density of 0.75 mA.cm^{-2} is applied.

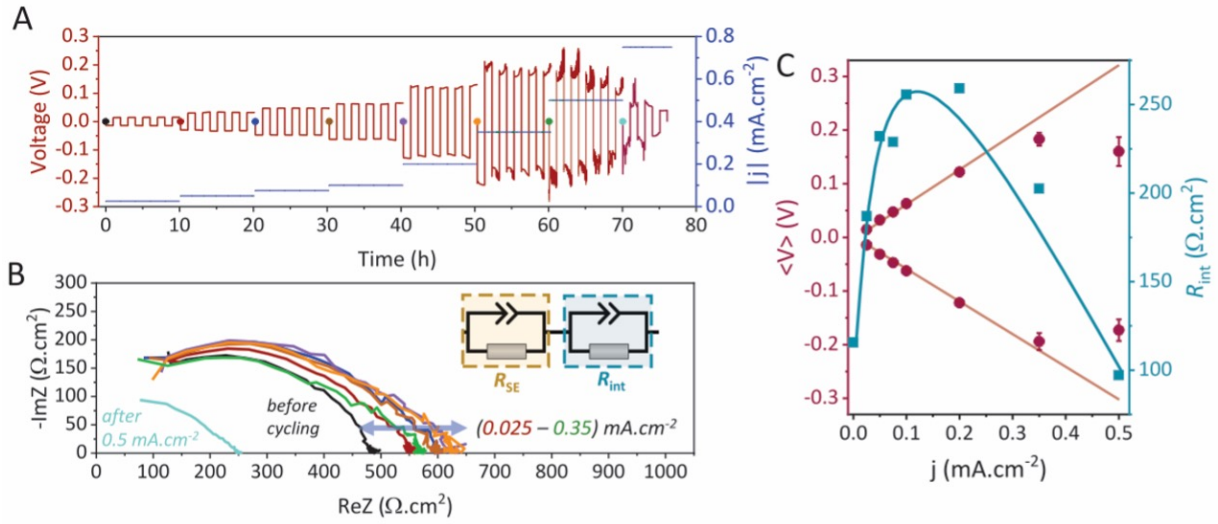


Figure 5.4 Rate capability of Li symmetric cells with β-Li_3PS_4. (A) Voltage profile of SS Li symmetric SS with β-Li_3PS_4 at 0.025-0.75 mA.cm^{-2}. The color dots represent the EIS measurements. Left Y-axis (vine) represents the volage, right Y-axis (blue) represents the magnitude of applied current density. (B) Nyquist plot of the Li-symmetric cell recorded within the frequency between 1 MHz and 200 mHz during cycling. The EIS spectra are colored in consistency with the thick dots in Panel A. The equivalent fitting circuit is shown in the inset. (C) Dependence of the average voltage (vine circles) and R_{int} (cyan squares) on the applied current density. The trendlines for the average voltage and R_{int} are represented by the solid vine and cyan lines, respectively.

The evolution in Nyquist plot during cell polarization confirms that the rate capability limit for Li deposition from β-Li_3PS_4 is around 0.35 mA.cm^{-2} in (**Figure 5.4 B)**. At current densities below 0.35 mA.cm^{-2}, R_{int} exhibited an increase from its initial value of 100 Ω.cm^2 to the value of 250 Ω.cm^2, measured after cycling at 0.1 and 0.2 mA.cm^{-2} (**Figure 5.4 C, right Y-axis)**. Meanwhile, raising the current density to 0.35 mA.cm^{-2} and then to 0.5 mA.cm^{-2} reduces R_{int} to 200 Ω.cm^2 and 95 Ω.cm^2, respectively. This conclusively demonstrates the instability of Li deposition at current densities exceeding 0.35 mA.cm^{-2}.

5.4 Improved Performance of LMA in SS Cells with Sulfide SEs

5.4.1 Dendrite-scavenging Multilayer SEs

Probing the interfacial compatibility between LMA and sulfidic SEs with various compositions demonstrates that the cells containing highly reactive SEs do not undergo short-circuiting. This phenomenon suggests that LMA-reactive SEs may be utilized as dendrite scavengers to extend the lifetime of LMAs. Conceptually, this approach could be illustrated by incorporating a simple bilayer pellet containing two $Li_{5.5}PS_{4.5}Cl_{1.5}$ outer layers and $Li_{10.35}Sn_{0.27}Si_{1.08}P_{1.65}S_{12}$ inner layer. If Li dendrites penetrate through $Li_{5.5}PS_{4.5}Cl_{1.5}$, they are scavenged by $Li_{10.35}Sn_{0.27}Si_{1.08}P_{1.65}S_{12}$, as schematically illustrated in **Figure 5.5 A**.

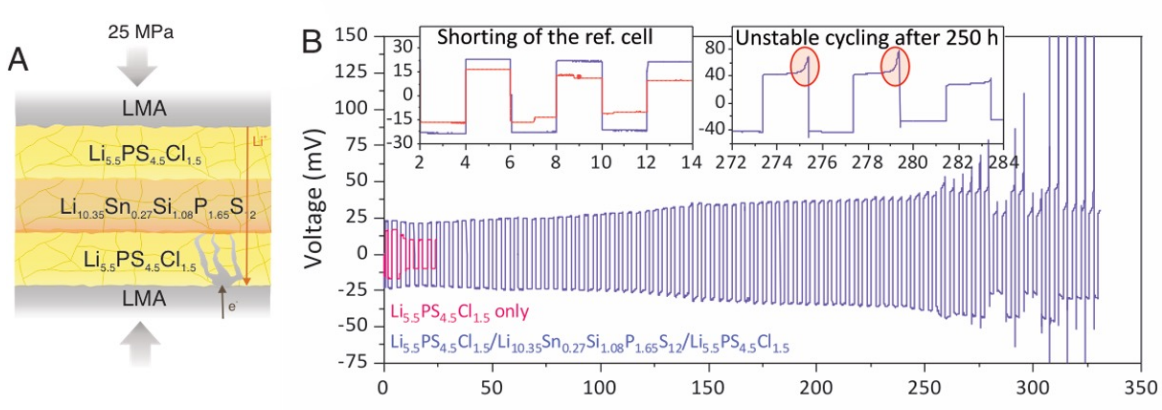


Figure 5.5 Performance of Li symmetric cells multilayer with sulfidic SE. (A) Schematic drawing of a Li symmetric SS cell with a multilayer SE pellet. The grey filament represents Li dendrites, which are scavenged by the layer of $Li_{10.35}Sn_{0.27}Si_{1.08}P_{1.65}S_{12}$. (B) Galvanostatic polarization of the Li symmetric cells containing $Li_{5.5}PS_{4.5}Cl_{1.5}$ (pink) and trialyer (blue) SE pellets recorded at 0.5 $mA.cm^{-2}$ (1 $mAh.cm^{-2}$). The inserts show the fast short-circuiting of the control cell after 7 hours and the unstable polarization of the cell with a trilayer SE after 250 hours of cycling.

Cycling Li symmetric cell with trilayer $Li_{5.5}PS_{4.5}Cl_{1.5}/Li_{10.35}Sn_{0.27}Si_{1.08}P_{1.65}S_{12}/Li_{5.5}PS_{4.5}Cl_{1.5}$ SE pellets at 0.5 $mA.cm^{-2}$ and 1 $mAh.cm^{-2}$ plating capacity demonstrates the viability of the proposed concept. While the control cell containing only $Li_{5.5}PS_{4.5}Cl_{1.5}$ shuts down after 7 hours of cycling, the cell employing the trilayer SE pellet can be cycled for 275 hours (**Figure 5.5 B**). Nevertheless, cell with modifed SE exhibits a slow but gradual increase in polarization during cycling. Thus suggests that the Li/ $Li_{5.5}PS_{4.5}Cl_{1.5}$ interface becomes unstable when 1 $mAh.cm^{-2}$ of Li is continuously plated and

stripped. Furthermore, the voltage fluctuating after 250 hours indicates the enhanced propagation of Li dendrites through the $Li_{5.5}PS_{4.5}Cl_{1.5}$ layers.

Electrochemical performance of the full Li||TiS_2 cell with a bilayer $Li_{5.5}PS_{4.5}Cl_{1.5}$/$Li_{10.35}Sn_{0.27}Si_{1.08}P_{1.65}S_{12}$ SE pellet also demonstrates that the scavenging effect of $Li_{10.35}Sn_{0.27}Si_{1.08}P_{1.65}S_{12}$ is temporary. At a rate of 0.2 C, equivalent to 0.325 mA.cm^{-2}, the full cell is cycled ten times without any signs of short-circuiting, as illustrated by the stable CE above 99 %(**Figure 5.6 A**). After that, the CE drops to ~ 88 % on the 11th and 12th but then recovers to 99 % for five more cycles. For example, the 15th cycle polarization profile is devoid of any voltage fluctuations on charge, indicating the stabilization of Li deposition.

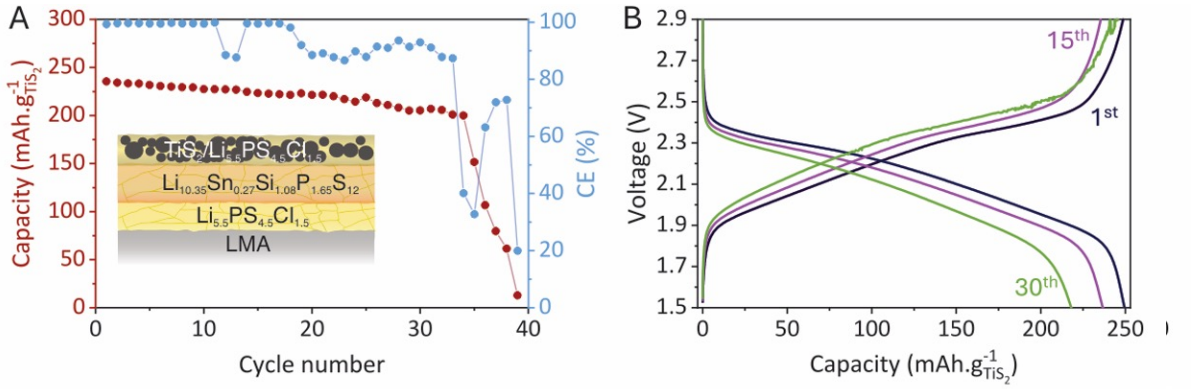


Figure 5.6 Performance of the Li||TiS_2 full cell with multilayer sulfidic SE. (A) Discharge capacity (left Y-axis) and CE (right Y-axis) of the Li||TiS_2 SSB cell containing the bilayer $Li_{5.5}PS_{4.5}Cl_{1.5}$/$Li_{10.35}Sn_{0.27}Si_{1.08}P_{1.65}S_{12}$ SE pellet. (B) The 1st(blue), 15th (purple), and 30th (green) galvanostatic cycles at 0.2 C. The voltage fluctuations exhibited by the green curve are due to the formation of soft Li shorts. The cell was cycled within the 1.5-2.9 V voltage window. The active material loading was 6.8 mg.cm^{-2}.

Since the decrease in CE observed for the 11th and 12th cycles is not accompanied by any significant drop in discharge capacity, it is reasonable to conclude that $Li_{10.35}Sn_{0.27}Si_{1.08}P_{1.65}S_{12}$ reacts with Li dendrites, which regains the CE. However, the scavenging effect of $Li_{10.35}Sn_{0.27}Si_{1.08}P_{1.65}S_{12}$ is limited to 18 cycles. After that, the CE drops to ~ 90 % and remains at this level for 10-15 cycle until the formation of hard Li shorts (**Figure 5.6 B**).

We note that when an areal capacity is restricted to 0.2-0.4 mAh.cm^{-2}, similar approaches can extend the cyclability to hundreds of cycles. This was exemplified by the case studies of SSB cells

containing multilayer $Li_{10}GeP_2S_{12}$[208] and $Li_{10}SnP_2S_{12}$[209] SEs. However, my work demonstrates that this approach is unsuitable for developing high-energy-density LMBs.

5.4.2 $114G_2$-assisted Improved Performance of LMA

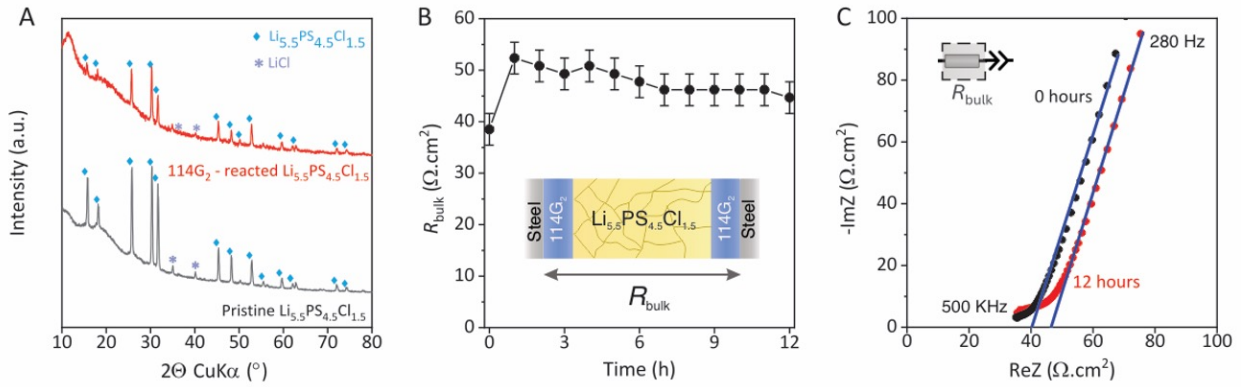


Figure 5.7 Chemical stability of $Li_{5.5}PS_{4.5}Cl_{1.5}$/$114G_2$ hybrid electrolytes. (A) XRD pattern of $Li_{5.5}PS_{4.5}Cl_{1.5}$ SE powder before (grey) and after (red) the reactions with $114G_2$. Marine blue rhombs and light get stars represent the peaks of $Li_{5.5}PS_{4.5}Cl_{1.5}$ and LiCl, respectively. (B) Change in the resistance of 2032 symmetric coin cells containing $Li_{5.5}PS_{4.5}Cl_{1.5}$/$114G_2$ hybrid electrolyte. The simplified cell design is shown in the inset. (C) Nyquist plot of the symmetric cell before (black dots) and after aging for 12 hours (red dots). The blue lines demonstrate the fitting with a simple equivalent circuit shown in the inset.

Introducing a thin liquid or polymer electrolyte interlayer between LMA and SE is a promising strategy for stabilizing the LMA/SE interface.[210,211] This approach was realized by wetting $Li_{5.5}PS_{4.5}Cl_{1.5}$ with the $114G_2$ solvate electrolyte. The chemical compatibility between $Li_{5.5}PS_{4.5}Cl_{1.5}$ with $114G_2$ was confirmed by combining EIS and XRD. Specifically, mixing the SE powder with $114G_2$ for 48 hours 80 °C reduces the crystallinity of $Li_{5.5}PS_{4.5}Cl_{1.5}$ but does not generate any additional crystalline phases (**Figure 5.7 A**). Furthermore, the EIS analysis of symmetrical coin cells containing $Li_{5.5}PS_{4.5}Cl_{1.5}$/$114G_2$ demonstrates that the cell resistance remains unchanged during the storage for 12 hours (**Figure 5.7 B**), except for the ~ 5 $\Omega.cm^2$ increase likely caused by the pressure relaxation. Notably, the observed chemical stability of $Li_{5.5}PS_{4.5}Cl_{1.5}$ in the presence of $114G_2$ agrees with the results reported for the composite electrolytes congaing $Li_{10}GeP_2S_{12}$ and $Li(G_3)_1TFSI$.[212]

The stability of Li deposition from hybrid $Li_{5.5}PS_{4.5}Cl_{1.5}/114G_2$ electrolyte was evaluated through cycling 2032 coin cells, the schematic design of which is shown in **Figure 5.8 A**. Since the density of the cold-pressed $Li_{5.5}PS_{4.5}Cl_{1.5}$ pellets typically is below 90 %, a layer of 3501 Celgard separator was placed on each side of the pellet to ensure that the solvate electrolyte does not squeeze into the pores of the SE pellet under pressure of ~ 0.1 MPa.

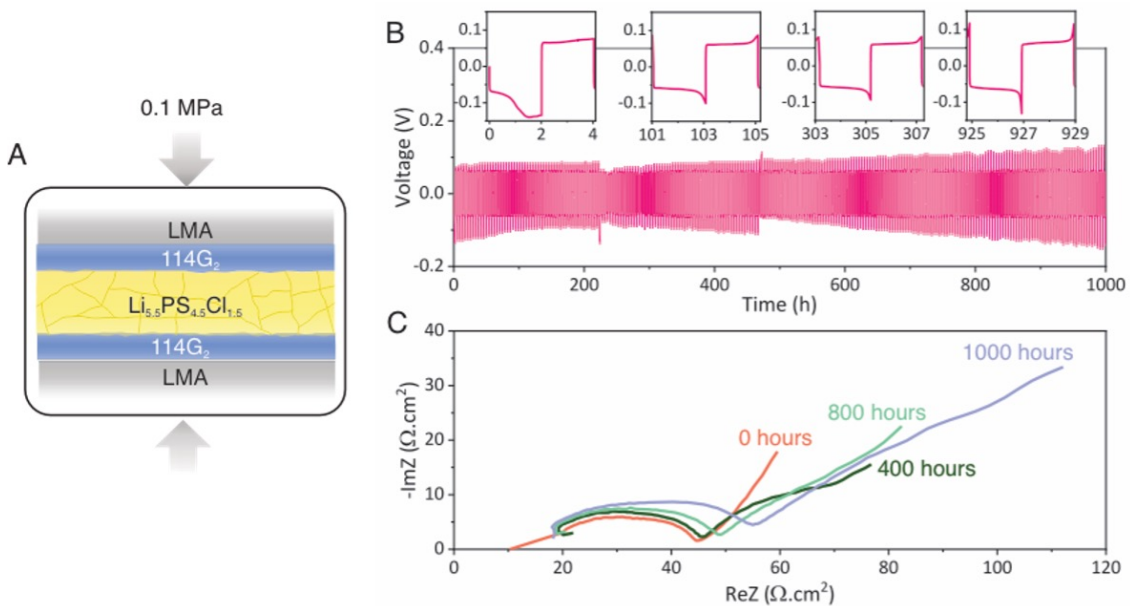


Figure 5.8 Performance of Li symmetric cells multilayer with $Li_{5.5}PS_{4.5}Cl_{1.5}$/114G2 hybrid electrolytes. (A) Schematic of the 2032 Li symmetric cell with hybrid $Li_{5.5}PS_{4.5}Cl_{1.5}/114G_2$ electrolyte. (B) Galvanostatic polarization of the Li symmetric cells at a current density of 0.5 $mA.cm^{-2}$ with a 1 $mAh.cm^{-2}$ capacity cutoff. The inset in (B) are the high-resolution voltage profiles at specific times. (C) The Nyquist plot of the Li symmetric cell acquired after 0, 400, 800, and 1000 hours of cycling.

The galvanostatic voltage profile of Li symmetric cells with $Li_{5.5}PS_{4.5}Cl_{1.5}$/114G2 hybrid electrolytes demonstrates the long-term cyclability of LMAs without any evidence of Li soft shorts (**Figure 5.8 B**). The cell maintains a stable overpotential of approximately 80 mV for 1000 hours. Since the available amount of Li is limited to 10 $mAh.cm^{-2}$, the lifetime of 1000 hours is equivalent to approximately 99 % CE. This demonstrates great chemical compatibility between LMAs, $114G_2$, and $Li_{5.5}PS_{4.5}Cl_{1.5}$. However, the voltage spikes at the end of each plating and stripping step appearing after cycling for 800 hours, indicate a limited stability of LMAs. The semicircle increase in **Figure 5.8 C** also suggests that the Li/$114G_2$ interphase growth is accelerated after 800 hours of continuous plating

and stripping. As a result, the electrochemical performance of LMAs is only temporarily improved by incorporating solvate interlayers.

5.5 Conclusions

This Chapter presents the case study of LMA stability in SS cells. The interfacial compatibility between LMAs and sulfide SEs was probed through cyclic voltammetry, EIS and galvanostatic cycling. It was demonstrated that if SEs contain a reducible semimetal or metal ion (i.e., Si^{4+} or Sn^{4+}), the LMA instability of these SEs is significantly enhanced and leads to noticeable lithium consumption. Overall, the observed LMA compatibility of the investigated SEs increase in order: $Li_{10.35}Sn_{0.27}Si_{1.08}P_{1.65}S_{12}$<$Li_{3.25}Si_{0.25}P_{0.75}S_4$<$Li_{5.5}PS_{4.5}Cl_{1.5}$< β-$Li_3PS_4$. Furthermore, β-$Li_3PS_4$ exhibits a high CE of Li deposition exceeding 99 %, although its rate capability is limited to 0.35 $mA.cm^{-2}$ at 25 °C and a pressure of 25 MPa.

The stability of SS cells with LMAs was improved by developing a sandwich electrolyte containing Li dendrite scavengers and wetting the Li/sulfidic SE interface with solvate electrolytes. Employing multilayer $Li_{10.35}Sn_{0.27}Si_{1.08}P_{1.65}S_{12}$/$Li_{5.5}PS_{4.5}Cl_{1.5}$ SEs extends the lifetime of Li symmetric cells from 7 hours to 275 hours when cycled at 0.5 $mA.cm^{-2}$ with a 1 $mAh.cm^{-2}$ capacity cutoff. Cycling Li||TiS_2 SSB cells with a capacity of 1.6 $mAh.cm^{-2}$ demonstrates that the introduction of $Li_{10.35}Sn_{0.27}Si_{1.08}P_{1.65}S_{12}$ scavengers temporarily suppresses Li dendrite propagation through sandwich SEs. However, the applicability of this approach is limited by 20-30 cycles.

Modifying the LMA/$Li_{5.5}PS_{4.5}Cl_{1.5}$ interface with a $114G_2$ interlayer improves the cyclability of Li symmetric cells to 1000 hours at 0.5 $mA.cm^{-2}$ (1 $mAh.cm^{-2}$) even when a Li reservoir is limited to 10 $mAh.cm^{-2}$. However, achieving excellent chemical compatibility is not enough to facilitate long-term Li cycling due to the slow diffusivity of Li^+ ions and Li atoms within the bulk solvate electrolytes and LMAs, respectively.

It is worth mentioning that I probed the stability of Li deposition at 25 °C, and the applied pressure was limited to 0.1 and 25 MPa. Meanwhile, recent studies demonstrate the improved performance of LMA when cycled at a pressure of 5 MPa.[213] Furthermore, my work did not include the modification of LMA to improve the diffusivity of Li. However, the efficacy of this approach was exemplified by the composite Ag/C composite anodes,[159] which leaves much space for further research.

Chapter 6
Interfacial Chemistry of Ta-doped LLZO in EPD Electrolytes

This chapter is adapted with permission from Surface Chemistry of LLZO Garnet electrolytes with Sulfur in Electron Pair Donor Solvents, Abhinandand Shyamsunder, Max Palmer, Ivan R. Kochetkov, Jeff Sakamoto and Linda F. Nazar, *ACS Applied Materials and Interfaces* **2023**, *15* (45), 52571-52580.
Copyright 2023 American Chemical Society.

6.1 Introduction

The Introduction details that Li-S batteries employing conventional DOL/DME electrolytes suffer from numerous challenges, such as the incomplete conversion of sulfur and limited kinetics at high concentrations of LPSs. Furthermore, designing Li-S batteries with an energy density exceeding 350 $Wh.kg^{-1}$ requires lowering the E/S ratio to 2.[214] This E/S ratio can be achieved if highly solvating electrolytes based on EPD solvents are employed. However, the severe reactivity between LMA and EPD electrolytes prevents the realization of this approach.[70] Therefore, there is an emerging call to develop novel Li-S batteries containing protected LMAs and EPD electrolytes.

In this Chapter, I report on the development of hybrid Li-S batteries employing an LMA protected with a Ta-substituted garnet SE, $Li_{6.5}La_3Ta_{0.5}Zr_{1.5}O_2$ (LLO), and an *N,N*-dimethylacetamide (DMA) liquid electrolyte. This work details the complex chemistry of LLZO is Li-S batteries with EPD electrolytes. Specifically, the interfacial reactivity between LLZO and sulfur in DMA is demonstrated through the combination of numerous characterization techniques. The instability of LLZO pellets originates from LiOH traces on their surface. LiOH catalyzes the oxidation of sulfur from the cathode, resulting in the formation of LPS. In turn, LPS react with LLZO, yielding a highly resistive layer comprised of thiosulfate, polythionate and La-O-S/La-S species. Meanwhile, a rapid reaction between H_3PO_4 and LLZO forms a thin layer with a low interfacial resistance of 40 $\Omega.cm^2$, which suppresses the side reactions. As a result, hybrid Li-S cells incorporating a phosphorylated LLZO and 1 M LiTFSI/DMA electrolyte deliver a high capacity of 1400 $mAh.g_S^{-1}$ and maintain almost a 100 % capacity retention throughout the cycling.

6.2 Experimental Methods

6.2.1 RAT of LLZO pellets

The pellets of $Li_{6.5}La_3Ta_{0.5}Zr_{1.5}O_2$ SE with a relative density of 98 % were supplied by M. Palmer (University of Michigan). Prior to shipping, the LLZTO pellets were heat treated at 400 °C for 3 h in an Ar-filled glovebox and sealed under Ar in an airtight container.

The LLZO pellets were immersed into freshly prepared 1 M HCl (Sigma-Aldrich) or 85 % H_3PO_4 (Sigma-Aldrich) for 30 s or 5 min, respectively. After that, the pellets were washed multiple times with acetone, dried with a heat gun, and immediately transferred to an Ar-filled box.

6.2.2 Preparation of Sulfur Cathodes

Firstly, 70 wt. % sulfur was hand-ground with 30 wt. % Ketjen Black (KB) carbon for 30 minutes. The well-ground mix was kept for 12 hours at 155 °C to allow the melt-infusion of sulfur into the pores of KB. The S_8/KB composite was mixed with Super P and PTFE binder (60 wt. % dispersion in water, Sigma-Aldrich) in isopropanol until an elastic rubber formed. The weight ratio between S_8/KB, Super P, and PTFE was 77:10:13. The obtained mixture was roll-casted onto a carbon-coated Al foil. The electrodes were dried overnight at 60 °C in the air. Finally, the electrodes were cut into 8 mm discs with a sulfur loading of approximately 3 $mg.cm^{-2}$.

6.2.3 Preparation of Sulfur Symmetric cells

The symmetric cells congaing LLZO, 1 M LiTFSI/DMA, and S_8-C electrodes were prepared using a modified Swagelok cell design. LLZO pellets were placed against an FFKM O-ring. After that, one ½'' diameter 3501 Celgard separator containing 30 µL electrolyte, and an S_8-C electrode were placed on one side of the LLZTO pellet. Another side of the LZTO pellet, placed against the O-ring, was interfaced with a 10 mm diameter 3501 Celgard separator containing 30 µL electrolyte and a S_8-C electrode. The cell was tightened between two Ti current collectors to a pressure of 3.4 MPa. The pressure was applied by a compressed Belleville washer.

The control symmetric cells (shown in **Figure 6.2 B**) were assembled following a similar procedure, except no LLZO was used. EIS was recorded between 1 MHz and 1 Hz with a 10 mV perturbation using a Biologic VMP3-1 potentiostat.

6.2.4 Preparation of Full Li||S cells

Li metal was interfaced against LLTO by hot-pressing at temperatures of 130-150 °C for 5 min at a pressure ranging between 0.5 and 1 MPa. The LMAs employed for cycling at 25 °C were prepared at the University of Michigan, while the LMAs employed for cycling at 50 °C were prepared at the University of Waterloo.

Next, Li/LLZO was incorporated into a Swagelok cell and sealed against the FFKM O-ring at 3.4 MPa following the abovementioned procedure. The other side of LLZO was contacted with an S_8-C electrode containing 20 μL of 1 M LiTFSI/DMA. P50 carbon paper was placed on the S_8-C electrode to improve the electric contact. The Li||S full cells were cycled at the University of Michigan within a voltage window of 1.8-2.9 V at 0.1 $mA.cm^{-2}$ (0.02 C) at 25 °C. Cycling at 50 °C was performed at the University of Waterloo at 0.5 $mA.cm^{-2}$ (0.1 C) and 1 $mA.cm^{-2}$ (0.2 C). The 50 °C cells were cycled between 1.7 and 2.6 V; the voltage was held at 2.6 V until the current decayed to 0.02 C.

6.2.5 XPS Analysis

XPS analysis was performed on a Thermo VG Scientific ESCALAB 250 instrument. The samples were transported to the measurement chamber under an Ar atmosphere. All spectra were fitted with Gaussian-Lorentzian functions and a Shirley-type background using CasaXPS software. The binding energy values were all calibrated using the C 1s peak at 284.8 eV. S*2p* and P2p peaks were fitted by sulfur doublets with an area ratio of 2:1 and a peak splitting of 1.18 eV and 0.86 eV, respectively. Zr 3d peaks were fitted with the $3d_{5/2}$ – 3 $d_{3/2}$ doublet with an area ratio of 3:2 and a splitting of 2.43 eV. The La 3d XPS was fitted with two sets of $3d_{5/2}$ – 3 $d_{3/2}$ doublets (main peaks and satellites). The full width at half maximum (FWHM) was identical for both spin-orbit coupling components of the peaks. For sputtering experiments, an X-ray spot size of 400 μm was sputtered using a 3kV Ar^+ ion beam over an area of about 1.5 mm x 1 mm at a rate of approximately 1 $nm.min^{-1}$.

6.2.6 UV-Vis Measurements

UV-Vis measurements were performed using a Thermo Scientifc Evolution 201 UV-Visible spectrophotometer in a 400-800 nm wavelength range. Quartz cuvettes with a path length of 1 mm were filled with the samples inside a glovebox.

6.3 High-energy-density Li-S Batteries with Hybrid LLZO/DMA Electrolytes

The theoretical energy density (ED) of a Li-S battery cell (**Figure 6.1 A**) can be estimated by using a simple model described by **Equation 6.1.**

$$ED_{\text{cell}} = \frac{\boldsymbol{Q \cdot V_{\text{cell}}}}{\boldsymbol{m_{\text{cell}}}} \qquad \textbf{Equation 6.1}$$

where Q is the areal capacity, V_{cell} is the average voltage, and m_{cell} is the total battery weight, including the electrodes, electrolytes, and current collectors.

To visualize the dependance of ED_{cell} on battery parameters, the ED-values were calculated by varying the thickness of LLZO and E/S ratio. **Figure 6.1 B** shows that Li-S batteries with LLZO/DMA achieve an energy density exceeding 300 Wh.kg^{-1} when thin LLZO membranes and high-capacity sulfur electrodes are employed. **Table 6.1** details the theoretical characteristics of a 345 Wh.kg^{-1} Li-S battery. It is noteworthy that achieving 345 Wh.kg^{-1} limits the thickness of LLZO to 30 µm if an areal capacity is 5 mAh.cm^{-2}. Since 5 mAh.cm^{-2} of Li is equivalent to a thickness of 25 µm, mechanical stresses and volume changes upon cycling must be considered to engineer long-term Li-S batteries. However, this work is focused on studying the solid-liquid electrolyte interface (SLEI) formed between LLZO and DMA-based electrolytes.

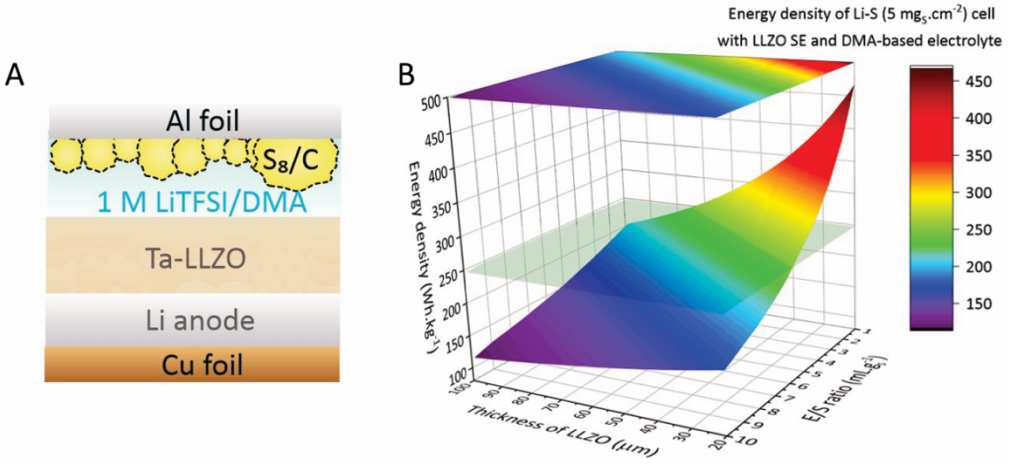


Figure 6.1 Energy density of Li-S batteries with LLZO/DMA electrolytes. (A) Schematic design of Li-S batteries with LLZO/DMA. (B) Dependance of the energy density on a thickness of LLZO and E/S ratio.

Table 6.1 Details of the 345 Wh.kg^{-1} Li-S battery with LLZO/DMA electrolyte

Parameter	**Value**
Areal S loading ($mg_S.cm^{-2}$)	5
Areal cathode capacity, ($mAh.cm^{-2}$) (80 % utilization of S)	6.7
E/S	2
Mass of DMA electrolyte (mg)	10
Mass of Li anode (20 % excess)	2.1
Thickness of SE (mm)	30
Mass of LLZO (mg)	15.3
Mass of 4 mm Cu and 8.5 mm Al (mg)	6.2
Total mass (mg)	42.7
Average voltage (V)	2.2
Energy (mWh)	14.7
Cell energy density (Wh.kg^{-1})	**345**

6.4 Reactivity Between LLZTO and S in EPD Electrolytes

The interfacial compatibility between LLZO and liquid electrolytes (LEs) was studied using EIS of sulfur symmetric cells. A Swagelok-type cell was modified with a perfluorinated O-ring to prevent electrolyte leakage (**Figure 6.1 A**). The cell design was adopted from Barchasz and co-workers[215] to eliminate the impedance contribution from the Li/LLZO interface. The S_8-C electrodes exhibit a very low impedance of 2 $\Omega.cm^2$ generated by electrical interparticle contact (**Figure 6.1 B, C**). To clean their surface, synthesized LLZO pellets were heat treated at 400 °C before the EIS measurements and labelled HT-LLZO.

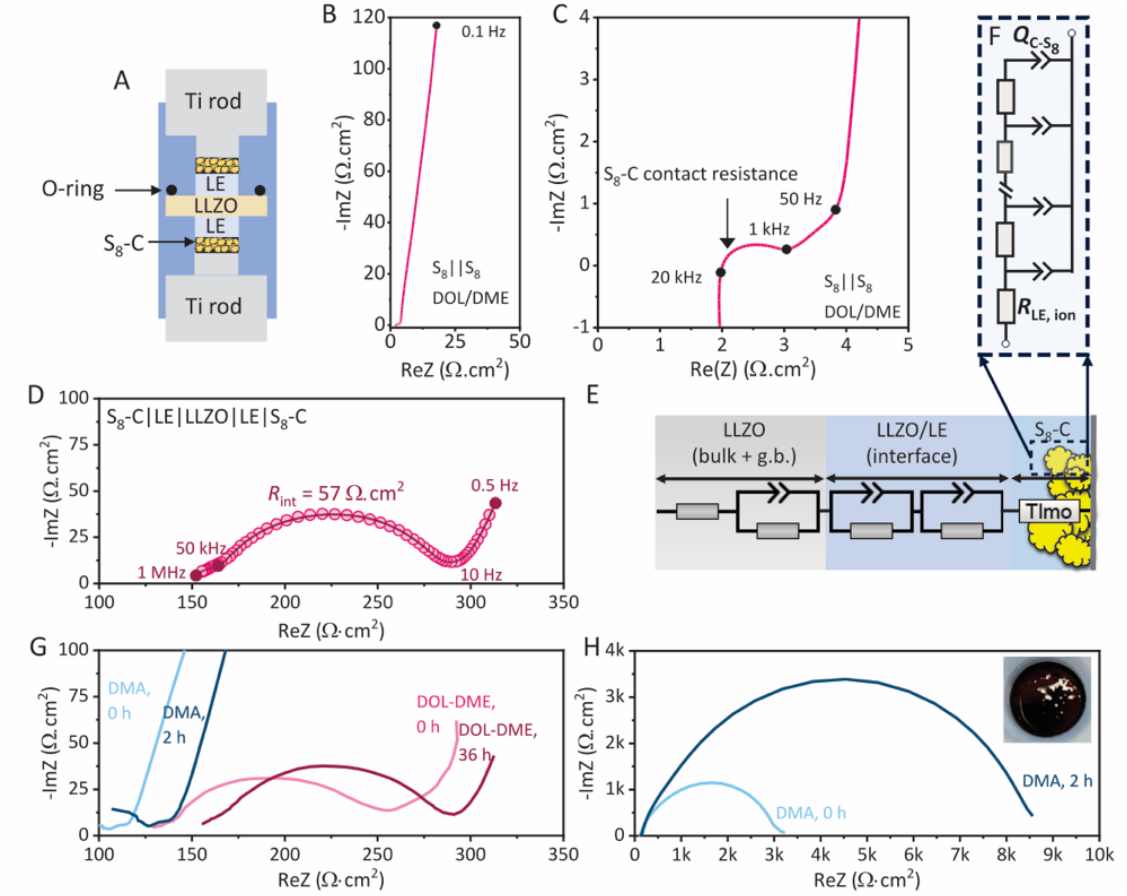


Figure 6.2 Instability of HT-LLZO in S/DMA. (A) Design of a modified Swagelok-type symmetric cell with hybrid LLZO/LE. Nyquist plots of symmetric cells with S_8-C electrodes and 1 M LiTFSI/DOL-DME electrolyte (B-C) without and (D) and with LLZO. (E) The equivalent circuit was used to fit the EIS data, and (F) TLM showing the capacitive behavior of S_8-C. (G, H) Change in Nyquist plot of the hybrid symmetric cells with LLZO/DOL-DME and LLZO/DMA during aging. The corresponding aging times are detailed in the plot.

A representative Nyquist plot of the symmetric cell with HT-LLZO and 1 M LiTFSI/DOL-DME electrolyte (**Figure 6.2 D**) consists of three frequency-separated regions. The plot is analyzed by employing the equivalent circuit adopted from the studies of other SLEIs (**Figure 6.2 E**).[210] The high-frequency portion of the spectrum (>50 kHz) comprises the bulk (R_{bulk}) and the grain boundary (R_{gb}) resistances of the LLZO membrane. As a result of the optimized processing of the membranes, the contribution of R_{gb} to the total resistance of LLZO does not exceed 5 %. The LLZO/LE interface is denoted by two depressed semicircles (R_1 and R_2) between 50 kHz and 10 Hz. These semicircles

represent the desolation of Li^+ ions and the transport of Li^+ across the SLEI interface, analogous to the charge transfer at the Li/LE interface. The resistance of a single LLZO/LE interface was calculated as a half sum of R_1 and R_2. The S_8-C electrodes contribute to the capacitive tail at a frequency below 10 Hz. The impedance of the S_8-C electrodes was fitted using the TLM with a reflective boundary condition (**Figure 6.2 F**).

The significantly different stability of the symmetric S_8-C cells in DOL-DME in comparison with that of the ones in DMA is shown in **Figure 6.2 G, H.** The cells with DOL-DME exhibit a low R_{int} of ~ 50 Ω.cm^2 that merely rises to ~ 58 Ω.cm^2 after 36 hours of storage. The observed behavior suggests that a stable LSEI between HT-LLZO and the DOL/DME electrolyte has formed. On the contrary, the SLEI between LLZO and DMA exhibits the rise in R_{int} from 1500 Ω.cm^2 to 11000 Ω.cm^2 after 12 hours of aging. Postmortem examination of the symmetric cells with LLZO/DMA demonstrates the coloration of DMA. In combination with a 7-fold increase in R_{int}, this suggests that LLZO reacts with sulfur in DMA.

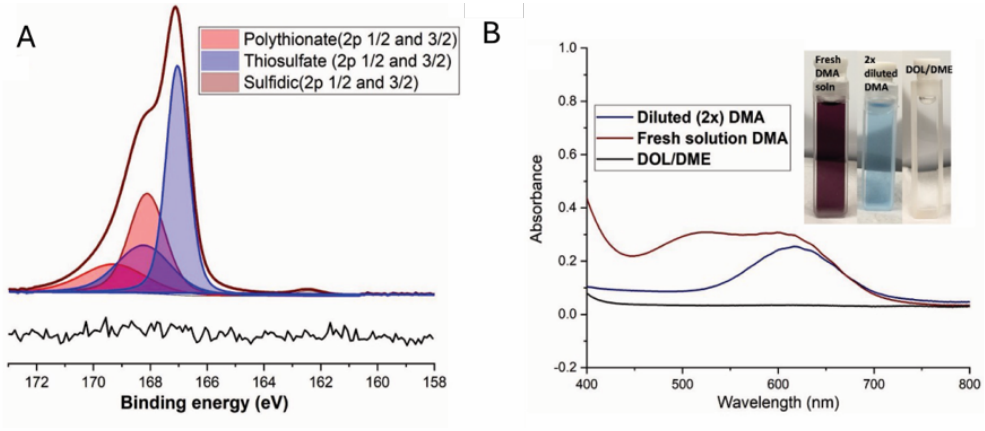


Figure 6.3 LLZO-triggered formation of $S_3^{\cdot-}$. (A) S 2p spectra of HT-LLZO extracted from the DMA (burgundy) and DOL/DME (black) cells showing the presence of sulfur impurities after aging in DMA. (B) UV-vis spectra of the burgundy liquid extracted from the DMA cell (wine), blue liquid (blue) obtained by diluting the burgundy liquid and the DOL-DME electrolyte (black) extracted from the control cell.

To understand the reactivity between LLZO and sulfur in DMA, the HT-LLZO pellet and the electrolyte from the DMA cell were analyzed, respectively, by XPS and UV-Vis spectroscopy. The S *2p* XPS reveals the precipitation of thiosulfate ($2p_{1/2}$-$2p_{3/2}$ at 168.2-167.0 eV) and polythionate ($2p_{1/2}$-$2p_{3/2}$ at 169.3-168.1 eV) along with the minute amounts of reduced sulfur species ($2p_{1/2}$-$2p_{3/2}$ at 163.6-162.4 eV) (**Figure 6.3 A**). In contrast, the S *2p* XPS of HT-LLZO stored in DOL/DME is devoid of any sulfur contaminants. The UV-vis spectrum of the DMA electrolyte collected from the mixture of LLZO and sulfur exhibits a broad band between 400 and 700 nm due to the formation of two overlapping peaks at 510 and 620 nm (**Figure 6.3 B)**. These peaks indicate the presence of the S_6^{2-} anion (510 nm) and $S_3^{\cdot-}$ radical (620 nm)[216,] responsible for the burgundy coloration DMA. Furthermore, if the solution is diluted with more DMA, the resultant pale blue solution contains only $S_3^{\cdot-}$ due to the equilibrium shift. Meanwhile, the electrolyte extracted from the control DOL/DME cell contains no detectable LPS.

Despite the heat treatment, the surface of HT-LLZTO contains LiOH and Li_2CO_3 traces.[217] When a DMA-containing electrolyte is utilized, the dissolution of LiOH triggers the oxidation of sulfur from the cathode, yielding $S_3^{\cdot-}$ and H_2O_2.[218] Subsequently, $S_3^{\cdot-}$ undergoes redox reactions with elemental sulfur from the cathode and generated H_2O_2 to form the species detected by S *2p* XPS (**Figure 6.3 C)**. These possible reaction pathways of $S_3^{\cdot-}$ were proposed by A. Shyamsunder, and the additional details of the mechanism including the NMR measurements can be found in our publication (*ACS Appl. Mater. Interfaces* 2023, 15, 45, 52571-52580).

6.5 Interfacial Reactivity between Acid-treated LLZO SEs and Sulfur in DMA

Since the reactivity between HT-LLZO and sulfur from the cathodes in DMA is catalyzed by LiOH and Li_2CO_3 surface impurities, HT-LLZO was treated with 1 M HCl to produce a surface-clean LLZO (denoted as HCl-LLZO). In this work, the rapid acid treatment of LLZO with HCl is denoted as HCl-RAT. Previously, this strategy was employed by Huo and co-workers to improve the wetting at the Li/LLZO interface.[219]

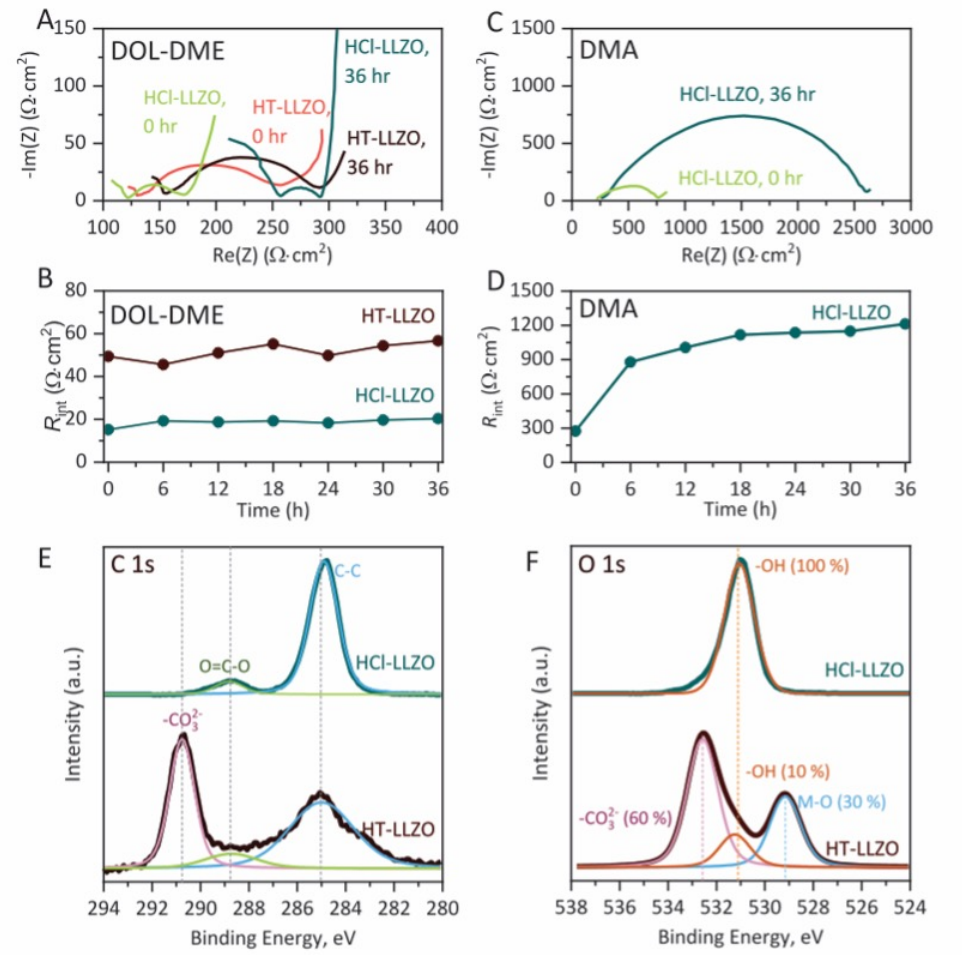


Figure 6.4 Effect of HCl-RAT on the surface chemistry of LLZO. (A) Nyquist plot of the sulfur symmetric cells with HT-LLZO (0 h – peach, 36 h -brown) and HCl-LLZO (0 h -light green, 36 h - cyan) in DOL-DME, and (B) change in R_{int} upon the storage for 36 h. (C) Nyquist plot of the symmetric cells with HCl-LLZO in DMA (0 h -light green, 36 h - cyan) and (D) change in R_{int} upon the storage for 36 h. (E) C 1s and (F) O 1s spectra of HT-LLZO after 10 min of Ar^+ sputtering (bottom panel) and HCl-LLZO (top panel). The deconvolution of the XPS spectra is detailed in the figure.

The Nyquist plot of the symmetric sulfur cells containing HCl-LLZO in DOL/DME demonstrates the efficacy of HCl-RAT. Indeed, HCl-RAT lowers the R_{int} from 50 (HT-LLZO) to 15 $\Omega.cm^{-2}$ (HCl-LLZO) (**Figure 6.4 A**). Since the reactivity between HT-LLZO and sulfur in DOL/DME is negligible, this improvement is attributed to the increase in the LLZO/electrolyte contact area. The temporal evolution of R_{int} between LLZO and sulfur in DOL/DME is not affected by HCl-RAT, which provides further confirmation that LiOH and Li_2CO_3 trace do not catalyze the surface reactions of

LLZO (**Figure 6.4 B**). However, the opposite is observed in the case of cells with DMA. Although HCl-RAT effectively decreases the R_{int} of the assembled from 1500 to 300 $\Omega.cm^{-2}$, it fails to inhibit the interfacial reactivity of HCl-LLZO, as indicated by a 4-fold increase in R_{int} after 36 hours of storage. Furthermore, the initial R_{int} observed for the cell with HCl-LLZO in DMA is 20 times higher than that in DOL/DME. This suggests that HCl-LLZO fails to entirely eliminate LiOH from the LLZO surface, as confirmed by XPS studies.

The C 1s spectra of HT-LLZO and HCl-LLZO are shown in **Figure 6.4 E.** The presence of Li_2CO_3 is clear in the XPS spectrum of HT-LLZO, although the sample was sputtered for 10 minutes with Ar plasma. On the other hand, the removal of Li_2CO_3 with HCl-RAT is proven by the absence of the peak at 291 eV in the spectrum of HCl-LLZO. The O 1s spectra of LLZO are more complex since they contain three major features assigned to Li_2CO_3 (532.6 eV), LiOH (531.3 eV), and the LLZO lattice oxygen (529.2 eV).[217] The surface of HT-LLZO is covered with Li_2CO_3 and LiOH, which contribute to 15 and 85 % of the oxygen signal, respectively (**Table 6.2**). However, the fraction of LiOH drops to 10 %, and the lattice oxygen appears at a level of 30 % after 10 minutes of sputtering. The minute amounts of LiOH and Li_2CO_3 are present on the surface of HT-LLZO even after 30 minutes of sputtering and contribute to 10 and 30 % of the total signal, respectively.

Table 6.2 Chemical composition of the LLZO surface. Distribution of oxygen species in the surface layer of the HT-LLZO and HCl-LLZO before and after sputtering with Ar^+ plasma.

	HT-LLZO			HCl-LLZO		
	0 min	10 min	30 min	0 min	10 min	20 min
Lattice O (%)	0	30	50	0	20	40
LiOH (%)	85	10	10	100	80	60
Li_2CO_3 (%)	15	60	40	0	0	0

The O 1s spectrum of HCl-LLZO reveals the different distribution between the oxygen-containing species. While Li_2CO_3 is removed by HCl-RAT, LiOH impurities are still present at the surface. Furthermore, the concentration of LiOH exceeds 60 % even after 20 minutes of sputtering (Table 6.1). Therefore, HCl-RAT promotes the growth of LiOH into the native LLZO. This phenomenon could be attributed to the Li^+/H^+ exchange reaction: HCl removes LiOH from the surface, but it is regenerated as Li^+ from the lattice exchanges with H^+. As a result, although the surface of HCl-LLZO is devoid of Li_2CO_3, it remains contaminated with LiOH, which results in the instability of the symmetric cells with S_8-C and DMA.

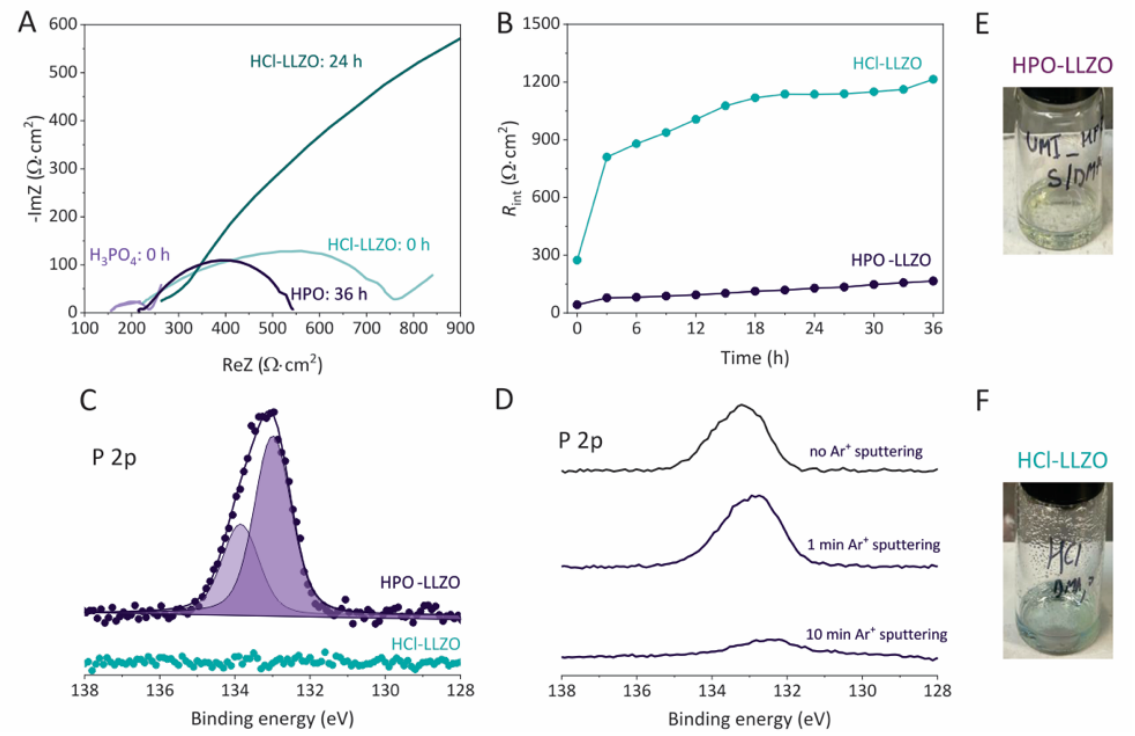


Figure 6.5 Stability of HPO-LLZO. (A) Nyquist plot of the assembled symmetric cells with HPO-LLZO (purple), and HCl-LLZO (cyan) before and after aging the cells for 36 hours. (B) Change in R_{int} of the cells from (A) during aging for 36 hours. (C) 2p P XPS of HPO-LZZO (purple) and HCl-LLZO (cyan). (D) Changes in the P 2p XPS of HPO-LLZO during Ar^+ sputtering (E, F) Different reactivity of S_8/DMA suspension with HCl-LLZO and HPO-LLZO.

A rapid reaction between HT-LLZO and H_3PO_4 (denoted as HPO-LLZO) is a more efficient strategy to tune the garnet surface composition. The Nyquist plot of the sulfur symmetric cell with HPO-LLZO in DMA demonstrates a 7.5-fold decrease from 300 $\Omega.cm^{-2}$ (HCl-LLZO) to 40 $\Omega.cm^{-2}$

(**Figure 6.4 A**). Although the R_{int} of HPO-LLZO merely increases on storage, it remains below that of HCl-LLZO immediately after cell assembly (**Figure 6.4 B**). The low interfacial impedance of HPO-LLZO demonstrates that HPO-RAT yields a stable SLEI. The surface phosphorylation is confirmed by the P 2p XPS spectrum of HPO-LLZO (**Figure 6.4 C**). The P-containing layer is approximately 10 nm because the P 2p signal almost vanishes after 10 minutes of Ar^+ sputtering (**Figure 6.4 D**). The ionic conductivity of Li_3PO_4 in its amorphous state (10^{-6}-10^{-8} $S.cm^{-1}$)[220,221] is sufficient to facilitate the transport of Li^+ across the 10 nm coating layer.

The better stability of phosphorylated LLZO is visualized by storing the garnet pellets in a sulfur DMA/suspension. While HCl-LLZO triggers the coloration after one hour of storage, the DMA suspension containing HPO-LLZO remains colorless. Consequently, HPO-RAT yields a phosphorylated Li^+-conducting coating layer, thus stabilizing the SLEI interface formed between LLZO and S/DMA.

6.6 XPS Study of Reactivity between RAT-LLZO and S in DMA

The improved stability of the SLEI between HPO-LLZO and sulfur in DMA is also confirmed by the XPS investigation of the acid-treated LLZO pellets extracted from the DMA cells. The S 2p spectra confirm that HPO-LLZO does not catalyze the oxidation of sulfur while the surface of HCl-LLZO is contaminated with Li_2S, $Li_2S_2O_3$ and $Li_2S_4O_6$ after being stored in the S/DMA suspension for 48 hours (**Figure 6.5 A**). La and Zr 3d XPS provide further insight into the better performance of HPO-LLZO. HPO-RAT converts some of the surface Zr^{4+} and La^{3+} to their phosphates, which is evidenced by the appearance of the additional doublets at 181.7 and 184.3 eV (**Figure 6.5 B**) and 851.8 and 853.0 eV (**Figure 6.5 C**), respectively. Meanwhile, La and Zr 3d spectra of HCl LLZO exhibit a single Zr doublet and a set of two La 3d doublets separated by 16.8 eV, consistent with the previous reports.[222] The phosphorylation of 40 % surface Zr and La significantly improves the stability of HPO-LLZO. In its absence, La^{3+} reacts with LPSs, as demonstrated by the appearance of the new set of peaks at lower binding energy in **Figure 6.5 C**. Interestingly, the reactivity of surface La^{3+} with LPS contrasts with the stability of Zr^{4+}. The La 3d XPS demonstrates the precipitation of ionically resistive La-S/La-O-S species on the surface of HCl-LLZO, which increases the interfacial resistance. It is worth mentioning

that the observed reactivity between the surface La^{3+} and LPS, resulting in the formation of La-S species and La_2O_3, also occurs during cycling Li-S cells with untreated LLZO in DOL/DME.[223,224]

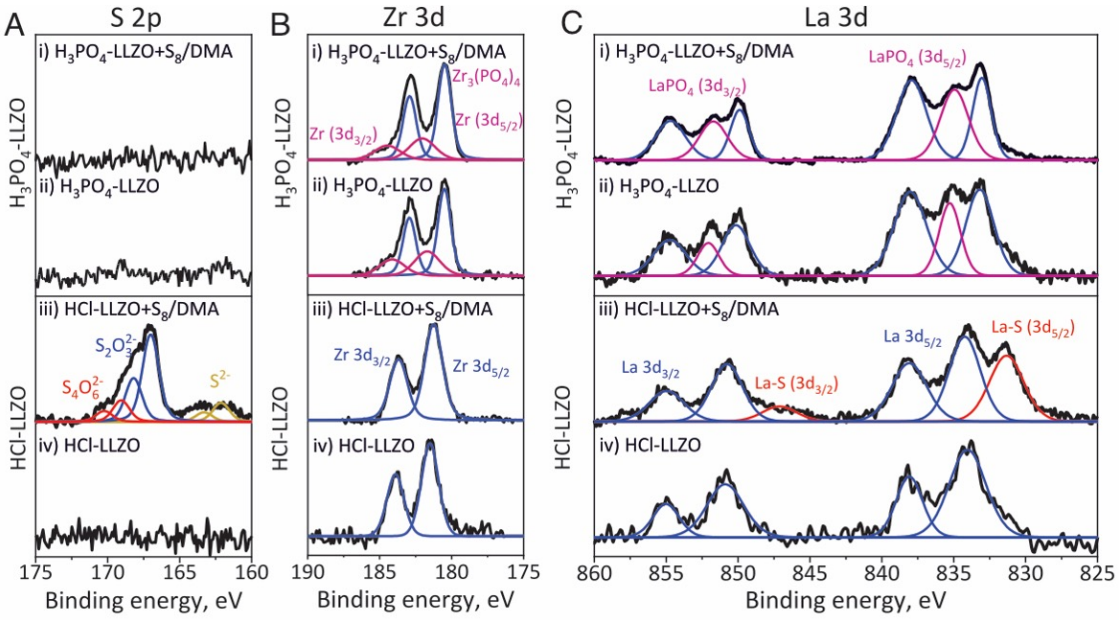


Figure 6.6 RAT-dependent interfacial stability of LLZO. (A) S 2p, (B) Zr 3d, (C) La 3d XPS spectra of HPO-LLZO (i) before and (ii) after reacting with S8/DMA suspension. The bottom panels represent HCl-LLZO (iii) before and (iv) after the similar reaction with S_8/DMA suspension. The deconvolution legend for each spectrum is detailed in the plot.

6.7 Electrochemical Performance of Li-S Batteries with LLZO/DMA

The applicability of our approach of stabilizing the SLEI between LLZO and S/DMA was assessed by cycling the Li||S_8 batteries at 25 and 50 °C. Since this work primarily focuses on the interfacial chemistry of LLZO, we employed a simple S_8-C cathode with a PTFE binder and a sulfur loading of 3 $mg.cm^{-2}$. Due the formation of voids at the Li/LLZO interface while discharging lithium batteries,[225] the room-temperature cells were cycled at a low current density of 0.1 $mA.cm^{-2}$. The electrochemical performance of the full cells containing HCl-LLZO and HPO-LLZO at 25 °C is summarized in **Figure 6.6 A, B**. The difference in polarization of the cells with HCl-LLZO and HPO-LLZO highlights the higher efficacy of HPO-RAT. While the Li||S_8 cell with HPO-LLZO exhibits overlapping voltage profiles of the 1st and the 5th cycles, the full cell with HCl-LLZO suffers from a pronounced polarization increase after 5 cycles. Comparing the capacity retention of Li-S batteres demonstrates that the cell with HPO-LLZO maintains a very high capacity of ~ 1400 $mAh.g^{-1}$ for 10 cycles, whereas the one with

HCl-LLZO loses approximately 50 $mAh.g^{-1}$ per cycle and retains only ~ 610 $mAh.g^{-1}$ after 10 cycles. This proves that phosphorylation of LLZO creates an efficient protective coating, which suppresses surface passivation even when cathodic redox reactions continuously regenerate LPS. In contrast, the LiOH-contaminated surface of HCl-LLZO triggers continuous LSEI growth, which increase the polarization and consumes electrochemically active LPS.

XPS analysis of the cycled HPO-LLZO confirms that its surface is free of any decomposition products. In particular, this is proven by the fact that La (**Figure 6.6 C**) and P (**Figure 6.6 D**) are detected on the pellet without Ar^{+} sputtering. Furthermore, the absence of peaks in the S 2p XPS spectrum indicates that the surface La^{3+} ions do not react with the LPS.

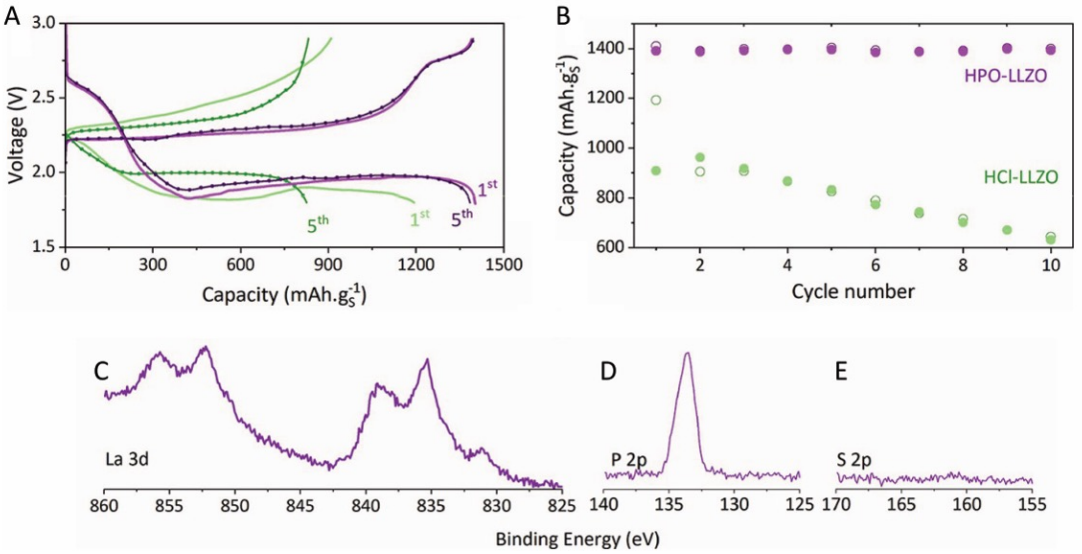


Figure 6.7 Room temperature performance of Li-S batteries with LLZO/DMA. (A) Galvanostatic polarization of the Li||S8-C cells with HPO-LLZO/DMA (purple) and HCl-LLZO/DMA (green) at a current density of 0.1 $mA.cm^{-2}$ (25 °C). The light-colored lines show the 1st cycle while the dark-colored lines denote the 5th cycle. (B) Evolution of the discharge (open cycles) and charge (filled circles) capacity delivered by the cells with HPO-LLZO/DMA (purple) and HCl-LLZO/DMA (green). (C) La 3d, (D) P 2p, and (E) S 2p XPS spectra of the cycled HPO-LLZO pellet.

It is important to note that full Li||S_8-C cells with HPO-LLZO maintain a high and stable capacity of 1400 mAh.g^{-1} although they employ very simple carbon-based cathodes. This suggests that the S_8↔Li_2S conversion is efficient when a current density is 0.1 mA.cm^{-2}. However, this current density is equivalent to a C-rate of 0.02, which is too low for practical Li-S batteries. To probe the battery performance under higher C-rates, we had to cycle the full Li||S_8-C with HPO-LLZO/DMA at 50 °C. We note that the rise in cycling temperature is required to improve the dynamic stability of the Li/LLZO interface when 2-3 mAh.cm^{-2} of Li are cycled. **Figure 6.8** shows the battery performance under higher C-rates.

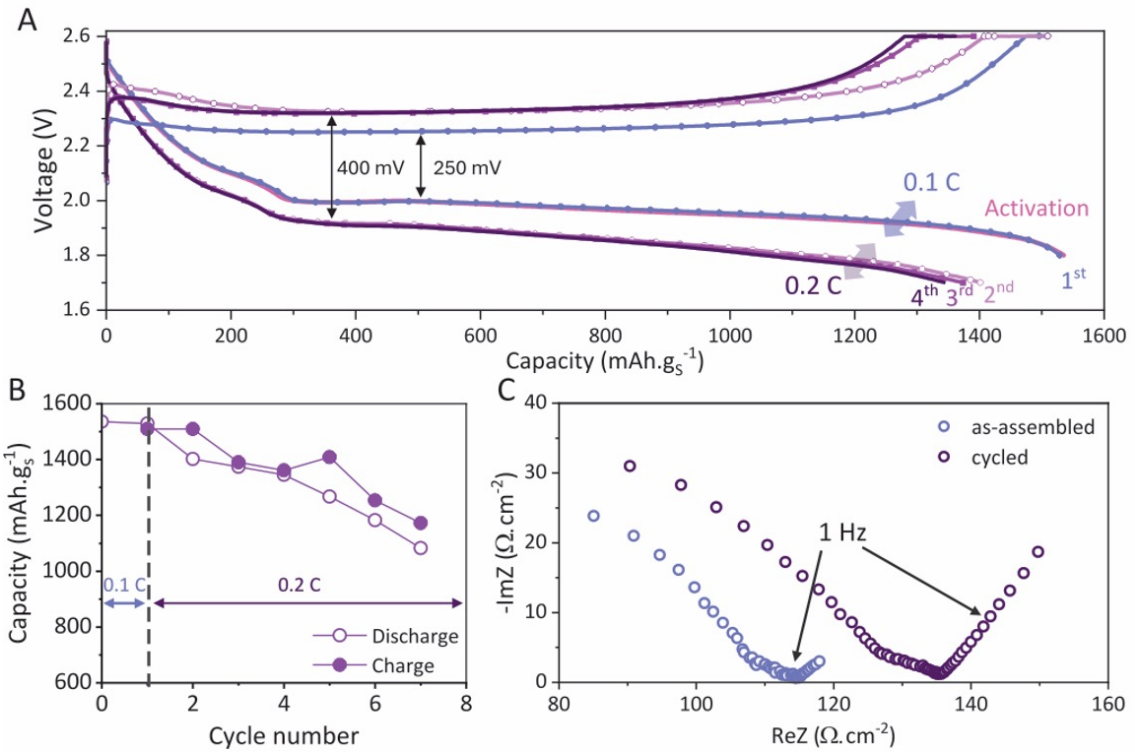


Figure 6.8 Cycling Li-S batteries with LLZO/DMA at higher C-rates. (A) Polarization of the full Li||S_8-C cells with HPO-LLZO/DMA cycled at 50 °C at the rates of 0.1 and 0.2 C, equivalent to 0.5 and 1 mA.cm^{-2}, respectively. (B) Discharge (open circles) and charge (filled circles) capacity of the cell shown in (A). (C) Nyquist plot of the cell before (grey blue) and after (purple) cycling at 50 °C. The EIS spectra were recorded at the charged state between 3 MHz and 200 mHz.

The cell was initially discharged at 0.1 C (0.5 mA.cm^{-2}), delivering almost 1535 mAh.g^{-1} of capacity (**Figure 6.8 A**). After that, the cell underwent a complete charge-discharge cycle at 0.1 C and

delivered a similar capacity of 1530 $mAh.g^{-1}$. The high capacity retention and overlapping voltage profiles between the activation and the 1st cycles indicate excellent initial reversibility at 0.1 C rate. The rise in current to 0.2 C (1 $mA.cm^{-2}$) increases the overpotential from 250 mV to 400 mV and lowers the discharge capacity to 1400 $mAh.g^{-1}$. The subsequent cycling at 0.2 C occurs with a capacity decay of 60 $mAh.g^{-1}$ per cycle, as shown in **Figure 6.8 B**. The change in the Nyquist (**Figure 6.8 C**) observed for the cycled cell suggests that the capacity fading at 0.2 C could be ascribed to the formation of voids at the Li/LLZO interface when high Li amounts are cycled at high current densities.[225]

6.8 Conclusions

This work, for the first time, demonstrates the complex interfacial chemistry between Ta-doped LLZO garnet solid electrolyte in an EPD solvent (DMA). Due to LiOH and Li_2CO_3 surface impurities, synthesized LLZO triggers the reduction of sulfur in DMA, which produces a highly reactive $S_3^{\cdot-}$ radical. $S_3^{\cdot-}$ undergoes a series of chemical reactions, yielding an insulating LSEI with an areal resistance above 5000 $\Omega.cm^2$. XPS analysis demonstrates that the interphase consists of thiosulfate, polythionate and La-S/La-O-S species. However, phosphorylation of LLZO by a rapid reaction with phosphoric acid creates a 10 nm Li^+-conducting layer, which lowers the interfacial resistance to 40 $\Omega.cm^2$ and suppresses the reactivity of LLZO.

Li-S batteries with phosphorylated LLZO and a cathode loading of 3 $mg_S.cm^{-2}$ exhibit a very high sulfur utilization of 1400 $mAh.g^{-1}$ at 25 °C and 1530 $mAh.g^{-1}$ at 50 °C, although the cells employed very simple carbon-based cathodes. In contrast, control cells with non-phosphorylated LLZO deliver a lower capacity of 1200 $mAh.g^{-1}$ and suffer from a capacity fade of 50 $mAh.g^{-1}$ per cycle at 25 °C. The electrochemical performance of Li-S batteries at a current density of 1 $mA.cm^{-2}$ suggests that future research should be focused on improving the Li/LLZO interface.

Chapter 7

Interfacial Reactivity Between Lithium Metal Chloride Electrolytes and High-energy Density NCM

This chapter is adapted with permission from Different Interfacial Reactivity of Lithium Metal Chloride Electrolytes with High Voltage Cathodes Determines Solid-State Battery Performance, Ivan R. Kochetkov, Tong-Tong Zuo, Raffael Ruess, Baltej Singh, Laidong Zhou, Kavish Kaup, Jürgen Janek and Linda F. Nazar. *Energy and Environmental Science* 2022, **15**, 3933-3944. Copyrights: The Royal Society of Chemistry 2022.

7.1 Introduction

As SOA LIBs with liquid electrolytes are approaching their theoretical energy density, the development of SSBs becomes one of the most promising strategies to meet ever-growing demand for rechargeable batteries with lower safety risks and higher energy density. As discussed in Chapter 1, 4 V CAMs containing highly conductive sulfidic SEs often exhibit a rapid capacity decay triggered by the chemical and electrochemical decomposition of sulfiude SEs. Protective coatings of CAMs [169–171] may overcome this challenge at the expense of higher potential manufacturing costs. On the other hand, replacing sulfide SEs with those containing a chloride anion sublattice is a more promising strategy due to the higher thermodynamic oxidation potential of 4.2-4.3 V vs. Li^+/Li.[172]

Since 2018, when Asano *et al.* discovered that trigonal Li_3YCl_6 exhibits a room temperature ionic conductivity of 0.5 $mS.cm^{-1}$,[137] the development of a new class of lithium metal chloride (Li-M-Cl) SEs has been receiving rapidly growing attention. Although significant progress has been achieved in improving the ionic conductivity to the values of 1-2 $mS.cm^{-1}$ at room temperature,[138–145] the performance of chloride SEs in SSBs containing Ni-rich NCM differs significantly. For example, the CAMs based on $LiNi_{0.85}Co_{0.1}Mn_{0.05}O_2$ exhibit excellent cycling performance for several hundred cycles when the SSB cells employ $Li_2Sc_{2/3}Cl_4$[140] or $Li_2In_{1/3}Sc_{1/3}Cl_4$[145] chlorospinel SEs as catholytes. However, the SSB cells employing $LiNi_{0.83}Co_{0.12}Mn_{0.05}O_2$-$Li_{2.5}Yb_{0.5}Zr_{0.5}Cl_6$[141] and $LiNi_{0.6}Co_{0.2}Mn_{0.2}O_2$-$Li_{2.5}Yb_{0.5}Zr_{0.5}Cl_6$[222] CAMs exhibit a noticeable capacity decay within the first 100 cycles despite the lower nickel content.

In this Chapter, I report on the systematic instigation which details the relationship between central metal cations $M^{3+/4+}$ in Li-M-Cl chloride SEs and the cycling performance of SSB cells employing $LiNi_{0.85}Co_{0.1}Mn_{0.05}O_2$ (NCM 85) high-energy-density CAM. The important role of $M^{3+/4+}$ is exemplified by three chloride SEs: Li_3InCl_6 (*LIC*), $Li_{2.5}Y_{0.5}Zr_{0.5}Cl_6$ (*LYZC*), and $Li_2In_{1/3}Sc_{1/3}Cl_4$ (*LSIC*). These SEs exhibit a similar room temperature ionic conductivity of 1-2 $mS.cm^{-1}$ and well-known crystal structures, which make them the perfect candidates to elucidate the role of M. Furthermore, these electrolytes are practically interesting due to their unique properties. In particular, *LSIC* enables stable cycling of the SSBs cells employing NCM85[31] and *LYZC* is cost-effective since it contains cheap and abundant Zr.[23] This work compares the chemical and electrochemical stability of the selected SEs and relates that to the cycling performance of the SSB cells employing LIC, LYZC, and LSIC as catholytes. By combining galvanostatic cycling and EIS, I demonstrate that the excellent capacity retention of the SSB cells containing NCM85-*LSIC* CAM is dictated by the stability of CEI formed between NCM85 and *LSIC*. Meanwhile, the interface formed between NCM85 and *LYZC* continuously grows, thus resulting in the capacity fading of SSB cells containing NCM85-*LYZC.* The NCM85 instability of *LYZC* is caused by the OER occurring when NCM85 is charged above 4.2 V, as proven by the ToF-SIMS study of NCM85 CAMs and by the cycling performance of SSB cells with $LiNi_{1/3}Co_{1/3}Mn_{1/3}O_2$ (NCM 111). Furthermore, this hypothesis was verified with DFT calculation, which verified that the interfacial reactivity between NCM85 and *LYZC* is thermodynamically favourable due to the formation of YOCl and ZrO_2.

7.2 Experimental methods

7.2.1 Synthesis of the SEs

Chloride SEs were synthesized by the solid-state reactions in an A-filled box ($p(O_2)/p < 0.5$ ppm, $p(H_2O)/p < 0.5$ ppm). LYZC and LSIC were synthesized following the previously reported procedures. In the case of LIC, the stochiometric amounts of LiCl (Sigma-Aldrich, 99.9%) and $InCl_3$ (Sigma-Aldrich, 99.99%) were hand-ground and sealed in a quartz tube under vacuum. The samples were heated to 450 °C at a rate of 5 $°C.min^{-1}$, kept at 450 °C for 48 hours and cooled to 25 °C at 1 $°C.min^{-1}$. Cl-rich argyrodite SE ($Li_{5.5}PS_{4.5}Cl_{1.5}$) was synthesized by a solid-state reaction at 550 °C for 48 hours with the heating and cooling rated of 5 $°C.min^{-1}$.

7.2.2 Assembly of SSB Cells and Electrochemical Measurements

The SSB cells were assembled in an Ar-filled glovebox following a similar protocol, as detailed in Chapter 5. In brief, the CAMs containing $LiNi_{0.85}Co_{0.1}Mn_{0.05}O_2$ (NCM85, BASF, D_{50} = 5 μm) or $LiNi_{1/3}Co_{1/3}Mn_{1/3}O_2$ (NCM111, NEI Corporation, D_{50} = 8 - 12 μm) and Li-M-Cl SEs were hand-ground for 1 hour in a weight ratio of 4:1. The CAMs (6.5-7.5 mg) were evenly spread over the $Li_{5.5}PS_{4.5}Cl_{1.5}$/Chloride SE bilayer pellet and pressed at 2 T for 5 min. Approximately 70 mg of $Li_{5.5}PS_{4.5}Cl_{1.5}$ and 40 mg of Li-M-Cl were used. Finally, a 10 mm In (100 μm thick) and an 8 mm 50 μm Li on Cu (China Lithium Energy) were attached to the $Li_{5.5}PS_{4.5}Cl_{1.5}$ side of the SE, and the SSB cells were tightened in home-made stainless steel cages to a constantly applied pressure of ~ 250 MPa.

The SSB cells were cycled within the voltage windows of 2.08 – 3.68 V and 2.08 – 3.98 V vs. In/InLi at 0.2 C (1 C = 200 $mA.g^{-1}$). The voltage vs. In/InLi was converted to the voltage vs. Li^+/Li by adding 0.62 for a more comprehensive illustration.

The EIS of the SSB cells was recorded between 1 MHz and 100 mHz with a voltage amplitude of 10 mV. In the case of in-situ EIS, the cells were held at 3.8 V vs. Li^+/Li every charge (0.01 C current cutoff) before the data acquisition. A similar constant current–constant voltage charging protocol was followed in the aging experiments. After charging to the cutoff voltage (4.1, 4.3, or 4.6 V vs. Li^+/Li), the SSB cells were aged for 30 hours, with EIS recorded hourly.

The oxidative stability of a chloride SE was determined by CV of SSB cells employing a carbon-SE composite as a working electrode and an In anode. The cells for CV were assembled similarly to the SSB full cells. The carbon-SE electrodes were prepared by hand-grinding 10 wt. % of C65 carbon (MTI) with 90 wt.% of chloride SE. The cells were cycled by stepwise CV between 2.7 V vs. Li^+/Li and a gradually increasing cutoff voltage at a scan rate of 0.1 $mV.s^{-1}$. Initially, the cells were cycled twice up to 4.1 V vs. Li^+/Li. After that, the cutoff voltage was raised to 4.3 and, finally, 4.6 V vs. Li^+/Li. The last scans to 4.6 V vs. Li^+/Li were analyzed to assess the SEs' oxidative stability.

7.2.3 UPS Measurements of Chloride SEs

UPS measurements of Li-M-Cl SE were conducted at the University of Giessen (Germany) by Dr. Raffael Ruess. In brief, an SE powder was dispersed in xylene and screen-printed on Al foil. The printed SE was densified at 100 MPa, yielding a thin film. The samples were loaded to a photoelectron chamber

without air exposure. UPS was carried out on a PHI5000 Versa Probe II system (Physical Electronics Inc) equipped with a He-Iα source (21.22 eV).

7.2.4 FIB-SEM

FIB-SEM images of SSB cathodes were recorded on a XEIA3 system (Tescan) at the University of Giessen (Germany). Prior to the measurement, the cathodes were covered by a copper tape to ensure a flat surface and reduce the curtaining effect. Cross-sections were cut by a 2.5 µA Xe-ion beam and polished with a 0.1 µA Xe-ion beam. SEM was performed on these cross-sections by probing with a 5 kV, 500 pA electron beam and detecting the backscattered electrons with an in-beam detector.

7.2.5 ToF-SIMs

The ToF-SIMS measurements and data processing were performed by Dr. Tong-Tong Zuo (University of Giessen). The detailed experimental procedure can be found in our publication (*Energy and Environmental Science* **2022**, *15*, 3933-3944). In brief, the CAM samples were transferred from the University of Waterloo to the University of Giessen under an argon atmosphere. Then, the samples were attached to a sample holder and moved to the ToF-SIMS instrument without air exposure. ToF-SIMS characterization was performed using a ToF-SIMS 5-100 system (IONTOF GmbH) equipped with a 25 keV Bi cluster primary ion gun for analysis. The analyzed area was set to 150 × 150 μm^2, and at least 10 mass spectra were collected at different regions of each sample. The ToF-SIMS data was analyzed with SurfaceLab 7.0 (IONTOF GmbH) software.

7.2.6 DFT Calculations

The DFT calculations of the interfacial reactivity between Li-M-Cl and Li_xNiO_2 were performed by D. B. Singh using the Vienna *ab initio* simulation package (VASP).[226,227] The planewave pseudopotentials with projector augmented wave (PAW) potentials for core electrons were used, and the exchange-correlation term was treated with the Perdew-Burke-Ernzerhof (PBE) version within the generalized gradient approximation (GGA).[228,229] All the DFT calculations were performed with input parameters compatible with the Materials Project (MP) database.[230] The ScOCl ground state, missing in the Materials Project (MP) database, was obtained using a reported structure from Springer Material.[231] To obtain the low energy configurations of LIC, LSIC, and LYZC we have generated, using pymatgen,[232] the 50 lowest Ewald energy structural orderings considering the partial occupancies of the atomic species in their experimental structures.[138,144] These structural orderings were computed

using DFT, and the lowest DFT energy configurations were used to explore the interface reaction energies. We have used a pseudo-binary mixing approach of two reactants to calculate interfacial reactivity among Li_xNiO_2 (an approximation to NCM85) and chloride SEs as described in detail elsewhere.[233,234] The calculated reaction energies and reaction products for the most energetically favorable reactions involving oxide chlorides as products, at various of charges of Li_xNiO_2, are summarized in **Table 7.2**.

7.3 Electrochemical Performance of NCM85 SSB with Chloride SEs

In this Chapter, cycling stability of the cathodes containing NCM and Li-M-Cl SEs was investigated using a two-electrode setup with a home-made In/InLi anode to minimize the risk of short-circuiting. The electrochemical performance of NCM85 SSB cells cycled at 0.2 C is summarized in **Figure 7.1**.

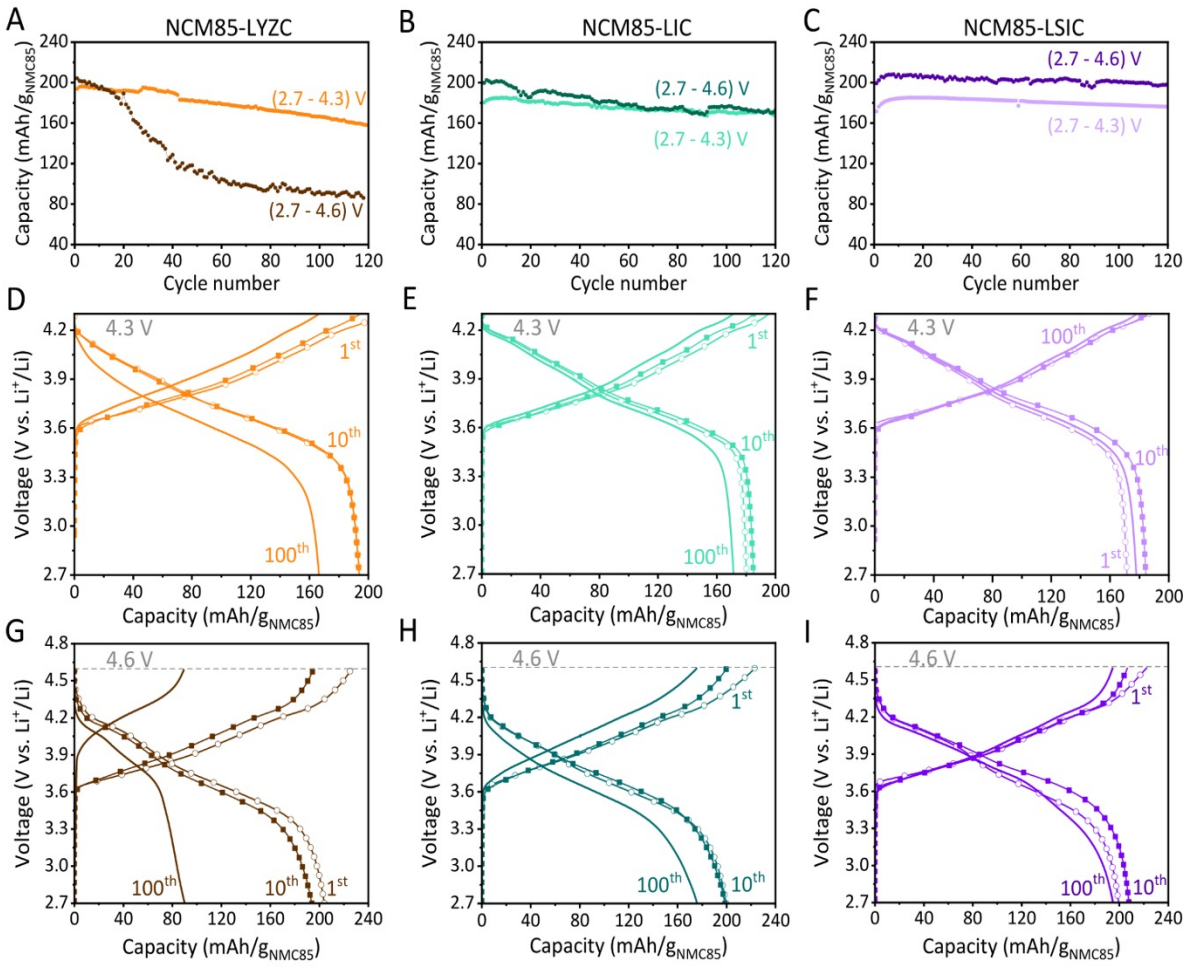


Figure 7.1 Electrochemical performance of the NCM85-*chloride SE* CAMs. (A-C) Capacity retention of the In/LiIn||NCM85 SSB cells containing (A) *LYZC*, (B) *LIC*, and (C) *LSIC* catholytes cycled at 0.2 C with the volage windows of 2.7-4.3 (light color) and 2.7.-4.6 (dark color) V vs. Li^+/Li. Polarization profile of the SSB cells with (D,G) *LYZC*, (E,H) *LIC*, and (F, I) *LSIC* cycled with upper voltage cutoffs of 4.3 and 4.6 V vs. Li^+/Li, respectively. The 1st, the 10th (solid squares line), and the 100th cycles are represented by open circles, solid squares, and solid lines, respectively.

The observed difference in capacity retention of NCM85 SSB cells containing LYZC, LIC, and LSIC suggests that there is a voltage-dependent direct relationship between cell performance and nature of the central metal cation $M^{3+/4+}$ in Li-M-Cl. The capacity of SSB cell with NCM85-*LYZC* cycled to 4.3 V continuously decays at a rate of 0.3 $mAh.g^{-1}$ per cycle to 160 mAh.g-1 after 120 cycles, which is equivalent to 80 % of its initial capacity (**Figure 7.1 A**). However, when a cutoff voltage is raised to 4.6 V, NCM85-*LYZC* loses almost 55 % of its initial capacity of 200 $mAh.g^{-1}$. The capacity retention of NCM85-*LIC* CAMs is remarkably different: it exhibits a moderate fading with approximate rates of 0.13 and 0.24 $mAh.g^{-1}$ at voltage cutoffs of 4.3 and 4.6 V, respectively. As a result, the NCM85 SSB cells with *LIC* catholyte retain a discharge capacity of 170 $mAh.g^{-1}$ when cycled to 4.3 or 4.6 V. The behavior observed for the SSB cells with NCM85-*LSIC* contrasts with that of NCM85-*LYZC* and NCM85-*LIC*. In particular, the NCM85-*LSIC* cathodes exhibit a much slower voltage-independent fade of approximately 0.08 $mAh.g^{-1}$ per cycle (**Figure 7.1 C**).

The capacity retention of SSB cells is consistent with their evolution of polarization during cycling. When the SSB cells containing NCM85-*LYZC* are cycled with a cutoff voltage of 4.3 V, their voltage profiles display a significantly increasing polarization, as demonstrated by the 10^{th} and 100^{th} cycles (**Figure 7.1 D**). Meanwhile, the NCM85-*LIC* CAM exhibits only a minor increase in polarization (**Figure 7.1 E**)., whereas the cathode containing NCM85-*LSIC* maintains a stable polarization after 100 cycles (**Figure 7.1 F**). Raising the cutoff voltage to 4.6 V signifies that the performance of NCM85 SSB cells depends on the nature of central ion $M^{3+/4+}$. Unlike the SSB cells employing not only NCM85-*LYZC* (**Figure 7.1 G**) but also NCM85-*LIC* (**Figure 7.1 H**), the NCM85-*LSIC* cathode exhibits only a minor polarization increase (**Figure 7.1 I**).

It is important to mention that the high utilization of NCM85 is achieved despite the absence of any conductive additives and the low content (20 wt. %) of chloride SE in the CAM. This indicates the formation of continuous ionic and electronic percolation pathways within the cathode, as confirmed by FIB-SEM images of the pristine NCM85-based cathodes (**Figure 7.2 A-C**). Furthermore, sufficient contact between the NCM85 particles is maintained after 120 cycles between 2.7 and 4.3 V at 0.2 C (**Figure 7.2 D-F**).

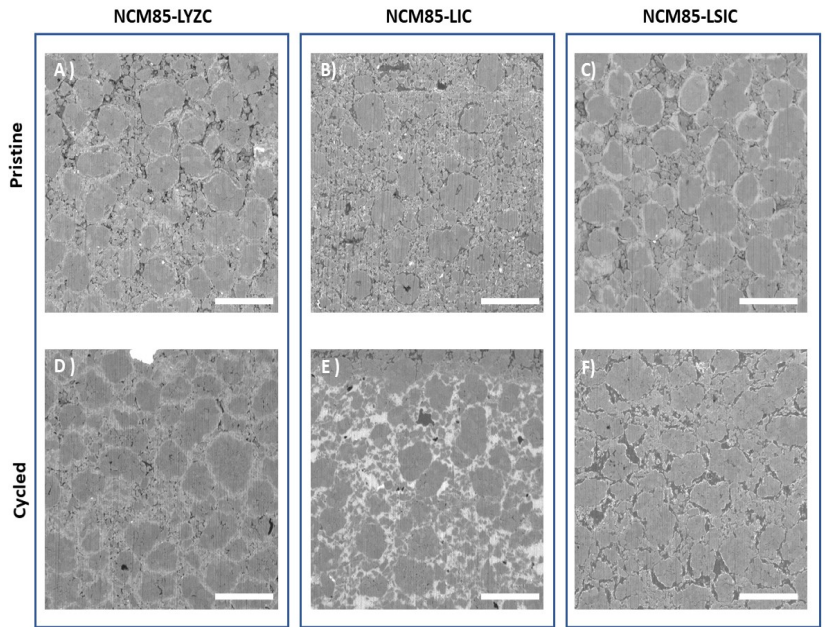


Figure 7.2 Microstructure of the NCM85-*Li-M-Cl* CAMs. (A-C) Back-scattered electron images of the NCM85 cathode composites with (A) *LYZC*, (B) *LIC*, and (C) *LSIC* SEs before cycling. (D-E) Back-scattered electron images of the NCM85 cathode composites with (D) *LYZC*, (E) *LIC*, and (F) *LSIC* SEs after 120 cycles at 0.2 C within the voltage window betweem 2.7 and 4.3 V vs. Li^+/Li.

Operando EIS studies of the NCM85 SSB cells confirm the efficient charge transport across the cathode and provide further explanation for the better stability of *LSIC*. **Figure 7.3** demonstrates the evolution of cathode resistance ($R_{cathode}$) recorded at 3.8 V during the cycling of the NCM85 SSBs between 2.7 and 4.3 V at 0.2 C. Since the EIS analysis of full SSB cells is more complicated than those of Li symmetric or sulfur symmetric cells, discussed in Chapters 4-6, the calculation of $R_{cathode}$ should be explained first.

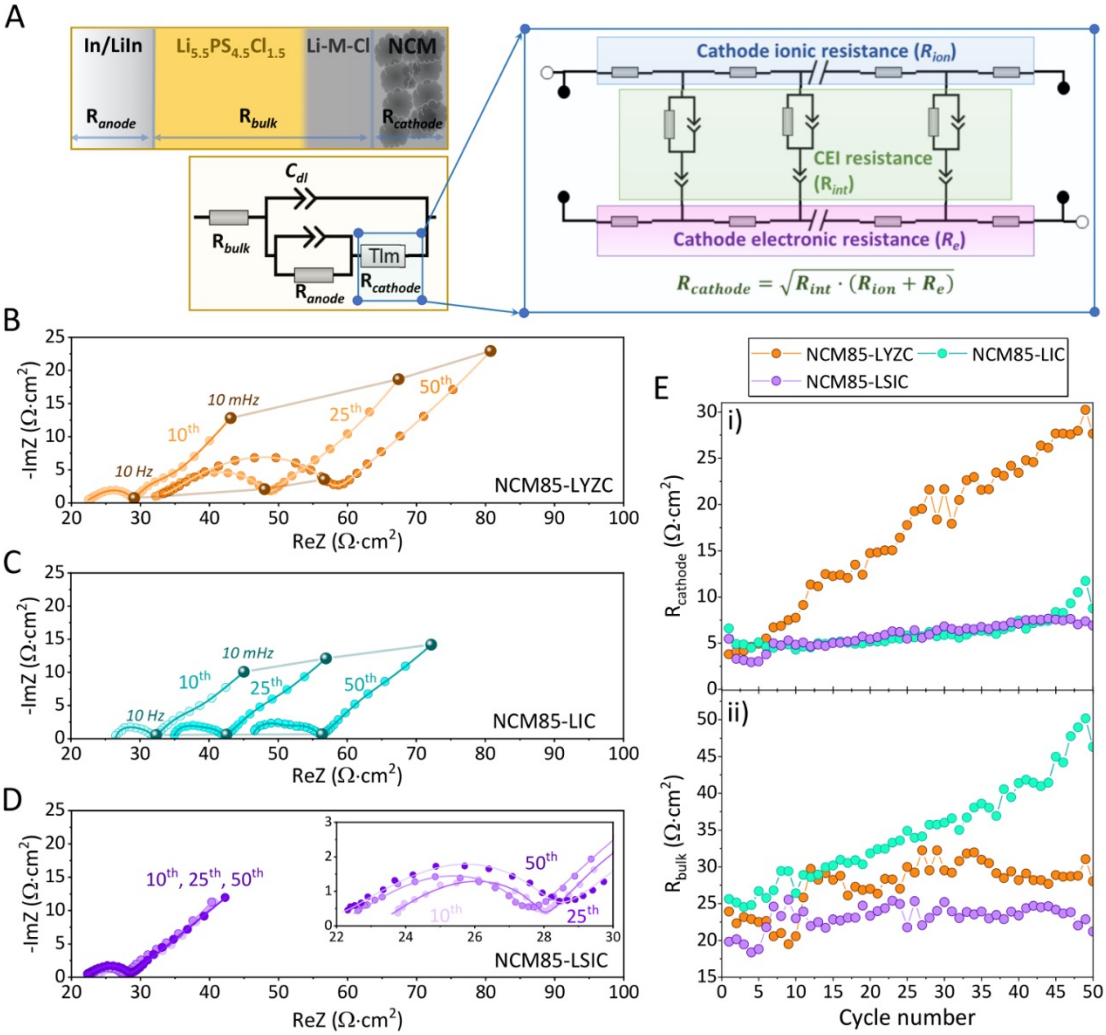


Figure 7.3 Evolution of $R_{cathode}$ during cycling the SSB cells. (A) Schematic of the NCM85 SSB cell and its equivalent circuit used to fit EIS spectra (left panel). The right panel shows the TLM scheme of the NCM85-based CAMs. (B-D) Representative Nyquist plots of the cells with (B) *LYZC*, (C) *LIC*, and (C) *LSIC* at 3.8 V vs. Li^+/Li between 1 MHz and 10 mHz after 10, 25, and 50 cycles (experimental data – dots, fitting - lines). The cells were cycled to a voltage cutoff of 4.3 V vs. Li^+/Li at 0.2 C. (E) Evolution of $R_{cathode}$ and R_{bulk} of the corresponding SSB cells.

The equivalent circuit employed to fit EIS of NCM85 SSB cells is shown in the left panel of **Figure 7.3 A**. The equivalent circuit contains the resistance of bilayer $Li_{5.5}PS_{4.5}Cl_{1.5}$/Li-M-Cl SE pellets (R_{bulk}), the capacitance of the double electric layer formed at the electrode-SE junction (C_{dl}),[235] and the electrodes' impedance. The impedance of an In/LiIn anode is observed at a frequency range below 10 Hz,[236] which is completely masked by the cathode. The NCM85-*SE* cathode generates a depressed

semicircle in the frequency range 10^5 – 10 Hz with a distinctive Gerischer-type shape,[237] which describes charge transport and charge transfer in mixed conducting solid-state materials (**Figure 7.3 B, C, D**). Since the charge transport within the NCM85-*SE* includes the ionic (R_{ion}), electronic (R_e), and interfacial (R_{int}) contributions, a transmission line model (TLM) with blocking boundary conditions was used to fit the experimental data.[235,238] The $R_{cathode}$ was calculated as the geometric average of R_{int} and (R_e+ R_{int}) because Gerischer-type (**Equation 7.1**) impedances cannot be deconvoluted into the individual components

$$R_{cathode} = \sqrt{R_{int} \cdot (R_e + R_{ion})} \qquad \textbf{Equation 7.1}$$

In consistency with the fastest capacity decay observed for NCM85-*LYZC* cathodes cycled to 4.3 V, the NCM85 SSB cells with *LYZC* catholyte suffered from a massive 7.5-fold increase from 4 to 30 Ω.cm^2 in $R_{cathode}$. In contrast, the $R_{cathode}$ of those containing *LIC* and *LSIC* increases by only 2.4 Ω.cm^2 (**Figure 7.3 E-i**). It is worth mentioning that **Figure 7.3-ii** indicates the possible $Li_{5.5}PS_{4.5}Cl_{1.5}$ instability of *LIC*. In contrast to the relative stability of R_{bulk} observed for the cells with *LYZC* and *LSIC*, the *LIC*-based cells exhibit a 2-fold increase from 25 to 50 Ω.cm^2. This could suggest the interfacial instability between LIC and $Li_{5.5}PS_{4.5}Cl_{1.5}$, as reported by Tarascon[239] and Zeier.[240] Nevertheless, a 25 Ω.cm^2 increase in R_{bulk} raises the cell polarization by only 7 mV at the given current density of 0.28 mA.cm^{-2}, which does not remarkably impact the cell capacity.

7.4 Voltage-dependent Interphase Growth between NCM85 and Li-M-Cl

To comprehensively understand the effect of cutoff voltage and the composition of Li-M-Cl on $R_{cathode}$, fully charged NCM85 SSB cells were stored for 30 hours at 4.1, 4.3, and 4.3 V. Prior to EIS, the cells were charged following a constant current – constant voltage protocol to ensure that a state state-of-charge (SOC) is achieved (**Figure 7.4 A)**. The cells were then stored at a given voltage, with EIS recorded every hour. In this work, the period of storing the cells is denoted as aging.

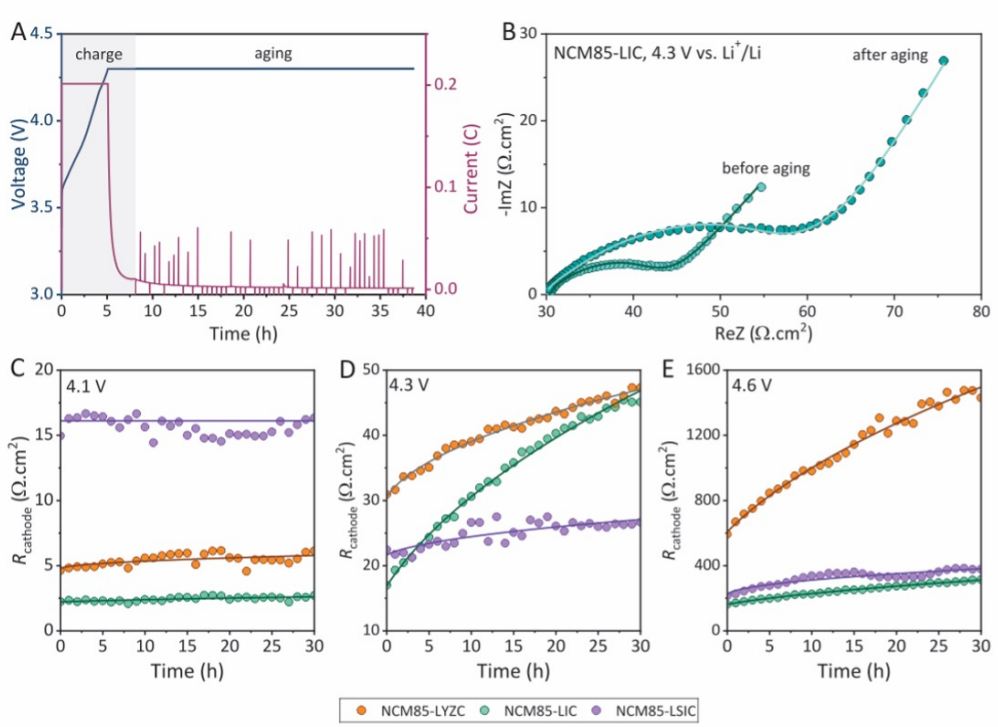


Figure 7.4 Growth of the NCM85/chorode SE interphase. (A) Aging of the In/InLi||NCM85 SSB cell with *LIC* at 4.3 V vs. Li^+/Li. The panel illustrates the representative experiment. (B) EIS of the cell from (A) before and aging. (C-E) Evolution of $R_{cathode}$ of the charged SSB cells to (C) 4.1, (D) 4.3, and (E) 4.6 V. The solid lines in (C-E) represent the parabolic fitting of the corresponding $R_{cathode}$.

Since the EIS measurements were performed after achieving a stable SOC, the temporal evolution of $R_{cathode}$ observed upon the measurements is dictated primarily by the chemical reactivity at the interface between delithiated NCM85 and Li-M-Cl. The increase in $R_{cathode}$, exemplified by the NCM85-LIC cathodes aged at 4.3 V (**Figure 7.4 B**), indicates the interphase formation during the aging step. **Figure 7.4 C** demonstrates that $R_{cathode}$ remains stable when the SSB cells are stored at 4.1 V, which agrees with the fact that chloride SEs do not undergo electrochemical oxidation below 4.2 – 4.3 V. Increasing the cutoff voltage to 4.3 V and above triggers the noticeable degradation of the SSB cells with NCM85-*LYZC* and NCM85-*LIC*. At the same time, the NCM85-*LSIC* cathodes exhibit more stable behavior. Since the $R_{cathode}$ at 4.3 and 4.6 V increases proportionally to $t^{0.5}$ (**Equation 7.2**), the growth of NCM85/Li-M-Cl interphase is a diffusion-controlled reaction with a kinetic constant k, similar to the mechanism reported for LGPS:[166]

$$R_{cathode}(t) = R_0 + k\cdot(t-t_0)^{0.5} \qquad \textbf{Equation 7.2}$$

where t_0 and R_0 are the empirical parameters, which indicate the onset of the interphase growth and the cathode resistance at that moment.

The kinetic constants of the NCM85-SE cathodes at 4.3 and 4.6 V are provided in **Table 7.1**. It is noteworthy that the NCM85-*LIC* cathodes exhibit higher *k* than that of the *LYZC*-based CAM (3.5 $\Omega.cm^2.h^{-0.5}$ *vs.* 6.3 $\Omega.cm^2.h^{-0.5}$) because the NCM85/*LYZC* interphase is formed before the EIS measurements. Indeed, the high initial resistance of the SSB cells with NCM85-*LYZC* explains their slower interphase growth at 4.3 V. In sharp contrast to the NCM85-*LYZC* and NCM85-*LIC* cathodes, the *LSIC*-based ones exhibit a minute increase in $R_{cathode}$, which results in a low kinetic constant of 0.47 $\Omega.cm^2.h^{-0.5}$. Under the increased cutoff voltage of 4.6 V, the SSB cells exhibit a higher $R_{cathode}$ due to the enhanced interfacial degradation and the lower electric conductivity of NCM materials at high SOC.[241] Although the NCM85-*LSIC* cathode displays V while aged at 4.6 V, the LIC and especially *LYZC*-containing counterparts suffer from more severe interfacial degradation, as indicated by the increase in *k:* 24 $\Omega.cm^2.h^{-0.5}$ (*LSIC*), 35 $\Omega.cm^2.h^{-0.5}$ (*LIC*), and 190 $\Omega.cm^2.h^{-0.5}$ (*LYZC*). Furthermore, the higher stability of NCM85-*LSIC* is evidenced by comparing the *k*-values normalized to $R_{cathode}$ at the beginning of aging (*k'*). The *k'*-values represent the temporal component of the interfacial growth. As shown in Table 7.1, the *k'*-value for NCM85-*LIC* (0.27 $h^{-0.5}$) at 4.6 V is almost twice that of NCM85-*LSIC* (0.14 $h^{-0.5}$). Meanwhile, aging the NCM85-*LYZC* cathodes at 4.6 V increases the *k* and *k'*-values from 4.4 $\Omega.h^{-0.5}$ to 0.14 $h^{-0.5}$ at 4.3 V to 240 $\Omega.h^{-0.5}$ to 0.40 $h^{-0.5}$, which indicates the enhanced chemical interfacial instability between LYZC and NCM85 at a higher SOC.

Table 7.1 Interfacial growth of NCM85-*SE* cathodes. The voltage-dependence of the rate constant *k* and normalized rate constant *k'* of the NCM85-*SE* cathodes

	4.3 V vs. Li^+/Li		4.6 V vs. Li^+/Li	
	k ($\Omega.cm^2.h^{-0.5}$)	*k*' ($h^{-0.5}$)	k ($\Omega.cm^2.h^{-0.5}$)	*k*' ($h^{-0.5}$)
NCM85-*LYZC*	3.5±0.9	0.14 ± 0.04	190±15	0.40 ± 0.03
NCM85-*LIC*	6.3±1.6	0.47 ± 0.12	35±4	0.27 ± 0.03
NCM85-*LSIC*	0.47±0.08	0.0028 ± 0.005	24±2	0.14 ± 0.01

7.5 Composition-dependent Electrochemical Stability of Li-M-Cl

The relationship between the oxidative stability of the Li-M-Cl SEs and the M^{n+} cation(s) was independently assessed via ultraviolet electron spectroscopy (UPS) and cyclic voltammetry (CV) of the C65-SE||In cells. Although UPS and CV may appear to be unrelated methods, their results for estimating the oxidative stability of SEs are linked. Indeed, UPS measures the energy required to remove a valence electron from the valence band of the SE to vacuum (E_{vb} vs. vacuum) (**Equation 7.3**):

$$Li_xM_yCl_z \rightarrow \left(Li_xM_yCl_z\right)^+ + e^-_{vacuum} \qquad \textbf{Equation 7.3}$$

Meanwhile, the oxidation onset determined via CV (E_{ox}) is ascribed to removing a ($Li^+ + e^-$) couple from the SEs.[163] Since the C65-SE||In cells are employed, the electrochemical oxidation can be schematically illustrated by **Equation 7.4**:

$$Li_xM_yCl_z \rightarrow Li_{x-1}M_yCl_z + Li^+_{In/LiIn} + e^-_{In/LiI} \qquad \textbf{Equation 7.4}$$

Therefore, the values of E_{ox} and E_{vb} can be linked by **Equation 7.5**

$$E_{ox} = \frac{E_{vb} - WF_{Li}}{e} + A \qquad \textbf{Equation 7.5}$$

where WF_{Li} is the work function of Li metal, and A is the constant, which accounts for the difference between the chemical potentials a Li^+ and electron in the In/InLi and Li-M-Cl.

The UPS spectra of three Li-M-Cl electrolytes are displayed in **Figure 7.5 A**. To calculate the valence band energy (E_{vb}), the density of states (DOS) near the valence band edge (8.0 – 9.0 eV) was approximated with a linear function, following the protocol developed for hybrid perovskite materials. As shown in the inset of **Figure 7.5 A**, the E_{vb}-value is equal to the intercept of the fitting line. The E_{vb}-values descend in the order *LSIC* (8.81 eV) > *LYZC* (8.67 eV) > *LIC* (8.48 eV), thus suggesting that *LSIS* is the least prone to oxidation. Meanwhile, the lowest E_{vb} exhibited by LIC could be ascribed to the higher electronegativity of In^{3+},[242] in accordance with the electronegativity scale developed by Diaz and Campero: χ (In^{3+}) = 1.87, χ (Y^{3+}) = 1.22, χ (Zr^{4+}) = 1.43, and χ (Sc^{3+}) = 1.29.[243]

CV analysis of the selected Li-M-Cl SE verifies the results of UPS. In consistency with the previous experimental and theoretical studies of the chloride electrolytes, there is no significant oxidation below 4.2 V. Above 4.2 V, electrochemical oxidation of the SEs generated an exponentially growing current, the onset of which is equal to the oxidative stability limit. As shown in the onset of

Figure 7.5 B, the oxidative stability limit increases from *LIC* (4.27 V) to *LYZC* (4.32 V) and *LSIC* (4.36 V). As expected, there is a clear correlation between the oxidative stability of the SEs and E_{VB}-values (**Figure 7.5 B**). [244]

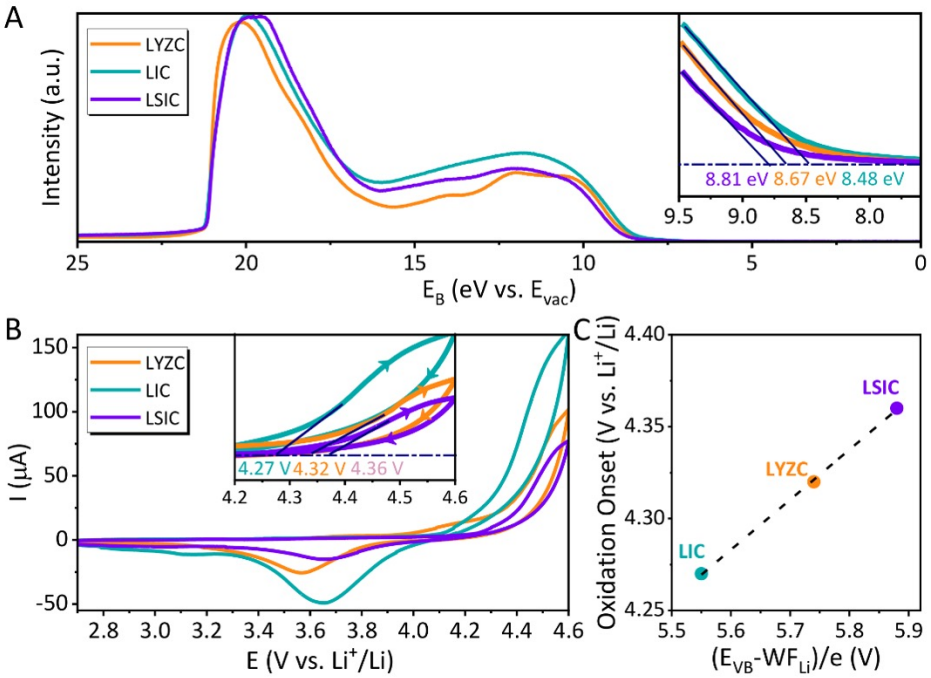


Figure 7.5 Oxidative stability of the chloride SEs. (A**)** UPS spectra of the Li-M-Cl SEs. The E_{VB}-values were calculated by extrapolating the DOS to the background (dashed-dot line) as shown in the inset. (B) CV of the C65-SE||In cells between 2.7 and 4.6 V vs. Li+/Li at 0.1 mV.s^{-1}. The inset shows the linear extrapolation of the anodic scan to estimate the oxidative stability of SEs. (C) The correlation between the oxidative stability limit estimated by CVA and E_{VB}. The work function of Li (WF_{Li} = 2.93 eV)[244] was subtracted from the E_{VB}-values for a more comprehensive illustration.

Cyclic voltammograms of the SE||In cells demonstrate that the selected Li-M-Cl SEs do not undergo electrochemical oxidation below 4.2 V, which agrees with the DFT-predicted[245] and experimentally measured[141,246] oxidative stability. When the voltage exceeds 4.2 V, the oxidation of SEs generates an exponentially growing current. The oxidation onset, the estimation of which is illustrated in the inset of **Figure 7.5 B**, increases from LIC to LSIC. More specifically, it obeys the trend identical to that of E_{vb}: *LSIC* (4.36 V) > *LYZC* (4.32 V) > *LIC* (4.27 V).

The highest intrinsic oxidative stability of *LSIC* explains the superior performance of the SSB cells employing NCM85-*LSIC*. However, the different performance of the NCM85-*LYZC* and NCM85-*LIC*-containing cathodes seemingly contradicts the observed trend in the oxidative stability of the SEs. This suggests that the capacity fading of the NCM85 SSB cell with *LYZC* must be dictated by chemical decomposition.

7.6 Interfacial Reactivity between Ni-rich NCM and Li-M-Cl

The H2→H3 phase transition in NCM, followed by the oxygen evolution reactions (OER) in NCM, is one of the driving forces for the degradation of NCM. Gasteiger demonstrated that the onset of OER decreases with a higher Ni content from 4.7 V vs. Li^+/Li for $LiNi_{1/3}Co_{1/3}Mn_{1/3}O_2$ to 4.3 V vs. Li^+/Li for $LiNi_{0.8}Co_{0.1}Mn_{0.1}O_2$.[247] Since I investigated the performance of NCM with a higher Ni content of 85 %, it is reasonable to except the OER at lower potentials. This is confirmed by the onset of the H2→H3 transition at approximately 4.16 V (**Figure 7.6 A**).

Meanwhile, the SSB cells employing $LiNi_{1/3}Co_{1/3}Mn_{1/3}O_2$ (NCM111) do not exhibit the H2→H3 transition below 4.3 V (**Figure 7.6 A**), which indicates that the performance of the NCM111 cathodes with *LIC* and *LYZC* is not affected by the OER and depends only on the intrinsic electrochemical stability of the chloride SEs. As a result, the SSB cells with NCM111 and *LIC* exhibit a 4-fold faster capacity decay in comparison with their *LYZC*-based counterpart (**Figure 7.6 B**). Furthermore, aging the NCM111 cells with *LYZC* and *LIC* demonstrates a more pronounced growth of the NCM111/LIC interphase (**Figure 7.6 C)**. Therefore, the better performance of the NCM111 cells with *LYZC*, compared to those containing *LIC*, is in concert with the higher electrochemical oxidative stability of *LYZC.*

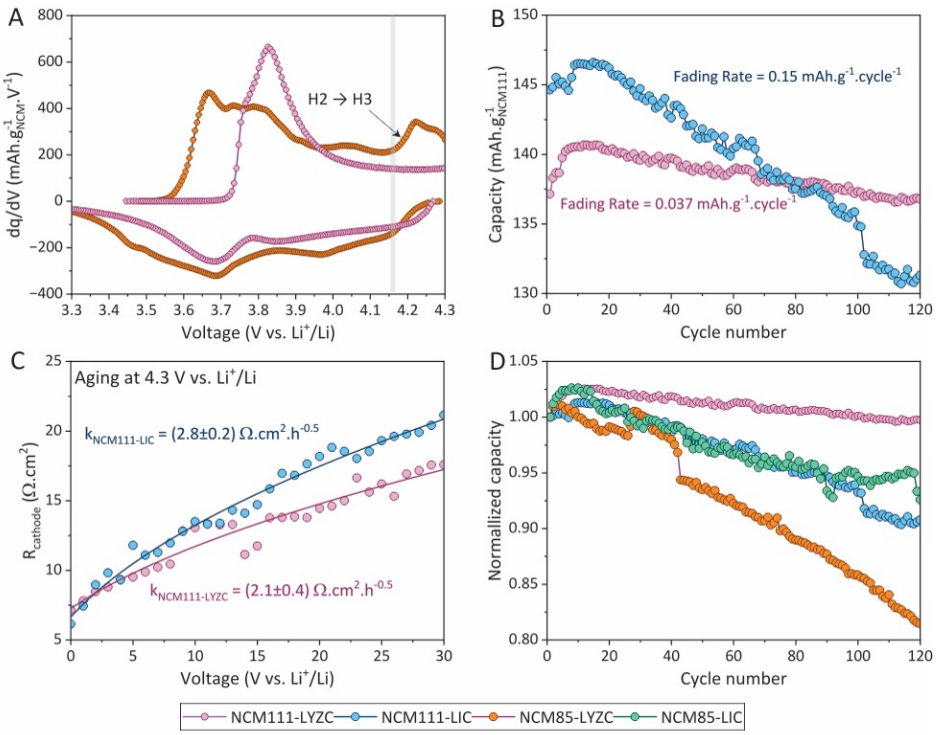


Figure 7.6 Effect of Ni content on the stability of NCM-*chloride SE* cathodes. (A) Differential capacity (*dQ/dV*) curves of the 1st cycle the SSB cells with the NCM85-*LYZC* and NCM111-*LYZC* cathodes. The cells were cycled a→t 0.2 C between 2.7 and 4.3 V vs. Li$^+$/Li. The grey line highlights the onset of the H2→H3 phase transition at 4.22 V. (B) Capacity retention of the NCM111 cells with *LYZ* and *LIC* at 0.2 C between 2.7 and 4.3 V vs. Li$^+$/Li. (C) Evolution of $R_{cathode}$ of the NCM111 cells with *LYZC* and *LIC* charged to 4.3 V vs. Li$^+$/Li. (D) Normalized capacity of the In/LiIn||NCM85 and In/LiIn||NCM111 SSB cells with *LYZC* and *LIC* SEs cycled at 0.2 C between 2.7 and 4.3 V vs. Li$^+$/Li.

The OER-triggered degradation of the NCM cells with *LYZC* is comprehensively illustrated by comparing the normalized capacity retention of the cells with *LYZC* and *LIC* (**Figure 7.6 D**). The similar capacity decay is observed for the NCM111-*LIC* and NCM85-*LIC* cathodes because the electrochemical oxidation of *LIC* drives their degradation. In contrast, the *LYZC*-containing NCM85 CAMs suffer from more severe capacity fading compared to their NCM111-based counterparts due to the lower chemical stability of LYZC with delighted NCM85. Furthermore, the continuous interphase growth observed for the NCM85-*LYZC* cathodes at 4.3 and especially 4.6 V suggests that the interfacial decomposition products facilitated the mass transfer of the species produced by the OER in NCM85. To better understand the interfacial reactivity between Ni-rich NCM and Li-M-Cl SE, the CEI was investigated by ToF-SIMS in combination with DFT calculations of the interfacial reactions.

Table 7.2 Reactivity between $Li_{1-x}NiO_2$ and Li-M-Cl SEs. DFT-predicted products and enthalpy of the interfacial reaction between $Li_{1-x}NiO_2$ and Li-M-Cl SEs at the various SOCs (x = 0, 0.25, 0.5, 1). The most energetically stable M-containing products are provided.

		Reaction Products	**ΔE_{rxt} (eV/atom)**
$LiNiO_2$	Li_3InCl_6	$LiClO_4$, NiO, LiCl, InClO	-0.060
	$Li_{2.125}Sc_{0.375}In_{0.25}Cl_4$	$LiClO_4$, NiO, LiCl, InClO, ScClO	-0.079
	$Li_{2.5}Y_{0.5}Zr_{0.5}Cl_6$	$LiClO_4$, NiO, LiCl, ZrO_2, YClO	-0.124
	Li_3YCl_6	$LiClO_4$, NiO, LiCl, YClO	-0.082
	Li_2ZrCl_6	$LiClO_4$, NiO, LiCl, ZrO_2	-0.155
$Li_{0.75}NiO_2$	Li_3InCl_6	$LiClO_4$, NiO, LiCl, InClO	-0.064
	$Li_{2.125}Sc_{0.375}In_{0.25}Cl_4$	$LiClO_4$, NiO, LiCl, InClO, ScClO	-0.081
	$Li_{2.5}Y_{0.5}Zr_{0.5}Cl_6$	$LiClO_4$, NiO, LiCl, ZrO_2, YClO	-0.122
	Li_3YCl_6	$LiClO_4$, NiO, LiCl, YClO	-0.084
	Li_2ZrCl_6	$LiClO_4$, NiO, LiCl, ZrO_2	-0.148
$Li_{0.5}NiO_2$	Li_3InCl_6	$LiClO_4$, NiO, LiCl, InClO	-0.071
	$Li_{2.125}Sc_{0.375}In_{0.25}Cl_4$	$LiClO_4$, NiO, LiCl, InClO, ScClO	-0.084
	$Li_{2.5}Y_{0.5}Zr_{0.5}Cl_6$	$LiClO_4$, NiO, LiCl, ZrO_2, YClO	-0.118
	Li_3YCl_6	$LiClO_4$, NiO, LiCl, YClO	-0.087
	Li_2ZrCl_6	$LiClO_4$, NiO, LiCl, ZrO_2	-0.138
$Li_{0.25}NiO_2$	Li_3InCl_6	$LiClO_4$, NiO, LiCl, InClO	-0.095
	$Li_{2.125}Sc_{0.375}In_{0.25}Cl_4$	$LiClO_4$, NiO, LiCl, InClO, ScClO	-0.103
	$Li_{2.5}Y_{0.5}Zr_{0.5}Cl_6$	$LiClO_4$, NiO, LiCl, ZrO_2, YClO	-0.127
	Li_3YCl_6	$LiClO_4$, NiO, LiCl, YClO	-0.106
	Li_2ZrCl_6	$LiClO_4$, NiO, LiCl, ZrO_2	-0.140

The interphase composition and reaction enthalpy (ΔE_{rx}) were predicted by simulating the reaction between $Li_{1-x}NiO_2$ and Li-M-Cl at different values of x. Varying x between 0 and 1 mimics the delithtiathion of NCM and OER since the OER occurs at approximately $x = 0.75$.[248] The outcome of the interfacial calculations (**Table 7.2)** predicts the formation of YOCl, ZrO_2, InOCl, and ScOCl. The relationship between the DFT-predicted reaction enthalpy and the nature of M^{n+} in Li-M-Cl suggests that the degradation of the NCM85-*LYZC* is thermodynamically driven. In fact, ΔE_{rx} between $Li_{1-x}NiO_2$ and *LYZC* is -0.124 eV per atom before delitihation ($x = 0$). In contrast, the $LiNiO_2$/*LIC* and $LiNiO_2$/*LSIC* interfaces exhibit significantly more positive reaction enthalpy of -0.060 and -0.079 eV per atom, respectively. The negative enthalpy of the reaction between $Li_{1-x}NiO_2$ and *LYZC* is primarily dictated by the formation of ZrO_2 rather than YOCl, as indicated by ΔE_{rx} of the corresponding reactions (**Table 7.2**). On the other hand, the fact that the Ni-rich NCM SSB cells with Li_2ZrCl_6 do not suffer from a strong capacity decay[249] indicates that the decomposition of Li_2ZrCl_6 efficiently passivates the interface with NCM. Therefore, it is reasonable to suggest that the formation of *YOCl* may promote continuous interfacial growth in the case of the NCM85-*LYZC* cathodes.

Probing the NCM85-*SE* cathodes by ToF-SIMS confirms the results of the DFT calculations and demonstrates the lower intrinsic electrochemical oxidation stability of *LIC*. As demonstrated earlier, only ToF-SIMS details the chemical composition of the CEI formed in SSB cells.[167] Among the variety of secondary ions generated by the NCM85-*SE* cathodes, the MCl_3^-/MCl_4^- and OCl^- signals were selected to represent the electrochemical and chemical decomposition of the SEs. Indeed, the electrochemical oxidation of Li-M-Cl generates a corresponding MCl_n chloride,[172] which would result in the rise of MCl_n^-. Meanwhile, since our DFT calculations predict the formation of M-oxide (ZrO_2) and M-oxychlorides (InOCl, YOCl, ScOCl), the OCl^- increase would suggest the chemical reactivity at the interface. It is worth mentioning that the ion current produced by the ionization of ZrO_2 is below the detection limit, and thus, the presence of ZrO_2 cannot be confirmed by ToF-SIMS.

The evolution of the MCl_n^- signal exhibited by the NCM85-*LYZC*, NCM85-*LIC*, and NCM85-*LSIC* cathodes after cycling to 4.3 V is demonstrated in **Figure 7.7 A-C** and summarized in **Figure 7.7 E**. In good consistency with the results of CV, cycling the *LYZC* (**Figure 7.7 A**) and *LSIC*-based cathodes (**Figure 7.7 C**) does not increase their MCl_n^- signals, whereas the noticeable rise in intensity of the $InCl_3^-$ peak exhibited by the NCM85-*LIC* cathode evidences its electrochemical instability (**Figure 7.7 B**). Indeed, while there is almost no accumulation of $InCl_3^-$ in the NCM85-*LSIC* cathodes after 120 cycles, the *LIC*-based CAM demonstrates a noticeable 1.4-fold increase in the intensity of $InCl_3^-$ (**Figure 7.7 E**).

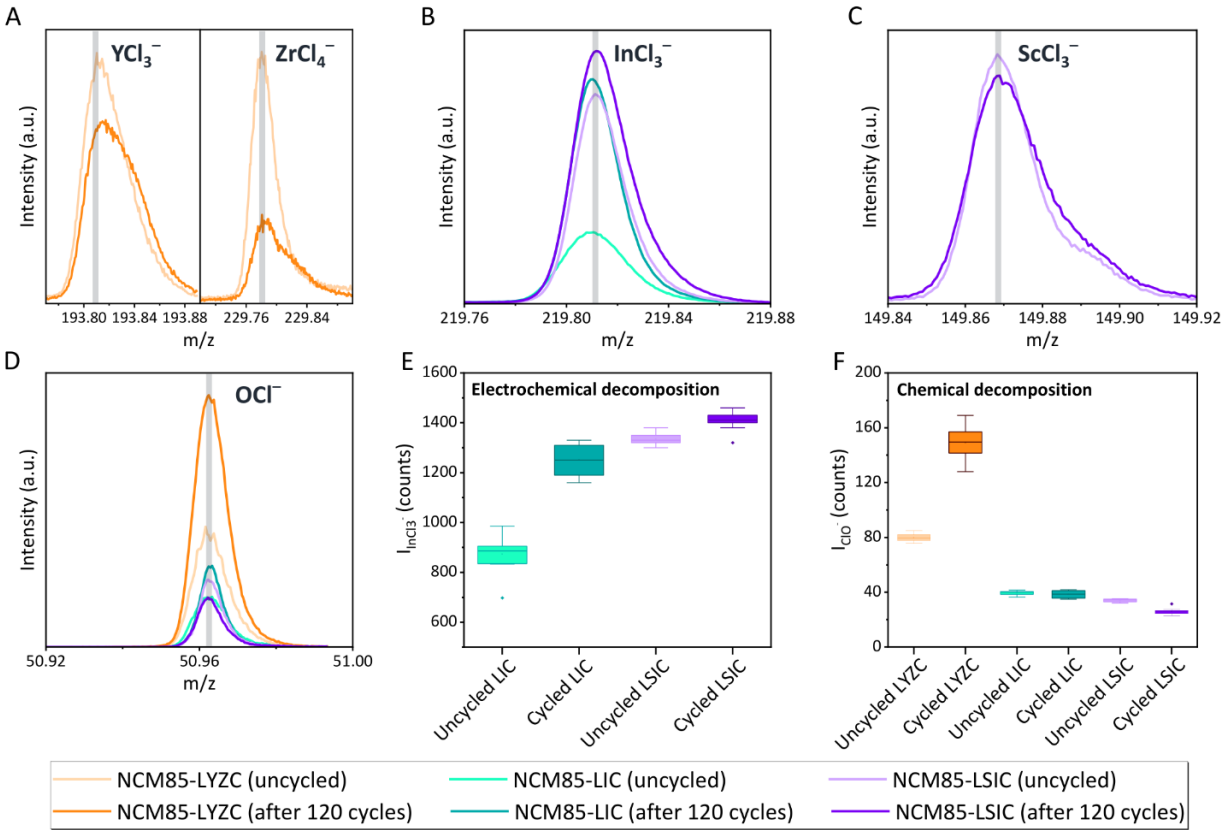


Figure 7.7 ToF-SIMS Analysis of the NCM85/chloride SE interphase. Evolution of the (A-C) MCl_n^- and (D) OCl^- signals produced by the NCM85-SE cathodes before and after cycling the SSB cells to 4.3 V for 120 cycles. (E-F) Quantification of the decomposition fragments of Li-M-Cl.

The evolution of the OCl^- fragment exhibited by SSB cells after 120 cycles to 4.3 V (**Figure 7.7 D, F**) directly proves that the nature of M in Li-M-Cl directly controls the CEI formation. In particular, the uncycled NCM-*LYZC* cathodes exhibit a 2-times higher count of OCl^- than the *LIC* and *LSIC*-based counterparts, which indicates the interfacial instability between *LYZC* and fully lithiated

NCM 85. It is noteworthy that the non-zero OCl^- counts observed for *LIC* and *LSIC* could be partially ascribed to the traces of moisture retained in the PEEK dies. Nevertheless, the change in the OCl^- exhibited by the SSB cells with *LYZC* after 120 cycles sharply contrasts with those employing *LIC* and *LSIC*. While the OCl^- remains unchanged or even drops in the case of the *LIC* and *LSIC*-based cathodes despite the negative DFT-calculated enthalpy of the reaction with delithiated NCM, cycling the SSB cells increases the OCl^- signal by approximately two times. Since all these SEs are expected to react with delithated NCM85 due to the negative ΔE_{rx}, it is reasonable to suggest that Sc^{3+} and $In3^+$, unlike Y^{3+}, may form a kinetically stable interface with NCM85.

7.7 Conclusions

This chapter investigates the origins of different electrochemical performance of high-energy-density NCM85 with three different solid electrolytes – *LYZC*, *LIC*, and *LSIC*. Through the combination of numerous electrochemical, characterization and computational techniques, we demonstrate that the central metal cation $M^{3+/4+}$ dictates the stability of SSB cells with Ni-based CAMs and governs the pathways of SE decomposition. Our findings suggest that the chemical instability between Li-M-Cl SEs and (de)lithiated Ni-rich NCM has a more severe impact on cell performance than the electrochemical oxidation of SEs when the OER in NCM occurs. This is exemplified by the performance of NCM85 SSB cells containing *LYZC* and *LIC.* Assessing the electrochemical stability of Li-M-Cl by UPS and CV indicates that7 it increases in the following order: *LIC*<*LYZC*<*LSIC.* However, OER in delithiated NCM85 triggers the formation of YOCl and, arguably, ZrO_2 at the NCM85/LYZC interface, which reduces the stability of *LYZC*-based cathodes in comparison with those employing *LIC*. However, the capacity fading of SSB cells in the absence of OER agrees with the oxidative stability of chloride SEs, as demonstrated by cells with NCM111.

Overall, this work demonstrates a comprehensive study which analyzes numerous aspects of utilizing the chloride SEs in conjunction with Ni-rich NCM materials, such as battery performance and (electro)chemical stability of the SEs. Moreover, the systematic approach developed here may be applied to evaluate the stability of new SE in SSB cells.

Chapter 8

Conclusions and Future Prospects

8.1 Conclusions

This thesis presents a multi-pronged experimental and theoretical analysis of lithium batteries with different cathode chemistries and electrolyte configurations. In Chapter 3 of this thesis, the efficacy of LiI as a potential redox mediator for Li-O_2 batteries was critically assessed. The combination of DEMS, chemical titrations and XRD demonstrated that, in contrast to previous reports, LiI impacts the battery performance. LiI lowers the yield of Li_2O_2, which is further aggravated by the presence of water, causing the formation of LiOH. While Li_2O_2 can be oxidized by electrochemically generated I_3^- and I_2, the oxidation of LiOH does not occur. Instead, LiOH triggers the disproportionation of I_2 and I_3^-, yielding $LiIO_3$. Furthermore, the redox shuttle effect of I-containing species reduces the charging voltage, which may be misinterpreted as improved battery performance.

Chapters 4 – 6 address the challenges of LMAs. In Chapter 4, I investigated the relationship between LiFSI-G_n-TTE (molar ratio of 1:1:4) solvate electrolytes' composition and the stability of LMAs. By combining Raman spectroscopy and AIMD simulations, it was demonstrated that the ionic association between Li^+ and FSI^- is considerably strengthened in G_1 and G_2. Therefore, the solvation structure of $114G_1$ contains the chains of FSI-linked ionic aggregates (FSI-AGGs), while only TTE-separated ion pairs (FSI-CIP) formed between FSI^- and G_4-chelated Li^+ exist in $114G_4$. Full-range EIS analysis of Li symmetric cells with $114G_n$ demonstrated that the FSI-AGGs yield fast interfacial transport of Li^+ in $114G_1$. In contrast, the formation of FSI-CIP impedes the reduction of Li^+ from 114 G_3 and $114G_4$. Furthermore, the chelation of Li^+ lowers the lithium transference number from 0.23 in $114G_1$ to below 0.05 in $114G_4$. Although all four solvate electrolytes facilitate Li deposition with a high CE that exceeds 99 %, the slow diffusivity of Li^+ within the bulk causes the deposition of high-surface-area Li. This increases Li consumption during SEI buildup and limits rate capability, which is especially noticeable when the applied current density exceeds 1 $mA.cm^{-2}$.

Chapter 5 presents a case study of LMA's stability in solid-state cells containing numerous sulfide SEs: $Li_{10.35}Sn_{0.27}Si_{1.08}P_{1.65}S_{12}$, $Li_{3.25}Si_{0.25}P_{0.75}S_4$, β-$Li_3PS_4$, and $Li_{5.5}PS_{4.5}Cl_{1.5}$. It demonstrates that

the presence of Si^{4+} and Sn^{4+} enhances the reactivity between Li and sulfide SEs. The interphase formed between Li and Si^{4+}/Sn^{4+}-free sulfide SEs inhibits the further interfacial reactivity. In contrast, interfacing Li with Si^{4+}/Sn^{4+}- containing sulfide SEs results in complete consumption of the LMA. Nevertheless, the formation of a kinetically stable interface between Li and SEs is not enough to facilitate stable Li cycling. This was exemplified by the cells with β-Li_3PS_4. At a low current density (0.1 mA.cm^{-2}) and Li plating capacity (0.1 mAh.cm^{-2}), β-Li_3PS_4 allows for long-term Li deposition with a CE above 99 %. However, the formation of Li dendrites is observed when the current density exceeds 0.35 mA.cm^{-2}. The lifetime of the LMA was improved by two different approaches. The incorporation of $Li_{10.35}Sn_{0.27}Si_{1.08}P_{1.65}S_{12}$ into the structure of a multilayer pellet extended the lifetime of Li symmetric cells from 7 to 275 hours at 0.5 mA.cm^{-2} (1 mAh.cm^{-2}). Similarly, wetting the Li/SE interface with $114G_2$ also resulted in long-term cycling of LMAs for 1000 hours. However, both strategies only postpone the failure of the LMA.

Chapter 6 is focused on the interfacial chemistry of Ta-doped LLZO in EPD electrolytes containing sulfur. In this work, DMA was selected as an EPD solvent. For the first time, it was demonstrated that the interfacial stability between LLZO and sulfur depends on the electrolyte. While LiOH and Li_2CO_3 trace on the surface of LLZO are inert in DOL/DME electrolytes, they trigger the formation of $S_3^{\cdot-}$ in DMA. When $S_3^{\cdot-}$ is formed, it undergoes numerous chemical reactions, which results in the precipitation of thiosulfate, polythionate and La-S/La-O-S species at the surface of LLZO. The passivated LLZO exhibits very high interfacial resistance that exceeds 5000 Ω.cm^2. Reacting LLZO pellets with acid improves their surface stability provided a proper acid is selected. For example, HCl successfully removes Li_2CO_3, but traces of LiOH remain on the surface, and HCl-treated LLZO still reacts with sulfur in DMA. Conversely, reacting sythesized LLZO with H_3PO_4 yields a 10 nm Li^+-conducting layer, which successfully suppresses side reactions. The protective layer containing Li_3PO_4, $LaPO_4$ and $Zr_3(PO_4)_4$ also stabilized LLZO surfaces in full Li-S batteries. Li-S batteries with HPO-LLZO and DMA deliver a high capacity above 1400 mAh.g^{-1}. However, improving cycling stability at current densities above 1 mA.cm^{-2} will require additional engineering of the Li/LLZO interface.

Chapter 7 details a comprehensive multi-pronged study of solid-state batteries with high-energy-density cathodes containing Ni-rich NCM85 and different Li-M-Cl SEs: $Li_{2.5}Y_{0.5}Zr_{0.5}Cl_6$ (*LYZC*), Li_3InCl_6 (*LIC*), and $Li_2Sc_{0.5}In_{0.5}Cl_4$ (*LSIC*). This study demonstrates that the performance of the NCM SSB cells employing Li-M-Cl SEs is dictated by the metal cation $M^{3+/4+}$. This is because the

electrochemical and chemical stability of the SEs is highly dependent on $M^{3+/4+}$. The intrinsic stability of the SEs was measured by two independent methods: CV and UPS. The results of CV and UPS demonstrate that the intrinsic stability to electrochemical oxidation increases from *LIC* to *LISC*. However, the cycling performance of the cathodes based on Ni-rich NCM85 primarily depends on the chemical stability at the NCM85/SE interface. Among the tested chloride SEs, LYZC exhibits the highest reactivity with (de)lithiated NCM85 due to the OER in NCM85 at voltages above 4.15 V, as predicted by DFT calculations and confirmed by ToF-SIMS. Therefore, the NCM85 SSB cells containing *LYZC* exhibit the fastest interfacial growth and capacity fading, especially when cycled to 4.6 V. However, cycling the NCM111 SSB cells demonstrates that capacity retention in the absence of the OER is dictated by the intrinsic electrochemical stability of the SEs. Apart from directly comparing the performance of the SSB cells with different chloride SEs, this chapter established a detailed approach to evaluate the applicability of novel chloride and fluoride SEs in SSBs.

8.2 Future Prospective

Since the demand for sustainable energy continuously increases, the call for safe and cheap high-energy-density batteries will remain urgent in the foreseeable future. Therefore, the research on lithium batteries will likely lean toward the development of technologies which can be scaled up. Nevertheless, the fundamental challenges raised by the limitations of Li batteries should also be addressed.

The development of rechargeable Li-O_2 batteries with organic electrolytes seems problematic due to LiO_2 instability of most salts and solvents along with kinetic limitations of ORR and OER. However, the reversible formation and decomposition of Li_2O in molten salt electrolytes at 150 °C could be a valid reason to design novel Li-O_2 batteries operating at elevated temperatures.[11] Furthermore, raising operating temperature close to lithium's melting point decreases the risk of Li dendrites. Nevertheless, the design of this battery is a complex engineering task, which first must address the instability of LMAs.

This work demonstrated that cycling LMAs at 1 $mA.cm^{-2}$ with a capacity limit of ~ 3 $mAh.cm^{-2}$ is challenging, although the employed liquid and solid electrolytes ($114G_n$ and HPO-LLZO) exhibit good chemical compatibility with Li. Meanwhile, increasing the energy density above 350-400 $Wh.kg^{-1}$ requires the areal capacity to be at least 4 $mAh.cm^{-2}$. The necessity to reversibly plate and strip at least 20 μm of Li every cycle calls for designing LMA architectures that accommodate plated Li. This could potentially be realized by expanding Samsung's approach to creating hybrid Ag-carbon polymer

membranes.[159] Developing thin LLZO SEs with controlled porosity at the anode side is another promising strategy to accommodate plated Li, as recently demonstrated by Wachsman *et al*.[250] The collaboration with organic chemists to explore novel liquid solvents is also a promising avenue to increase the rate capability of LMAs. This is illustrated by the recent success in synthesizing numerous novel salts and solvents, which improves the lithium transference number to 0.8.[251,252]

Future Li-S battery research should consider improving cathode architecture for better capacity retention and rate capability. Incorporating flexible and electronically conducting binders into a cathode architecture could mitigate volume changes caused by the conversion reactions in EPD electrolytes. Furthermore, reducing the E/S ratio from 10 to below 2 requires a comprehensive cathode design. Introducing DMA-based gel polymer electrolytes could be a potential strategy to decrease the E/S ratio and improve the mechanical properties of sulfur cathodes. Furthermore, replacing sulfur with Li_2S opens a broad avenue toward anodeless LMBs, which could considerably cut manufacturing costs. A complete shift to SSBs with S or Li_2S cathodes should not be ignored.

The improvement of SSB with high-voltage cathodes is also an intriguing research field. For example, detailing the mechanism of interfacial reactivity between Ni-rich NCM and LYZC SE remains an intriguing task. In addition, suppressing the reactivity between In^{3+} in LSIC and sulfide SEs should also be addressed in future studies. On the one hand, the high cost of Sc and In calls for the search of alternative halide or oxyhalide electrolytes with high Li^+-conductivity and stability with Ni-rich NCM. For example, a new class of lithium-metal-oxy-chloride materials with a room temperature ionic conductivity of 10-12 $mS.cm^{-1}$ was recently discovered.[253] These novel SEs significantly improve the rate capability of the SSB cells. Besides developing novel electrolytes, improving cycling/structural stability of Ni-rich NCM materials should also be considered. Indeed, synthesizing single-crystal doped NCM with an improved electric conductivity is essential to boost the energy density and rate capability of the SSBs.

References

(1) Placke, T.; Kloepsch, R.; Dühnen, S.; Winter, M. Lithium Ion, Lithium Metal, and Alternative Rechargeable Battery Technologies: The Odyssey for High Energy Density. *Journal of Solid State Electrochemistry* **2017**, *21* (7), 1939-1964.

(2) Bruce, P. G. Energy Storage beyond the Horizon: Rechargeable Lithium Batteries. *Solid State Ionics* **2008**, *179* (21–26), 752-760.

(3) Masias, A.; Marcicki, J.; Paxton, W. A. Opportunities and Challenges of Lithium Ion Batteries in Automotive Applications. *ACS Energy Letters* **2021**, *6* (2), 621–630.

(4) Kwak, W.-J.; Rosy; Sharon, D.; Xia, C.; Kim, H.; Johnson, L. R.; Bruce, P. G.; Nazar, L. F.; Sun, Y.-K.; Frimer, A. A.; Noked, M.; Freunberger, S. A.; Aurbach, D. Lithium–Oxygen Batteries and Related Systems: Potential, Status, and Future. *Chemical Reviews* **2020**, *120* (14), 6626–6683.

(5) Manthiram, A.; Fu, Y.; Su, Y. S. Challenges and Prospects of Lithium-Sulfur Batteries. *Accounts of Chemical Research* **2013**, *46* (5), 1125-1134.

(6) Sun, X.; Mu, X.; Zheng, W.; Wang, L.; Yang, S.; Sheng, C.; Pan, H.; Li, W.; Li, C. H.; He, P.; Zhou, H. Binuclear Cu Complex Catalysis Enabling Li–CO_2 Battery with a High Discharge Voltage above 3.0 V. *Nature Communications* **2023**, *14* (1), 536.

(7) Usiskin, R.; Lu, Y.; Popovic, J.; Law, M.; Balaya, P.; Hu, Y.-S.; Maier, J. Fundamentals, Status and Promise of Sodium-Based Batteries. *Nature Review Materials* **2021**, *6* (11), 1020–1035.

(8) Liang, Y.; Dong, H.; Aurbach, D.; Yao, Y. Current Status and Future Directions of Multivalent Metal-Ion Batteries. *Nature Energy* **2020**, *5* (9), 646–656.

(9) Kundu, D.; Adams, B. D.; Duffort, V.; Vajargah, S. H.; Nazar, L. F. A High-Capacity and Long-Life Aqueous Rechargeable Zinc Battery Using a Metal Oxide Intercalation Cathode. *Nature Energy* **2016**, *1* (10), 16119.

(10) Choi, N. S.; Chen, Z.; Freunberger, S. A.; Ji, X.; Sun, Y. K.; Amine, K.; Yushin, G.; Nazar, L. F.; Cho, J.; Bruce, P. G. Challenges Facing Lithium Batteries and Electrical Double-Layer Capacitors. *Angewandte Chemie International Edition* **2012**, *51,* 9994-10024.

(11) Xia, C.; Kwok, C. Y.; Nazar, L. F. A High-Energy-Density Lithium-Oxygen Battery Based on a Reversible Four-Electron Conversion to Lithium Oxide. *Science* **2018**, *361* (6404), 777-781.

(12) Johnson, L.; Li, C.; Liu, Z.; Chen, Y.; Freunberger, S. A.; Ashok, P. C.; Praveen, B. B.; Dholakia, K.; Tarascon, J.-M.; Bruce, P. G. The Role of LiO_2 Solubility in O_2 Reduction in Aprotic Solvents and Its Consequences for Li–O_2 Batteries. *Nature Chemistry* **2014**, *6* (12), 1091–1099.

(13) Adams, B. D.; Radtke, C.; Black, R.; Trudeau, M. L.; Zaghib, K.; Nazar, L. F. Current Density Dependence of Peroxide Formation in the Li-O2 Battery and Its Effect on Charge. *Energy and Environmental Science* **2013**, *6* (6), 1772-1778.

(14) Aetukuri, N. B.; McCloskey, B. D.; Garciá, J. M.; Krupp, L. E.; Viswanathan, V.; Luntz, A. C. Solvating Additives Drive Solution-Mediated Electrochemistry and Enhance Toroid Growth in Non-Aqueous Li-O_2 Batteries. *Nature Chemistry* **2015**, *7* (1), 50-56.

(15) Lim, H.-D.; Lee, B.; Bae, Y.; Park, H.; Ko, Y.; Kim, H.; Kim, J.; Kang, K. Reaction Chemistry in Rechargeable Li–O2 Batteries. *Chemical Society Review* **2017**, *46* (10), 2873–2888.

(16) Kwak, W.-J.; Park, J.-B.; Jung, H.-G.; Sun, Y.-K. Controversial Topics on Lithium Superoxide in Li–O_2 Batteries. *ACS Energy Letters* **2017**, *2* (12), 2756–2760.

(17) Halder, A.; Wang, H.-H.; Lau, K. C.; Assary, R. S.; Lu, J.; Vajda, S.; Amine, K.; Curtiss, L. A. Identification and Implications of Lithium Superoxide in Li–O_2 Batteries. *ACS Energy Letters* **2018**, *3* (5), 1105–1109.

(18) McCloskey, B. D.; Bethune, D. S.; Shelby, R. M.; Girishkumar, G.; Luntz, A. C. Solvents Critical Role in Nonaqueous Lithium-Oxygen Battery Electrochemistry. *The Journal of Physical Chemistry Letters* **2011**, *2* (10), 1161-1166, 1161-1166.

(19) Freunberger, S. A.; Chen, Y.; Peng, Z.; Griffin, J. M.; Hardwick, L. J.; Bardé, F.; Novák, P.; Bruce, P. G. Reactions in the Rechargeable Lithium-O_2 Battery with Alkyl Carbonate Electrolytes. *The Journal of American Chemical Society* **2011**, *133* (20), 8040-8047.

(20) Chen, Y.; Freunberger, S. A.; Peng, Z.; Bardé, F.; Bruce, P. G. Li–O2 Battery with a Dimethylformamide Electrolyte. *The Journal of American Chemical Society* **2012**, *134* (18), 7952–7957.

(21) Sharon, D.; Afri, M.; Noked, M.; Garsuch, A.; Frimer, A. A.; Aurbach, D. Oxidation of Dimethyl Sulfoxide Solutions by Electrochemical Reduction of Oxygen. *The Journal of Physical Chemistry Letters* **2013**, *4* (18), 3115–3119.

(22) Adams, B. D.; Black, R.; Williams, Z.; Fernandes, R.; Cuisinier, M.; Berg, E. J.; Novak, P.; Murphy, G. K.; Nazar, L. F. Towards a Stable Organic Electrolyte for the Lithium Oxygen Battery. *Advanced Energy Materials* **2015**, *5* (1), 1400867.

(23) Oh, S. H.; Yim, T.; Pomerantseva, E.; Nazar, L. F. Decomposition Reaction of Lithium Bis(Oxalato)Borate in the Rechargeable Lithium-Oxygen Cell. *Electrochemical and Solid-State Letters* **2011**, *14* (12), A185.

(24) Nasybulin, E.; Xu, W.; Engelhard, M. H.; Nie, Z.; Burton, S. D.; Cosimbescu, L.; Gross, M. E.; Zhang, J.-G. Effects of Electrolyte Salts on the Performance of Li–O_2 Batteries. *The Journal of Physical Chemistry C* **2013**, *117* (6), 2635–2645.

(25) Crystallization, L. O. L.; Black, R.; Oh, S. H.; Lee, J.; Yim, T.; Adams, B.; Nazar, L. F. Screening for Superoxide Reactivity in Li-O_2 Batteries: Effect on Li_2O_2/LiOH Crystallization. *The Journal of American Chemical Society* **2012**, *134* (6), 2902-2905.

(26) McCloskey, B. D.; Speidel, A.; Scheffler, R.; Miller, D. C.; Viswanathan, V.; Hummelshøj, J. S.; Nørskov, J. K.; Luntz, A. C. Twin Problems of Interfacial Carbonate Formation in Nonaqueous Li-O_2 Batteries. *The Journal of Physical Chemistry Letters* **2012**, *3* (8), 997-1001.

(27) Itkis, D. M.; Semenenko, D. A.; Kataev, E. Y.; Belova, A. I.; Neudachina, V. S.; Sirotina, A. P.; Hävecker, M.; Teschner, D.; Knop-Gericke, A.; Dudin, P.; Barinov, A.; Goodilin, E. A.; Shao-Horn, Y.; Yashina, L. V. Reactivity of Carbon in Lithium-Oxygen Battery Positive Electrodes. *Nano Letters* **2013**, *13* (10), 4697-4701.

(28) Adams, B. D.; Black, R.; Radtke, C.; Williams, Z.; Mehdi, B. L.; Browning, N. D.; Nazar, L. F. The Importance of Nanometric Passivating Films on Cathodes for Li-Air Batteries. *ACS Nano* **2014**, *8* (12), 12483-12493.

(29) Mccloskey, B. D.; Valery, A.; Luntz, A. C.; Gowda, S. R.; Wallraff, G. M.; Garcia, J. M.; Mori, T.; Krupp, L. E. Combining Accurate O_2 and Li_2O_2 Assays to Separate Discharge and Charge Stability Limitations in Nonaqueous Li-O_2 Batteries. *The Journal of Physical Chemistry Letters* **2013**, *4* (17), 2989-2993.

(30) Kang, S.; Mo, Y.; Ong, S. P.; Ceder, G. A Facile Mechanism for Recharging Li_2O_2 in Li-O_2 Batteries. *Chemistry of Materials* **2013**, *25* (16), 3328-3336.

(31) Ganapathy, S.; Adams, B. D.; Stenou, G.; Anastasaki, M. S.; Goubitz, K.; Miao, X. F.; Nazar, L. F.; Wagemaker, M. Nature of Li_2O_2 Oxidation in a Li-O_2 Battery Revealed by Operando X-Ray Diffraction. *The Journal of American Chemical Society* **2014**, *136* (46), 16335-16344.

(32) Viswanathan, V.; Thygesen, K. S.; Hummelshøj, J. S.; Nørskov, J. K.; Girishkumar, G.; McCloskey, B. D.; Luntz, A. C. Electrical Conductivity in Li_2O_2 and Its Role in Determining Capacity Limitations in Non-Aqueous Li-O_2 Batteries. *The Journal of Chemical Physics* **2011**, *135* (21), 214704.

(33) McCloskey, B. D.; Bethune, D. S.; Shelby, R. M.; Mori, T.; Scheffler, R.; Speidel, A.; Sherwood, M.; Luntz, A. C. Limitations in Rechargeability of Li-O2 Batteries and Possible Origins. *The Journal of Physical Chemistry Letters* **2012**, *3* (20), 3043–3047.

(34) Zhou, B.; Guo, L.; Zhang, Y.; Wang, J.; Ma, L.; Zhang, W. H.; Fu, Z.; Peng, Z. A High-Performance Li–O2 Battery with a Strongly Solvating Hexamethylphosphoramide Electrolyte and a LiPON-Protected Lithium Anode. *Advanced Materials* **2017**, *29* (30), 1701568.

(35) Piana, M.; Wandt, J.; Meini, S.; Buchberger, I.; Tsiouvaras, N.; Gasteiger, H. A. Stability of a Pyrrolidinium-Based Ionic Liquid in Li-O_2 Cells. *Journal of Electrochemical Society* **2014**, *161* (14), A1992.

(36) Matsuda, S.; Hashimoto, K.; Nakanishi, S. Efficient Li_2O_2 Formation via Aprotic Oxygen Reduction Reaction Mediated by Quinone Derivatives. *The Journal of Physical Chemistry C* **2014**, *118* (32), 18397-18400.

(37) Gao, X.; Chen, Y.; Johnson, L.; Bruce, P. G. Promoting Solution Phase Discharge in Li-O_2 Batteries Containing Weakly Solvating Electrolyte Solutions. *Nature Materials* **2016**, *15* (8), 882-888.

(38) Liu, T.; Frith, J. T.; Kim, G.; Kerber, R. N.; Dubouis, N.; Shao, Y.; Liu, Z.; Magusin, P. C. M. M.; Casford, M. T. L.; Garcia-Araez, N.; Grey, C. P. The Effect of Water on Quinone Redox Mediators in Nonaqueous Li-O_2 Batteries. *The Journal of American Chemical Society* **2018**, *140* (4), 1428-1437.

(39) Yang, L.; Frith, J. T.; Garcia-Araez, N.; Owen, J. R. A New Method to Prevent Degradation of Lithium-Oxygen Batteries: Reduction of Superoxide by Viologen. *Chemical Communications* **2015**, *51* (9), 1705-1708.

(40) Sun, D.; Shen, Y.; Zhang, W.; Yu, L.; Yi, Z.; Yin, W.; Wang, D.; Huang, Y.; Wang, J.; Wang, D.; Goodenough, J. B. A Solution-Phase Bifunctional Catalyst for Lithium-Oxygen Batteries. *The Journal of American Chemical Society* **2014**, *136* (25), 8941-8946.

(41) Kwak, W. J.; Mahammed, A.; Kim, H.; Nguyen, T. T.; Gross, Z.; Aurbach, D.; Sun, Y. K. Controllable and Stable Organometallic Redox Mediators for Lithium Oxygen Batteries. *Materials Horizons* **2020**, *7* (1), 214-222.

(42) Lim, H. D.; Song, H.; Kim, J.; Gwon, H.; Bae, Y.; Park, K. Y.; Hong, J.; Kim, H.; Kim, T.; Kim, Y. H.; Leprõ, X.; Ovalle-Robles, R.; Baughman, R. H.; Kang, K. Superior Rechargeability and Efficiency of Lithium-Oxygen Batteries: Hierarchical Air Electrode Architecture Combined with a Soluble Catalyst. *Angewandte Chemie International Edition* **2014**, *53* (15), 3926-3931.

(43) Liu, T.; Leskes, M.; Yu, W.; Moore, A. J.; Zhou, L.; Bayley, P. M.; Kim, G.; Grey, C. P. Cycling Li-O_2 Batteries via LiOH Formation and Decomposition. *Science* **2015**, *350* (6260), 530-533.

(44) Liang, Z.; Lu, Y. C. Critical Role of Redox Mediator in Suppressing Charging Instabilities of Lithium-Oxygen Batteries. *The Journal of American Chemical Society* **2016**, *138* (24), 7574-7583.

(45) Bergner, B. J.; Schürmann, A.; Peppler, K.; Garsuch, A.; Janek, J. TEMPO: A Mobile Catalyst for Rechargeable Li-O_2 Batteries. *The Journal of American Chemical Society* **2014**, *136* (42), 15054-15064.

(46) Chen, Y.; Freunberger, S. A.; Peng, Z.; Fontaine, O.; Bruce, P. G. Charging a Li-O_2 Battery Using a Redox Mediator. *Nature Chemistry* **2013**, *5* (6), 489-494.

(47) Kundu, D.; Black, R.; Adams, B.; Nazar, L. F. A Highly Active Low Voltage Redox Mediator for Enhanced Rechargeability of Lithium-Oxygen Batteries. *ACS Central Science* **2015**, *1* (9), 510-515.

(48) Kwak, W. J.; Kim, H.; Petit, Y. K.; Leypold, C.; Nguyen, T. T.; Mahne, N.; Redfern, P.; Curtiss, L. A.; Jung, H. G.; Borisov, S. M.; Freunberger, S. A.; Sun, Y. K. Deactivation of Redox

Mediators in Lithium-Oxygen Batteries by Singlet Oxygen. *Nature Communications* **2019**, *10* (1), 1380.

(49) Kwak, W.-J.; Park, J.; Kim, H.; Joo, J. M.; Aurbach, D.; Byon, H. R.; Sun, Y.-K. Oxidation Stability of Organic Redox Mediators as Mobile Catalysts in Lithium–Oxygen Batteries. *ACS Energy Letters* **2020**, *5* (6), 2122–2129.

(50) Schürmann, A.; Luerßen, B.; Mollenhauer, D.; Janek, J.; Schröder, D. Singlet Oxygen in Electrochemical Cells: A Critical Review of Literature and Theory. *Chemical Reviews* **2021**, *121* (20), 124450-12464.

(51) Ahn, S.; Zor, C.; Yang, S.; Lagnoni, M.; Dewar, D.; Nimmo, T.; Chau, C.; Jenkins, M.; Kibler, A. J.; Pateman, A.; Rees, G. J.; Gao, X.; Adamson, P.; Grobert, N.; Bertei, A.; Johnson, L. R.; Bruce, P. G. Why Charging Li–Air Batteries with Current Low-Voltage Mediators Is Slow and Singlet Oxygen Does Not Explain Degradation. *Nature Chemistry* **2023**, *15*, 1022-1029.

(52) Lee, H. W.; Kim, J. Y.; Kim, J. E.; Jo, Y. J.; Dewar, D.; Yang, S.; Gao, X.; Bruce, P. G.; Kwak, W. J. Effect of Singlet Oxygen on Redox Mediators in Lithium-Oxygen Batteries. *Journal of Material Chemistry A* **2023**, *11* (30), 16003-16008.

(53) Liu, Y.; Elias, Y.; Meng, J.; Aurbach, D.; Zou, R.; Xia, D.; Pang, Q. Electrolyte Solutions Design for Lithium-Sulfur Batteries. *Joule* **2021**, *5* (9), 2323–2364.

(54) Cuisinier, M.; Cabelguen, P. E.; Evers, S.; He, G.; Kolbeck, M.; Garsuch, A.; Bolin, T.; Balasubramanian, M.; Nazar, L. F. Sulfur Speciation in Li-S Batteries Determined by Operando X-Ray Absorption Spectroscopy. *The Journal of Physical Chemistry Letters* **2013**, *4* (19), 3227-3232.

(55) Manthiram, A.; Fu, Y.; Chung, S.-H.; Zu, C.; Su, Y.-S. Rechargeable Lithium–Sulfur Batteries. *Chemical Reviews* **2014**, *114* (23), 11751–11787.

(56) Pang, Q.; Liang, X.; Kwok, C. Y.; Kulisch, J.; Nazar, L. F. A Comprehensive Approach toward Stable Lithium–Sulfur Batteries with High Volumetric Energy Density. *Advanced Energy Materials* **2017**, *7* (6), 1601630.

(57) Kwok, C. Y.; Pang, Q.; Worku, A.; Liang, X.; Gauthier, M.; Nazar, L. F. Impact of the Mechanical Properties of a Functionalized Cross-Linked Binder on the Longevity of Li-S Batteries. *ACS Applied Materials and Interfaces* **2019**, *11* (25), 22481-22491.

(58) Cheng, X. B.; Yan, C.; Huang, J. Q.; Li, P.; Zhu, L.; Zhao, L.; Zhang, Y.; Zhu, W.; Yang, S. T.; Zhang, Q. The Gap between Long Lifespan Li-S Coin and Pouch Cells: The Importance of Lithium Metal Anode Protection. *Energy Storage Materials* **2017**, *6*, 18-25.

(59) Fan, F. Y.; Chiang, Y.-M. Electrodeposition Kinetics in Li-S Batteries: Effects of Low Electrolyte/Sulfur Ratios and Deposition Surface Composition. *Journal of Electrochemical Society* **2017**, *164* (4), A917.

(60) Zhao, M.; Li, B. Q.; Zhang, X. Q.; Huang, J. Q.; Zhang, Q. A Perspective toward Practical Lithium-Sulfur Batteries. *ACS Central Science* **2020**, *6* (7), 1095-1104.

(61) Liang, X.; Garsuch, A.; Nazar, L. F. Sulfur Cathodes Based on Conductive MXene Nanosheets for High-Performance Lithium–Sulfur Batteries. *Angewandte Chemie International Edition* **2015**, *54* (13), 3907–3911.

(62) Liang, X.; Kwok, C. Y.; Lodi-Marzano, F.; Pang, Q.; Cuisinier, M.; Huang, H.; Hart, C. J.; Houtarde, D.; Kaup, K.; Sommer, H.; Brezesinski, T.; Janek, J.; Nazar, L. F. Tuning Transition Metal Oxide-Sulfur Interactions for Long Life Lithium Sulfur Batteries: The "Goldilocks" Principle. *Advanced Energy Materials* **2016**, *6* (6), 1501636.

(63) Li, W.; Yao, H.; Yan, K.; Zheng, G.; Liang, Z.; Chiang, Y. M.; Cui, Y. The Synergetic Effect of Lithium Polysulfide and Lithium Nitrate to Prevent Lithium Dendrite Growth. *Nature Communications* **2015**, *6*, 7436.

(64) Cuisinier, M.; Cabelguen, P. E.; Adams, B. D.; Garsuch, A.; Balasubramanian, M.; Nazar, L. F. Unique Behaviour of Nonsolvents for Polysulphides in Lithium-Sulphur Batteries. *Energy and Environmental Science* **2014**, *7* (8), 2697-2705.

(65) Nakanishi, A.; Ueno, K.; Watanabe, D.; Ugata, Y.; Matsumae, Y.; Liu, J.; Thomas, M. L.; Dokko, K.; Watanabe, M. Sulfolane-Based Highly Concentrated Electrolytes of Lithium Bis(Trifluoromethanesulfonyl)Amide: Ionic Transport, Li-Ion Coordination, and Li-S Battery Performance. *The Journal of Physical Chemistry C* **2019**, *123* (23), 14229-14238.

(66) Pang, Q.; Shyamsunder, A.; Narayanan, B.; Kwok, C. Y.; Curtiss, L. A.; Nazar, L. F. Tuning the Electrolyte Network Structure to Invoke Quasi-Solid State Sulfur Conversion and Suppress Lithium Dendrite Formation in Li–S Batteries. *Nature Energy* **2018**, *3* (9), 783-791.

(67) Dokko, K.; Tachikawa, N.; Yamauchi, K.; Tsuchiya, M.; Yamazaki, A.; Takashima, E.; Park, J.-W.; Ueno, K.; Seki, S.; Serizawa, N.; Watanabe, M. Solvate Ionic Liquid Electrolyte for Li–S Batteries. *Journal of Electrochemical Society* **2013**, *160* (8), A1304.

(68) Cuisinier, M.; Hart, C.; Balasubramanian, M.; Garsuch, A.; Nazar, L. F. Radical or Not Radical: Revisiting Lithium-Sulfur Electrochemistry in Nonaqueous Electrolytes. *Advanced Energy Materials* **2015**, *5* (16), 1401801.

(69) He, Q.; Gorlin, Y.; Patel, M. U. M.; Gasteiger, H. A.; Lu, Y.-C. Unraveling the Correlation between Solvent Properties and Sulfur Redox Behavior in Lithium-Sulfur Batteries. *Journal of Electrochemical Society* **2018**, *165* (16), A4027.

(70) Baek, M.; Shin, H.; Char, K.; Choi, J. W. New High Donor Electrolyte for Lithium–Sulfur Batteries. *Advanced Materials* **2020**, *32* (52), 2005022.

(71) Cheng, X.-B.; Zhang, R.; Zhao, C.-Z.; Zhang, Q. Toward Safe Lithium Metal Anode in Rechargeable Batteries: A Review. *Chemical Review* **2017**, *117* (15), 10403–10473.

(72) Lin, D.; Liu, Y.; Cui, Y. Reviving the Lithium Metal Anode for High-Energy Batteries. *Nature Nanotechnology* **2017**, *12* (3), 194–206.

(73) Goodenough, J. B.; Kim, Y. Challenges for Rechargeable Li Batteries. *Chemistry of Materials* **2010**, *22* (3), 587–603.

(74) Qian, J.; Henderson, W. A.; Xu, W.; Bhattacharya, P.; Engelhard, M.; Borodin, O.; Zhang, J. G. High Rate and Stable Cycling of Lithium Metal Anode. *Nature Communications* **2015**, *6*, 6362.

(75) Boyle, D. T.; Kong, X.; Pei, A.; Rudnicki, P. E.; Shi, F.; Huang, W.; Bao, Z.; Qin, J.; Cui, Y. Transient Voltammetry with Ultramicroelectrodes Reveals the Electron Transfer Kinetics of Lithium Metal Anodes. *ACS Energy Letters* **2020**, *5* (3), 701-709.

(76) Aurbach, D.; Ein-Ely, Y.; Zaban, A. The Surface Chemistry of Lithium Electrodes in Alkyl Carbonate Solutions. *Journal of Electrochemical Society* **1994**, *141* (1), L1.

(77) Peled, E.; Golodnitsky, D.; Ardel, G. Advanced Model for Solid Electrolyte Interphase Electrodes in Liquid and Polymer Electrolytes. *Journal of Electrochemical Society* **1997**, *144* (8), L208.

(78) Markevich, E.; Salitra, G.; Chesneau, F.; Schmidt, M.; Aurbach, D. Very Stable Lithium Metal Stripping-Plating at a High Rate and High Areal Capacity in Fluoroethylene Carbonate-Based Organic Electrolyte Solution. *ACS Energy Letters* **2017**, *2* (6), 1321-1326.

(79) Menkin, S.; Okeefe, C. A.; Gunnarsdóttir, A. B.; Dey, S.; Pesci, F. M.; Shen, Z.; Aguadero, A.; Grey, C. P. Toward an Understanding of SEI Formation and Lithium Plating on Copper in Anode-Free Batteries. *The Journal of Physical Chemistry C* **2021**, *125* (30), 16719-16372.

(80) Park, M. S.; Ma, S. B.; Lee, D. J.; Im, D.; Doo, S. G.; Yamamoto, O. A Highly Reversible Lithium Metal Anode. *Scientific Reports* **2014**, *4*, 3815.

(81) Aurbach, D. Review of Selected Electrode-Solution Interactions Which Determine the Performance of Li and Li Ion Batteries. *Journal of Power Sources* **2000**, *89* (2), 206-218.

(82) Li, Y.; Qi, Y. Energy Landscape of the Charge Transfer Reaction at the Complex Li/SEI/Electrolyte Interface. *Energy and Environmental Science* **2019**, *12* (4), 1286-1294.

(83) Krauss, F. T.; Pantenburg, I.; Roling, B. Transport of Ions, Molecules, and Electrons across the Solid Electrolyte Interphase: What Is Our Current Level of Understanding? *Advanced Materials Interfaces* **2022**, *9* (8), 2101891.

(84) Guo, R.; Gallant, B. M. Li_2O Solid Electrolyte Interphase: Probing Transport Properties at the Chemical Potential of Lithium. *Chemistry of Materials* **2020**, *32* (13), 5525-5533.

(85) Lorger, S.; Narita, K.; Usiskin, R.; Maier, J. Enhanced Ion Transport in Li_2O and Li_2S Films. *Chemical Communications* **2021**, *57* (53), 6503-6506.

(86) Hu, T.; Tian, J.; Dai, F.; Wang, X.; Wen, R.; Xu, S. Impact of the Local Environment on Li Ion Transport in Inorganic Components of Solid Electrolyte Interphases. *The Journal of American Chemical Society* **2023**, *145* (2), 1327-1333.

(87) Shadike, Z.; Lee, H.; Borodin, O.; Cao, X.; Fan, X.; Wang, X.; Lin, R.; Bak, S. M.; Ghose, S.; Xu, K.; Wang, C.; Liu, J.; Xiao, J.; Yang, X. Q.; Hu, E. Identification of LiH and Nanocrystalline LiF in the Solid–Electrolyte Interphase of Lithium Metal Anodes. *Nature Nanotechnology* **2021**, *16* (5), 549-554.

(88) Chazalviel, J. N. Electrochemical Aspects of the Generation of Ramified Metallic Electrodeposits. *Physical Review A* **1990**, *42* (12), 7355-7367.

(89) Landesfeind, J.; Gasteiger, H. A. Temperature and Concentration Dependence of the Ionic Transport Properties of Lithium-Ion Battery Electrolytes. *Journal of Electrochemical Society* **2019**, *166* (14), A3079.

(90) Monroe, C.; Newman, J. Dendrite Growth in Lithium/Polymer Systems: A Propagation Model for Liquid Electrolytes under Galvanostatic Conditions. *Journal of Electrochemical Society* **2003**, *150* (10), A1377.

(91) Bai, P.; Li, J.; Brushett, F. R.; Bazant, M. Z. Transition of Lithium Growth Mechanisms in Liquid Electrolytes. *Energy and Environmental Science* **2016**, *9* (10), 3221-3229.

(92) Bai, P.; Guo, J.; Wang, M.; Kushima, A.; Su, L.; Li, J.; Brushett, F. R.; Bazant, M. Z. Interactions between Lithium Growths and Nanoporous Ceramic Separators. *Joule* **2018**, *2* (11), 2434-2449.

(93) Biswal, P.; Stalin, S.; Kludze, A.; Choudhury, S.; Archer, L. A. Nucleation and Early Stage Growth of Li Electrodeposits. *Nano Letters* **2019**, *19* (11), 8191-8200.

(94) Barton, J. L.; Bockris, J. O. The Electrolytic Growth of Dendrites from Ionic Solutions. *Proceedings of the Royal Society A* **1962**, *268* (1335), 485–505.

(95) Wood, K. N.; Kazyak, E.; Chadwick, A. F.; Chen, K. H.; Zhang, J. G.; Thornton, K.; Dasgupta, N. P. Dendrites and Pits: Untangling the Complex Behavior of Lithium Metal Anodes through Operando Video Microscopy. *ACS Central Science* **2016**, *2* (11), 790-801.

(96) Lin, D.; Liu, Y.; Cui, Y. Reviving the Lithium Metal Anode for High-Energy Batteries. *Nature Nanotechnology* **2017**, *12*, 194-206.

(97) Kozen, A. C.; Lin, C.-F.; Pearse, A. J.; Schroeder, M. A.; Han, X.; Hu, L.; Lee, S.-B.; Rubloff, G. W.; Noked, M. Next-Generation Lithium Metal Anode Engineering via Atomic Layer Deposition. *ACS Nano* **2015**, *9* (6), 5884–5892.

(98) Chen, L.; Connell, J. G.; Nie, A.; Huang, Z.; Zavadil, K. R.; Klavetter, K. C.; Yuan, Y.; Sharifi-Asl, S.; Shahbazian-Yassar, R.; Libera, J. A.; Mane, A. U.; Elam, J. W. Lithium Metal Protected by Atomic Layer Deposition Metal Oxide for High Performance Anodes. *Journal of Materials Chemistry A* **2017**, *5* (24), 12297-12309.

(99) Zhao, Y.; Amirmaleki, M.; Sun, Q.; Zhao, C.; Codirenzi, A.; Goncharova, L. V.; Wang, C.; Adair, K.; Li, X.; Yang, X.; Zhao, F.; Li, R.; Filleter, T.; Cai, M.; Sun, X. Natural SEI-Inspired Dual-Protective Layers via Atomic/Molecular Layer Deposition for Long-Life Metallic Lithium Anode. *Matter* **2019**, *1* (5), 1215-1231.

(100) Pang, Q.; Zhou, L.; Nazar, L. F. Elastic and Li-Ion–Percolating Hybrid Membrane Stabilizes Li Metal Plating. *Proceedings of the National Academy of Sciences of the United States of America* **2018**, *115* (49), 12389-12394.

(101) Li, S.; Huang, J.; Cui, Y.; Liu, S.; Chen, Z.; Huang, W.; Li, C.; Liu, R.; Fu, R.; Wu, D. A Robust All-Organic Protective Layer towards Ultrahigh-Rate and Large-Capacity Li Metal Anodes. *Nature Nanotechnology* **2022**, *17* (6), 613-621.

(102) Kim, M. S.; Ryu, J. H.; Deepika; Lim, Y. R.; Nah, I. W.; Lee, K. R.; Archer, L. A.; Il Cho, W. Langmuir–Blodgett Artificial Solid-Electrolyte Interphases for Practical Lithium Metal Batteries. *Nature Energy* **2018**, *3* (10), 880-898.

(103) Liang, X.; Pang, Q.; Kochetkov, I. R.; Sempere, M. S.; Huang, H.; Sun, X.; Nazar, L. F. A Facile Surface Chemistry Route to a Stabilized Lithium Metal Anode. *Nature Energy* **2017**, *2*, 17119.

(104) Wang, R.; Yu, J.; Tang, J.; Meng, R.; Nazar, L. F.; Huang, L.; Liang, X. Insights into Dendrite Suppression by Alloys and the Fabrication of a Flexible Alloy-Polymer Protected Lithium Metal Anode. *Energy Storage Materials* **2020**, *32*, 178-184.

(105) Ma, L.; Kim, M. S.; Archer, L. A. Stable Artificial Solid Electrolyte Interphases for Lithium Batteries. *Chemistry of Materials* **2017**, *29* (10), 4181-4189.

(106) Zhao, Q.; Tu, Z.; Wei, S.; Zhang, K.; Choudhury, S.; Liu, X.; Archer, L. A. Building Organic/Inorganic Hybrid Interphases for Fast Interfacial Transport in Rechargeable Metal Batteries. *Angewandte Chemie International Edition* **2018**, *57* (4), 992-996.

(107) Paul-Orecchio, A. G.; Stockton, L.; Weeks, J. A.; Dolocan, A.; Wang, Y.; Mullins, C. B. Alloying Indium Additive Enables Fast-Charging Lithium Metal Batteries. *ACS Energy Letters* **2023**, 4228–4234.

(108) Shimizu, M.; Umeki, M.; Arai, S. Suppressing the Effect of Lithium Dendritic Growth by the Addition of Magnesium Bis(Trifluoromethanesulfonyl)Amide. *Physical Chemistry Chemical Physics* **2018**, *20* (2), 1127-1133.

(109) Pang, Q.; Liang, X.; Shyamsunder, A.; Nazar, L. F. An In Vivo Formed Solid Electrolyte Surface Layer Enables Stable Plating of Li Metal. *Joule* **2017**, *1* (4), 871-886.

(110) Aurbach, D.; Pollak, E.; Elazari, R.; Salitra, G.; Kelley, C. S.; Affinito, J. On the Surface Chemical Aspects of Very High Energy Density, Rechargeable Li–Sulfur Batteries. *Journal of Electrochemical Society* **2009**, *156* (8), A694.

(111) Adams, B. D.; Carino, E. V.; Connell, J. G.; Han, K. S.; Cao, R.; Chen, J.; Zheng, J.; Li, Q.; Mueller, K. T.; Henderson, W. A.; Zhang, J. G. Long Term Stability of Li-S Batteries Using High Concentration Lithium Nitrate Electrolytes. *Nano Energy* **2017**, *40*, 607-617.

(112) Zhang, L.; Ling, M.; Feng, J.; Mai, L.; Liu, G.; Guo, J. The Synergetic Interaction between LiNO3 and Lithium Polysulfides for Suppressing Shuttle Effect of Lithium-Sulfur Batteries. *Energy Storage Mater* **2018**, *11*, 24-29.

(113) Shi, Q.; Zhong, Y.; Wu, M.; Wang, H.; Wang, H. High-Capacity Rechargeable Batteries Based on Deeply Cyclable Lithium Metal Anodes. *Proceedings of the National Academy of Sciences of the United States of America* **2018**, *115* (22), 5676-5680.

(114) Weber, R.; Genovese, M.; Louli, A. J.; Hames, S.; Martin, C.; Hill, I. G.; Dahn, J. R. Long Cycle Life and Dendrite-Free Lithium Morphology in Anode-Free Lithium Pouch Cells Enabled by a Dual-Salt Liquid Electrolyte. *Nature Energy* **2019**, *4* (8), 683-689.

(115) Fan, X.; Ji, X.; Chen, L.; Chen, J.; Deng, T.; Han, F.; Yue, J.; Piao, N.; Wang, R.; Zhou, X.; Xiao, X.; Chen, L.; Wang, C. All-Temperature Batteries Enabled by Fluorinated Electrolytes with Non-Polar Solvents. *Nature Energy* **2019**, *4* (10), 882-890.

(116) Yu, Z.; Wang, H.; Kong, X.; Huang, W.; Tsao, Y.; Mackanic, D. G.; Wang, K.; Wang, X.; Huang, W.; Choudhury, S.; Zheng, Y.; Amanchukwu, C. V.; Hung, S. T.; Ma, Y.; Lomeli, E. G.; Qin, J.; Cui, Y.; Bao, Z. Molecular Design for Electrolyte Solvents Enabling Energy-Dense and Long-Cycling Lithium Metal Batteries. *Nature Energy* **2020**, *5* (7), 526-533.

(117) Zhao, Y.; Zhou, T.; Mensi, M.; Choi, J. W.; Coskun, A. Electrolyte Engineering via Ether Solvent Fluorination for Developing Stable Non-Aqueous Lithium Metal Batteries. *Nature Communications* **2023**, *14* (1), 299.

(118) Mao, M.; Ji, X.; Wang, Q.; Lin, Z.; Li, M.; Liu, T.; Wang, C.; Hu, Y. S.; Li, H.; Huang, X.; Chen, L.; Suo, L. Anion-Enrichment Interface Enables High-Voltage Anode-Free Lithium Metal Batteries. *Nature Communications* **2023**, *14* (1), 1082.

(119) Ueno, K.; Yoshida, K.; Tsuchiya, M.; Tachikawa, N.; Dokko, K.; Watanabe, M. Glyme-Lithium Salt Equimolar Molten Mixtures: Concentrated Solutions or Solvate Ionic Liquids? *The Journal of Physical Chemistry B* **2012**, *116* (36), 11323-11331.

(120) Cao, X.; Jia, H.; Xu, W.; Zhang, J.-G. Review—Localized High-Concentration Electrolytes for Lithium Batteries. *Journal of Electrochemical Society* **2021**, *168* (1), 010522.

(121) Ren, X.; Zou, L.; Cao, X.; Engelhard, M. H.; Liu, W.; Burton, S. D.; Lee, H.; Niu, C.; Matthews, B. E.; Zhu, Z.; Wang, C.; Arey, B. W.; Xiao, J.; Liu, J.; Zhang, J. G.; Xu, W. Enabling High-Voltage Lithium-Metal Batteries under Practical Conditions. *Joule* **2019**, *3* (7), 1662-1676.

(122) Li, T.; Zhang, X.-Q.; Shi, P.; Zhang, Q. Fluorinated Solid-Electrolyte Interphase in High-Voltage Lithium Metal Batteries. *Joule* **2019**, *3* (11), 2647–2661.

(123) Wi, T. U.; Park, S. O.; Yeom, S. J.; Kim, M. H.; Kristanto, I.; Wang, H.; Kwak, S. K.; Lee, H. W. Revealing the Dual-Layered Solid Electrolyte Interphase on Lithium Metal Anodes via Cryogenic Electron Microscopy. *ACS Energy Letters* **2023**, *8* (5), 2193-2200.

(124) Janek, J.; Zeier, W. G. A Solid Future for Battery Development. *Nature Energy* **2016**, *1* (9), 16141.

(125) Janek, J.; Zeier, W. G. Challenges in Speeding up Solid-State Battery Development. *Nature Energy* **2023**, *8* (3), 230–240.

(126) Zhang, Z.; Shao, Y.; Lotsch, B.; Hu, Y.-S.; Li, H.; Janek, J.; Nazar, L. F.; Nan, C.-W.; Maier, J.; Armand, M.; Chen, L. New Horizons for Inorganic Solid State Ion Conductors. *Energy and Environ Science* **2018**, *11* (8), 1945–1976.

(127) Tina Casey. *BMW's Excellent Solid-State EV Battery Adventure*. https://cleantechnica.com/2023/01/21/bmws-excellent-solid-state-ev-battery-adventure/.

(128) Zaman, W.; Hatzell, K. B. Processing and Manufacturing of next Generation Lithium-Based All Solid-State Batteries. *Current Opinion in Solid State Materials Science* **2022**, *26* (4), 101003.

(129) Wang, C.; Fu, K.; Kammampata, S. P.; McOwen, D. W.; Samson, A. J.; Zhang, L.; Hitz, G. T.; Nolan, A. M.; Wachsman, E. D.; Mo, Y.; Thangadurai, V.; Hu, L. Garnet-Type Solid-State Electrolytes: Materials, Interfaces, and Batteries. *Chemical Reviews* **2020**, *120* (10), 4257–4300.

(130) Zhao, G.; Suzuki, K.; Okumura, T.; Takeuchi, T.; Hirayama, M.; Kanno, R. Extending the Frontiers of Lithium-Ion Conducting Oxides: Development of Multicomponent Materials with γ-Li_3PO_4-Type Structures. *Chemistry of Materials* **2022**, *34* (9), 3948–3959.

(131) Jun, K. J.; Sun, Y.; Xiao, Y.; Zeng, Y.; Kim, R.; Kim, H.; Miara, L. J.; Im, D.; Wang, Y.; Ceder, G. Lithium Superionic Conductors with Corner-Sharing Frameworks. *Nature Materials* **2022**, *21* (8), 924-931.

(132) Kamaya, N.; Homma, K.; Yamakawa, Y.; Hirayama, M.; Kanno, R.; Yonemura, M.; Kamiyama, T.; Kato, Y.; Hama, S.; Kawamoto, K.; Mitsui, A. A Lithium Superionic Conductor. *Nature Materials* **2011**, *10* (9), 682–686.

(133) Kraft, M. A.; Ohno, S.; Zinkevich, T.; Koerver, R.; Culver, S. P.; Fuchs, T.; Senyshyn, A.; Indris, S.; Morgan, B. J.; Zeier, W. G. Inducing High Ionic Conductivity in the Lithium Superionic Argyrodites $Li_{6+x}P_{1-x}Ge_xS5_I$ for All-Solid-State Batteries. *The Journal of American Chemical Society* **2018**, *140* (47), 16330 - 16339.

(134) Adeli, P.; Bazak, J. D.; Park, K. H.; Kochetkov, I.; Huq, A.; Goward, G. R.; Nazar, L. F. Boosting Solid-State Diffusivity and Conductivity in Lithium Superionic Argyrodites by Halide Substitution. *Angewandte Chemie International Edition* **2019**, *58* (26), 8681 - 8686.

(135) Zhou, L.; Assoud, A.; Zhang, Q.; Wu, X.; Nazar, L. F. New Family of Argyrodite Thioantimonate Lithium Superionic Conductors. *The Journal of American Chemical Society* **2019**, *141* (48), 19002-19013.

(136) Feng, X.; Chien, P. H.; Wang, Y.; Patel, S.; Wang, P.; Liu, H.; Immediato-Scuotto, M.; Hu, Y. Y. Enhanced Ion Conduction by Enforcing Structural Disorder in Li-Deficient Argyrodites $Li_{6-x}PS_{5-x}Cl_{1+x}$. *Energy Storage Materials* **2020**, *30*, 67 - 73.

(137) Asano, T.; Sakai, A.; Ouchi, S.; Sakaida, M.; Miyazaki, A.; Hasegawa, S. Solid Halide Electrolytes with High Lithium-Ion Conductivity for Application in 4 V Class Bulk-Type All-Solid-State Batteries. *Advanced Materials* **2018**, *30* (44), 1803075.

(138) Li, X.; Liang, J.; Luo, J.; Norouzi Banis, M.; Wang, C.; Li, W.; Deng, S.; Yu, C.; Zhao, F.; Hu, Y.; Sham, T. K.; Zhang, L.; Zhao, S.; Lu, S.; Huang, H.; Li, R.; Adair, K. R.; Sun, X. Air-Stable Li_3InCl_6 Electrolyte with High Voltage Compatibility for All-Solid-State Batteries. *Energy and Environmental Science* **2019**, *12* (9), 2665 – 2671.

(139) Park, K. H.; Kaup, K.; Assoud, A.; Zhang, Q.; Wu, X.; Nazar, L. F. High-Voltage Superionic Halide Solid Electrolytes for All-Solid-State Li-Ion Batteries. *ACS Energy Letters* **2020**, *5* (2), 533 – 539.

(140) Zhou, L.; Kwok, C. Y.; Shyamsunder, A.; Zhang, Q.; Wu, X.; Nazar, L. F. A New Halospinel Superionic Conductor for High-Voltage All Solid State Lithium Batteries. *Energy Environmental Science* **2020**, *13* (7), 2056 – 2063.

(141) Kim, S. Y.; Kaup, K.; Park, K. H.; Assoud, A.; Zhou, L.; Liu, J.; Wu, X.; Nazar, L. F. Lithium Ytterbium-Based Halide Solid Electrolytes for High Voltage All-Solid-State Batteries. *ACS Mater Lett* **2021**, *3* (7), 930 – 938.

(142) Park, J.; Han, D.; Kwak, H.; Han, Y.; Choi, Y. J.; Nam, K. W.; Jung, Y. S. Heat Treatment Protocol for Modulating Ionic Conductivity via Structural Evolution of $Li_{3-x}Yb_{1-x}M_xCl_6$ (M = Hf^{4+}, Zr^{4+}) New Halide Superionic Conductors for All-Solid-State Batteries. *Chemical Engineering Journal* **2021**, *425* (1), 130630.

(143) Kwak, H.; Han, D.; Lyoo, J.; Park, J.; Jung, S. H.; Han, Y.; Kwon, G.; Kim, H.; Hong, S. T.; Nam, K. W.; Jung, Y. S. New Cost-Effective Halide Solid Electrolytes for All-Solid-State Batteries: Mechanochemically Prepared Fe^{3+}-Substituted Li_2ZrCl_6. *Advanced Energy Materials* **2021**, *11* (12), 2003190.

(144) Kwak, H.; Han, D.; Son, J. P.; Kim, J. S.; Park, J.; Nam, K. W.; Kim, H.; Jung, Y. S. Li^+ Conduction in Aliovalent-Substituted Monoclinic Li_2ZrCl_6 for All-Solid-State Batteries: $Li_{2+x}Zr_{1-x}M_xCl_6$ (M = In, Sc). *Chemical Engineering Journal* **2022**, *437*, 135413.

(145) Zhou, L.; Zuo, T. T.; Kwok, C. Y.; Kim, S. Y.; Assoud, A.; Zhang, Q.; Janek, J.; Nazar, L. F. High Areal Capacity, Long Cycle Life 4 V Ceramic All-Solid-State Li-Ion Batteries Enabled by Chloride Solid Electrolytes. *Nature Energy* **2022**, *7* (1), 83-93.

(146) Cao, D.; Sun, X.; Li, Q.; Natan, A.; Xiang, P.; Zhu, H. Lithium Dendrite in All-Solid-State Batteries: Growth Mechanisms, Suppression Strategies, and Characterizations. *Matter* **2020**, *3* (1), 57–94.

(147) Han, F.; Westover, A. S.; Yue, J.; Fan, X.; Wang, F.; Chi, M.; Leonard, D. N.; Dudney, N. J.; Wang, H.; Wang, C. High Electronic Conductivity as the Origin of Lithium Dendrite Formation within Solid Electrolytes. *Nature Energy* **2019**, *4* (3), 187–196.

(148) Ning, Z.; Li, G.; Melvin, D. L. R.; Chen, Y.; Bu, J.; Spencer-Jolly, D.; Liu, J.; Hu, B.; Gao, X.; Perera, J.; Gong, C.; Pu, S. D.; Zhang, S.; Liu, B.; Hartley, G. O.; Bodey, A. J.; Todd, R. I.; Grant, P. S.; Armstrong, D. E. J.; Marrow, T. J.; Monroe, C. W.; Bruce, P. G. Dendrite Initiation and Propagation in Lithium Metal Solid-State Batteries. *Nature* **2023**, *618* (7964), 287–293.

(149) Connell, J. G.; Fuchs, T.; Hartmann, H.; Krauskopf, T.; Zhu, Y.; Sann, J.; Garcia-Mendez, R.; Sakamoto, J.; Tepavcevic, S.; Janek, J. Kinetic versus Thermodynamic Stability of LLZO in Contact with Lithium Metal. *Chemistry of Materials* **2020**, *32* (23), 10207–10215.

(150) Otto, S. K.; Riegger, L. M.; Fuchs, T.; Kayser, S.; Schweitzer, P.; Burkhardt, S.; Henss, A.; Janek, J. In Situ Investigation of Lithium Metal–Solid Electrolyte Anode Interfaces with ToF-SIMS. *Advanced Materials Interfaces* **2022**, *9* (13), 2102387.

(151) Wenzel, S.; Randau, S.; Leichtweiß, T.; Weber, D. A.; Sann, J.; Zeier, W. G.; Janek, J. Direct Observation of the Interfacial Instability of the Fast Ionic Conductor $Li_{10}GeP_2S_{12}$ at the Lithium Metal Anode. *Chemistry of Materials* **2016**, *28* (7), 2400–2407.

(152) Riegger, L. M.; Schlem, R.; Sann, J.; Zeier, W. G.; Janek, J. Lithium-Metal Anode Instability of the Superionic Halide Solid Electrolytes and the Implications for Solid-State Batteries. *Angewandte Chemie International Edition* **2021**, *60* (12), 6718.

(153) Wenzel, S.; Sedlmaier, S. J.; Dietrich, C.; Zeier, W. G.; Janek, J. Interfacial Reactivity and Interphase Growth of Argyrodite Solid Electrolytes at Lithium Metal Electrodes. *Solid State Ionics* **2018**, *318*, 102–112.

(154) Wenzel, S.; Weber, D. A.; Leichtweiss, T.; Busche, M. R.; Sann, J.; Janek, J. Interphase Formation and Degradation of Charge Transfer Kinetics between a Lithium Metal Anode and Highly Crystalline $Li_7P_3S_{11}$ Solid Electrolyte. *Solid State Ionics* **2016**, *286*, 24–33.

(155) Lee, S.; Lee, K. S.; Kim, S.; Yoon, K.; Han, S.; Lee, M. H.; Ko, Y.; Noh, J. H.; Kim, W.; Kang, K. Design of a Lithiophilic and Electron-Blocking Interlayer for Dendrite-Free Lithium-Metal Solid-State Batteries. *Science Advances* **2022**, *8* (30), eabq0153.

(156) Nagao, K.; Nagata, Y.; Sakuda, A.; Hayashi, A.; Deguchi, M.; Hotehama, C.; Tsukasaki, H.; Mori, S.; Orikasa, Y.; Yamamoto, K.; Uchimoto, Y.; Tatsumisago, M. A Reversible Oxygen Redox Reaction in Bulk-Type All-Solid-State Batteries. *Science Advances* **2020**, *6* (25), eaax7236.

(157) Nagao, M.; Hayashi, A.; Tatsumisago, M. Bulk-Type Lithium Metal Secondary Battery with Indium Thin Layer at Interface between Li Electrode and Li_2S-P_2S_5 Solid Electrolyte. *Electrochemistry* **2012**, *80* (10), 734–736.

(158) Shao, Y.; Wang, H.; Gong, Z.; Wang, D.; Zheng, B.; Zhu, J.; Lu, Y.; Hu, Y. S.; Guo, X.; Li, H.; Huang, X.; Yang, Y.; Nan, C. W.; Chen, L. Drawing a Soft Interface: An Effective Interfacial Modification Strategy for Garnet-Type Solid-State Li Batteries. *ACS Energy Letters* **2018**, *3* (6), 1212-1218.

(159) Lee, Y. G.; Fujiki, S.; Jung, C.; Suzuki, N.; Yashiro, N.; Omoda, R.; Ko, D. S.; Shiratsuchi, T.; Sugimoto, T.; Ryu, S.; Ku, J. H.; Watanabe, T.; Park, Y.; Aihara, Y.; Im, D.; Han, I. T. High-Energy Long-Cycling All-Solid-State Lithium Metal Batteries Enabled by Silver–Carbon Composite Anodes. *Nature Energy* **2020**, *5* (4), 299-308.

(160) Kim, J. S.; Yoon, G.; Kim, S.; Sugata, S.; Yashiro, N.; Suzuki, S.; Lee, M. J.; Kim, R.; Badding, M.; Song, Z.; Chang, J. M.; Im, D. Surface Engineering of Inorganic Solid-State Electrolytes via Interlayers Strategy for Developing Long-Cycling Quasi-All-Solid-State Lithium Batteries. *Nature Communication* **2023**, *14* (1), 782.

(161) Spencer-Jolly, D.; Agarwal, V.; Doerrer, C.; Hu, B.; Zhang, S.; Melvin, D. L. R.; Gao, H.; Gao, X.; Adamson, P.; Magdysyuk, O. V.; Grant, P. S.; House, R. A.; Bruce, P. G. Structural Changes in the Silver-Carbon Composite Anode Interlayer of Solid-State Batteries. *Joule* **2023**, *7* (3), 503-514.

(162) Minnmann, P.; Quillman, L.; Burkhardt, S.; Richter, F. H.; Janek, J. Editors' Choice—Quantifying the Impact of Charge Transport Bottlenecks in Composite Cathodes of All-Solid-State Batteries. *Journal of Electrochemical Society* **2021**, *168* (4), 040537.

(163) Schwietert, T. K.; Arszelewska, V. A.; Wang, C.; Yu, C.; Vasileiadis, A.; de Klerk, N. J. J.; Hageman, J.; Hupfer, T.; Kerkamm, I.; Xu, Y.; van der Maas, E.; Kelder, E. M.; Ganapathy, S.; Wagemaker, M. Clarifying the Relationship between Redox Activity and Electrochemical Stability in Solid Electrolytes. *Nature Materials* **2020**, *19* (4), 428-435.

(164) Zuo, T. T.; Walther, F.; Teo, J. H.; Rueß, R.; Wang, Y.; Rohnke, M.; Schröder, D.; Nazar, L. F.; Janek, J. Impact of the Chlorination of Lithium Argyrodites on the Electrolyte/Cathode Interface in Solid-State Batteries. *Angewandte Chemie International Edition* **2023**, *62* (7), e202213228.

(165) Zhang, W.; Richter, F. H.; Culver, S. P.; Leichtweiss, T.; Lozano, J. G.; Dietrich, C.; Bruce, P. G.; Zeier, W. G.; Janek, J. Degradation Mechanisms at the $Li_{10}GeP_2S_{12}/LiCoO_2$ Cathode Interface in an All-Solid-State Lithium-Ion Battery. *ACS Applied Materials and Interfaces* **2018**, *10* (26), 22226-22236.

(166) Zuo, T. T.; Rueß, R.; Pan, R.; Walther, F.; Rohnke, M.; Hori, S.; Kanno, R.; Schröder, D.; Janek, J. A Mechanistic Investigation of the $Li_{10}GeP_2S_{12}|LiNi_{1-x-y}Co_xMn_yO_2$ Interface Stability in All-Solid-State Lithium Batteries. *Nature Communications* **2021**, *12* (1), 6669.

(167) Walther, F.; Koerver, R.; Fuchs, T.; Ohno, S.; Sann, J.; Rohnke, M.; Zeier, W. G.; Janek, J. Visualization of the Interfacial Decomposition of Composite Cathodes in Argyrodite-Based All-Solid-State Batteries Using Time-of-Flight Secondary-Ion Mass Spectrometry. *Chemistry of Materials* **2019**, 3745–3755.

(168) Bartsch, T.; Strauss, F.; Hatsukade, T.; Schiele, A.; Kim, A. Y.; Hartmann, P.; Janek, J.; Brezesinski, T. Gas Evolution in All-Solid-State Battery Cells. *ACS Energy Letters* **2018**, *3* (10), 2539–2543.

(169) Kim, A. Y.; Strauss, F.; Bartsch, T.; Teo, J. H.; Hatsukade, T.; Mazilkin, A.; Janek, J.; Hartmann, P.; Brezesinski, T. Stabilizing Effect of a Hybrid Surface Coating on a Ni-Rich NCM Cathode Material in All-Solid-State Batteries. *Chemistry of Materials* **2019**, *31* (23), 9664–9672.

(170) Jung, S. H.; Oh, K.; Nam, Y. J.; Oh, D. Y.; Brüner, P.; Kang, K.; Jung, Y. S. Li_3BO_3-Li_2CO_3: Rationally Designed Buffering Phase for Sulfide All-Solid-State Li-Ion Batteries. *Chemistry of Materials* **2018**, *30* (22), 8190 – 8200.

(171) Ma, Y.; Teo, J. H.; Walther, F.; Ma, Y.; Zhang, R.; Mazilkin, A.; Tang, Y.; Goonetilleke, D.; Janek, J.; Bianchini, M.; Brezesinski, T. Advanced Nanoparticle Coatings for Stabilizing Layered Ni-Rich Oxide Cathodes in Solid-State Batteries. *Advanced Functional Materials* **2022**, *32* (23), 2111829.

(172) Wang, S.; Bai, Q.; Nolan, A. M.; Liu, Y.; Gong, S.; Sun, Q.; Mo, Y. Lithium Chlorides and Bromides as Promising Solid-State Chemistries for Fast Ion Conductors with Good Electrochemical Stability. *Angewandte Chemie International Edition* **2019**, *58* (24), 8039.

(173) Dietzek, B.; Cialla, D.; Schmitt, M.; Popp, J. Introduction to the Fundamentals of Raman Spectroscopy. *Springer Series in Optical Sciences* **2010**, *158*, 47-52.

(174) R. Black. The Impact of Degradation Reactions on Aprotic Metal-O_2 Battery Performance, University of Waterloo, 2016.

(175) Kim, T.; Choi, W.; Shin, H. C.; Choi, J. Y.; Kim, J. M.; Park, M. S.; Yoon, W. S. Applications of Voltammetry in Lithium Ion Battery Research. *Journal of Electrochemical Science and Technology* **2020**, *11* (1), 14–25.

(176) Lazanas, A. C.; Prodromidis, M. I. Electrochemical Impedance Spectroscopy─A Tutorial. *ACS Measurement Science Au* **2023**, *3* (3), 162-193.

(177) Vadhva, P.; Hu, J.; Johnson, M. J.; Stocker, R.; Braglia, M.; Brett, D. J. L.; Rettie, A. J. E. Electrochemical Impedance Spectroscopy for All-Solid-State Batteries: Theory, Methods and Future Outlook. *ChemElectroChem*. **2021**, *8*, 1930.

(178) Kwak, W. J.; Hirshberg, D.; Sharon, D.; Shin, H. J.; Afri, M.; Park, J. B.; Garsuch, A.; Chesneau, F. F.; Frimer, A. A.; Aurbach, D.; Sun, Y. K. Understanding the Behavior of Li-Oxygen Cells Containing LiI. *Journal of Materials Chemistry A* **2015**, *3* (16), 8855–8864.

(179) Schwenke, K. U.; Metzger, M.; Restle, T.; Piana, M.; Gasteiger, H. A. The Influence of Water and Protons on Li_2O_2 Crystal Growth in Aprotic Li-O_2 Cells. *Journal of Electrochemical Society* **2015**, *162* (4), A573.

(180) Louli, A. J.; Eldesoky, A.; Weber, R.; Genovese, M.; Coon, M.; deGooyer, J.; Deng, Z.; White, R. T.; Lee, J.; Rodgers, T.; Petibon, R.; Hy, S.; Cheng, S. J. H.; Dahn, J. R. Diagnosing and Correcting Anode-Free Cell Failure via Electrolyte and Morphological Analysis. *Nature Energy* **2020**, *5* (9), 6933-702.

(181) Rudola, A.; Du, K.; Balaya, P. Monoclinic Sodium Iron Hexacyanoferrate Cathode and Non-Flammable Glyme-Based Electrolyte for Inexpensive Sodium-Ion Batteries. *Journal of Electrochemical Society* **2017**, *164* (6), A1098–A1109.

(182) Han, S.-D.; Sommer, R. D.; Boyle, P. D.; Zhou, Z.-B.; Young, V. G.; Borodin, O.; Henderson, W. A. Electrolyte Solvation and Ionic Association: Part IX. Structures and Raman Spectroscopic Characterization of LiFSI Solvates. *Journal of Electrochemical Society* **2022**, *169* (11), 110544.

(183) Yamada, Y.; Yaegashi, M.; Abe, T.; Yamada, A. A Superconcentrated Ether Electrolyte for Fast-Charging Li-Ion Batteries. *Chemical Communications* **2013**, *49* (95), 11194-11196.

(184) Fawdon, J.; Ihli, J.; Mantia, F. La; Pasta, M. Characterising Lithium-Ion Electrolytes via Operando Raman Microspectroscopy. *Nature Communications* **2021**, *12* (1), 4053.

(185) Machida, K.; Miyazawa, T. Infrared and Raman Spectra of Polyethyleneglycol Dimethylethers in the Liquid State. *Spectrochimica Acta* **1964**, *20* (12), 1865-1873.

(186) Yang, X.; Su, Z.; Wu, D.; Hsu, S. L.; Stidham, H. D. Raman Analysis of a Conformational Distribution of Poly(Ethylene Oxide) and Its Model Compound in the Liquid State. *Macromolecules* **1997**, *30* (13),

(187) Brouillette, D.; Irish, D. E.; Taylor, N. J.; Perron, G.; Odziemkowski, M.; Desnoyers, J. E. Stable Solvates in Solution of Lithium Bis(Trifluoromethylsulfone)Imide in Glymes and Other Aprotic Solvents: Phase Diagrams, Crystallography and Raman Spectroscopy. *Physical Chemistry Chemical Physics* **2002**, *4* (24), 3796–3802.

(188) Henderson, W. A. Glyme-Lithium Salt Phase Behavior. *The Journal of Physical Chemistry B* **2006**, *110* (26), 13177 – 13183.

(189) Zhang, C.; Ueno, K.; Yamazaki, A.; Yoshida, K.; Moon, H.; Mandai, T.; Umebayashi, Y.; Dokko, K.; Watanabe, M. Chelate Effects in Glyme/Lithium Bis(Trifluoromethanesulfonyl)Amide Solvate Ionic Liquids. I. Stability of Solvate Cations and Correlation with Electrolyte Properties. *The Journal of Physical Chemistry B* **2014**, *118* (19), 5144 - 5153.

(190) Ren, F.; Li, Z.; Chen, J.; Huguet, P.; Peng, Z.; Deabate, S. Solvent–Diluent Interaction-Mediated Solvation Structure of Localized High-Concentration Electrolytes. *ACS Applied Materials and Interfaces* **2022**, *14* (3), 4211 – 4219.

(191) Drvarič Talian, S.; Bobnar, J.; Sinigoj, A. R.; Humar, I.; Gaberšček, M. Transmission Line Model for Description of the Impedance Response of Li Electrodes with Dendritic Growth. *The Journal of Physical Chemistry C* **2019**, *123* (46), 27997 – 28007.

(192) Sälzer, F.; Pateras Pescara, L.; Franke, F.; Müller, C.; Winkler, J.; Schwalm, M.; Roling, B. Assessing the Ion Transport Properties of Highly Concentrated Non-Flammable Electrolytes in a Commercial Li-Ion Battery Cell. *Battery & Supercaps* **2020**, *3* (1), 117.

(193) Wang, M.; Huai, L.; Hu, G.; Yang, S.; Ren, F.; Wang, S.; Zhang, Z.; Chen, Z.; Peng, Z.; Shen, C.; Wang, D. Effect of LiFSI Concentrations to Form Thickness- and Modulus-Controlled SEI Layers on Lithium Metal Anodes. *The Journal of Physical Chemistry C* **2018**, *122* (18), 9825–9834.

(194) Weng, S.; Zhang, X.; Yang, G.; Zhang, S.; Ma, B.; Liu, Q.; Liu, Y.; Peng, C.; Chen, H.; Yu, H.; Fan, X.; Cheng, T.; Chen, L.; Li, Y.; Wang, Z.; Wang, X. Temperature-Dependent Interphase Formation and Li^+ Transport in Lithium Metal Batteries. *Nature Communications* **2023**, *14* (1), 4474.

(195) Yao, Y. X.; Chen, X.; Yan, C.; Zhang, X. Q.; Cai, W. L.; Huang, J. Q.; Zhang, Q. Regulating Interfacial Chemistry in Lithium-Ion Batteries by a Weakly Solvating Electrolyte. *Angewandte Chemie International Edition* **2021**, *60* (8), 4090.

(196) Wohde, F.; Balabajew, M.; Roling, B. Li^+ Transference Numbers in Liquid Electrolytes Obtained by Very-Low-Frequency Impedance Spectroscopy at Variable Electrode Distances. *Journal of Electrochemical Society* **2016**, *163* (5), A714.

(197) Dong, D.; Sälzer, F.; Roling, B.; Bedrov, D. How Efficient Is Li^+ Ion Transport in Solvate Ionic Liquids under Anion-Blocking Conditions in a Battery? *Physical Chemistry Chemical Physics* **2018**, *20* (46), 29174 – 29183.

(198) Evans, J.; Vincent, C. A.; Bruce, P. G. Electrochemical Measurement of Transference Numbers in Polymer Electrolytes. *Polymer* **1987**, *28* (13), 2324 – 2328.

(199) Pham, T. D.; Bin Faheem, A.; Kim, J.; Oh, H. M.; Lee, K. K. Practical High-Voltage Lithium Metal Batteries Enabled by Tuning the Solvation Structure in Weakly Solvating Electrolyte. *Small* **2022**, *18* (14), 2107492.

(200) Chen, Y.; Li, M.; Liu, Y.; Jie, Y.; Li, W.; Huang, F.; Li, X.; He, Z.; Ren, X.; Chen, Y.; Meng, X.; Cheng, T.; Gu, M.; Jiao, S.; Cao, R. Origin of Dendrite-Free Lithium Deposition in Concentrated Electrolytes. *Nature Communications* **2023**, *14* (1), 2655.

(201) Fang, C.; Li, J.; Zhang, M.; Zhang, Y.; Yang, F.; Lee, J. Z.; Lee, M. H.; Alvarado, J.; Schroeder, M. A.; Yang, Y.; Lu, B.; Williams, N.; Ceja, M.; Yang, L.; Cai, M.; Gu, J.; Xu, K.; Wang, X.; Meng, Y. S. Quantifying Inactive Lithium in Lithium Metal Batteries. *Nature* **2019**, *572* (7770), 511 – 515.

(202) Aurbach, D.; Youngman, O.; Gofer, Y.; Meitav, A. The Electrochemical Behaviour of 1,3-Dioxolane—$LiClO_4$ Solutions—I. Uncontaminated Solutions. *Electrochimica Acta* **1990**, *35* (3), 625–638.

(203) Liu, J.; Bao, Z.; Cui, Y.; Dufek, E. J.; Goodenough, J. B.; Khalifah, P.; Li, Q.; Liaw, B. Y.; Liu, P.; Manthiram, A.; Meng, Y. S.; Subramanian, V. R.; Toney, M. F.; Viswanathan, V. V.; Whittingham, M. S.; Xiao, J.; Xu, W.; Yang, J.; Yang, X. Q.; Zhang, J. G. Pathways for Practical High-Energy Long-Cycling Lithium Metal Batteries. *Nature Energy* **2019**, *4*, 180-186.

(204) Park, K. J.; Hwang, J. Y.; Ryu, H. H.; Maglia, F.; Kim, S. J.; Lamp, P.; Yoon, C. S.; Sun, Y. K. Degradation Mechanism of Ni-Enriched NCA Cathode for Lithium Batteries: Are Microcracks Really Critical? *ACS Energy Letters* **2019**, *4* (6), 1394-1400.

(205) Adams, B. D.; Zheng, J.; Ren, X.; Xu, W.; Zhang, J. G. Accurate Determination of Coulombic Efficiency for Lithium Metal Anodes and Lithium Metal Batteries. *Advanced Energy Materials* **2018**, *8* (7), 1702097.

(206) Zhou, L.; Assoud, A.; Shyamsunder, A.; Huq, A.; Zhang, Q.; Hartmann, P.; Kulisch, J.; Nazar, L. F. An Entropically Stabilized Fast-Ion Conductor: $Li_{3.25}[Si_{0.25}P_{0.75}]S_4$. *Chemistry of Materials* **2019**, *31* (19), 7801–7811.

(207) Kang, D.; Hart, N.; Xiao, M.; Lemmon, J. P. Short Circuit of Symmetrical Li/Li Cell in Li Metal Anode Research. *Acta Physico - Chimica Sinica* **2021**, *37* (2), 200801.

(208) Ye, L.; Li, X. A Dynamic Stability Design Strategy for Lithium Metal Solid State Batteries. *Nature* **2021**, *593* (7858), 218-222.

(209) Ge, Z.; Chen, N.; Wang, R.; Ma, R.; Fan, B.; Le coq, D.; Zhang, X.; Ma, H.; Xue, B. Constructing Dendrite Suppressing Mixed Sulfide Solid Electrolyte for High-Rate Lithium Metal Batteries. *Chemical Engineering Journal* **2023**, *467*, 143409.

(210) Busche, M. R.; Drossel, T.; Leichtweiss, T.; Weber, D. A.; Falk, M.; Schneider, M.; Reich, M. L.; Sommer, H.; Adelhelm, P.; Janek, J. Dynamic Formation of a Solid-Liquid Electrolyte Interphase and Its Consequences for Hybrid-Battery Concepts. *Nature Chemistry* **2016**, *8* (5), 426–434.

(211) Simon, F. J.; Hanauer, M.; Henss, A.; Richter, F. H.; Janek, J. Properties of the Interphase Formed between Argyrodite-Type Li_6PS_5Cl and Polymer-Based PEO_{10}:LiTFSI. *ACS Applied Material and Interfaces* **2019**, *11* (45), 42186–42196.

(212) Oh, D. Y.; Nam, Y. J.; Park, K. H.; Jung, S. H.; Cho, S. J.; Kim, Y. K.; Lee, Y. G.; Lee, S. Y.; Jung, Y. S. Excellent Compatibility of Solvate Ionic Liquids with Sulfide Solid Electrolytes: Toward Favorable Ionic Contacts in Bulk-Type All-Solid-State Lithium-Ion Batteries. *Advanced Energy Materials* **2015**, *5* (22), 1500865.

(213) Kasemchainan, J.; Zekoll, S.; Spencer Jolly, D.; Ning, Z.; Hartley, G. O.; Marrow, J.; Bruce, P. G. Critical Stripping Current Leads to Dendrite Formation on Plating in Lithium Anode Solid Electrolyte Cells. *Nature Materials* **2019**, *18* (10), 1105–1111.

(214) Bhargav, A.; He, J.; Gupta, A.; Manthiram, A. Lithium-Sulfur Batteries: Attaining the Critical Metrics. *Joule* **2020**, 2 (19), 285–291.

(215) Waluś, S.; Barchasz, C.; Bouchet, R.; Alloin, F. Electrochemical Impedance Spectroscopy Study of Lithium–Sulfur Batteries: Useful Technique to Reveal the Li/S Electrochemical Mechanism. *Electrochimica Acta* **2020**, *359*, 136944.

(216) Martin, R. R.; Doub, W. H.; Roberts, J. L.; Sawyer, D. T. Electrochemical Reduction of Sulfur in Aprotic Solvents. *Inorganic Chemistry* **1973**, *12* (8), 1921–1925.

(217) Sharafi, A.; Kazyak, E.; Davis, A. L.; Yu, S.; Thompson, T.; Siegel, D. J.; Dasgupta, N. P.; Sakamoto, J. Surface Chemistry Mechanism of Ultra-Low Interfacial Resistance in the Solid-State Electrolyte $Li_7La_3Zr_2O_{12}$. *Chemistry of Materials* **2017**, *29* (18), 7961–7968.

(218) Hojo, M.; Sawyer, D. T. Hydroxide-Induced Reduction of Elemental Sulfur (S_8) To The Trisulfur Anion Radical ($S_3^{\cdot-}$). *Inorganic Chemistry* **1989**, *28* (6), 1201–1202.

(219) Huo, H.; Chen, Y.; Zhao, N.; Lin, X.; Luo, J.; Yang, X.; Liu, Y.; Guo, X.; Sun, X. In-Situ Formed Li_2CO_3-Free Garnet/Li Interface by Rapid Acid Treatment for Dendrite-Free Solid-State Batteries. *Nano Energy* **2019**, *61*, 119–125.

(220) Bates, J. B.; Dudney, N. J.; Gruzalski, G. R.; Zuhr, R. A.; Choudhury, A.; Luck, C. F.; Robertson, J. D. Electrical Properties of Amorphous Lithium Electrolyte Thin Films. *Solid State Ionics* **1992**, *53–56* (Part 1), 647–654.

(221) Ohnishi, T.; Takada, K. Sputter-Deposited Amorphous Li_3PO_4 Solid Electrolyte Films. *ACS Omega* **2022**, *7* (24), 21199–21206.

(222) Sunding, M. F.; Hadidi, K.; Diplas, S.; Løvvik, O. M.; Norby, T. E.; Gunnæs, A. E. XPS Characterization of in Situ Treated Lanthanum Oxide and Hydroxide Using Tailored Charge Referencing and Peak Fitting Procedures. *Journal of Electron Spectroscopy and Related Phenomena* **2011**, *184* (7), 399–409.

(223) Qu, H.; Ju, J.; Chen, B.; Xue, N.; Du, H.; Han, X.; Zhang, J.; Xu, G.; Yu, Z.; Wang, X.; Cui, G. Inorganic Separators Enable Significantly Suppressed Polysulfide Shuttling in High-Performance Lithium-Sulfur Batteries. *Journal of Materials Chemistry A* **2018**, *6* (46), 23720–23729.

(224) Shi, C.; Hamann, T.; Takeuchi, S.; Alexander, G. V.; Nolan, A. M.; Limpert, M.; Fu, Z.; O'Neill, J.; Godbey, G.; Dura, J. A.; Wachsman, E. D. 3D Asymmetric Bilayer Garnet-Hybridized High-Energy-Density Lithium-Sulfur Batteries. *ACS Applied Materials and Interfaces* **2022**, 15 (1), 751–760.

(225) Lee, K.; Kazyak, E.; Wang, M. J.; Dasgupta, N. P.; Sakamoto, J. Analyzing Void Formation and Rewetting of Thin in Situ-Formed Li Anodes on LLZO. *Joule* **2022**, *6* (11), 2547–2565.

(226) Kresse, G.; Furthmüller, J. Efficiency of Ab-Initio Total Energy Calculations for Metals and Semiconductors Using a Plane-Wave Basis Set. *Computational Materials Science* **1996**, *6* (1), 15–50.

(227) Kresse, G.; Furthmüller, J. Efficient Iterative Schemes for Ab Initio Total-Energy Calculations Using a Plane-Wave Basis Set. *Physical Review B* **1996**, *54* (16), 11169–11186.

(228) Blöchl, P. E. Projector Augmented-Wave Method. *Physical Review B* **1994**, *50* (24), 17953–17979.

(229) Perdew, J. P.; Burke, K.; Ernzerhof, M. Generalized Gradient Approximation Made Simple. *Phys Review Letters* **1996**, *77* (18), 3865–3868.

(230) Jain, A.; Ong, S. P.; Hautier, G.; Chen, W.; Richards, W. D.; Dacek, S.; Cholia, S.; Gunter, D.; Skinner, D.; Ceder, G.; Persson, K. A. Commentary: The Materials Project: A Materials Genome Approach to Accelerating Materials Innovation. *APL Materials* **2013**, *1* (1), 011002.

(231) *ScOCl (ScClO, T = 540 K) Crystal Structure*: https://materials.springer.com/isp/crystallographic/docs/sd_1238827.

(232) Ong, S. P.; Richards, W. D.; Jain, A.; Hautier, G.; Kocher, M.; Cholia, S.; Gunter, D.; Chevrier, V. L.; Persson, K. A.; Ceder, G. Python Materials Genomics (Pymatgen): A Robust, Open-Source Python Library for Materials Analysis. *Computational Materials Science* **2013**, *68*, 314–319.

(233) Richards, W. D.; Miara, L. J.; Wang, Y.; Kim, J. C.; Ceder, G. Interface Stability in Solid-State Batteries. *Chemistry of Materials* **2016**, *28* (1), 266–273.

(234) Zhu, Y.; He, X.; Mo, Y. First Principles Study on Electrochemical and Chemical Stability of Solid Electrolyte–Electrode Interfaces in All-Solid-State Li-Ion Batteries. *Journal of Materials Chemistry A* **2016**, *4* (9), 3253–3266.

(235) Moškon, J.; Žuntar, J.; Drvarič Talian, S.; Dominko, R.; Gaberšček, M. A Powerful Transmission Line Model for Analysis of Impedance of Insertion Battery Cells: A Case Study on the NMC-Li System. *Journal of Electrochemical Society* **2020**, *167* (14), 140639.

(236) Kwok, C. Y.; Xu, S.; Kochetkov, I.; Zhou, L.; Nazar, L. F. High-Performance All-Solid-State Li_2S Batteries Using an Interfacial Redox Mediator. *Energy and Environmental Science* **2023**, *16* (2), 610–618.

(237) Boukamp, B. A.; Bouwmeester, H. J. M. Interpretation of the Gerischer Impedance in Solid State Ionics. *Solid State Ionics* **2003**; *157* (1-4), 29–33.

(238) Braun, P.; Uhlmann, C.; Weiss, M.; Weber, A.; Ivers-Tiffée, E. Assessment of All-Solid-State Lithium-Ion Batteries. *Journal of Power Sources* **2018**, *393*, 119–127.

(239) Koç, T.; Marchini, F.; Rousse, G.; Dugas, R.; Tarascon, J. M. In Search of the Best Solid Electrolyte-Layered Oxide Pairing for Assembling Practical All-Solid-State Batteries. *ACS Applied Energy Materials* **2021**, *4* (12), 13575–13585.

(240) Rosenbach, C.; Walther, F.; Ruhl, J.; Hartmann, M.; Hendriks, T. A.; Ohno, S.; Janek, J.; Zeier, W. G. Visualizing the Chemical Incompatibility of Halide and Sulfide-Based Electrolytes in Solid-State Batteries. *Advanced Energy Materials* **2023**, *13* (6), 2203673.

(241) Märker, K.; Reeves, P. J.; Xu, C.; Griffith, K. J.; Grey, C. P. Evolution of Structure and Lithium Dynamics in $LiNi_{0.8}Mn_{0.1}Co_{0.1}O_2$ (NMC811) Cathodes during Electrochemical Cycling. *Chemistry of Materials* **2019**, *31* (7), 2545–2554.

(242) Nethercot, A. H. Prediction of Fermi Energies and Photoelectric Thresholds Based on Electronegativity Concepts. *Physical Review Letters* **1974**, *33* (18), 1088–1091.

(243) Campero, A.; Diáz Ponce, J. A. Averaged Scale in Electronegativity Joined to Physicochemical Perturbations. Consequences of Periodicity. *ACS Omega* **2020**, *5* (40), 25520 – 25542.

(244) Hozl, F. K. Schulte, *Work function of metals,* in *Holzl's, Schulte's, Wagner's Solid Surface Physics. Springer Tracts in Modern Physics*, Springer, Berlin, Heidelberg, 1979, vol. 85, p. 28.

(245) Schwietert, T. K.; Vasileiadis, A.; Wagemaker, M. First-Principles Prediction of the Electrochemical Stability and Reaction Mechanisms of Solid-State Electrolytes. *JACS Au* **2021**, *1* (9), 1488 – 1496.

(246) Xu, G.; Luo, L.; Liang, J.; Zhao, S.; Yang, R.; Wang, C.; Yu, T.; Wang, L.; Xiao, W.; Wang, J.; Yu, J.; Sun, X. Origin of High Electrochemical Stability of Multi-Metal Chloride Solid Electrolytes for High Energy All-Solid-State Lithium-Ion Batteries. *Nano Energy* **2022**, *92*, 106674.

(247) Jung, R.; Metzger, M.; Maglia, F.; Stinner, C.; Gasteiger, H. A. Oxygen Release and Its Effect on the Cycling Stability of $LiNi_xMn_yCo_zO_2$ (NMC) Cathode Materials for Li-Ion Batteries. *Journal of Electrochemical Society* **2017**, *164* (7), A1361.

(248) Li, H.; Liu, A.; Zhang, N.; Wang, Y.; Yin, S.; Wu, H.; Dahn, J. R. An Unavoidable Challenge for Ni-Rich Positive Electrode Materials for Lithium-Ion Batteries. *Chemistry of Materials* **2019**, *31* (18), 7574–7583.

(249) Kwak, H.; Han, D.; Lyoo, J.; Park, J.; Jung, S. H.; Han, Y.; Kwon, G.; Kim, H.; Hong, S. T.; Nam, K. W.; Jung, Y. S. New Cost-Effective Halide Solid Electrolytes for All-Solid-State Batteries: Mechanochemically Prepared Fe^{3+}-Substituted Li_2ZrCl_6. *Advanced Energy Materials* **2021**, *11* (12), 2003190.

(250) Shi, C.; Takeuchi, S.; Alexander, G. V.; Hamann, T.; O'Neill, J.; Dura, J. A.; Wachsman, E. D. High Sulfur Loading and Capacity Retention in Bilayer Garnet Sulfurized-Polyacrylonitrile/Lithium-Metal Batteries with Gel Polymer Electrolytes. *Advanced Energy Materials* **2023**, *13*, 2301656.

(251) Zhang, G.; Chang, J.; Wang, L.; Li, J.; Wang, C.; Wang, R.; Shi, G.; Yu, K.; Huang, W.; Zheng, H.; Wu, T.; Deng, Y.; Lu, J. A Monofluoride Ether-Based Electrolyte Solution for Fast-Charging and Low-Temperature Non-Aqueous Lithium Metal Batteries. *Nature Communications* **2023**, *14* (1), 1081.

(252) Xia, Y.; Zhou, P.; Kong, X.; Tian, J.; Zhang, W.; Yan, S.; Hou, W.; Zhou, H. Y.; Dong, H.; Chen, X.; Wang, P.; Xu, Z.; Wan, L.; Wang, B.; Liu, K. Designing an Asymmetric Ether-like Lithium Salt to Enable Fast-Cycling High-Energy Lithium Metal Batteries. *Nature Energy* **2023**, *8* (9), 934–945.

(253) Tanaka, Y.; Ueno, K.; Mizuno, K.; Takeuchi, K.; Asano, T.; Sakai, A. New Oxyhalide Solid Electrolytes with High Lithium Ionic Conductivity >10 mS cm^{-1} for All-Solid-State Batteries. *Angewandte Chemie International Edition* **2023**, *62* (13), e202217581.

(254) Hittorf, W. Ueber die Wanderungen der Ionen während der Elektrolyse. *Annalen der Physik und Chemie* **1853**, *165*, 177-211.

Appendix A

Oxygen Evolution in the Presence of LiI

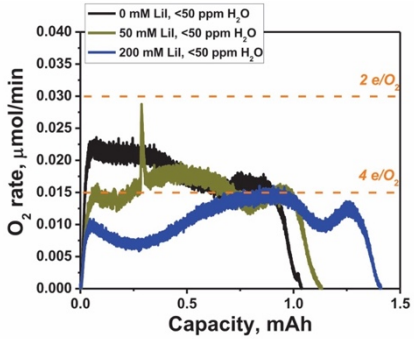


Figure A1.1 Oxygen evolution at different [LiI]. The cells were discharged to a capacity of 1 mAh and then charged under Ar flow using the home-made DEMS. The cells were cycled at 0.1mA.cm^{-2} as shown in **Figure 3.2 A**

Appendix B

Reactivity between LiI and O_2^-

The chemical instability of LiI in the presence of O_2^- was probed by dissolving 0.2 M LiI into 5 ml of G_4 with 500 ppm D_2O. G_4 was selected due to its higher stability against O_2^- than DME. Then 1.5 mmol KO_2 (Sigma Aldrich) and 2.5 mmol 18-crown-6 ether were added. The mixture became light brown, indicating the formation of I_3^- (**Figure B1.1 A**). After 12 hours of stirring, the solid was collected and analyzed with ^{1}H NMR. The 1H NMR spectrum indicates the formation of lithium formate and lithium acetate (**Figure B1.1 B**).

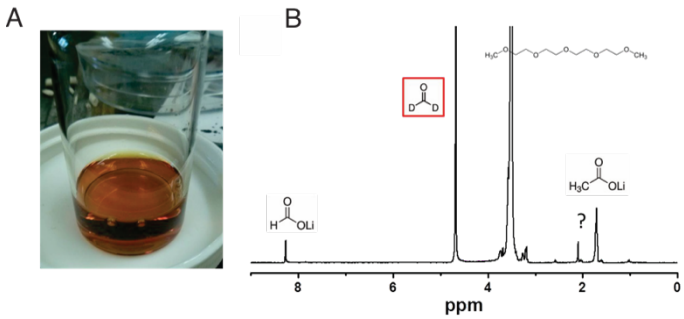


Figure B1.1 Reactivity between LiI and O_2^- A) Coloration of the LiI solution in the presence of KO_2. B) ^{1}H NMR of the reacted solid

Appendix C

Determination of t_{Li} by the Bruce-Vincent Method

Lithium transference number is one of the most critical characteristics of the binary liquid electrolyte because it demonstrates the contribution of Li^+-containing species to the total ion transport. The true value for t_{Li} cannot be determined using the Hittorf approach based on a direct chemical analysis of different sections of the electrolyte after passing a known amount of charge[254], as it is experimentally challenging for the systems with Li electrodes. In practice, t_{Li} is often measured by the Bruce-Vincent method.[198] The method is based on the low voltage dc (ΔV <15 mV) polarization of the Li-symmetric cells, and the t_{Li} is the ratio of the current at a steady state (j_{ss}) to the current at 0 s (j_0), corrected for the change in the interfacial impedance:

$$t_{Li}=\frac{j_{SS}\left(\Delta V - j_0 R_{before}\right)}{j_0\left(\Delta V - j_{SS} R_{after}\right)}$$

The example of measuring t_{Li} by the Bruce-Vincent method is provided in **Figure C.1.** It results in the o t_{Li} of 0.34. This value is overestimated in comparison with the values (0.22) obtained via EIS and the DFT-predicted t_{Li}-values of the equimolar LiTFSI/G_1 electrolytes.[197]

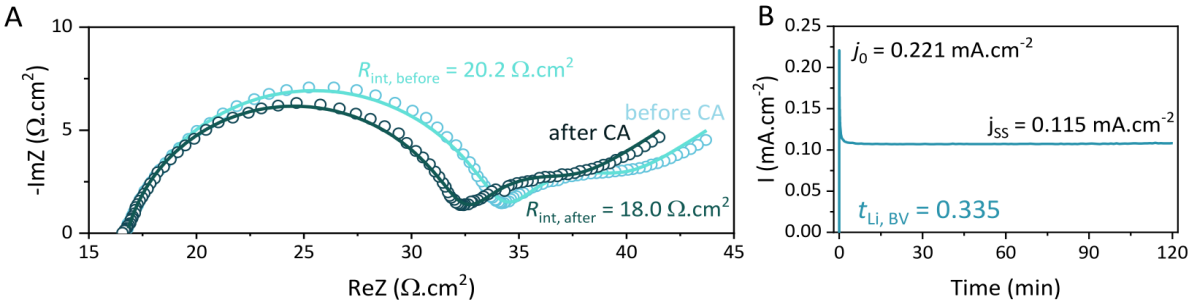


Figure C.1 (A) Nyquist plot of the Li symmetric cell with 114G_1 before and after the polarization step. (B) Polarization of the Li symmetric cell at a constant voltage of 10 mV.